Doctoral theses at NTNU, 2022:401

Trygve Lindahl Schanche

Pretreatment of manganese ores in $CO/CO_2/H_2$ atmospheres

Doctoral thesis

NTNU
Norwegian University of Science and Technology
Thesis for the Degree of
Philosophiae Doctor
Faculty of Natural Sciences
Department of Materials Science and Engineering

NTNU
Norwegian University of
Science and Technology

Trygve Lindahl Schanche

Pretreatment of manganese ores in $CO/CO_2/H_2$ atmospheres

Thesis for the Degree of Philosophiae Doctor

Trondheim, December 2022

Norwegian University of Science and Technology
Faculty of Natural Sciences
Department of Materials Science and Engineering

NTNU
Norwegian University of
Science and Technology

NTNU
Norwegian University of Science and Technology

Thesis for the Degree of Philosophiae Doctor

Faculty of Natural Sciences
Department of Materials Science and Engineering

ISBN 978-82-326-6893-9 (printed ver.)
ISBN 978-82-326-5267-9 (electronic ver.)
ISSN 1503-8181 (printed ver.)
ISSN 2703-8084 (online ver.)

Doctoral theses at NTNU, 2022:401

Printed by NTNU Grafisk senter

Preface

This thesis is submitted to the Norwegian University of Science and Technology (NTNU) as a partial fulfillment of the requirements for the degree Philosophiae Doctor. The research presented in this thesis was conducted at the Department of Materials Science and Engineering (DMSE) at NTNU – Trondheim, under the supervision of Professor Merete Tangstad, and the experimental work was done by the author. Two master students working on prereduction of manganese ores, were co-supervised by the author. Scientific papers based on the students works were written and submitted for publication.

This work was funded by the project "KPN reduced CO_2 emissions in metal production", The author gratefully acknowledge the financial support from the Research Council of Norway (Grant number: 280968) and our industrial partners Elkem ASA, TiZir Titanium & Iron AS, Eramet Norway AS, Finnfjord AS, and Wacker Chemicals Norway AS.

The purpose of this thesis was to investigate the kinetics of manganese raw materials during pre-treatment in a separate unit using different gas atmospheres. Two commercial manganese ores were investigated for this purpose, and were supplied by Eramet Norway AS.

Part of the work presented in this thesis have been included in the following scientific papers:

- Schanche TL, Tangstad M. Isothermal reduction of Nchwaning Manganese ore in $CO/CO_2/H_2$ atmospheres. *The 16th International Ferro-Alloys Congress* (INFACON XVI), 2021
- Schanche TL, Tangstad, M. Prereduction of Nchwaning ore in $CO/CO_2/H_2$ gas mixtures. *Minerals* 2021, *11*, 1097

Co-authored publications:

- Mukono T, Reiersen HS, Schanche TL, Wallin M, Tangstad M. Prereduction behavior of manganese ores with solid carbon and in CO/CO_2 gas atmosphere. *Metall Mater Trans B*. Published online August 16, 2022. doi:10.1007/s11663-022-02611-5
- Davies J, Schanche TL. Tangstad M, du Preez SP, Pre-reduction of United Manganese of Kalahari ore in CO/CO_2, H_2, and H_2/H_2O gas atmospheres. *Metall Mater Trans B*. (Submitted for publication)

Acknowledgements

While undertaking a PhD is in many cases a lonesome endeavor, it is also a product of cooperation and support from the surrounding people.

First and foremost, I would like to acknowledge my supervisor Prof. Merete Tangstad (NTNU). You are truly an expert in the field of metallurgy, but perhaps more importantly, an excellent supervisor. Thank you for valuable and interesting discussions, for helping me simplify when I over-complicate and complicate when I'm over-simplifying. Your valuable advice and feedback have improved this thesis as a product, and me as a scientist. I would also like to acknowledge my co-supervisors; Dr. Maria Wallin, I appreciate our discussions, your advice and that your door is always open, and Dr. Eli Ringdalen, for facilitating and showing interest in the work.

I would also like to thank my many great colleagues at NTNU. I have appreciated the discussions with my fellow prereducers; Leandro de Jesus, Trine Larssen, Dmitry Sukhomlinov, Didier Ngoy and Tichaona Mukono. I have also appreciated the many, and sometimes useful, discussions with the PhD's and Post Doc's in the department. Particularly my office mates throughout these years; Mado, Hamideh, Hossein, Dmitry, Trine and Tich, as well as my fellow project mates; Vince, Si-Trygve and Gerrit. My "Light Metal" bandmates; Andrea, Erlend, Karin, Bendik, Andreas, Kristian, Sigvart, Solveig and Håkon are also acknowledged for facilitating an artistic outlet during the PhD. I would also like to acknowledge the most excellent master students I was fortunate to cooperate with, Jamey Davies and Henrik Reiersen.

The experimental work was made possible with the assistance of Nicholas Smith-Hanssen (SINTEF), Jonas Gjøvik (SINTEF), Dmitry Slizovskiy (NTNU), Yingda Yu (NTNU), Ben Snook (NTNU), Pål Skaret (NTNU), Berit Vinje-Kramer (NTNU), Kristin Høydalsvik Wells (NTNU) and Bendik Sægrov-Sorte (SINTEF). I would also like to acknowledge Stein Rørvik (SINTEF) for the CT measurements, Morten Raanes (NTNU) for the EPMA analysis and Stefanie Lode at the Norwegian Laboratory for Mineral and Materials Characterisation, (MiMaC) with the support from The Research Council of Norway (grant 269842/F50), for the Quantitative mineralogical analysis.

Finally, I would like to thank my family for all their support and motivation. I am especially grateful to my loving and supporting wife Aimée, who tolerates my nerding about manganese production and challenges me to speak about it in understandable terms, and to my children Anja, Emil and Runa, for enduring my monologues on metallurgy and for tolerating my absence in the last months of this work.

Abstract

During industrial production of manganese ferroalloys, the manganese raw materials are prereduced in the low temperature zone of the submerged arc furnace (SAF). The endothermic Boudouard reaction ($CO_2 + C = 2CO$) consumes most of the CO_2 produced above 800 °C and will consume CO_2 from the prereduction reactions occurring above this temperature, resulting in excess consumption of energy and carbon. The energy and carbon consumption are affected by additional factors such as ore quality, flux addition and operational conditions, however calculations and industrial measurements indicate that reduction in the range of 300 kWh and 70 kg C per ton alloy produced is theoretically possible by improved prereduction. Pretreatment of the ore may thus be used to reduce this excess carbon and energy consumption.

In this work, the prereduction behavior of two commercial manganese ores is investigated in conditions simulating a pretreatment unit. In the pretreatment unit, moisture and bound water is evaporated and the raw materials are prereduced prior to their addition to the furnace. This will improve the overall prereduction thus reducing the excess carbon and energy consumption. To avoid the Boudouard reaction in the pretreatment unit, prereduction was investigated at temperatures below 800 °C. Prereduction in different CO/CO_2 mixtures were studied to simulate the use of furnace off-gas. In addition, reduction in $CO/CO_2/H_2$ gas mixtures, with similar pO_2 to the utilized CO/CO_2 mixtures, was studied was studied to evaluate the effect of H_2.

The investigated ores represent different types of raw materials. Nchwaning ore is a dense ore, mainly consisting of Mn_2O_3 type oxides in addition to a small amount of carbonates, while Comilog ore is a porous ore that consist of MnO_2 type oxides and has a significant content of bound water. During reduction of Nchwaning ore, the Mn_2O_3 oxides were reduced to MnO without formation of Mn_3O_4. Iron oxides were reduced to FeO which was stabilized in solid solution with MnO. Carbonates other than calcite decomposed. The reduction of Comilog ore is characterized by a rapid initial decomposition of bound H_2O in parallel with MnO_2 reduction. MnO_2 is reduced directly to MnO above 370 °C, while some accumulation of Mn_3O_4 occurs below this temperature due to the relatively slower reduction of Mn_3O_4 to MnO compared to MnO_2 to Mn_3O_4. Both the different porosities and mineral composition of the ores cause differences in their reactivity. The reduction of Comilog ore is initiated and completed at lower temperatures compared to Nchwaning ore, hence, most of the experiments on Comilog ore were conducted in the temperature range 365-455 °C, whereas the less reactive Nchwaning ore was reduced between 605-790 °C.

The reduction rate increased with increasing temperature and decreasing pO_2, as expected. In hydrogen containing gas mixtures, the reduction rate was higher compared to CO/CO_2 gas mixtures at constant pO_2, and it is suggested that this is caused by the improved diffusion properties of hydrogen. Modeling revealed an increased reduction rate by a factor 1.8-3.4 for Nchwaning and 1.7-1.9 for Comilog ore by using a hydrogen containing gas mixture at constant partial pressure. The dependency on reducing gas content was higher for CO/CO_2 gas mixtures compared to hydrogen containing gas mixture i.e., the reduction rate is more severely retarded by depletion of reducing gas when hydrogen is not present.

The improved reduction rate using hydrogen in the gas mixture makes it possible to pretreat the ores at lower temperatures when hydrogen is utilized, or to achieve a higher degree of prereduction at the same temperature compared to the use of CO/CO_2 gas mixtures alone.

With the addition of H_2 to the gas mixture, the water gas shift reaction ($CO + H_2O = CO_2 + H_2$) is expected. From the off-gas at the end of the experiments, it was seen that the reaction occurred above 410 °C, and approached equilibrium with increasing temperature towards 790 °C. The addition of H_2 was also seen to facilitate carbon deposition between 455-605 °C.

It was found that the Comilog ore samples reduced at 455 °C and below, oxidized upon exposure to air at room temperature, which was caused by oxidation of MnO to Mn_3O_4. The degree of reoxidation at constant temperature was lower in the samples reduced with hydrogen in the gas mixture, which may be due to that the formed MnO is more evenly distributed throughout the particles and thus less accessible to oxygen compared to the samples reduced in CO/CO_2 gas mixtures. Reoxidation of Nchwaning ore was not observed. Nchwaning ore was reduced at higher temperatures compared to Comilog ore, and the monoxide (MnO) -phase has a higher content of FeO. Both factors are known to stabilize MnO against reoxidation.

After each experiment, the ore was sieved and the ore on each sieve was weighed to determine the decrepitation of the ores. The decrepitation of Nchwaning ore was found to be a function of degree of reduction while the decrepitation of Comilog ore was also dependent on reduction temperature. Comilog ore reduced at low temperatures decrepitated more compared to when higher temperatures were used despite a higher degree of reduction for the latter case.

Prereducing manganese ores to MnO-FeO is feasible at low temperatures (515-790 °C). The remaining contribution to the excess carbon and energy consumption industrially is the reduction of FeO to metallic iron and decomposition of calcite. It was seen that improving the prereduction has a

significant impact on the composition and amount of off-gas from the furnace. i.e., reducing carbon and energy consumption simultaneously reduces the reducing gas content and the amount of off-gas from the SAF.

Contents

Preface i
Acknowledgements ii
Abstract iii
1 Introduction and background 1
1.1 Introduction 1
1.2 Background 2
1.2.1 Overview of ferroalloy production 2
1.2.2 Energy and carbon consumption 3
1.3 Scope of thesis 7
2 Literature review 8
2.1 Industrial production 8
2.1.1 Pretreatment of raw materials 9
2.2 Manganese raw materials 12
2.2.1 Ore 12
2.2.2 Sinter 14
2.2.3 Briquettes 14
2.2.4 Nodules 15
2.3 Equilibrium relations during prereduction 16
2.4 The prereduction rate of Manganese raw materials 21
2.4.1 The effect of mineral composition and porosity on prereduction 22
2.4.2 Effect of temperature and heating rate on prereduction 27
2.4.3 Effect of particle size on prereduction 30
2.4.4 Effect of gas composition on prereduction 31
2.4.5 Summary of influences on kinetics of prereduction 35
2.5 Decrepitation and disintegration 36
3 Materials and method 45
3.1 Raw materials 45
3.1.1 Nchwaning ore 46

3.1.2 Comilog ore 48
3.2 Apparatus 50
3.3 Temperature 52
3.4 Weight measurements 53
3.5 Characterization 58
3.6 Gas atmospheres and oxygen pressure 59
3.7 Experiment overview 61
3.8 Related work 61
4 Results 63
4.1 Reduction of Nchwaning ore 63
4.1.1 Weight loss and reduction behavior 63
4.1.2 Off-gas analysis 69
4.2 Characterisation of Nchwaning ore 75
4.2.1 XRD - Phase evolution 75
4.2.2 Quantitative Mineralogical Analysis - Unreduced ore 78
4.2.3 EPMA - Partly reduced ore 82
4.2.4 Decrepitation 85
4.3 Reduction of Comilog ore 86
4.3.1 Weight loss and reduction behavior 86
4.3.2 Reduction behavior of Comilog at 605 °C and 515 °C 88
4.3.3 Off-gas analysis for Comilog at 605 °C and 515 °C 90
4.3.4 Reduction behavior of Comilog at 455 °C, 410 °C and 365 °C 94
4.3.5 Off-gas analysis for Comilog at 455 °C, 410 °C and 365 °C 98
4.3.6 Reoxidation after reduction 102
4.4 Characterization of Comilog 103
4.4.1 AMS - Unreduced ore 103
4.4.2 µCT measurements 106
4.4.3 Decrepitation 109
4.5 Carbon deposition 111
5 Discussion 112

5.1 Reduction behavior 112
5.1.1 Reduction behavior of Nchwaning ore 112
5.1.2 Reduction behavior of Comilog ore 116
5.2 Reduction rate 125
5.2.1 The effect of hydrogen on reduction 126
5.2.2 Modeling 128
5.2.3 Model simulations 133
5.3 Miscellaneous side effects 137
5.3.1 Water gas shift reaction 137
5.3.2 Carbon deposition 138
5.3.3 Reoxidation 141
5.3.4 Decrepitation 143
5.4 Industrial implications 146
6 Conclusions and future work 148
7 References 151
Appendix A Weight deviations 166
Appendix B XRD patterns for Nchwaning ore 173
Appendix C Thermocouple error correction 176
Appendix D Off-gas analysis correction 177
Appendix E Cumulative size distributions 181
Appendix F Mineralogy measurements 183
Appendix G Binary diffusion coefficients 185

1 Introduction and background

1.1 Introduction

The roadmap for the Norwegian process industries presents the vision of "Combining growth and zero emissions by 2050"[1]. To approach the vision, development of technologies that have a potential of reducing the carbon footprint from the process industry is needed.

Initiatives in the ferroalloy industry are already underway on topics such as; replacing fossil carbon inputs with renewable carbon sources[2,3], changing operational parameters to reduce specific carbon emissions[4], agglomeration techniques to recycle waste streams[5–7] and carbon capture for utilization or storage(CCU/CCS)[8]. Most of the cost of CCU/CCS lies in the CO_2 capture and separation step[9], hence the off-gas from the manganese ferroalloy furnaces, with its high CO_2 content, is ideally suited for relatively low cost carbon capture[9]. An additional technological improvement for the manganese ferroalloy industry is the pretreatment and prereduction of manganese ores prior to its addition to the furnace. The main sources of fossil carbon emissions in the furnace originate from the added carbon materials and the electrical power consumption, the latter being dependent on the local electricity greenhouse gas emission factor[10]. Sufficient pretreatment will reduce excess carbon and excess energy consumption during smelting, thus reducing consumption of fossil carbon in the process[11,12].

9.4: "…retrofit industries to make them sustainable, with increased resource efficiency and greater adoption of clean and environmentally sound technologies and industrial processes..."

12.1: "...achieve the sustainable management and efficient use of natural resources."

Goal 13: "Take urgent action to combat climate change and its impact."

Figure 1-1: UN's sustainable development goals[13] with high relevance for the implementation of a pretreatment unit in manganese ferroalloy production.

The implementation of a pretreatment unit in manganese ferroalloy production is in alignment with the UN sustainable development goals[13]. By retrofitting submerged arc furnaces with pretreatment units, there is a potential to increase the resource efficiency and reduce the added resources such as electric energy and carbon materials. The maturity of the technology itself makes swift implementation possible. Development goals and selected quotes with high relevance for the pretreatment of manganese ores is shown in Figure 1-1.

In the context of a pretreatment unit, there is a need to improve the fundamental understanding of the pretreatment process and its implications on the energy consumption and emissions from the metal production process. The off gas from the submerged arc furnace (SAF) constitutes an excellent energy source for a pre-treatment unit due to its high energy content and its availability at the plant. Pretreatment and prereduction of ores may also be relevant for preparing raw materials for processes such as electrolysis or metallothermic reduction[14,15], thus the acquired knowledge may also have applications also outside the scope of improving the SAF process.

1.2 Background

In this section, a general description of manganese ferroalloy production is given and the main features effecting the carbon and energy consumption is elaborated upon. Relevant industrial figures and experiences regarding energy consumption, carbon consumption and pretreatment is included, and common raw materials presented.

1.2.1 Overview of ferroalloy production

Manganese ferroalloys are mostly produced in submerged arc furnaces (SAF) where ore, coke and fluxes are added together with electric energy to produce alloy, slag and off gases. The raw materials added to the top of the furnace are descending towards the lower parts where they are consumed. Electric energy is supplied by three electrodes. The area below and around the electrode tips is known as the coke bed zone, where the oxidic raw materials are molten and the final reduction to metal takes place according to reaction (8).

The CO-gas from the coke-bed zone ascends through the pre-reduction zone (see Figure 1-2) and may pre-reduce the higher manganese- and iron oxides according to reactions (1) - (6). These reactions are mostly exothermic and will contribute to pre-heating the charge materials thus lowering the electric energy consumption. Carbonates in the ore and fluxes decompose endothermically as exemplified in reaction (7). Production of ferromanganese of 78% Mn requires typically a 7,5 Mn/Fe weight ratio[16] which may be achieved by mixing raw materials with different iron content.

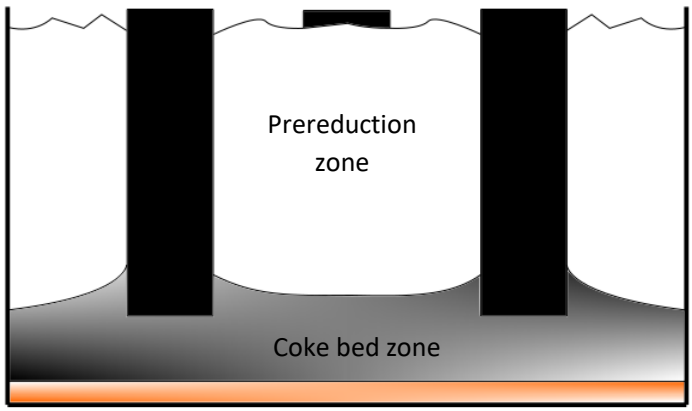

Figure 1-2: Sketch of a submerged arc furnace (SAF) with electrodes. The coke-bed zone and the pre-reduction zone is indicated.

$$2MnO_2 + CO = Mn_2O_3 + CO_2 \qquad \Delta H°_{298K} = -201.8\frac{kJ}{mol} \qquad (1)$$

$$3Mn_2O_3 + CO = 2Mn_3O_4 + CO_2 \qquad \Delta H°_{298K} = -176.7\frac{kJ}{mol} \qquad (2)$$

$$Mn_3O_4 + CO = 3MnO + CO_2 \qquad \Delta H°_{298K} = -53.2\frac{kJ}{mol} \qquad (3)$$

$$3Fe_2O_3 + CO = 2Fe_3O_4 + CO_2 \qquad \Delta H°_{298K} = -39.6\frac{kJ}{mol} \qquad (4)$$

$$Fe_3O_4 + CO = 3FeO + CO_2 \qquad \Delta H°_{298K} = 37.4\frac{kJ}{mol} \qquad (5)$$

$$FeO + CO = Fe + CO_2 \qquad \Delta H°_{298K} = -17.9\frac{kJ}{mol} \qquad (6)$$

$$CaCO_3 = CaO + CO_2 \qquad \Delta H°_{298K} = 178{,}2\frac{kJ}{mol} \qquad (7)$$

$$MnO + C = Mn + CO \qquad \Delta H°_{298K} = -274.7\frac{kJ}{mol} \qquad (8)$$

1.2.2 Energy and carbon consumption

The energy requirement of the SAF is dependent on factors such as input and output material composition and temperature which is determined by the operating philosophy and conditions. Tangstad et al.[12] calculated the effect of temperature changes of the material flows in and out of the furnace. Increasing the temperature of the input materials by 100 °C was seen to decrease the specific energy consumption of the furnace by 82 kWh/ton alloy produced while a 100 °C lower off-gas temperature would decrease the energy consumption with 26 kWh/ton alloy. More highly oxidized input materials will decrease the energy consumption due to increased extent of exothermal reactions (reactions (1)-(3)).

Conversely, higher content of carbonates in the ore or added as fluxes increases the energy consumption due to its endothermal decomposition (reaction (7)). Use of low-grade ores may increase the specific power consumption by thermal losses due to increased slag volume, and due to reduced yield of manganese caused by dilution of MnO in the slag. From industrial data, it has been seen that power consumption is positively correlated to the amount of flux added to the furnace and to the amount of slag produced[17].

The MnO content in the slag will influence the manganese yield and is mainly determined by the slag basicity. The basicity is the ratio between basic and acidic oxides[16] and is adjusted by addition of fluxes to the furnace. The amount of flux in the charge mix is chosen based on the chemical composition of the raw materials and on whether the slag from the process is discarded or repurposed for SiMn production[16].

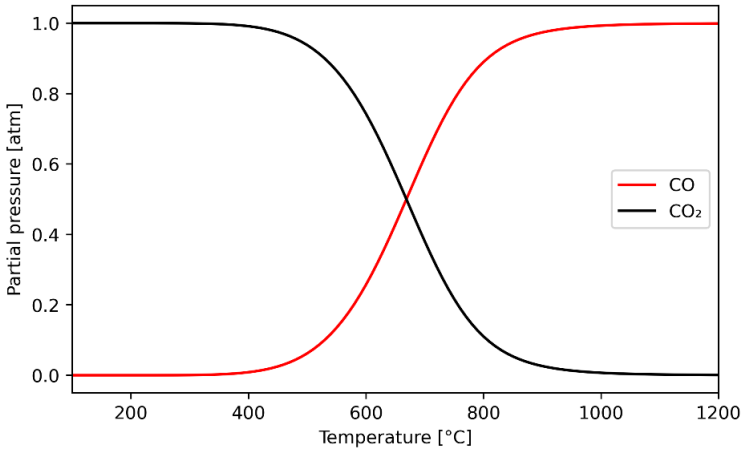

Figure 1-3: The equilibrium partial pressures of CO and CO_2 for the Boudouard reaction (9) with carbon activity of one. Calculated using HSC chemistry 9[18].

Carbon is consumed in the metal producing reaction (equation (8)), by dissolution of carbon in the alloy and by the Boudouard reaction (equation (9)). The Boudouard reaction will consume most of the CO_2 produced above about 800 °C[16]. Figure 1-3 shows the equilibrium partial pressures of CO and CO_2 as a function of temperature at furnace conditions (carbon activity of unity). The reaction is highly endothermic and contributes to an excessive carbon consumption according to equation (9). In addition, a high extent of the Boudouard reaction will increase the energy losses during production due to increased energy in the furnace off gases[19,20].

$$C + CO_2 = 2CO \qquad \Delta H°_{298K} = 172{,}4\,\frac{kJ}{mol} \qquad (9)$$

The CO_2 consumed in the Boudouard reaction may originate from the reduction of higher oxides (reactions (1) - (6)) or the decomposition of carbonates (i.e. reaction (7)). The amount CO_2 from higher oxides depends on the ore reactivity. Carbonates in the ores are often present as calcite ($CaCO_3$), kutnohorite, rhodochrosite and dolomite[21–25] ($CaCO_3$, $CaMn(CO_3)_2$, $MnCO_3$ and $CaMg(CO_3)_2$, respectively). Calcite and dolomite are commonly used as fluxes[16]. Figure 1-4 shows the stability of some of the carbonates as a function of temperature and CO_2 partial pressure. Calcium- magnesium- and manganese-carbonate decompose ($p_{CO_2} = 1$) at 892 °C, 398 °C and 346 °C, respectively. Dolomite decomposes at 427 °C to calcite and MgO. Thermal analysis of kutnohorite shows two endothermic peaks[26], indicating a similar decomposition mechanism to dolomite.

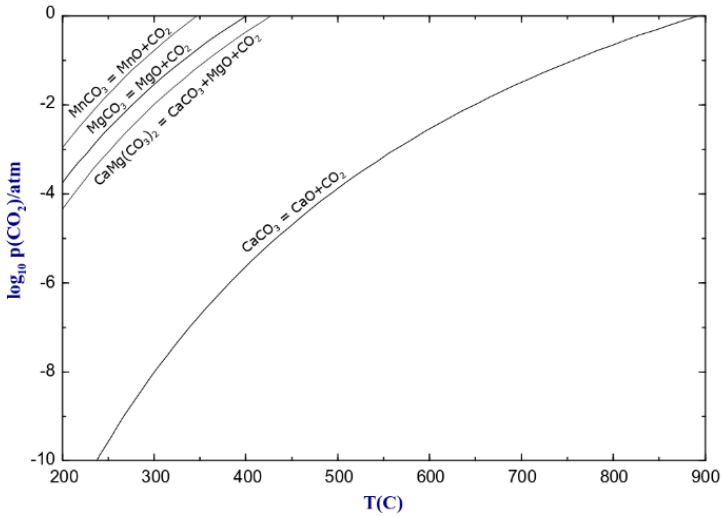

Figure 1-4. The stability of carbonates as a function of CO_2 partial pressure and temperature. Calculated using Factsage[27] with the FToxid, FTmisc and FactPS databases

The kinetics of carbonate decomposition depend on temperature and CO_2 content in the atmosphere[28,29]. The carbonates other than calcite may decompose at temperatures below 800 °C[30,31], limiting their CO_2 contribution to the Boudouard-reaction, however calcite is stable at 800 °C in carbon dioxide partial pressures above 0.21 atm (Figure 1-4). Hence, the CO_2 from the calcite added to the furnace will react with carbon, effectively doubling the energy consumption and CO_2 emissions compared to calcite decomposition alone (reactions (7)-(9)).

Ishak and Tangstad defined the proportion of CO_2 from reduction of Mn_3O_4 to MnO, Fe_3O_4 to metallic iron and decomposition of calcium carbonate, not reacting according to the Boudouard reaction as the degree of pre-reduction (DPR) [32], that is, if no CO_2 from these sources react with C, the DPR is 100 %. The DPR was measured on 3 industrial furnaces over a 6-year period, and was typically

between 0-40 %, up to 60 % in good periods and never below zero. Thus, on average, no CO_2 from the reduction of oxides higher than Mn_3O_4 reacted in the Boudouard reaction[32]. Simulations on different charge mixtures has shown a potential to reduce the carbon- and energy consumption up to 69 kg C and 350 kWh per ton alloy produced[33]. From other industrial plants, Ahmed et al.[17] reported an excess consumption during prereduction (i.e. Boudouard reaction) of 78 kg C and 309 kWh per ton alloy and from Pais et al.[34], the excess consumption was found to be 80 kg C and 320 kWh per ton alloy during prereduction to MnO-FeO. In Figure 1-5, the excess energy and carbon consumption due to the Boudouard reaction has been calculated based on a fixed industrial charge mixture[35]. If the DPR can be increased from 40 % to 100 %, the carbon and energy consumption can be reduced by 76 kg and 303 kWh respectively per ton alloy produced, corresponding well with simulations and with the excess consumption seen in industry.

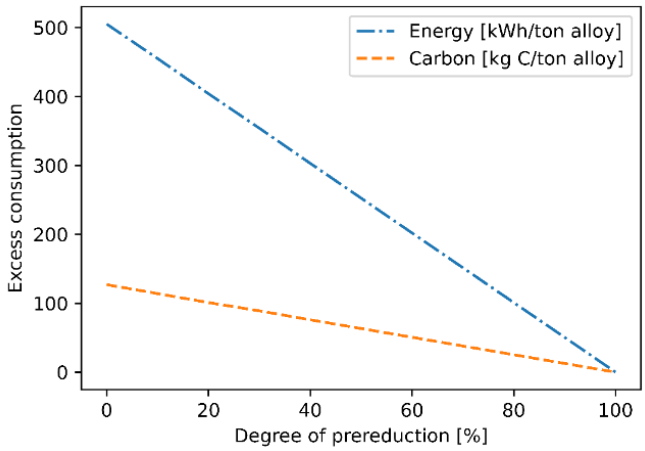

Figure 1-5: Calculated excess consumption of carbon and energy as a function of degree of prereduction (DPR). Calculated using the charge mixture in[12].

The DPR is influenced by several factors. Lower residence time of the raw materials in the furnace will increase the fraction of higher oxides and carbonates reacting in the Boudouard active zone, decreasing the DPR[36]. Higher water content will also decrease the DPR[32]. High amounts of water will require that more energy is used for evaporation which will keep the raw materials at lower temperatures for longer time in the furnace. This will effectively give a lower residence time for the raw materials in the pre-reduction zone. The CO-reactivity of raw materials is related to the DPR in that the CO-reactivity measures the ability of manganese materials to be reduced to MnO by CO. In highly reactive ores, a lower fraction of higher manganese oxides will remain at high temperatures[37], improving the DPR.

1.3 Scope of thesis

The present work aims to study the prereduction kinetics of manganese ores under conditions that are obtainable in an external pretreatment unit. The focus is on the effect of different temperatures and gas atmospheres, where the utilization of CO- rich furnace off-gases is taken into account. Temperatures below 800 °C are considered such that implementation under conditions where also reductant is passed through the pretreatment unit is possible. Two commercial ores with different properties will be investigated. Most of the previous investigations on prereduction of manganese ore has been done using non-isothermal experiments to simulate the conditions in the SAF, this work will use isothermal experiments to simulate possible conditions in a pretreatment unit.

The thesis will be divided into 6 Chapters. Chapter 2 contains the theoretical background where previous lab, pilot and industrial experience regarding energy consumption, carbon consumption and pretreatment is included. The thermodynamics under prereduction conditions is covered as well as the kinetics of prereduction under different conditions. The literature concerning decrepitation of manganese ores has also been reviewed.

In chapter 3, the utilized ores, experimental setup, and conditions are described in addition to details regarding the characterization methods. Details regarding the selection of gas mixtures is also covered.

Chapter 4 reports the experimental results from the reduction experiments and from the different characterization methods used in this work. The results from the two different ores are presented separately.

In Chapter 5, the results from this work are discussed and compared to other investigations. The reduction behavior of the two ores and the reduction rate is covered in the context of different temperatures and gas mixtures. Phenomena other than reduction, i.e., the occurrence of the water gas shift reaction, carbon deposition, decrepitation and reoxidation is covered as well as the influence of pretreatment on industrial operation.

Chapter 6 summarizes and highlights the main findings in this work in addition to suggestions for future work.

2 Literature review

During prereduction in industrial furnaces, higher manganese oxides are reduced to MnO, iron oxides to FeO or Fe and carbonates in ore or fluxes decompose. The fraction of these reactions occurring below 800 °C has a significant impact on the carbon and energy consumption as stated in the previous section. The reactivity of the different manganese sources and how they react under different influences is important input for improvement of the manganese ferroalloy production technology.

This section includes a review on published data from industrial production on energy and carbon consumption in addition to experiences from pretreatment of raw materials in pilot and industrial scale. Different raw materials are described with emphasis on their effect on furnace performance. Literature on the gaseous reduction of manganese raw materials is reviewed, with a focus on parameters which influence the kinetics of reduction in comparison with relevant equilibrium relations. The equilibrium composition and stability of intermediate phases during reduction may be affected by the chemical and phase composition of the original material while the kinetics are influenced of factors such as temperature, particle size, porosity, and gas composition. Decrepitation of the materials may indirectly influence the kinetics since it affects the particle size of the material.

2.1 Industrial production

In Table 2-1, manganese recovery, energy consumption and carbon consumption from industrial production of HCFeMn is given. The manganese yield, specific energy- and carbon consumption is seen to vary significantly between the different plants, which is related to the different use of raw materials and different operation strategy. Plant C was run with a high basicity, improving the manganese yield with the expense of increased energy consumption, and discarding the slag[16]. The relatively low manganese recovery in SMC was probably due to the use of low grade ores, the plant was running with a similar basicity as plant C[38]. The Union Carbide plant had the lowest specific carbon consumption which was due to the use of highly oxidized ore with a high manganese content that gave a relatively high manganese yield, despite producing a high MnO slag suitable for repurposing in SiMn production[39].

Larssen et al.[20] conducted a materials and energy balance on HCFeMn production assuming a degree of prereduction of 25 %. An energy consumption of 2456 kWh/ton and carbon consumption of 358 kg C/ton was found, aligning well with the numbers from industrial production seen in Table 2-1.

Cowx and Nussbaum[19] made a mass and energy balance on HCFeMn smelting and found that the specific energy and carbon consumption could be reduced by 343 kWh/ton and 75 kg C/ton by using an external prereduction unit.

Also, the excess energy of the furnace gas could be reduced from 1516 to 382 kWh/ton FeMn.

Table 2-1: Operation results from production of HCFeMn from industrial plants.

Plant	Raw materials	Mn recovery [%]	Specific energy consumption [kWh/ton alloy]	Specific carbon consumption [kg C/ton alloy]	Source
JMC*	Ore, sinter	78	2100	-	Tomioka et al. [40]
Plant A	Ore	77	2400	360	Olsen et al. [16]
Union Carbide	Ore**, Sinter	82	2152	306	Tangstad et al. [39]
Plant C	-	91	3395	-	Olsen et al. [16]
SEAS	Sinter	81	2554	355	Pais et al. [34]
SMC	Low grade ores, Sinter	75	2990	394	Eissa et al.[38] / Ahmed et al.[17]

*Pretreatment operation at the plant

**Dried and sieved ore

Davidsen[4] ran a 4 month industrial trial producing SiMn without the use of fluxes. A materials and energy balance on a simplified charge mixture predicted a reduction of 204 kWh/t and 9 kg C/batch (1 batch = 1000 kg Mn sources) by changing the dolomite input from 60 kg/batch to 0. The predicted disadvantage was lower manganese recovery (79.7 % to 77.8%). In the industrial trial, the specific energy consumption was reduced by 197 kWh/t and carbon consumption by 9 kg/batch. Furnace stability and tapping conditions remained stable during the trial. A similar effect of the decreased use of fluxes is expected in HCFeMn production; the reduced basicity lowers the manganese yield and reduced amount of carbonates in the furnace reduces carbon and energy consumption. If carbonates are decomposed during pre-treatment, the same effect may be achieved without sacrificing the manganese recovery.

2.1.1 Pretreatment of raw materials

The raw materials may be treated in a pre-treatment unit before they enter the furnace, as indicated in Figure 2-1. The off gas from the SAF constitutes an excellent energy source for a pre-treatment unit due to its high energy content

and its availability at the plant. Previously, pre-reduction of manganese ore has been conducted in a rotary kiln, where they used HCMnFe furnace off gas (70 % CO, 25 % CO_2, 5% H_2) as fuel with the addition of coke for reduction[41].

Excessive moisture and excessive oxygen in the charge materials may lead to unstable furnace operation, i.e., furnace eruptions. There are safety limitations regarding the amount of moisture and excessive oxygen that enters the SAF[42,43]. By pre-treating the raw materials, the moisture will be removed, and higher oxides will be reduced, thus promoting stable furnace operation. The reduction of higher oxides have the added advantage of supplying energy to the charge mixture in the pre-treatment unit due to the high exothermicity of their reaction with CO gas (reactions (1), (2) and (3)). In sum, the safety regulations regarding oxygen and moisture contents are fulfilled by pre-treating the charge materials, thus increasing the flexibility in the choice of charge mixture for production.

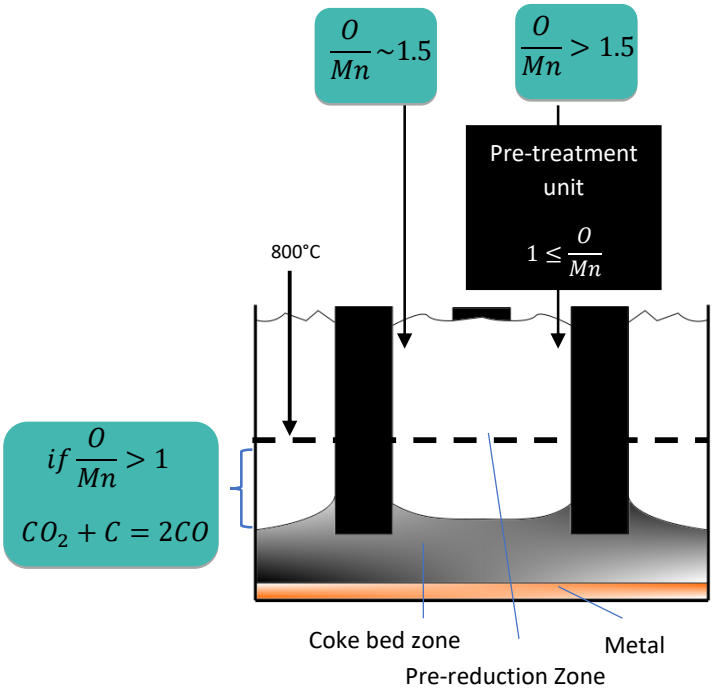

Figure 2-1: Sketch of a submerged arc furnace and a pre-treatment unit.

As previously mentioned, most CO_2 produced above 800 °C will be consumed in the Boudouard reaction. The addition of a pre-treatment unit using the furnace off-gas as the energy source will effectively increase the residence time of the ore at reducing conditions, thus increasing the degree of pre-

reduction[36]. To improve the pre-reduction further, it is possible to add additional fuel to the pre-treatment unit.

Julia et al[44] pretreated ores in a pilot scale rotary kiln. The kiln was fueled with gas and tests were conducted with and without coal. Two different ores were used, containing predominantly MnO_2 and Mn_2O_3, respectively. The energy consumption during heating without coal was higher for the MnO_2 ore due to higher extent of endothermal decomposition reactions (reaction (1)). In the presence of coal, the energy consumption for the MnO_2 ore was more than halved, while little effect (< 5% difference) was seen for the Mn_2O_3 ore.

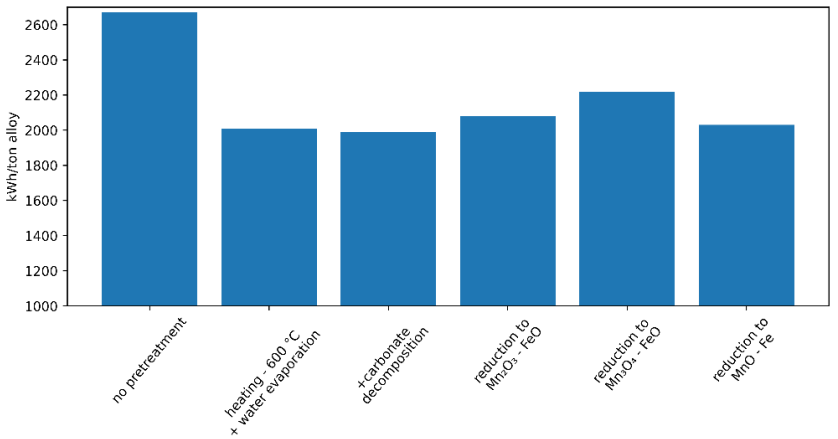

Figure 2-2: The electric energy consumption of a high carbon ferromanganese furnace based on mass and energy balances [12]. The use of a pre-treatment unit with no, partial and complete pre-reduction of the raw materials is considered.

Industrially, pretreatment of manganese ores has been conducted in rotary kilns fueled by CO rich furnace off gas and solid fuels[45,46,41,12]. Teguri et al.[41] implemented pretreatment where the primary goal was to fully decompose all carbonates in the ore. HCMnFe furnace off-gas (70 % CO, 25 % CO_2, 5% H_2) and coke was used as fuel for the rotary kiln. Satisfactory removal of carbonates was achieved with a 9 h residence time in the reactor at 1150 - 1250 °C. In addition to the decomposition of carbonates, prereduction to O/Mn=1.19 (1 year average) was achieved. In another plant, a rotary kiln was used for heating and partial pre-reduction at lower temperatures 600 - 700 °C [46]. The rotary kiln was fueled by furnace off-gas, tire chips, coal and kerosene [45]. A materials and energy balance revealed that the energy consumption of the SAF was reduced by 25 % if the pretreatment evaporated the water content, decomposed the carbonates and preheated the raw materials to 600 °C [12]. The effect of different states of prereduction on electrical energy consumption of the furnace can be seen in Figure 2-2. Pretreatment reduces the electric energy consumption and the

magnitude of the reduction in power consumption depends on the degree of which the exothermic reactions take place inside the furnace. Viewing the pretreatment unit and the furnace as one system, this effect cancels out since the exothermal reactions happening in the pretreatment unit will reduce the energy consumption of the pretreatment unit. The case of full external prereduction (rightmost column) has a relatively low power consumption due to the absence of the Boudouard reaction (reaction (9)).

In a pre-treatment unit, furnace off-gas may be utilized as a source of reductant and energy. The amount and composition of the furnace off-gas may not be of sufficient quantity and quality to achieve the desired level of reduction. If additional fuel should be added in the pre-treatment unit, H_2 may be a good candidate to avoid increasing the carbon footprint of the overall process.

2.2 Manganese raw materials

2.2.1 Ore

Pochart et al.[42] classifies the major manganese ores as oxidized, semi-oxidized or carbonated, corresponding to the oxidation state of manganese and carbonate content. The oxidized ores contain high amounts of oxygen, and the oxidation state of manganese is close to MnO_2. Groote Eylandt (GE), Companhia Vale do Rio Doce (CVRD) and Comilog are examples of oxidized ores (see Table 2-2). Semi-oxidized ores have oxygen contents close to that of Mn_2O_3 (e.g. Nchwaning and Wessels) while carbonated ores contain high amounts of carbonates (e.g. Gloria and Mamatwan), specifically calcite and kutnohorite[47]. The carbonated ores have many of the same phases as the semi-oxidized ores, however the ratio between carbonates and oxides is higher. Oxides in the semi-oxidized and the carbonated ores are often in the form of Braunite (I or II).

Singh et al.[48] uses a different classification using silicate, oxidized and carbonate ores. The oxidized ores in this classification, contain both the oxidized and semi-oxidized ores as defined by Pochart et al.[42], with the exception of Braunite ores that fall into the silicate classification. Morro da mina ore is a silicate ore where the main silicate minerals are spessartine and tephroite, however it also contains significant amounts of rhodochrosite[22]. Carbonate ores (Singh et al.[48]) are ores where the major minerals are carbonates, such as Nsuta carbonate ore[21]. Ores may also be characterized based on their gangue content, such as *ferruginous ores* that contain 13-23 % Fe and 25-35 % Mn or *siliceous ores* containing more than 15 % Si in addition to 23-30 % Mn[48].

In ferroalloy production, the different ore types will influence the behavior of the furnace in various ways. More highly oxidized ores will produce additional heat through the exothermal reduction with CO, however the amount of highly oxidized ore in the furnace is limited for safety reasons[42] [43]. Carbonate containing

ores and carbonate ores will require additional energy due to the endothermal decomposition of carbonates, however this effect cancels out if these carbonates displace the addition of fluxing agents. Low grade ores with high contents of gangue materials may cause excessive slag formation with associated losses by thermal energy and reduced manganese yield through dilution of MnO in the slag. The mix of ores, fluxes and other manganese sources for ferroalloy production is chosen on the basis of factors like Mn/Fe ratio, P-content, excess oxygen content and availability.

Table 2-2: Major phases (minerals) found in manganese raw materials (ores). Ore short names, GE= Groote Eylandt, Com=Comilog, Nch=Nchwaning, Wes=Wessels, Glo=Gloria, Nsu=Nsuta carbonate and Mor=Morro da mina. Marks (x) indicate minerals identified in the ores based on XRD-analysis. The phase identification of GE and Com ores was aided by mineralogical analysis. References: GE and Com [49], Nch and Glo [23], Wes [25], Nsu [21], Mor [24].

Mineral	Chemical formula	GE	Com	Nch	Wes	Glo	Nsu	Mor
Pyrolusite	MnO_2	x	x					
Ramsdellite	MnO_2		x					
Cryptomelane	KMn_8O_{16}	x	x					
Nsutite	$Mn_{1-x}Mn_xO_{2-2x}OH_{2x}$		x					
Lithiophorite	$(Al,Li)MnO_2(OH)_2$		x					
Bixbyite	$(Mn,Fe)_2O_3$			x	x	x		
Braunite	$3(Mn,Fe)_2O_3*MnSiO_3$			x	x	x		
Braunite II	$7(Mn,Fe)_2O_3*CaSiO_3$			x	x	x		
Bementite	$Mn_7Si_6O_{15}(OH)_8$					x		
Johannsenite	$CaMnSi_2O_6$				x			
Hausmanite	Mn_3O_4			x		x		
Jacobsite	$MnFe_2O_4$					x		
Marokite	$CaMn_2O_4$			x		x		
Manganite	MnOOH	x		x	x			
Goethite	FeOOH		x					
Hematite	Fe_2O_3		x	x	x	x		
Kutnohorite	$CaMn(CO_3)_2$			x		x		
Calcite	$CaCO_3$			x		x	x	
Dolomite	$CaMg(CO_3)_2$						x	x
Rhodochrosite	$MnCO_3$						x	x
Quartz	SiO_2	x	x				x	
Barite	$BaSO_4$			x		x		
Tephroite	Mn_2SiO_4							x
Rhodonite	$(Mn,Fe,Mg,Ca)SiO_3$							x
Spessartine	$Mn_3Al_2(SiO_4)_3$							x

2.2.2 Sinter

Fines from the mines are often agglomerated by sintering. The oxidation state of manganese in sinter is between MnO and Mn_3O_4[16,34]. Using sinter in production has been seen to improve the stability of furnace operation, reducing the amount of blow-outs and eruptions and reducing the electrode consumption[34,50]. Sinter has a higher electrical resistivity compared to ores, contributing to deeper electrode penetration and higher productivity[34,51,52]. From previous investigations, it is seen that sintering may reduce the porosity and reactivity compared to the lump ore[37]. Due to the lower oxygen content of sinter compared to ores, it is expected that using sinter will contribute to increasing the energy consumption in the furnace, however it has been seen industrially that the carbon consumption is lower[34]. There are several reasons for the lower carbon consumption using sinter. Good charge permeability ensures a good distribution of reducing gas in the charge, deeper electrode penetration will increase the size of the pre-reduction zone thus increasing the residence time of the raw materials at pre-reduction conditions, and sinter does not contain chemically bound water or carbonates. In addition, it is possible to avoid carbonates in the charge mixture since fluxes may be incorporated in the sinter. From materials and energy balances the decomposition of carbonates contributes to 7% and 5,6% of the energy consumption for HCFeMn and SiMn respectively[51], however these numbers will depend on the charge mix.

2.2.3 Briquettes

Briquetting is a cold bonding process using binders to agglomerate fines[16]. In addition to upgrading ore fines, it may be used to repurpose manganese containing fines and sludges from filters and gas cleaning facilities at ferroalloy plants, which will improve the total utilization of the manganese resource and reduce the need for landfilling waste materials. Excellent chemical and mechanical properties of briquettes have been seen in lab scale[5,6,53–57], and larger scale experiments have been conducted[5–7,57].

Diaz et al.[6] produced briquettes using fines from manganese ores and metal fines in addition to filter dust and gas cleaning sludge together with an organic binder. The briquettes had similar mechanical strength, less fines generation and higher strength after heating and reduction compared to manganese ore. A pilot scale experiment was conducted where standard HCFeMn charge mixture was compared to a charge mixture containing 30 % briquettes. The gas permeability through the charge improved when the briquette containing charge mixture was used, and the specific energy consumption decreased which may have been caused by improved prereduction.

Davey[7] made briquettes using off-grade metal fines and dust from production. Using 10 % briquettes in the charge mixture caused a reduction in the

specific energy consumption of 7.4 % and reduced the specific carbon consumption with 11.4 %.

Bizhanov et al.[5] produced briquettes using ore fines and baghouse dust from a ferroalloy plant with Portland cement as binder. The briquettes were tested in a full-scale operation, increasing the fraction of briquettes in the charge mixture incrementally from 5 % up to 40 % over a period of several weeks. During the campaign there were good furnace conditions, improved gas permeability in the charge compared to normal operation and uniform temperature distribution at the top of the furnace. Decreased specific energy consumption was also observed.

2.2.4 Nodules

Nodulizing is a process used for treatment of carbonate ore fines in rotary kiln at 1145-1260 °C. The process decomposes carbonates, evaporates water and agglomerate the material[21,58,59]. Tangstad et al.[60] investigated the properties of Autlan nodules from Hidalgo, Mexico. Chemical analysis showed that all carbonates were decomposed, and the content of CaO and MgO was sufficient to produce HCFeMn without additional fluxes. The manganese was present as manganosite, galaxite and tephroite, corresponding to the oxidation state of MnO. The mechanical strength was higher compared to commercial ores and the porosity was between 3-9 %. The nodules were found to behave similarly to ores in pilot scale experiments[61].

2.3 Equilibrium relations during prereduction

The stability of ores may be influenced by the overall chemical composition and phase compositions. Table 2-3 shows results from chemical analysis of selected manganese ores and it is seen that the Mn/Fe ratio and content of other oxides vary substantially. The amount of carbonate phases, e.g., calcite, is represented by the amount of CO_2 in Table 2-3. Carbonate phases were discussed in section 1.2.2, where calcite was seen to be the only stable carbonate decomposing above 800 °C, and that carbonates are stabilized by partial pressure of CO_2, as can be seen by the decomposition reaction $CaCO_3 = CaO + CO_2$ (reaction (7)).

Table 2-3: The SiO_2, Al_2O_3, CaO, MgO and CO_2 content, the total manganese content and the Mn/Fe ratio of a selection of manganese ores. All values are on a mass basis.

Ore	Mn/Fe	Mn_{tot}	SiO_2	Al_2O_3	CaO	MgO	CO_2	Ref.
GE	9,2	61,5	4,4	1,19	0,03	-	N.A.	[62]
GE	14,1	63,4	6,09	3,9	0,18	-	N.A.	[49]
CVRD	5,1	51,1	9,01	10,3	0,21	0,36	N.A.	[49]
Comilog	31,0	64,4	5,85	7,1	0,08	-	N.A.	[49]
Nchwaning	4,9	50,2	8	0,3	3,5	0,6	1,8	[25]
Nchwaning	3,4 -5,1	41,3-45,5	3,9-6,5	0,3-0,4	3,8-8,9	0,5-1,1	0,8-4,3	[23]
Mamatwan	7,9	38,6	6,1	0,2	13,9	4	16,1	[25]
Gloria*	6,7	35,7	6,2	0,3	14,6	3,9	17,4	[23]
Wessels	3,9	47,7	2,8	0,4	4,9	0,4	0,8	[25]
Wessels	4,9	54,2	4,18	1,5	8,3	0,7	N.A.	[49]
Wessels	4,4	48,2	3,2	0,4	5,4	-	N.A.	[62]
Wessels WH	5,8	52,3	3,9	0,3	4,8	0,3	0,9	[63]
Wessels W1	3,9	47,8	3,1	0,4	4,8	0,2	0,7	[63]
Wessels W4	1,9	35,3	5,51	0,3	9,41	0,2	1,1	[64]
Um Bogma H	2,9	30,7	2,4	1,0	2,3	0,9	N.A.	[65]
Um Bogma M	2,2	27,2	5,1	2,1	2,3	1,5	N.A.	[65]
Um Bogma L	1,1	22,3	2,1	1,0	3,0	1,6	N.A.	[65]

∗**2 measurements averaged**

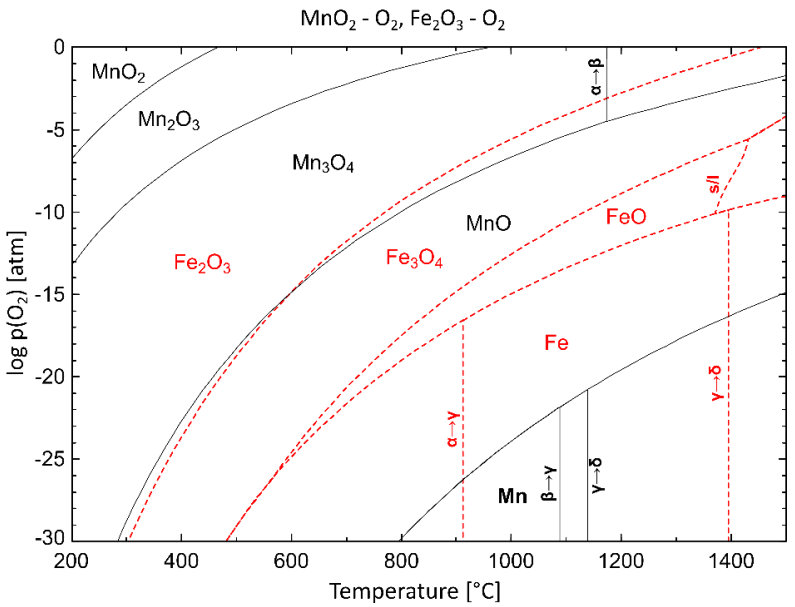

Figure 2-3: Phase diagram for the Mn-O (black solid lines) and Fe-O (red dashed lines) systems. The figure shows the stability of phases as functions of temperature and oxygen partial pressure. Calculated with Factsage using the FToxid, FTmisc and FactPS databases[27].

The manganese- and iron- oxides in the ore will be transformed as the ores are added to the furnace. Figure 2-3 shows the stability of the pure manganese- and iron- oxides as a function of temperature and oxygen partial pressure. With increasing temperature and decreasing oxygen partial pressure, MnO_2 and Mn_2O_3 will be reduced or decompose while Fe_2O_3 is the stable iron containing phase. The reducing conditions of Mn_3O_4 to MnO is close to that of reduction of Fe_2O_3 to Fe_3O_4. Fe_3O_4 may be reduced to FeO and Fe in the stability range of MnO. The stepwise reduction of manganese- and iron- oxides according to equilibrium conditions is summarized in Table 2-4. If prereduction to step 6, that is MnO and Fe, is accomplished below 800 °C industrially, there will be no CO_2 from reduction of oxides available for the Boudouard reaction, C + CO2 = 2CO (reaction (9)) (see section 1.2.2).

Table 2-4: Shows the stepwise reduction according to equilibrium of pure manganese and iron oxides. Step 3-4 has been simplified as both MnO/Fe_2O_3 and Mn_3O_4/Fe_3O_4 can coexist in small areas depending on the oxygen partial pressure (Figure 2-3).

Step	**1**	**2**	**3**	**4**	**5**	**6**
MnO_x	MnO_2	Mn_2O_3	Mn_3O_4	MnO	MnO	MnO
FeO_x	Fe_2O_3	Fe_2O_3	Fe_2O_3	Fe_3O_4	FeO	Fe

While Figure 2-3 shows the coexistence areas when Mn and Fe is not in solution, Figure 2-4 shows the stability of Mn-Fe oxides in solution at 800 °C as a function of Mn/Fe ratio and oxygen partial pressure. It can be seen that the different oxides show various degrees of solid solubility. The composition of selected ores has been indicated. The magnetite phase (Fe_3O_4) may contain almost 75 % Mn cations at 800 °C, stabilizing a higher fraction of manganese in the higher oxides compared to pure Mn_3O_4. FeO and MnO display complete solid solubility, and the decreased activity of FeO in solid solution with MnO stabilizes the FeO and makes metallic iron form at lower oxygen partial pressures than pure FeO[66].

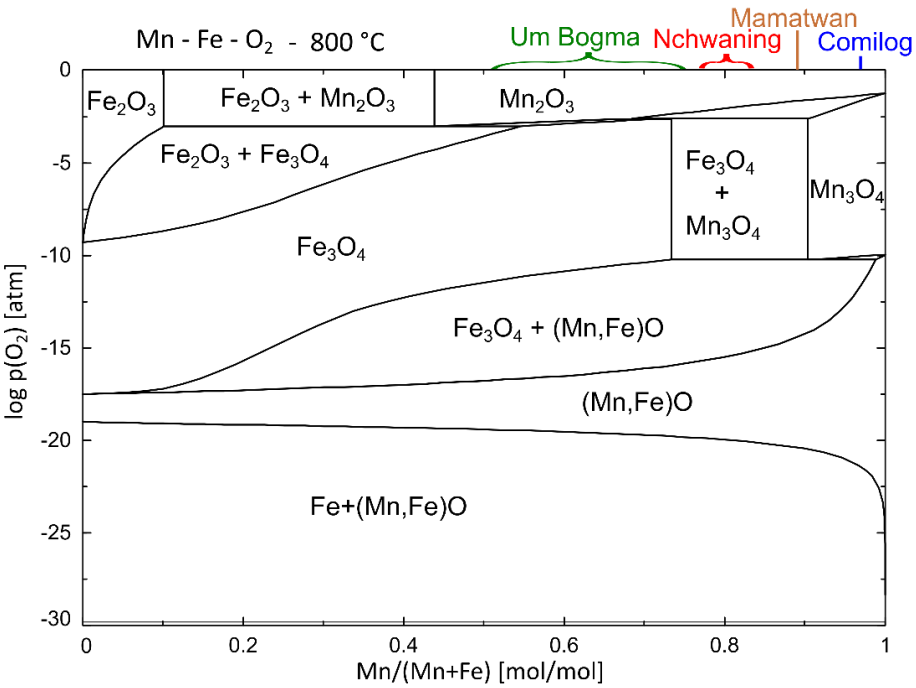

Figure 2-4: Phase diagram for the Mn-Fe-O_2 system at 800 °C showing the stable phases as functions of oxygen partial pressure and composition. For clarity in the figure, the phases are labeled as their pure oxide, i.e. the magnetite phase is labeled Fe_3O_4 even though $(Fe,Mn)_3O_4$ could be an appropriate label to indicate the dissolved manganese cations in the phase. The composition of selected ores is indicated. Calculated with Factsage using the FToxid, FTmisc and FactPS databases[27].

The stabilization effect caused by mixed oxides has been observed experimentally[65,67–71]. The stabilization of Mn_3O_4 due to high iron content was observed by Fahim et al.[65] when reducing different grades of Um Bogma ore with CO. Larssen et al[70] observed that FeO was stabilized in solid solution with MnO during reduction of Comilog and Nchwaning ore. The conditions were such that metallic iron was expected to form according to Figure 2-3. The same was observed by Lobo[67] under reduction of Nchwaning ore. During reduction of

synthetic pellets made from MnO_2 and Fe_2O_3, Liu et al.[68,69] observed the formation of $(Mn,Fe)_3O_4$ above 800 °C. $(Mn,Fe)_3O_4$ was formed in reaction between Mn_3O_4 + Fe_3O_4 and MnO + Fe_3O_4 where the reaction with MnO occurred at lower temperatures. It has also been seen that Fe (and Mn) may be stabilized in aluminates (galaxite) and silicates (tephroite and rhodonite)[72], and that Mg and Ca enter the monoxide phase[25,49,73–76].

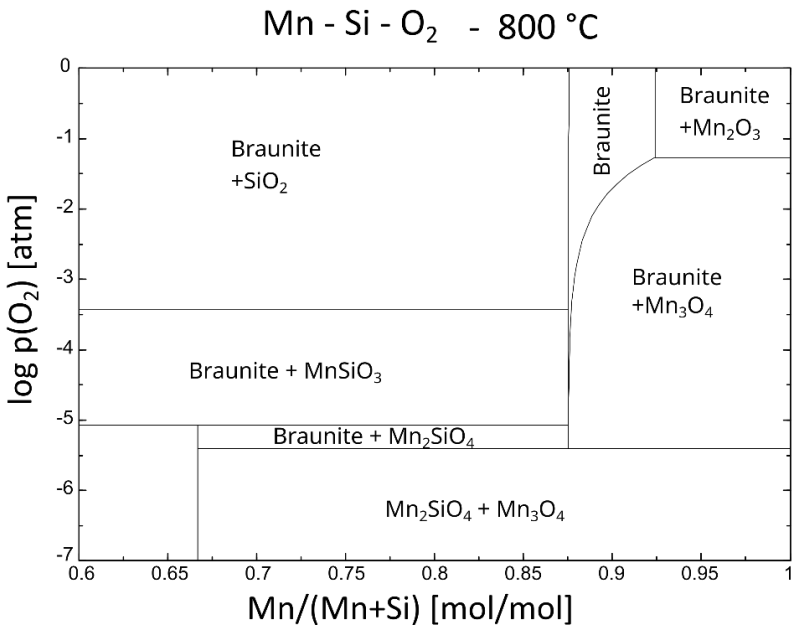

Figure 2-5: An isothermal section of the Mn-Si-O_2 phase diagram showing the stable phases at 800 °C as a function of composition and oxygen partial pressure. Calculated with Factsage using the FToxid, FTmisc and FactPS databases[27].

SiO_2 is a component in most ores (Table 2-3) however the chemical analysis does not state in which form it is present. In GE and Comilog ore, SiO_2 is present as quartz whereas in Wessels it is present in Braunite (I and II)[49]. The stability of bixbyite ($(Mn,Fe)_2O_3$) versus braunite ($(Mn,Fe)_2O_3 \cdot (Mn,Ca)SiO_3$) has previously been suggested to account for observed differences in reducibility of ores[77–79]. The isothermal section of the Mn-Si-O_2 phase diagram in Figure 2-5 shows that the oxygen pressure at which braunite decomposes is about 10^{-5}, compared to below 10^{-1} for bixbyite (Mn_2O_3) at 800 °C. A 70 % CO – 30% CO_2 gas mixture establishes a high driving force of reduction for either of the minerals, with an oxygen partial pressure of approximately 10^{-19} at 800 °C[80]. The driving force for reduction is several orders of magnitude larger than the difference between the minerals, thus, the observed difference in reducibility may be due to kinetics.

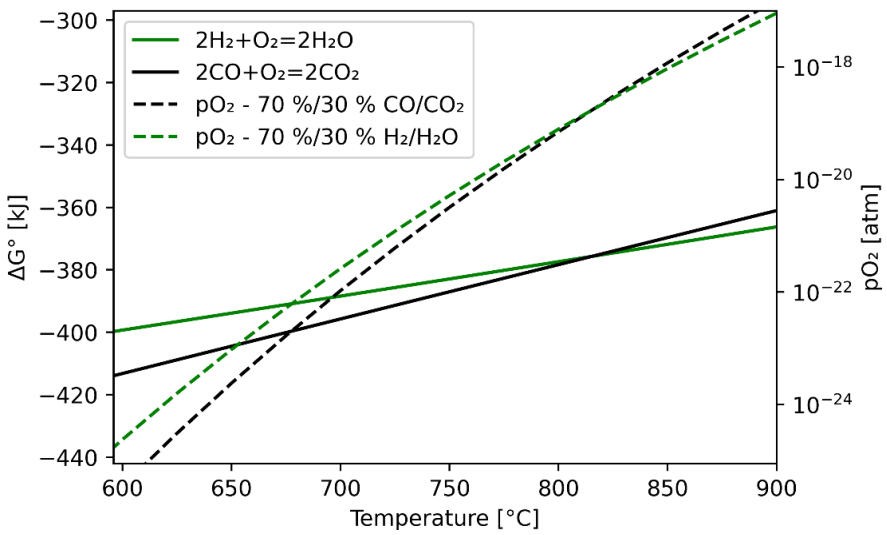

Figure 2-6: The Gibbs free energy of oxidation og H_2 and CO and the equilibrium oxygen partial pressures of a 70 % CO – 30 % CO_2 and a 70 % H_2 – 30 % H_2O gas mixture. The driving force for the gas mixtures are equal at about 815 °C. Calculated using HSC chemistry 9[18].

As previously mentioned, preheating and prereduction of ores may reduce the carbon and energy consumption during production. Different gas atmospheres will impose different driving forces for reduction- and decomposition reactions. As seen above (i.e., Figure 2-3), a higher oxygen pressure gives a lower driving force for reduction, thus using air instead of a reducing gas like CO or H_2, will lower the reduction rate as well as yielding a higher oxidation level at equilibrium. The Gibbs free energy of oxidation of CO and H_2 as a function of temperature is shown in Figure 2-6. It can be seen that the thermodynamic driving force for oxidation of H_2 and CO is equal at about 815 °C, and that H_2 is a stronger reductant than CO at higher temperatures than 815 °C. The oxygen partial pressure of H_2/H_2O and CO/CO_2 mixtures containing 70 % reducing gas shown in Figure 2-6 gives the same information as the Gibbs free energy. Using the equilibrium oxygen partial pressure to describe the driving force is useful since it allows for direct comparison of the thermodynamic potential of different gas mixtures.

MnO is quite stable during reduction, even at low CO contents as seen in Figure 2-7 where the oxygen partial pressure of CO/CO_2 gas mixtures containing 30 % and 70 % CO has been superimposed on the Mn-O_2 phase diagram. MnO is stable in CO/CO_2 gas mixtures containing 1 % - 99 % CO and in H_2/H_2O mixtures containing 1 % - 99 % H_2[81].

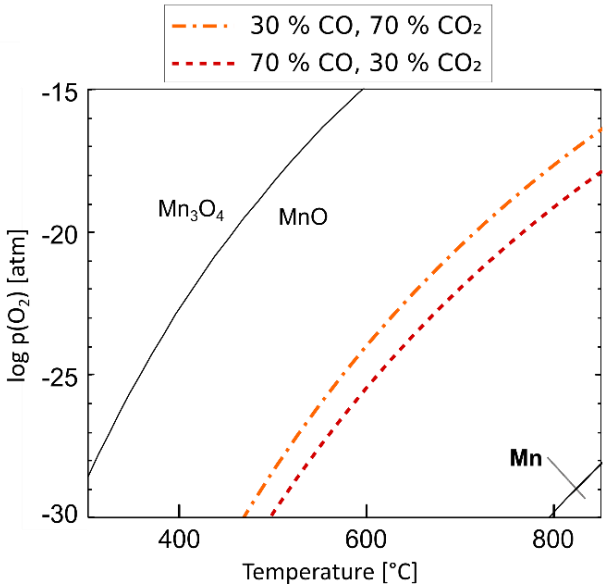

Figure 2-7: Oxygen partial pressures of CO/CO_2 gas mixtures with 30 % and 70 % CO, respectively, superimposed on the Mn-O_2 phase diagram. The phase diagram was calculated using Factsage[27] with the FToxid, FTmisc and FactPS databases. Equilibrium gas compositions were calculated using HSC chemistry 9[18].

In the stability range of MnO at 800 °C, iron may be in the form of magnetite (Fe_3O_4), wüstite (FeO) or metallic iron (Fe) (Figure 2-3). Obtaining metallic iron below 800 °C would be beneficial for the energy and carbon consumption during industrial production, however it is seen that the iron is stabilized as FeO either in solid solution with manganese, calcium and magnesium or in silicates and aluminates. Hence, the highest achievable prereduction of manganese- and iron- oxides below 800 °C is MnO-FeO. Metallic iron has been observed after isothermal reduction of low grade agglomerates (Mn/Fe=3.2) in H_2 above 900 °C[82–85]

2.4 The prereduction rate of Manganese raw materials

The distance from equilibrium describes the driving force for the reaction, and the rate of the reaction is given by the driving force between the gas and the oxide, as well as other kinetic variables. In the previous section it was seen that the chemical composition influences the equilibria during reduction. The reduction rate is dependent on the reducing conditions i.e., temperature, heating rate and gas composition. Additionally, the reduction rate depends on the properties of the raw material such as porosity, mineral composition, and particle size. In the following, the influence of the different parameters on the prereduction of manganese raw materials is reviewed.

2.4.1 The effect of mineral composition and porosity on prereduction

Factors such as the mineral composition and porosity of raw materials has been seen to influence the kinetics during reduction. There are large differences in phase- and chemical composition of raw materials from different sources (Table 2-2 and Table 2-3 respectively), and there are differences in porosity. The mineral composition is seen to have an impact on the kinetics when the porosity is low, while in porous ores and agglomerates, the reactivity is correlated with porosity. The porosity increases during reduction and with carbonate decomposition[37,86,87].

Ling et al.[88] made pellets from manganese ore and calcite, engineering the porosity after calcination by different additions of calcite. The reduction rate of MnO in methane was seen to increase with increasing porosity of the pellet.

Lobo[67] reduced Nchwaning pellets and lump ore isothermally at 950 °C and observed a significantly higher reduction rate for pellets compared to lump ore. The porosity of the pellets was higher compared to the lump ore.

In general, different ores have different reactivities as observed in several investigations. Tangstad et al.[79] that reviewed 6 laboratory investigations focused on the reactivity of various manganese ores. Comilog and GE stand out as the most reactive ores in the studies. The authors explain this by that bixbyite is reduced faster than braunite. Bixbyite (Mn_2O_3) is an intermediate phase during prereduction of Comilog and GE ores.

In Berg[77] and in Berg and Olsen[78] minerals were isolated from GE, Nchwaning and NAM (Namibian ore) ores to investigate the reduction kinetics of the separate minerals. Braunite minerals were more difficult to reduce compared to bixbyite. This was believed to be due to that that bond strengths in between Si and O are higher compared to Mn and O and the need for solid state diffusion in the separation of products from the reduction of Braunite (I and II). Topochemical reduction was observed in reduction of GE and Nchwaning, and the initial porosity is low for both ores[39,53]. In diffusion-controlled reduction of dense particles, a concentration gradient will be established across the product layer[89], causing the virgin material to be exposed to lower levels of reducing gas compared to the bulk gas composition. Hence, the increased stability of braunite compared to bixbyite (Figure 2-5) may influence the reduction rate in this case. The reduction rate of bixbyite from Nchwaning was higher compared to bixbyite from GE due to improved product layer diffusivity. The bixbyite from Nchwaning ore had a higher porosity compared to the GE bixbyite[78]. The reduction of Braunite I in NAM ore was observed to be considerably faster compared to the reduction of Braunite I in Nchwaning[77]. No reaction front was observed in the NAM Braunite and the ore was observed to have more cracks and pores compared to Nchwaning.

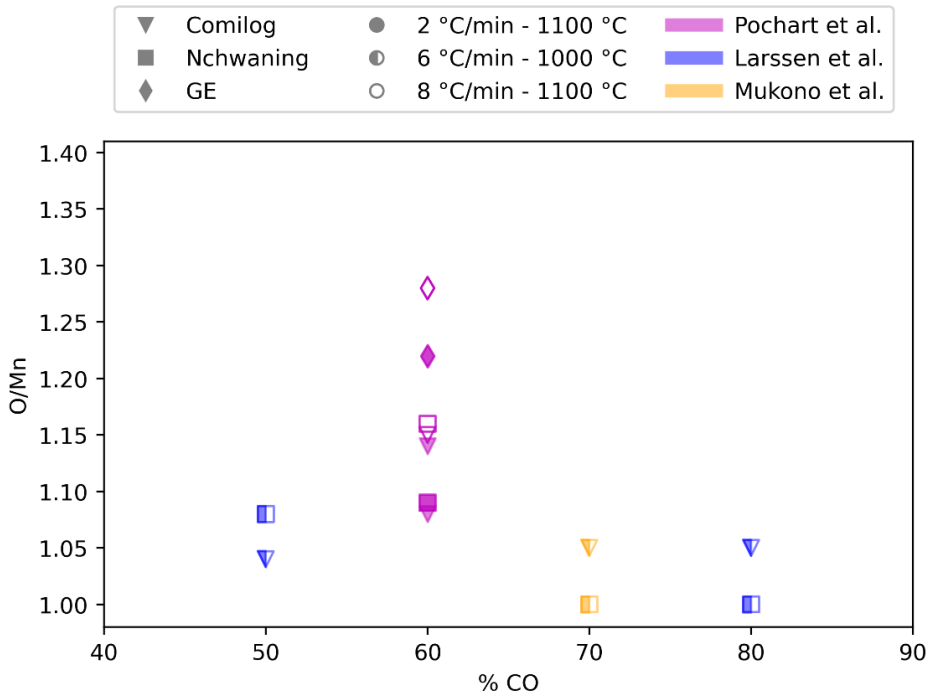

Figure 2-8: The O/Mn ratio after reduction in CO/CO_2 atmospheres with different CO contents. The results from Pochard et al.[42] is compared to results from Larssen et al.[70] and Mukono et al.[87] obtained at an intermediate heating rate, similar median particle size and lower end temperature.

Pochart et al.[42] reduced GE, Comilog, Mamatwan and Nchwaning ores in CO/CO_2 atmospheres. Two different heating rates were employed, 2 °C/min and 8 °C/min, corresponding to the minimum and maximum heating rates observed in industrial furnaces. It was found that oxidized ores (GE and Comilog) in most cases has a lower reactivity compared to the semi-oxidized ore (Nchwaning), contradicting other observations[23,37,79].

Figure 2-8 compares the results from Pochart et al.[42] with investigations using similar particle size fractions. It can be seen that the O/Mn ratio after reduction is higher in Pochart et al.[42], despite the end temperature was 100 °C higher. Pochart et al.[42] used off-gas analysis to determine the O/Mn ratio while the other investigations used the chemical analysis and weight loss data in conjunction to determine the O/Mn ratio[70,87], the latter is believed to be more robust. Later studies[33,90,91] have observed oxygen evolution when heating Comilog ore, also in the presence of CO[90]. If oxygen was not measured in the off-gas analysis in Pochart et al.[42], it would cause an underestimation of the reactivity of the oxidized ores. The observed effects of heating rate (section 2.4.2) and particle size (section 2.4.3) in Pochart et al.[42] is consistent with other investigations.

Table 2-5. The O/Mn ratio and porosity of different ores at 800 °C during reduction in a gas mixture of CO/CO_2 = 70/30.

Raw material	O/Mn	Porosity [%]	Reference
Gloria ore	1.2	6	[23]
Nchwaning ore	1.3-1.4	2.3	[23]
Nchwaning* ore	1.22-1.28	0-1	[32, 37]
Nchwaning* ore	1.23	5.3	[53]
Nchwani-ng* M	1.00	39.4	[53]
Nchwaning* B	1.05	20.9	[53]
Nchwaning* pellets**	1.04	42.3	[37]
Comilog ore	1.02-1.09	24.0-48.9	[32, 37]
Comilog ore	1,14	22.5	[53]
Comilog M	1.00	45.2	[53]
Comilog B	1.05	28.3	[53]
Comilog sinter	1.09-1.13	13.6	[32, 37]
Comilog pellets**	1.07	16.3	[37]
Urucum ore	1.15	17.5	[53]
Urucum M	1.00	34.7	[53]
Urucum B	1.02	28	[53]
CVRD ore	1.04	38.4	[37]
CVRD sinter	1.18	13	[37]
CVRD pellets**	1.14	9.5	[37]
Ore A~	1.00	22.6	[54]
Ore A - Briquette	1.00-1.01	24.3	[54]
Ore A - Sinter	1.10-1.14	17.7	[54]
Ore A - Pellet~¤	1.10-1.15	11.9	[54]
Ore B	1.00-1.04	18.5	[54]
Ore B - Briquette	1.00-1.01	22.2	[54]
Ore B - Sinter	1.11	11.1	[54]
Ore B – Pellet¤	1.10-1.22	4.7	[54]

*Nchwaning ore which is named Asman or Assmang in the reference

** Crushed ore to <0,2 mm pelletized and sintered at 1100 °C for 30 min

~Smaller particle size, +4,5 mm for ore and +6,3 for pellets

¤ Crushed ore to 20 µm (d50), pelletized and sintered at 1200 °C for 30 min

M – briquettes with 10 % molasses binder, B - briquettes with 5 % bentonite binder

Several investigations have measured the CO-reactivity under similar conditions and set-up[32,54,23,37,53]. The reactivity was assessed from the excess oxygen at 800 °C where O/Mn ratio at 800 °C is inversely proportional to the reactivity. Approximately 200 g ore in the size fraction 10-14.7 mm was heated to 1100 °C with a 10 °C/min heating rate in a 70 % CO/30 % CO_2 atmosphere. The gas atmosphere was chosen as it is believed to be close to the gas composition around

700-900 °C in industrial furnaces. Table 2-5 and Figure 2-9 show the porosity and the O/Mn ratio at 800 °C from these investigations.

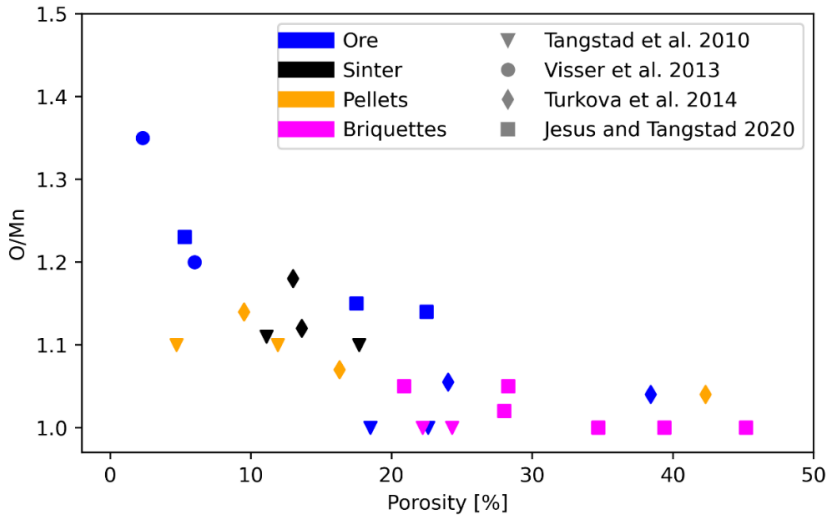

Figure 2-9: The O/Mn ratio at 800 °C from reactivity tests as a function of initial porosity[23,37,53,54]. The O/Mn ratio is inversely proportional to the reactivity; hence the reactivity increases with increasing porosity across the raw materials.

Visser et al.[23] claimed that the higher CO-reactivity of Comilog compared to the Nchwaning and Gloria ores was due to the higher porosity of Comilog ore. Turkova et al.[37] reported that Nchwaning ore had the lowest CO-reactivity and the lowest porosity. Conversely, the Nchwaning pellets had the highest CO-reactivity and the highest porosity. It can also be seen that the sinters from CVRD and Comilog had a lower reactivity and porosity compared to their lump ores (Table 2-5). The porosity of the raw materials was found to increase with temperature and with extent of reduction (the latter is shown in Figure 2-10). Tangstad et al.[54] tested lump ore, briquettes, sinter and pellets of two different ores. The lump ore and the briquettes were close to fully reduced at 800 °C, and their porosity were higher compared to the pellets and sinter. Jesus and Tangstad [53] tested lump ore and briquettes made from Urucum, Nchwaning and Comilog ore and found that Urucum and Comilog had a higher CO reactivity compared to Nchwaning. Two types of briquettes were made from each ore and both types displayed a higher reactivity compared to the ores. The porosity of the briquettes was higher compared to the lump ores and the briquettes with highest porosity also had the highest reactivity.

In the reduction of carbonate containing ores, oxide reduction and carbonate decomposition may happen simultaneously. The decomposition of

carbonates may increase the local CO_2 concentration that in turn may retard the reduction rate of the oxides and decomposition rate of carbonates due to lower driving force. On the other hand, carbonate decomposition increases porosity due to the associated volume change of carbonate decomposition.

Sukhomlinov and Tangstad[86] observed that the reduction of higher manganese oxides and decomposition of carbonates in United Manganese of Kalahari (UMK) ore occurred mainly at about 700 °C and 900 °C, respectively. This was later confirmed by Mukono et al.[87] that in addition observed some carbonate decomposition at 700 °C, hence the carbonates in UMK decomposes in two steps at about 700 °C and 900 °C. In Nchwaning ore, the carbonates decomposed in a single step at about 900 °C[87] and for both ores, carbonate decomposition coincided with an increase in the porosity. The porosity was seen to increase at lower temperatures in UMK than in Nchwaning ore and Nchwaning ore had a lower reactivity compared to UMK[87]. Figure 2-10 shows the correlation between porosity and O/Mn ratio for different ores where it is seen that the porosity increases with increased extent of reduction (=lower O/Mn ratio).

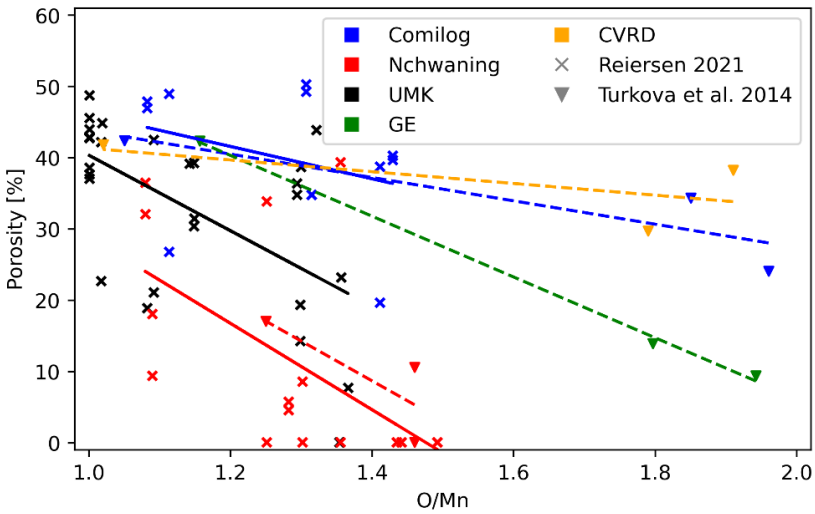

Figure 2-10: Measured porosity of different ores after reduction (up to 950 °C) as a function of O/Mn ratio from chemical analysis. Added trendlines; Turkova et al.[37] – dashed, Reiersen[92] – Solid. As the degree of reduction increases (decreased O/Mn ratio), the porosity is seen to increase.

In dig-outs from pilot scale experiments, Mukono et al.[93] observed that UMK ore had a greater extent of prereduction compared to Nchwaning ore throughout the prereduction zone of the furnace. UMK and Nchwaning ores contain similar minerals though UMK has a higher initial porosity[92,94] and a higher carbonate content (UMK is from the same ore body as Gloria[95,96] , see Table 2-2).

As mentioned previously, Berg[77] observed that braunite had significantly different reactivities depending on which ore it originated from, and that the fastest was associated with a higher amount of cracks and pores. This indicates reduced diffusion resistance and is in line with the observed correlation between increased reactivity and porosity from later works[23,32,37,53,54]. The same behavior is seen in oxidized ores where GE ore has a lower porosity (5-7%)[39] and reactivity compared to Comilog ore[42], even though the phase composition is similar (Table 2-2). The reactivity of pellets[37,54,67] improved compared to the original ore only when the porosity was increased and vice versa, though the heat-treatment during induration of the pellets may have influenced the reactivity since all carbonates were decomposed. The briquettes[53,54] however are not heat treated, hence the phase composition is identical to the lump ore and the improved reactivity can be correlated directly to the improved porosity. Increased porosity due to carbonate decomposition correlates with improved prereduction in ores with similar mineral composition[87,93], thus the possible retarding effect from increased local CO_2 content has a limited impact compared to the increased porosity. The positive correlation between porosity and reactivity, indicates that a lower mass transfer resistance within the materials improves the reduction rate. The contact area between the reducing gas and unreduced material will be higher in a porous ore compared to a dense ore. In conclusion, the phase composition and carbonate content may influence the reduction kinetics of manganese ores, however the influence from porosity is more significant.

2.4.2 Effect of temperature and heating rate on prereduction

Manganese reduction has been investigated through isothermal and non-isothermal experiments. Isothermal experiments have the advantage of obtaining data for specific temperatures that ideally is well suited for modeling. However, manganese oxide materials tend to react at low temperatures, thus a substantial degree of reduction may have occurred before the sample reaches the set isothermal temperature. Non-isothermal reduction on the other hand, explores the entire temperature range, making it possible to identify at which temperatures different reactions starts. The disadvantage is that the early stage of reduction is always investigated at low temperatures, and late stages always at high temperatures. Several investigations have been conducted both isothermally and non-isothermally at different temperatures and heating rates.

Ishak[97] reduced Comilog ore isothermally in CO/CO_2 atmospheres. Most of the samples were calcined at 1100 °C in nitrogen to convert the manganese oxides to Mn_3O_4. In addition, a few samples were pre-reduced at 290-300 °C in pure CO to a similar composition and tested at 900 °C and 1000 °C. It was found that both diffusion through the product layer and chemical reaction controlled the reduction

rate in the range 900-1100 °C, where the diffusion had a stronger effect at high temperatures and the chemical reaction at low temperatures. Reduction rate was higher in the pre-reduced samples compared to the calcined samples indicating that the calcination prior to reduction influences the structure of the ore, and hence the reduction rate of Mn_3O_4[97]. At higher temperatures (1000 °C) this difference vanished due to sintering effects during reduction. Berg and Olsen[78] also observed that reduction was retarded at high temperatures in siliceous ores due to sintering effects.

The reduction rate was seen to increase with increasing temperature during isothermal reduction of pellets and briquettes from a low grade Egyptian ore 750 °C to 950 °C in hydrogen[82,83].

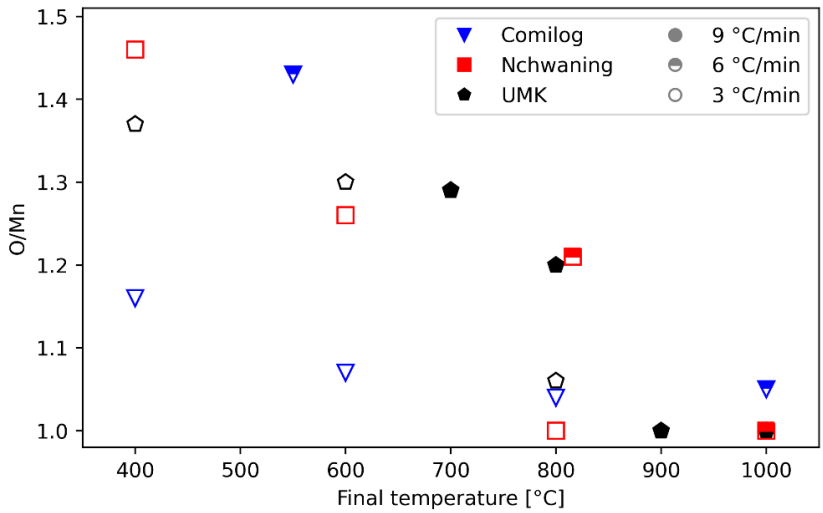

Figure 2-11: The O/Mn ratio as a function of final temperature during non-isothermal reduction at different heating rates. Biørnstad[94,98]: 10-13.2 mm particles at 3 °C/min .Larssen et al[70]: 11.2-15 mm particles at 6 °C/min. Mukono et al[87]: 10-12.5 mm particles at 9 °C/min. The ore is more reduced at lower heating rates and higher temperature as expected.

Mukono et al.[87] (Reiersen[92]) reduced Comilog, Nchwaning and UMK ores non-isothermally in CO/CO_2 gas mixtures containing 70 % CO. Based on the weight loss and reduction rate curves it is seen that prereduction of Nchwaning and UMK ore was completed at 1000 °C when employing a 3 °C/min heating rate but reduction was incomplete with 6 °C/min and 9 °C/min. Comilog was fully reduced for all heating rates. Chemical analysis, on the other hand, indicated that the UMK and Nchwaning were fully reduced in all cases whereas Comilog was not. Comilog has a low iron content compared to Nchwaning and UMK (Table 2-3) and it has been seen previously that the O/Mn ratio is underestimated in the chemical analysis when iron is present as Fe_3O_4 or FeO [Sarina Bao – unpublished work in the Prema project]. Figure 2-11 shows the O/Mn ratio after non-isothermal

reduction to different temperatures where it is seen that increased temperature and lower heating rates give a lower O/Mn ratio after reduction.

Larssen et al.[99] reduced Comilog and Nchwaning ores non-isothermally at 6 °C/min. Reduction was complete below 600 °C for the Comilog ore, whereas for Nchwaning ore, in the majority of experiments the reduction was not completed at 800°C. Temperature profiles from reduction of each ore is shown in Figure 2-12. At the onset of exothermal reactions (around 30 min reduction time) a substantial increase in the temperature for Comilog ore is observed. The reduction rate is increased due to the higher temperature until the ore is mostly reduced. Nchwaning ore shows a small temperature increase at the same point in time and the accompanying increase of reduction rate is several orders of magnitude lower compared to Comilog. Several investigations have reported this phenomenon during reduction of oxidized ores[37,42,87,92,94,100]

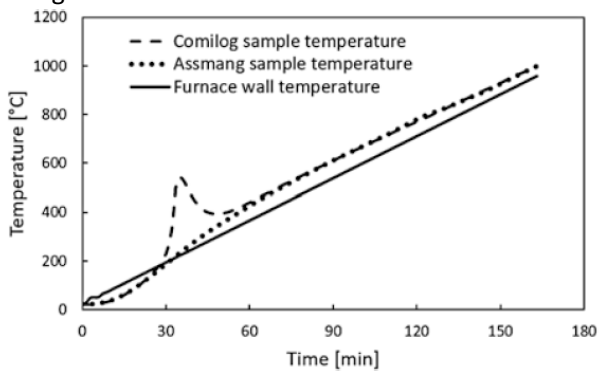

Figure 2-12: Measured temperatures in Assmang (=Nchwaning) and Comilog during reduction. From Larssen et al. [99]

The exothermal effect on the temperature of experiments may partly explain why oxidized ores often are more reactive compared to semi-oxidized ores that has been reduced under the same conditions, despite that approximately twice the amount of oxygen needs to be removed from the oxidized ores to convert them to MnO. The exothermal peak has been seen to occur at lower temperatures for smaller particle size fractions[94,100], smaller particle sizes give a higher peak temperature compared to larger particles of the same ore[42,100], and, highly reactive ores have a higher peak temperature compared to less reactive ores with the same particle size distribution (Figure 2-12)[99].

Larssen et al.[100] found that the exothermal peak initiated around 580 °C for the reduction of Comilog ore in the particle size fraction 11.2-15 mm. The magnitude of the exothermal peak decreased with decreasing heating rate and with increasing CO content in the reducing gas. This was due to that more MnO_2 had been reduced prior to the onset temperature of the exothermal peak (580 °C).

The same effect of heating rate on the exothermal peak was also observed in Mukono et al.[87].

To summarize; increased temperature has been seen to improve the reduction rate during isothermal reduction of both fines[101], agglomerates[82,83] and lumpy ores[70,97], though the reduction rate may be retarded at high temperatures due to sintering effects[78,97]. High heating rates during non-isothermal reduction lowers the degree of reduction compared to low heating rates[42,87,92,100], and high heating rates increase the temperature deviation caused by exothermal reactions in oxidized (MnO_2) ores[87,92].

2.4.3 Effect of particle size on prereduction

The particle size of the material influence the kinetics of reduction, and in general smaller particles show higher reduction rates. In industrial production, a high amount of fines can be detrimental for the furnace operation[16,42,43], on the other hand, the slower reduction of larger lumps negatively influences the carbon and energy consumption.

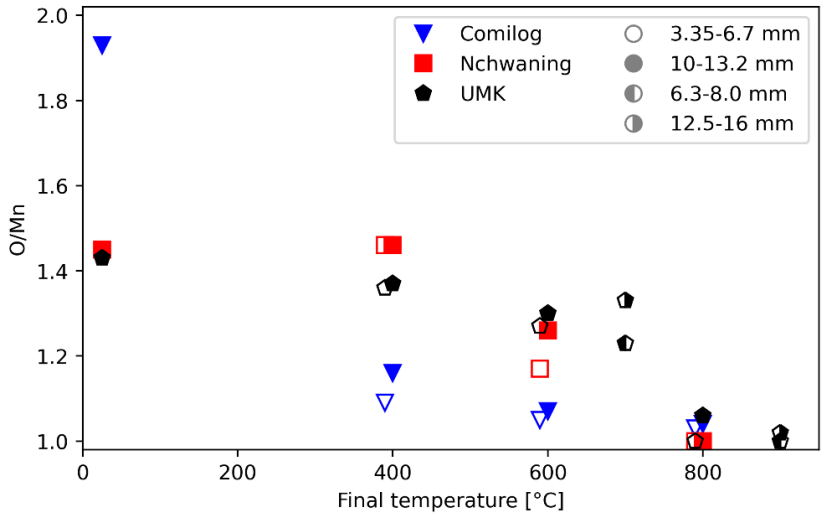

Figure 2-13: Shows the O/Mn ratio after non-isothermal reduction various final temperatures. Biørnstad et al[94,98]: 3 °C/min in a 70% CO 30 % CO_2 atmosphere (hollow and filled symbols). Sukhomlinov and Tangstad[86]: 6 °C/min in a 80% CO 20 % CO_2 atmosphere (half filled symbols). Original O/Mn ratio is also included (values at 25 °C)[94,98]. The final O/Mn ratio is lower for smaller particle size fractions.

Increased reduction rate with decreasing particle size has been reported by several authors when reducing different particle size fractions of ore fines (< 1 mm)[63,64,101–103], and lump ores[42,70,86,94,97,98,100]. Kor[104] observed an increased reduction rate with decreasing size of synthetic pellets with diameters in the range

0.6-8 mm. In addition to the improvement of oxide reduction with decreasing particle size, Sukhomlinov and Tangstad[86] observed that the decomposition of carbonates was independent on particle size.

Pochart et al.[42] observed that the reactivity of different ores decreased with increasing particle size and that the reactivity of larger particle size fractions were more influenced by higher heating rates.

Figure 2-13 shows the O/Mn ratio after non-isothermal reduction. It can be seen that the O/Mn ratio of smaller particle size fraction is consistently lower than that of the larger particle size fraction at each temperature. At 400 °C, most of the reduction in Comilog ore has already occurred, whereas UMK and Nchwaning ore still have a O/Mn ratio close to their original compositions.

Larssen et al.[100] reduced Nchwaning and Comilog ore in the particle size fractions, 0.5-1.36 mm, 3.33-4.00 mm, 11.2-15 mm, and 30-40 mm in CO/CO_2 atmospheres. Decreasing raw materials size was found to correlate with lower reduction temperature and increased reduction rate. Modeling revealed that the reduction rate was proportional to the inverse median particle size.

The size of a particle determines the maximum distance of which the gas must travel through the particle during reduction. In general, increasing particle size will increase the influence of mass transfer on the overall kinetics[89]. Higher heating rate gives less time for the particle to be reduced, thus it will amplify the differences in reactivity as seen when reducing larger particles[42].

2.4.4 Effect of gas composition on prereduction

Reduction and decomposition in various gases or gas mixtures (i.e., CO, CO_2, H_2, H_2O, CH_4, air, N_2, and Ar) have been investigated. Reduction with CH_4[62,105–110], H_2[49,82,83,111–113], experiments where the driving force has been mediated by addition of CO_2 and/or H_2O[23,32,37,42,53–55,67–70,77,78,87,97,99–101] and reduction in the presence of solid carbon[75,76,87,92,103,114–118] has been reported. Reduction with CH_4 is mainly done at higher temperatures to produce alloy and has been covered in recent reviews by Elliott et al.[119] and Cheraghi et al.[81]. Studies using solid carbon is often conducted at higher temperatures (above 1000 °C) where the prereduction reactions are very fast, and thus poorly resolved. Reduction by solid carbon is dependent on the oxidation of carbon by CO_2 to produce CO for reduction[104,114–116,119] which is slow at lower temperatures[120,121]. An example of this can be seen in Figure 2-14 where the O/Mn ratio of Comilog ore after heating with and without coal in rotary kiln is compared to ore reduced in a CO/CO_2 gas mixture. The $\Delta G°$ values for reduction with C and CO in Figure 2-14 show that the driving force for reduction with solid carbon is higher compared to reduction with CO, however, the Boudouard reaction is not fast enough to establish the equilibrium driving force in the gas mixture in this temperature range.

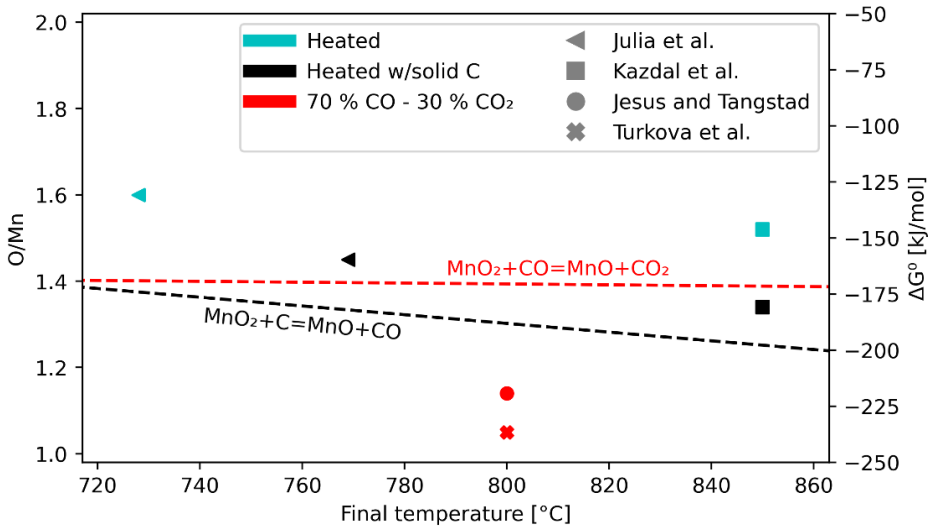

Figure 2-14: O/Mn ratio of Comilog ore after heating without reductants, heating with coal and reduced with CO[33,37,44,53]. Julia et al.[44]: 0-40 mm particles with and without coal for 45 minutes. Kazdal et al.[33]: 5-20 mm particles with and without coal at 850 °C for 180 minutes. ΔG° for reduction with C and CO is shown on the secondary axis. ΔG° values from HSC chemistry 9[18]. Turkova et al.[37]: 10-15 mm particles in 70 % CO – 30 % CO2 for 78 minutes. Jesus and Tangstad[53]: 9-15 mm particles in 70 % CO – 30 % CO2 for 78 minutes.

If ore is heated in inert or oxidizing atmospheres some changes may occur depending on the composition of the ore. MnO_2 and Mn_2O_3 decomposes in air (pO_2=0.21) at 455 °C and 931 °C, respectively, whereas Mn_3O_4 and Fe_2O_3 are stable to temperatures above 1400 °C (Figure 2-3). Carbonates in the ore may also decompose, as previously mentioned (Figure 1-4). Different fractions of reducing gas in a gas mixture, and type of reducing gas will also influence the kinetics of reduction.

$$2MnOOH = Mn_2O_3 + H_2O \qquad (10)$$

Synthetic and natural manganese oxides and hydroxides have been studied in small scale (milligrams) TGA analysis in oxidizing and inert gases. Manganite decomposes according to reaction (10) however the product oxide may oxidize or decompose depending on the temperature and atmosphere. At 500-600 °C, decomposition of manganite is according to reaction (10), and Mn_2O_3 is seen to further decompose to Mn_3O_4 at 800-900 °C[122]. The reduction of synthetic MnO_2 in air and inert atmospheres commences at 550-600 °C, reducing stepwise through the oxides eventually forming Mn_3O_4 at 950-1050 °C[123]. Synthetic Mn_3O_4 and MnO oxidizes to Mn_2O_3 in air above 500 °C[123,124], decomposing back to Mn_3O_4 above 1000 °C[123]. In natural MnO_2, a progressive weight loss was observed between 200-580 °C due to decomposition of bound water and partial reduction[124].

Different natural ores have also been investigated in inert gases on a larger scale (g-kg). Oxygen measurements in the off-gas have shown that oxygen is released from Comilog ore in the temperature range 300-800 °C[33,90,91]. Fines (-63µm) has been seen to react at significantly lower temperatures compared to larger particle sizes (> 5mm)[33]. In carbonate containing ores, CO_2 release has been observed above 500 °C[90,91]. Higher heating rates correlate with higher decomposition temperatures for both oxides and carbonates[33,90,91].

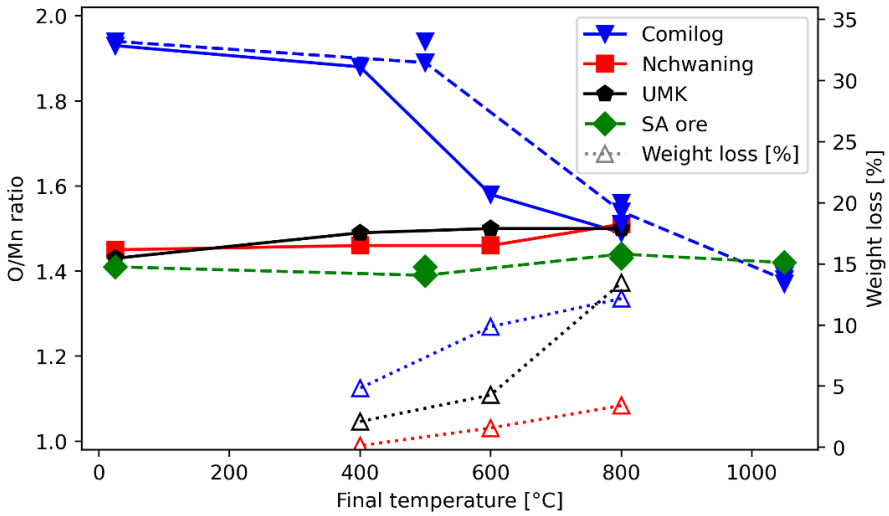

Figure 2-15: O/Mn ratio and weight loss (open triangles) after heat treatment of ores to various temperatures. Biørnstad [94,98]: 3 °C/min in synthetic air with 10-13.2 mm particles, solid and dotted lines (O/Mn ratio and weight loss). Kazdal et al.[33]: 7.5 °C/min in N_2 with 5-8 mm, 10-12 mm and 18-20 mm particles, dashed lines. SA ore = unspecified South African ore.

Figure 2-15 shows the O/Mn ratio after heating ores non-isothermally to different temperatures. The main reduction of the O/Mn ratio of Comilog ore occurs above 500 °C. Comilog heated in N_2 (dashed lines) is seen to have decomposed less compared to Comilog heated in synthetic air (solid lines), despite that N_2 is expected to give a higher driving force for decomposition compared to synthetic air (section 2.3). The heating rate in the N_2 experiments were 2.5 times higher compared to the synthetic air experiments, giving the ore less time to approach equilibrium.

The initial O/Mn ratio of Nchwaning, UMK and SA ore in Figure 2-15 is between 1.4-1.5 prior to heating which is observed to increase slightly with temperature up to 800 °C. Biørnstad[94,98] observed a weight loss in all ores during the heat treatment (Figure 2-15). For the UMK and Nchwaning ore, the oxidation of hausmannite (O/Mn=1.33) to bixbyite (O/Mn=1.5) will result in a weight

increase, though there are other factors contributing to the observed weight loss. Above 500 °C, carbonates[90] and manganite[122,124] will start decomposing, contributing to the weight loss, in addition, UMK and Nchwaning were not dried prior to the experiments[94,98] and any free moisture present would also contribute to the weight loss. For Comilog ore, the weight loss is associated with bound water and decomposition of higher oxides, and the weight loss behavior correlate with the reduction behavior.

Julia et al.[44] heated Nchwaning and Comilog ore in a pilot scale rotary kiln fired by gas. The O/Mn ratio of Comilog ore was reduced from 1.9 in the original ore to 1.6 after heating to 728 °C, and the ore was seen to contain mostly Mn_2O_3 with minor amounts of MnO_2. No reduction was found for the Nchwaning ore, as the changes in Nchwaning ore were smaller than the variability in the original ore.

Mn_2O_3 is the stable manganese oxide at 800 °C in air (Figure 2-3 and Figure 2-4, pO_2=0.21). In general, MnO_2 decomposes and is mostly converted to Mn_2O_3 as the temperature approaches 800 °C. This constitutes approximately half of the removable oxygen during prereduction of oxidized ores. A slight oxidation to O/Mn ≈ 1.5 in air has been observed for ores with lower initial O/Mn ratio in the same temperature region and is in line with the equilibria and with observations from synthetic materials.

Barner and Mantell[112] studied the reduction of synthetic pyrolusite (MnO_2) fines (<0.22 mm) isothermally with H_2 in the temperature range 200-500 °C. Mn_3O_4 was the product below 250 °C and high diffusional resistance through the Mn_3O_4 layer was encountered with increasing temperature. Above 325 °C, the product from reduction was MnO. Belgian Congo pyrolusite ore was seen to react considerably faster compared to the synthetic pyrolusite. In De Bruijn et al.[113] (fines < 0.13 mm), a more porous material was investigated , and the dense Mn_3O_4 layer encountered by the former investigation was not observed. At 275 °C, MnO_2 was converted directly to Mn_3O_4 followed by the relatively slower reduction of Mn_3O_4 to MnO. At 325 °C, MnO_2 was reduced to Mn_3O_4 which immediately changed to MnO whereas at 400 °C, only MnO_2 and MnO was observed. When investigating the individual reduction steps, it was found that the reactivity was influenced by the method of preparation of the intermediate oxides (reduction, oxidation, decomposition, calcination), even though the samples originated from the same ore[113]. Zaki et al.[123] used H_2 to reduce synthetic MnO_2 in non-isothermal experiments (20 mg samples) and found that MnO_2 was reduced to MnO without the formation of stable intermediaries. This was also seen in a later study by Zaki et al. in reduction with CO gas[125].

Reduction in CO/CO_2 gas mixtures with varying CO content has been investigated by several researchers, and increasing CO content is seen to improve the reduction rate[70,86,99–101,126]. Sukhomlinov and Tangstad[86] also observed that the

rate of carbonate decomposition decreased with increasing CO_2 content, and that increased CO_2 content increased the carbonate decomposition temperature. Larssen et al[100] observed that the reduction rate was proportional to the input CO partial pressure with order 0.7 and 1.5 for Comilog and Nchwaning ore respectively. The results were consistent for multiple particle size fractions (0.5-1.36 mm, 3.33-4.0 mm and 11.2-15 mm). Gao et al.[101] found that the reaction was first order with respect to CO content when reducing ore fines (<1mm).

Addition of H_2 to CO/CO_2 gas mixtures has been seen to improve the reduction rate og manganese ores[126,127]. Ngoy et al.[126] reduced Comilog and Nchwaning in CO/CO_2 and $CO/CO_2/H_2$ gas mixtures with similar oxygen partial pressures and observed that the addition of H_2 improved the reduction rate by 20-30 %. Larssen and Tangstad[127] investigated the same ores in CO/CO_2, $CO/CO_2/H_2$ and $CO/CO_2/H_2O$ atmospheres, adjusting the compositions such that the oxygen partial pressures were equal at 800 °C. Both H_2 and H_2O promoted the reduction of Comilog ore due to the water-gas-shift reaction, though the improved reduction in the presence of H_2O did not occur below 430 °C. H_2 was seen to promote the reduction of Nchwaning ore. Carbon deposition occurred above 400 °C during reduction of Nchwaning ore.

Kononov et al.[118] observed that the carbothermal reduction of MnO proceeded at a higher rate in helium compared to argon due to the increased diffusion coefficients of CO and CO_2 in helium. The rate was further improved when hydrogen was present due to its involvement in the reduction process. The same observation was made by Eom and Min[117] where the rate of manganese carbide formation was correlated with the CO gas diffusivity. It was concluded that the improved reaction rate in the presence of H_2 was caused by CH_4 produced in the reaction between H_2 and C. Hashizume[128] observed CH_4 formation in carbothermal reduction in the presence of hydrogen. The CH_4 started forming above 800 °C, peaking at 1050 °C. High activity of the carbon dissociated from CH_4 was the reason for the improved reduction in the presence of H_2.

2.4.5 Summary of influences on kinetics of prereduction

The wide stability range of MnO shows that the reduction of higher manganese oxides is a matter of kinetics rather than thermodynamics. The exception is in ores with high iron contents, where higher oxides may be stabilized due to lower activity in solid solution. This effect is also seen in the case of iron oxides, where lowered activity causes stabilization of FeO in different phases depending on the overall chemical composition. Iron alone may be stable as metal or different oxides depending on the reduction potential of the atmosphere. Solid carbon establishes a higher driving force compared to CO above 700 °C, however slow kinetics makes it unsuitable as a reductant at low temperatures. Smaller particle sizes, higher reducing gas content, increased porosity and higher temperatures all increase the reactivity of manganese raw materials. Smaller particles may adversely impact furnace stability, making it less suitable for industrial production. Higher

temperatures give higher reaction rates until sintering occurs, and higher porosity improves reactivity. High reducing gas content improves reactivity, but also risks carbon deposition, particularly when CO and H_2 are combined in high concentrations. Increased diffusivity in the reducing gas by introduction of He or H_2 improves the kinetics, and reduction in the presence of H_2 and C may result in formation of CH_4, which in turn established a high driving force and improves reduction. Metallic iron was observed in samples reduced above 900 °C in H_2 but not in samples reduced non-isothermally to 1100 °C in CO/CO_2 mixtures, indicating that H_2 improves the reduction of iron oxides, as seen in iron ore reduction. Decomposition of carbonates improves porosity and the content of MnO_2 increases temperatures due to high exothermicity.

2.5 Decrepitation and disintegration

It has been shown previously that the particle size affects reactivity of ores. The particle size range prior to experiments or industrial production is often known, though the particle size during and after heating and reduction is not always reported. Obtaining information about the particle size evolution during experiments is not trivial due to the nature of reduction experiments, but it may be measured after the conclusion of the experiment. The decrepitation/disintegration behavior during heating and reduction is of interest since it affects the particle size of the material. If the particles break in the early stages of reduction, reactivity is measured on a smaller particle size fraction than intended, increasing the perceived reactivity. In industrial production, a high amount of fines in the furnace can be detrimental to furnace operation[42,50]. Knowledge about the mechanisms and behavior of different ores may be used to improve the utilization of fines in the furnace. Is should be possible to utilize a higher proportion of fines from an ore that decrepitates less without adverse effects on charge permeability and furnace performance.

Different approaches are utilized for determining the decrepitation behavior of manganese ores and different measures of decrepitation is used. Figure 2-16 shows an overview over different approaches used in literature. The decrepitation behavior has been studied by heating ore in inert- or reducing-gases, without or after tumbling and with tumbling in a rotating kiln at high temperature. Decrepitation is assessed by the difference between the input and output particle size distribution. Most commonly, the decrepitation is given as the wt % of material above or below a certain sieve size, e.g., the lowest sieve size of the initial particle size fraction, a specific fraction based on standard methods, or a sieve size based on the definition of fines, though there does not seem to be consensus in the literature regarding the definition of fines. Some authors use a stack of sieves, determining the size distribution to get higher resolution data.

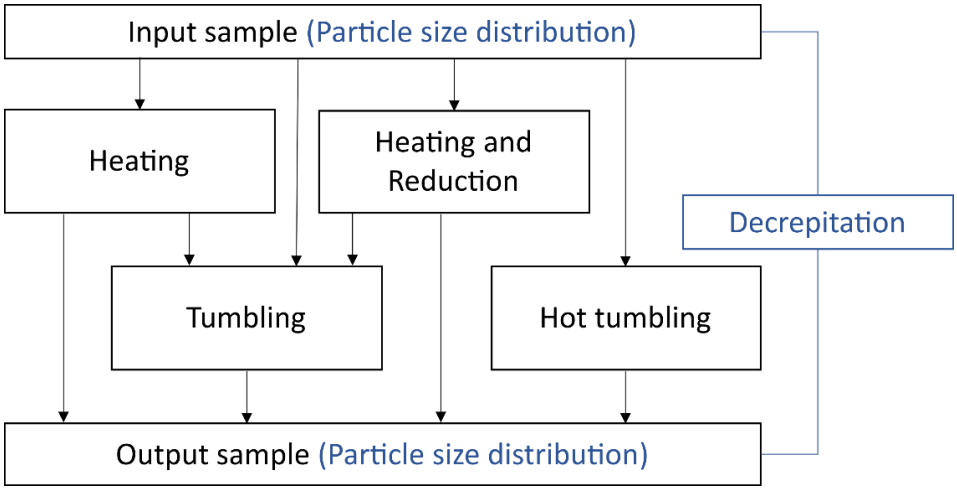

Figure 2-16: The measure of decrepitation is taken from some measured difference in particle size distribution. Several influences on decrepitation have been investigated in literature.

Several investigations were conducted where samples were heated to different temperatures in a reducing atmosphere consisting of 70 % CO and 30% CO_2 followed by tumbling and sieving[23,39,94,98]. The diameter and depth of the tumbler was 200 mm and 100 mm respectively and it had four lifters (100 mm × 16 mm × 4 mm). Tangstad et al.[39] investigated Nchwaning ore, Mamatwan ore and Comilog ore and sinter after heating in reducing atmosphere to 1100 °C. Comilog ore decrepitated the most, which was explained by its higher porosity compared to the other materials. Decrepitation decreased with decreasing porosity of the raw materials, and the porosity increased with the degree of reduction, i.e., the least porous and least reduced materials has the highest mechanical strength. Visser et al.[23] investigated Nchwaning ore and Gloria ore up to 1100 °C, while Biørnstad[94,98] investigated Comilog, Nchwaning and UMK ore up to 400 °C, 600 °C and 800 °C. For these investigations, tumbling was done for 30 min at 40 rpm. The decrepitation, displayed as remaining material larger than 4.75 mm, is shown in Figure 2-17. It can be seen that decrepitation increases with increased reduction temperature for all ores. UMK and Gloria ores originate from the same ore body and is thus assumed to behave similarly. Comilog ore decrepitates the most, and the carbonated UMK and Gloria ores decrepitates the least, which is in agreement with the findings in Tangstad et al.[39]. It is also seen that the increased decrepitation after tumbling is highest for Comilog ore, which is the most porous ore in the investigation.

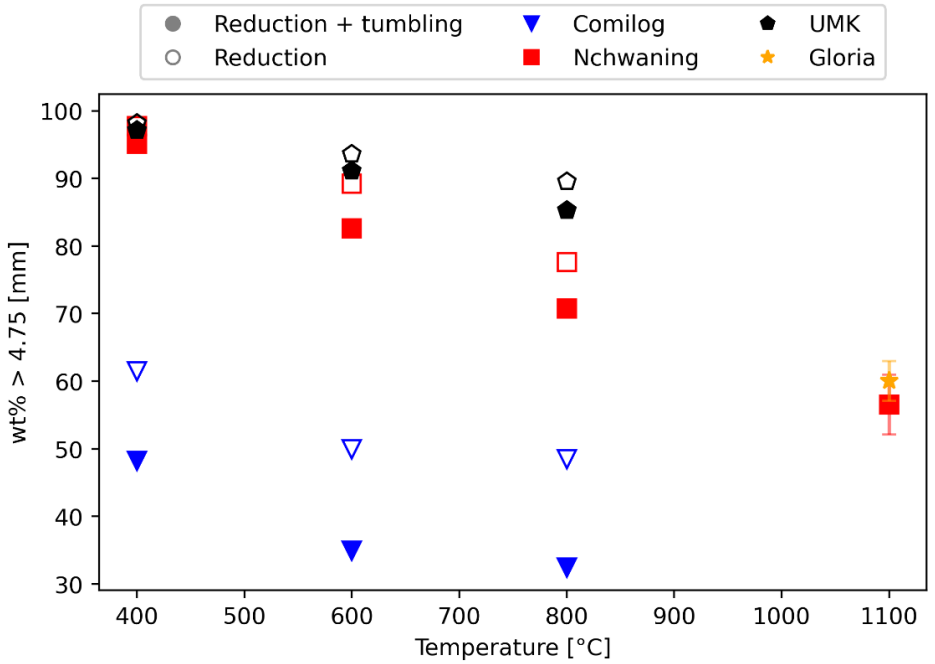

Figure 2-17: The decrepitation of various ores measured as the weight fraction above 4.75 mm after heating in a 70 % CO – 30 % CO_2 atmosphere to different temperatures. Error bars, indicating the standard deviation, is added where multiple measurements were made. Data from Visser et al.[23] at 1100 °C with initial particle size 10-14.7 mm and 10 °C/min heating rate. Data from Biørnstad[94,98] up to 800 °C with initial particle size 10-13.2 mm and 3 °C/min heating rate. Hollow symbols indicate the decrepitation after heating/reduction before tumbling, filled symbols are after tumbling.

Tangstad et al.[54] measured the mechanical strength after reduction for of lump ore, briquettes and pellets from two oxidized ores, ore A and ore B. Sinter from ore A was also investigated. The heating and tumbling procedure was identical to that in Visser et al.[23]. Two indices were calculated; The Cohesion index (CI), defined as the quantity of material in the original size range after tumbling (> 6.3 mm for pellets, > 4.3 mm for ore A and > 10 mm otherwise) and the Thermal stability index (TI) defined as the quantity of material > 1.6 mm after tumbling. The Thermal stability and Cohesion indices can be seen in Table 2-6. There is a negative correlation between porosity and the cohesion and thermal indices; Pellets have the highest cohesion and thermal stability and lowest porosity while briquettes have the lowest cohesion and thermal stability and the highest porosity. Sinter (A) have a higher cohesion and thermal stability compared to lump ore, while the porosity is lower.

Table 2-6: Cohesion (CI) and thermal (TI) indices for materials based on two oxidized ores [54]

Ore	Material	CI	TI	Porosity [%]
A	Lump ore	29	61	22.6
	Sinter	35	80	17.7
	Pellets	94	96	11.9
	Briquettes	0	30	24.3
B	Lump ore	14	64	18.5
	Pellets	96	92	4.68
	Briquettes	0	31	22.2

Biswas et al.[129] investigated decrepitation by experiments and modelling. The experiments were conducted heating an Indian low-grade ore with a particle size range of 6-10 mm in a setup purged with nitrogen. Decrepitation was caused by evaporation of water from moisture and from hydrated minerals causing stress and rupture within the particles (100-500 °C) and change in crystal structure caused by the volume change during decomposition of tetragonal MnO_2 to cubic Mn_2O_3 (500-700 °C). In addition, phase transformation causing stress between the parent matrix and the nucleated phase caused cracks in the interface between the phases. Increased heating rate increased decrepitation due to higher stress caused by a higher thermal gradient. The decrepitation increased with temperature, holding time and with introduction of a static load.

Faria et al.[22] tested the decrepitation behavior of Azul, Urucum, Morro da Mina and Wessel manganese ores by applying the standard decrepitation test for iron ores[130]. Samples of 0.5 kg manganese ore were placed in a pre-heated oven at 700 °C for 30 min followed by screening at 6.3 mm, 3.35 mm, 1.18 mm and 0,5 mm mesh screens. The tests were done on moist (as received), dried (105 °C) and heat treated (200 °C for 48 hours) samples, with particle size range commonly used in ferroalloy plants (6.3-19 mm)[22]. Mineralogical characterization and chemical analysis were done to classify the ores. The prevailing phase in the ores from Azul and Urucum was cryptomelane. Azul ore contained higher amounts of hydrated minerals (e.g., todorokite, gibbsite) compared to Urucum ore. Morro da Mina ore consisted mainly of carbonates (rhodochrosite) and silicates (e.g., spessartine) while the main phases in Wessels ore were braunite, bixbyite and dolomite. The silicate-carbonate ore from Morro da Mina showed little decrepitation ($I_{-6.3mm}$ = 0.4 %), while the dried samples from Azul, Urucum and Wessels obtained a decrepitation index ($I_{-6.3mm}$) of 6 %, 10 % and 12 % respectively. Moist samples decrepitated more, and heat-treated samples decrepitated less compared to dried samples showing that moisture contributes to decrepitation. The ores responded differently to the drying and heat treatment. Among the ores, Urucum showed the

highest influence from water content; The decrepitation indices were highest for the moist samples and among the lowest for the heat-treated samples compared to the other ores in the study. Azul ore decrepitated less compared to Urucum ore which is unexpected since Azul ore has a higher content of hydrated minerals[131]. However, Azul ore has a higher total pore volume and larger average pore diameter, indicating that porosity may act as an internal pressure relief. Apart from Morro da mina ore, that showed almost no decrepitation, Wessels is least influenced by water content and is also the least porous ore[22].

Similar to Faria et al.[22], Moholwa et al.[132] used the iron ore decrepitation standard [130] to test two different South African manganese ores. The decrepitation index of the ores ($I_{-6.3mm}$) was found to be 13 % and 10.8 % for Ore #A and Ore #B respectively. The chemical analysis of the ores indicates that Ore #A is a carbonated ore whereas Ore #B is a semi oxidized ore similar to Wessels (see section 2.2).

In Larssen[133], the decrepitation behavior of Nchwaning and Comilog ore after reduction was investigated. The bulk of the experiments were conducted with a 6 °C/min heating rate to different temperatures. A few experiments were also conducted using other heating rates (3 °C/min and 9 °C/min). Decrepitation was found to be mainly a function of the extent of reduction. Similar extent of decrepitation was observed even though different gas mixtures were employed, and no significant differences were observed during dilution of ore with quartz to suppress the exothermal peak temperature in Comilog ore.

Reiersen[92] investigated the decrepitation after reduction of Nchwaning, Comilog and UMK ore in 70 % CO – 30 % CO_2. Samples were reduced employing heating rates of 3 °C/min, 6 °C/min, and 9 °C/min up to 1000 °C. Nchwaning ore tended to produce fines when it decrepitated, whereas UMK tended to crack into larger particles. Comilog was found to decrepitate the most, and UMK to decrepitates the least of the three ores, which is in line with the findings in previous investigations[23,39,94,98](Figure 2-17).

Both Larssen[133] and Reiersen[92] observed that the decrepitation of Comilog ore decreased with increasing heating rate (3,6 and 9 °C/min). This is unexpected considering the findings in Biswas.[129], where increased heating rate was found to increase decrepitation due to increased thermal stresses. However, Faria et al.[22] observed that the decomposition of hydrated minerals had a lower effect on decrepitation in the ores with highest porosity. Hence, it may be the case that Comilog ore is less susceptible to decrepitation by thermal stresses due to its high porosity. Larssen[133] inferred that the decreased decrepitation with increased heating rate for Comilog ore was due to increased susceptibility towards decrepitation during reduction at lower temperatures. Biørnstad[94,98] found that less than 2 wt% of Comilog was below 3.35 mm after heating in air to 800 °C even

though all MnO_2 had decomposed to Mn_2O_3, changing the O/Mn ratio from 1.93 to 1.49, i.e. half of the oxygen down to MnO was removed. For comparison, 36 wt% of Comilog ore was below 3.35 mm using the same heating program with reducing gas (O/Mn = 1.04). Hence, the decrepitation of Comilog ore seem to be associated with the reduction of Mn_2O_3 and Mn_3O_4.

Figure 2-18 shows the decrepitation, displayed as the wt% of material above 3.35 mm after experiments, as a function of the final O/Mn ratio from the investigations of Larssen[133], Biørnstad[94,98] and Reiersen[92]. It can be seen that Comilog decrepitates more than Nchwaning and UMK. Increased heating rate is associated with less decrepitation for Comilog but more decrepitation for UMK. The effect of heating rate on Nchwaning ore from these results are inconclusive.

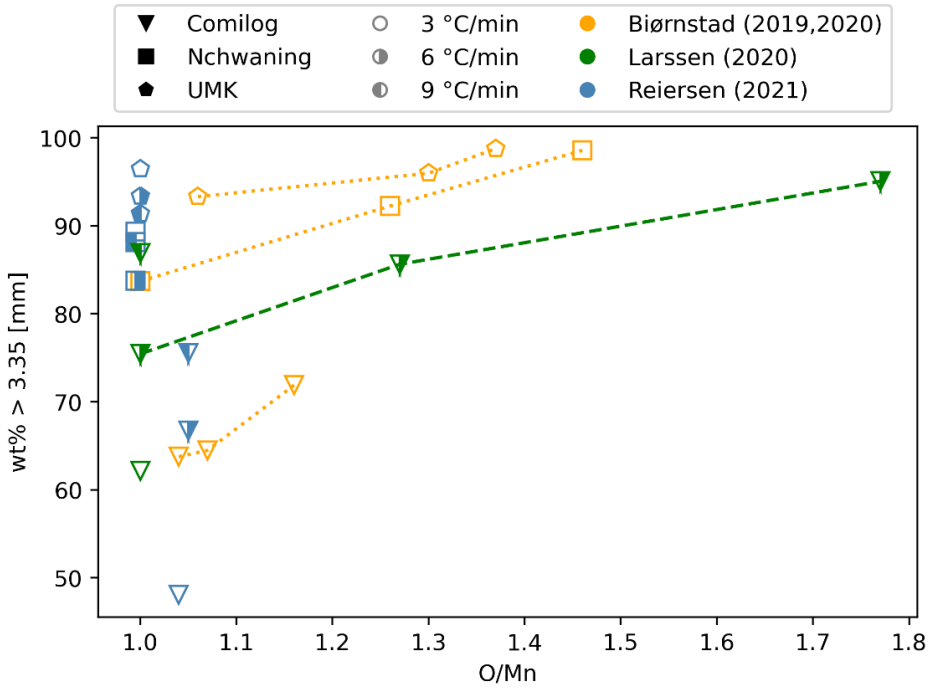

Figure 2-18: The wt% larger than 3.35 mm after reduction in 70 % CO- 30 % CO_2 as a function of O/Mn ratio. The initial particle size in Biørnstad[94,98], Larssen[133],and Reiersen[92] were 10-13.2 mm, 11.2-15 mm and 10-12.5 mm, respectively. .

Moholwa[134] investigated the decrepitation of three carbonated South African ores in air during tumbling at 600 °C, 800 °C and 1000 °C in a rotary kiln. The decrepitation was seen to increase with increasing temperature, with increasing rotational velocity and with decreasing initial particle size range. The effect of temperature was correlated to the decomposition of kutnohorite above 600 °C and to decomposition of calcite above 800 °C. The total amount of carbonates in the different ores was positively correlated with decrepitation.

Biørnstad[94,98] also investigated the decrepitation using two different particle size ranges (10-13.2 mm and 3.35-6.7) of Nchwaning, Comilog and UMK ore. For UMK and Nchwaning ore, the decrepitation, assessed as wt % < 3.35 mm, was higher for the smaller particle size range. This is consistent with the results from Moholwa[134] and is reasonable since less particles will have to break in the smaller size range compared to in the bigger size range in order to increase the fraction of material below 3.35 mm. For Comilog ore, Biørnstad[94,98] observed that the larger particle size range decrepitated more upon reduction compared to the smaller particle size range. Similar degrees of reduction were observed for both cases

Faria et al.[135] investigated the disintegration of Urucum ore upon heating in air and nitrogen followed by tumbling. The measure of disintegration was defined as wt.% of material below 6.3 mm. There was no significant difference between the sample heated in air and the samples heated in nitrogen and no significant difference between samples heated to 500 °C and 700 °C. The fines generation up to 700 °C was mainly due to elimination of structural water whereas at 1000 °C, disintegration was increased due to decomposition of cryptomelane and pyrolusite as well as partial decomposition of Bixbyite.

In Faria et al.[136], disintegration of Azul ore and pellets (11-13 mm) was investigated and Faria et al.[137] investigated disintegration of Morro da Mina ore. The experimental work was similar to that in Faria et al.[135] except for the use of a higher heating rate in the latter works. Additional tests were done in 99.5 % CO/0.5% N_2 gas at 1000 °C for Azul ore and pellets and Morro da Mina ore. Selected results are shown in Table 2-7, where it can be seen that increased temperature increased decrepitation in Air and N_2, and samples reduced in CO decrepitated more than samples heated in Air and N_2 for the same temperature. In addition, tumbling is seen to have a higher influence on decrepitation for the carbonate ore (Morro da Mina) compared to the pellets and the oxidized ore (Azul).

Table 2-7: Weight % of samples passing through a 6.3 mm sieve. Samples heated and held isothermally for 1 h. Measured after 0 min and 30 min tumbling. Data from [135–137]

Wt.% < 6.3 mm [%]	***Heating rate [°C/min]***	**No heating**	**500 - 700 °C**		**1000 °C**			
Atmosphere			*Air/N_2*		*Air/N_2*		*99.5% CO (2/5/15 l/min)*	
Tumbling [min]		*30*	*0*	*30*	*0*	*30*	*0*	*30*
Urucum ore	*10*	1	6-8	7-10	17-19	37-40	-	-
Azul ore	*25*	2,2	-	-	11	24	16/16/13	21/22/19
Azul pellets	*25*	0.3	-	-	0.06	0.16	0.84/1.4/0.90	1.5/2.1/1.5
Morro da Mina ore	*25*	0.7	-	-	9.8	21	14/14/11	24/25/20

Decrepitation is influenced by phase transformations taking place in the ores. Decomposition of higher oxides or Braunite will give volume changes that induces internal tensions in the particle that can create cracks and cause crack propagation[22,129,131,135]. Decomposition of carbonates is associated with a higher volume change compared to the oxides (Table 2-7) causing a substantial increase in porosity that decrease the ores mechanical strength which increases the level of decrepitation, particularly after tumbling. This effect may explain why the carbonated ore in Moholwa et al.[132] shows a higher decrepitation index compared to the semi-oxidized ore. Table 2-8 shows the changes in molar volume of the solids for decomposition of oxides and carbonates.

Table 2-8: The change in molar volume in the solids for decomposition of carbonates and oxides. Data from HSC chemistry [18].

Reaction	ΔV_m [m^3/mol]
$CaCO_3 = CaO + CO_2$	20.1
$MgCO_3 = MgO + CO_2$	16.4
$MnCO_3 = MnO + CO_2$	17.9
$MnO_2 = 1/2\ Mn_2O_3 + 1/4\ O_2$	-0.86
$1/2\ Mn_2O_3 = 1/3\ Mn_3O_4 + 1/12\ O_2$	10.7
$1/3\ Mn_3O_4 = MnO + 1/3\ O_2$	7.65
$1/2\ Fe_2O_3 = 1/3\ Fe_3O_4 + 1/12\ O_2$	1,86
$1/3\ Fe_3O_4 = FeO + 1/3\ O_2$	8,86

The less porous carbonated ores (Mamatwan, UMK and Gloria) has a higher strength compared to the porous oxidized Comilog ore[23,39,92,94,98]. The same trend can be seen in the decrepitation experiments by Faria et al.[22] where Morro da Mina (carbonated, non-porous) decrepitated the least. This was not the case after reduction and tumbling (Table 2-7) where the disintegration of Morro da Mina[137] was similar to Azul (oxidized, porous)[136]. This discrepancy may be due to higher degree of decomposition of carbonates in Morro da Mina ore compared to Mamatwan and Gloria ore. Decomposition of carbonates is associated with a substantial change in molar volume (Table 2-8), increasing the porosity of the particles. The carbonates in Morro da Mina ore is mostly Rhodochrosite ($MnCO_3$) which decomposes at a lower temperature compared to Calcite ($CaCO_3$) and kutnohorite ($CaMn(CO_3)_2$), that are the main carbonate phase in Gloria[23] and Mamatwan ore[25] respectively. Hence, the increase in porosity due to carbonate decomposition for Morro da Mina will be higher. This observation is consistent with the findings from Moholwa[134], who observed decrepitation associated with the decomposition of kutnohorite at lower temperatures, and increased decrepitation at higher temperatures associated with the decomposition of calcite.

As seen in Tangstad et al.[39] and Tangstad et al.[54], there is a negative correlation between porosity and mechanical strength. The same correlation is seen in the results from tumbling of unheated ores (Table 2-7) where the fines generation is higher for the ores with higher porosity[22].

Jesus and Tangstad[55] pressed briquettes from Urucum ore tailings using three different top sieve sizes of 2.0 mm, 1.0 mm and 0.250 mm. The briquettes were 10 mm in diameter and minimum 10 mm high. Three batches were made using bentonite, molasses, and molasses + coke respectively. Lump ore >9.5 mm was used for comparison. The samples were reduced in 70 % CO/30 % CO_2 with a heating rate of 10 °C/min to 1100 °C. Decrepitation was measured as the wt% of reduced material retained in a 9.5 mm sieve. For the briquettes made with molasses and with bentonite, more than 98 % was retained on a 9.5 mm sieve, compared to 86 % and 58 % for composite pellets and the lump ore, respectively.

Heat treated materials (sinter and pellets) show a lower tendency for disintegration compared to lump ores[39,54,136]. As mentioned previously, mechanical strength decreases with increasing porosity but in addition, moisture (free and bound) will evaporate and higher oxides decompose during heat treatment, hence there will be less influence from water content and phase transformations to the disintegration of these materials.

3 Materials and method

Manganese ores were crushed and sieved, reduced and analyzed with different techniques. The main result from the experiments is the weight loss curve, which in conjunction with the measured temperature, off-gas analysis and subsequent chemical analysis reveal how the ores behave under different conditions. In this section, the details regarding the specific materials, experimental procedures and analyses will be presented.

3.1 Raw materials

Nchwaning ore and Comilog ore was obtained from industry. The ores were crushed and sieved and the 9.52 – 15 mm fraction was selected for the experiments. The material was split with a riffle splitter to batches of approximately 800 g material. Prior to the experiments, the batches were dried until constant weight at 105 °C to remove any moisture before it was split into smaller samples by the cone and quartering technique. Individual particles were randomly removed from each sample to achieve the desired sample weight. Comilog ore was diluted with an equal amount of quartz to reduce the exothermal superheating described in the literature review. The Nchwaning experiments were run with 150 g ore, whereas the Comilog experiments were done with 75 g ore and 75 g quartz to keep the total sample weight similar for both ores. The height of the sample material in the crucible was 4 – 4.5 cm for Nchwaning ore and 6.5 – 7 cm for the Comilog/Quartz mixture, and each type of sample is shown in Figure 3-1. Some experiments were conducted using only quartz as an inert material to establish the influence from the furnace itself on the results. After the experiments, the samples were sieved in 9.5 mm, 6.7 mm, 4.75 mm 3.35 mm and 500 µm sieves to determine the decrepitation. One quarter of each sample was split out for chemical analysis.

(a) (b)

Figure 3-1: (a) 150 g Nchwaning ore and (b) 75 g Comilog ore and 75 g quartz.

3.1.1 Nchwaning ore

Nchwaning ore is a high grade Wessels type ore originating from the Kalahari manganese field in South Africa[47,96]. It consists mainly of Braunite (I and II), bixbyite and hausmannite, and has a low carbonate content. Initial experimental results revealed unexpected variance between parallel experiments, and a high variation was observed in the chemical analysis. For these reasons, an increased number of samples were analyzed, and parallel experiments were conducted in a large proportion of the experiments.

Three samples of unreduced material (150 g) were selected for chemical analysis and the results can be seen in table I. The O/Mn ratio can be calculated from the reported MnO_2 and is found to be 1.50 ± 0.01. All excess oxygen above MnO is reported as MnO_2, however MnO_2 is not necessarily present, as in the case of Nchwaning ore, where O/Mn=1.5 corresponds to Mn_2O_3.

Table 3-1: Shows the mean and standard deviation (s) from chemical analysis of three unreduced Nchwaning ore samples. The analysis was done by SINTEF Norlab.

Unreduced sampls (n=3)		
	mean	**s**
Mn	48,66	3,25
Fe	8,75	2,42
SiO_2	4,38	0,23
Al_2O_3	0,42	0,11
CaO	5,93	0,61
MgO	0,57	0,31
P	0,024	0,003
S	0,157	0,032
TiO_2	0,01	0,01
K_2O	0,00	0,00
BaO	0,57	0,17
MnO_2†	38,75	1,97
CO_2*	2,5	0,5

†Titrimetric *Combustion IR

The content of the different elements is concentrated during reduction due to removal of matter (i.e., O, H_2O and CO_2). Manganese and iron is not removed during reduction, thus their ratio is constant and may be used as an indication of the heterogeneity of the ore. Figure 3-2 shows the Mn/Fe ratio from chemical analysis of the reduced Nchwaning samples in addition to the average Mn/Fe ratio. The difference between the average Mn/Fe ratio determined by three unreduced samples and the one determined by all the reduced samples is 0.03 %, hence the results from the three unreduced samples are representative for

the ore. It can however be pointed out that the Mn/Fe ratio is varying from about 2 to 9 and that the standard deviation is 27 %.

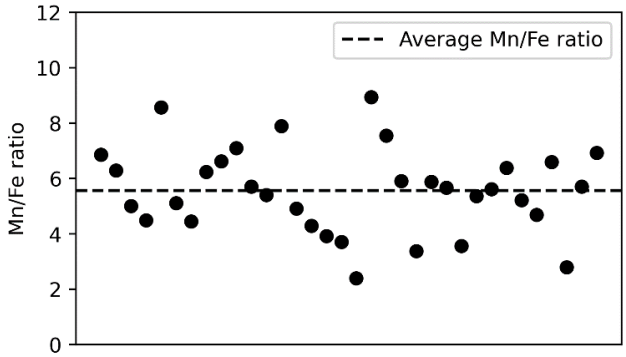

Figure 3-2: Heterogeneity of Nchwaning ore represented by the Mn/Fe ratio. Mn/Fe ratio of reduced samples of Nchwaning ore (circles) and the average Mn/Fe ratio. There is a 0.03 % difference between the average Mn/Fe ratio determined by the three unreduced samples compared to the ratio determined by all samples. Standard deviation is 27.3 %.

The possible sources of weight loss during the experiments are due to reduction of manganese and iron oxides in addition to decomposition of carbonates and manganite. Based on the analysis of the unreduced samples in Table 3-1, the theoretical weight loss from the reduction of the manganese and iron oxides in Nchwaning ore was calculated and is shown in Table 3-2. Although there is a small proportion of carbonates in the ore (2.5 +-0.5 % CO_2) it accounts for a disproportional part of the weight loss if all CO_2 is removed, thus insight into the decomposition during the experiments is necessary to properly describe the reduction of oxides. Manganite (MnOOH) in the ore will decompose to Mn_2O_3 and H_2O, also contributing to the weight loss. Manganite in the range 1-8% has previously been reported in Nchwaning ore[23,70,138], implying a weight loss of 0.1-0.82 % by H_2O by decomposition, which was not included in Table 3-2.

Table 3-2: Contribution to the weight loss [%] from carbonates, manganese oxides and iron oxides. Calculated based on the chemical analysis of the unreduced samples shown in Table 3-1. Me =Mn, Fe. The influence of the weight loss on the fractional conversion (α) is also included. Numbers in parenthesis indicate the influence if carbonates decompose.

Weightloss [%]	Mn	Fe	Sum	α
$(Carbonates \rightarrow CO_2)$	-	-	0 % (2.5 %)	0.00 (0.23)
$Me_2O_3 \rightarrow Me_3O_4$	2.4 %	0.43 %	2.8 %	0.33 (0.26)
$Me_3O_4 \rightarrow MeO$	4.7 %	0.84 %	5.6 %	0.66 (0.51)
Total	7.1 %	1.3 %	8.4 % (10.9 %)	1

The fractional conversion, α, is defined in equation (11) where w_0 is the initial weight and w(t) is the measured weight as a function of time. w_r is the weight of a fully reduced sample and is here set to 10.75 %, corresponding to the highest weight loss achieved in reduction of Nchwaning in this work. The fractional conversion based on the sources of weight loss is also included in Table 3-2.

$$\alpha = \frac{w_0 - w(t)}{w_0 - w_r} \qquad (11)$$

XRD of the unreduced ore (Figure 3-3) reveals braunite ($3(Mn,Fe)_2O_3 \cdot MnSiO_3$), braunite II ($7(Mn,Fe)_2O_3 \cdot CaSiO_3$) and bixbyite ($(Mn,Fe)_2O_3$) as the major manganese containing phases. These phases correspond to manganese in the Mn^{3+} state (Mn_2O_3), which is consistent with the chemical analysis. Bixbyite, braunite and braunite II have many overlapping peaks as seen in Figure 3-3, but may be qualitatively distinguished based on the minor peaks[139]. Hematite (Fe_2O_3), manganite (MnOOH), hausmannite (Mn_3O_4) and calcite ($CaCO_3$) are also identified in the diffraction pattern.

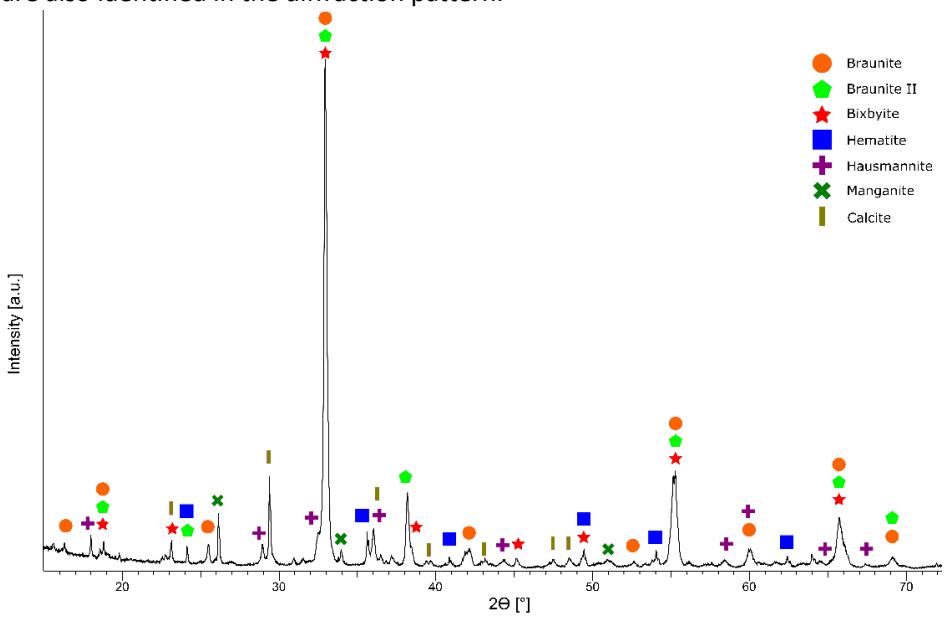

Figure 3-3: X-ray diffraction spectrum of unreduced Nchwaning ore.

3.1.2 Comilog ore

Comilog ore is an oxidized ore containing a variety of manganese containing phases such as pyrolusite (MnO_2), ramsdellite (MnO_2), cryptomelane (KMn_8O_{16}), nsutite ($Mn_{1-x}Mn_xO_{2-2x}OH_{2x}$) and lithiophorite ($(Al,Li)MnO_2(OH)_2$), all which are

close to MnO_2 (=Mn 4+)[49,70,73]. The chemical analysis is given in Table 3-3, where the MnO_2 content yields an O/Mn ratio of 1.91, revealing that a small fraction of manganese is at a lower oxidation state, i.e., in the lithiophorite and nsutite.

Iron is found in goethite (FeOOH) and hematite (Fe_2O_3). Goethite will decompose to hematite and water according to equation (12)[140,141], thus all iron may be considered to be hematite when calculating the theoretical weight loss from oxides.

$$2FeOOH = Fe_2O_3 + H_2O \qquad (12)$$

Evaporation of water constitute a significant source of weight loss in Comilog ore and several of the identified phases also contain bound water (i.e., Nsutite, Goethite and Gibbsite). Nsutite releases structural water between 120 °C – 400 °C [141] and goethite decomposes to hematite and water between 210 °C – 350 °C[142] which is in line with previous observations from manganese ores that found that hydrated minerals decompose in the temperature range 100 °C – 500 °C [22,129].

Table 3-3: Chemical analysis of unreduced Comilog ore.

Mn	51.4
Fe	3.58
SiO_2	3.31
Al_2O_3	5.11
CaO	0.05
MgO	0.13
P	0.14
S	0.007
TiO_2	0.12
K_2O	0.8
BaO	0.25
MnO_2†	74.26
CO_2*	0.15

†Titrimetric *Combustion IR

Table 3-4 shows the contribution to the weight loss from reduction of oxides and evaporation of water, in addition to the impact on the fractional conversion for each stage. The water content was estimated to be 4.9 % from the experimental data, which corresponds to 26 % of the total weight loss of Comilog ore. This is similar to previous studies that have identified 4.9-6.5 wt% bound water in Comilog ores [39,70].

Table 3-4: Shows the contributions to the theoretical weight loss of Comilog ore based on chemical analysis and reported values for bound water content. Me =Mn, Fe. The influence of the weight loss on the fractional conversion (α) is also included.

Weightloss [%]	Mn	Fe	Sum	α
$H_2O \rightarrow H_2O(g)$	-	-	4.9	0.26
$MeO_2 \rightarrow Me_2O_3$	6.2	-	6.2	0.32
$Me_2O_3 \rightarrow Me_3O_4$	2.5	0.2	2.7	0.14
$Me_3O_4 \rightarrow MeO$	4.9	0.3	5.3	0.28
Total	13.7	0.5	19.1	1

Since Comilog ore is known to display a high temperature increase during reduction [42,70,90], an equal amount of quartz (by mass) was mixed with the ore to reduce the excess temperature caused by the exothermic reactions. This approach has been utilized previously in non-isothermal reduction of Comilog ore[94,133]

At one point during the Comilog campaign, it was observed that the sample temperature increased after the reduced samples were removed from the crucible. This was believed to occur due to oxidation of the samples and efforts were made to quantify any weight increase by directly emptying the sample onto the external scale. The samples heated rapidly, and this approach did not yield trustworthy data. Hence, for the remaining experiments, the sample was left in the crucible to cool in Ar gas. When the sample temperature was below 25 °C, synthetic air was introduced, and the temperature and weight increase was measured.

3.2 Apparatus

The experiments were conducted in a thermogravimetric (TG) setup. The setup consisted of a vertical resistance furnace (Entech VTF 80/15), the position of which can be adjusted vertically to surround the crucible. The crucible is made of high-temperature stainless steel (steel grade 253 MA) and was suspended in a balance (Mettler Toledo PR2003DR) to record the weight changes continuously throughout the experiment. Figure 3-4a shows a sketch of the crucible where it is seen that the gas passes through the double wall where it is preheated prior to interaction with the sample. The gas inlet and outlet are connected to the crucible by flexible synthetic rubber tubing, as can be seen in Figure 3-4 (b and c), and a thermocouple in an alumina tube is positioned such that the tip is in the center of the sample material (Figure 3-4 a and c). Figure 3-4 b and c show the crucible when the furnace is in its upper and lower position, respectively. Multiple gases can be used, and there are separate mass flow controllers for each gas (Bronkhorst F-201C). Ar,

CO, CO_2, and H_2 with purity of 99.999%, 99.97%, 99.9992%, and 99.9%, respectively, were used in the experiments. Synthetic air containing 21 % O_2 and 79 % N_2 was used in some experiments. The gases are mixed before entering the crucible.

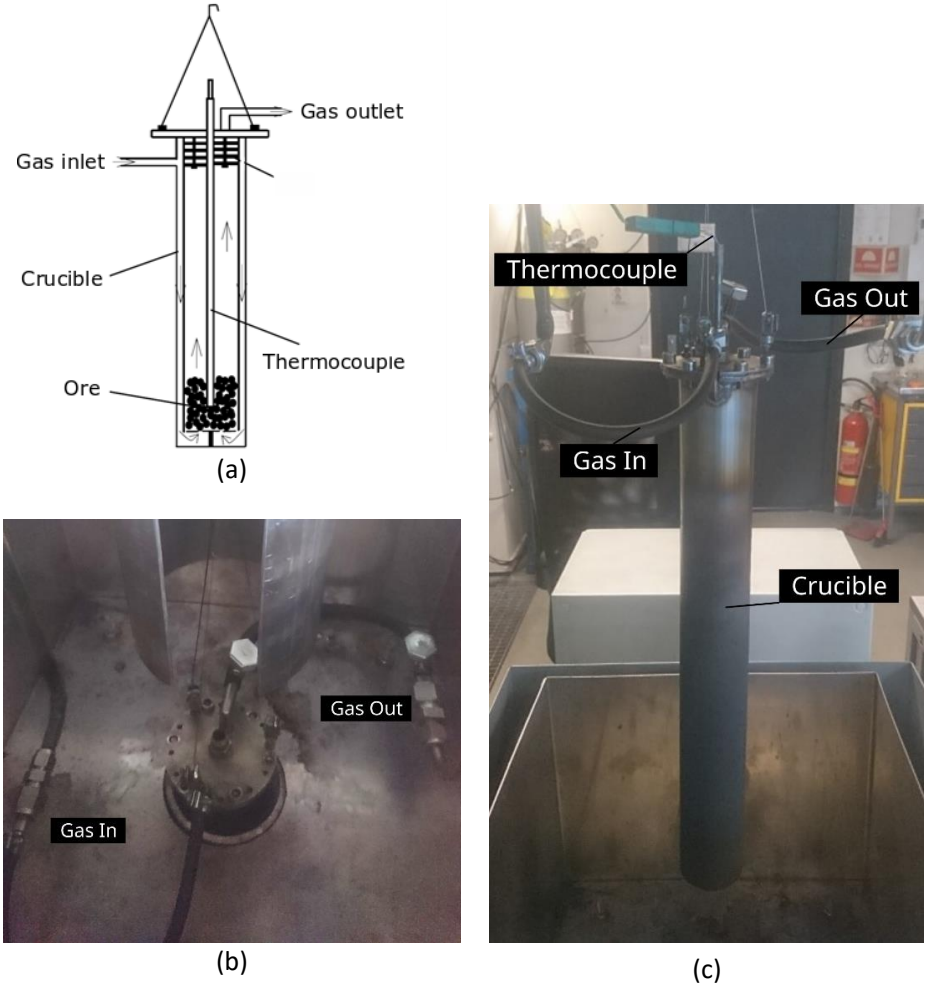

Figure 3-4: (a) Sketch of the crucible; (b) top view of the crucible when the furnace is in its upper position. Gas inlet and outlet is indicated; (c) Side view of the crucible when the furnace is in its lower position. Inlet and outlet gas, crucible and thermocouple input has been indicated.

The CO and CO_2 content of the off-gas was measured by infrared absorption (Uras 26, ABB). The gas exiting the crucible is run through wash bottles containing water to avoid uncontrolled condensation and to achieve a consistent temperature in the off-gas analyzer. The sample temperature, off-gas analysis and weight loss were continuously recorded. The sample weight was measured on an external scale (Ohaus Pioneer PA4202) before and after the experiments.

3.3 Temperature

To assess the temperature stability in the crucible, an experiment was done with quartz in Ar where the thermocouple was placed 0 cm, 5 cm and 10 cm from the lowest position (bottom position of the sample) and kept until the temperature was stable, 10-15 minutes. The temperature was seen to vary between 2 and 2.7 °C/cm with no particular differences or trends for different heights or temperatures. Sample heights of 4.5 cm and 7 cm gives hence a maximum temperature difference of ± 6.1 °C and ± 9.5 °C compared to the measured sample temperature for the Nchwaning and Comilog experiments, respectively.

To obtain isothermal conditions, the furnace was preheated to the desired temperature before it was raised and kept in position throughout the experiments. Figure 3-5 shows the measured sample temperature during three different experiments with Nchwaning ore at different setpoint temperatures and a reference experiment in argon. There is an initial rapid increase of the temperature after the preheated furnace has been raised to surround the crucible. The sample reaches a peak temperature at the end of the heating period when ore is present. The difference between the experiments in Ar and in reducing gas at 790 °C show the effect of the exothermal reactions on the sample temperature. It can be seen that the temperature deviation between the reduction experiment and the reference experiment becomes significant above 600 °C for Nchwaning ore (inserted axis in Figure 3-5), indicating that the exothermal reactions initiate around 600 °C.

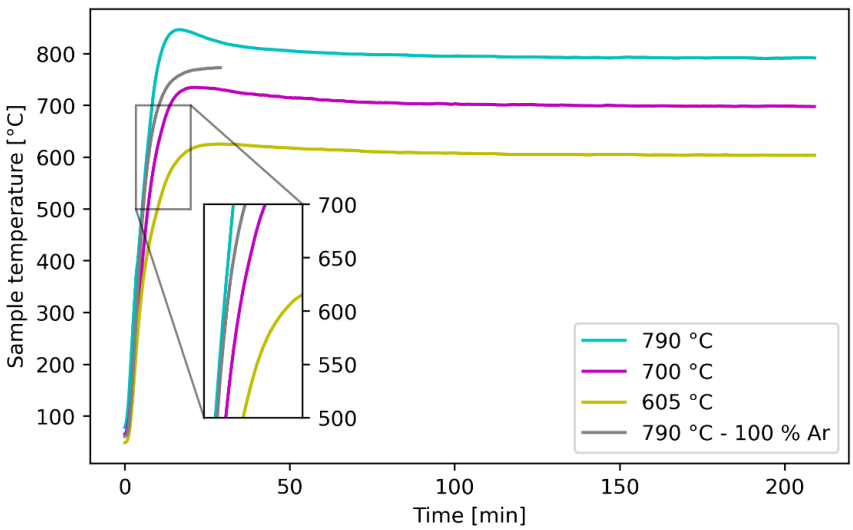

Figure 3-5: The sample temperature measured while reducing Nchwaning ore in a 70 % CO – 30 % CO_2 gas mixture and a reference experiment with Nchwaning ore and Ar. The inserted axis shows that temperature deviation between the reference experiment and the reduction experiment becomes significant above 600 °C.

In Figure 3-6, the measured sample temperature of Comilog ore is shown for different gas mixtures using an identical temperature program for all experiments. A reference experiment with quartz and Ar was also included. The reference experiment is seen to deviate from the others around 200-250 °C, indicating the initiation of exothermal reactions for Comilog ore. The hydrogen containing gas mixture with the highest reducing gas composition (red curve) is seen to initiate below this temperature. There is a significant exothermal effect in Comilog ore, and the highest peak temperature is seen to be at about 100 °C higher than the final stable temperature. The experiments with the lowest initial temperature peaks, still have ongoing exothermal reactions at the end of the experiment which explains the higher temperature at this point.

The initiation of exothermal reactions below the set temperature and the exothermal peak means that part of the reduction occurs outside the desired isothermal range for both ores. Hence, the experiments are not truly isothermal, and the measured temperature must be incorporated when modeling. For naming purposes, the stable temperature at the end of the experiments was selected.

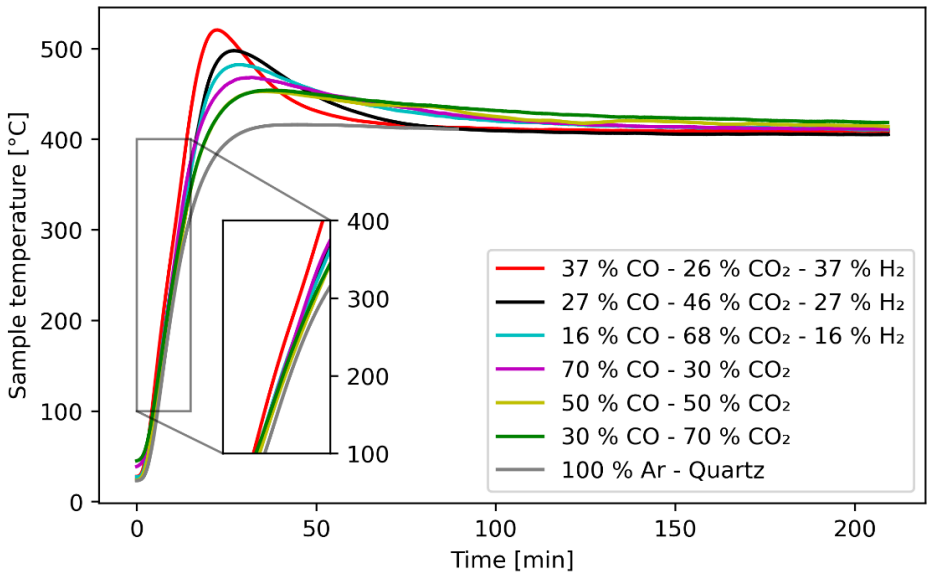

Figure 3-6: Temperature measurements from experiments using the same temperature program using 6 different gas mixtures with Comilog ore in addition to a reference experiment with quartz and argon. The exothermal peak is highest in the hydrogen containing atmospheres.

3.4 Weight measurements

To verify the weight given by the furnace balance, the sample material was weighed on an external scale before and after the experiments. The sample

material was removed, and the crucible was cleaned mechanically and with compressed air. This cleaning procedure was also done prior to the experiments to remove any residues or dust from previous experiments.

There were some unexplained variances in the weight loss of the experiments in addition to side effects caused by rising and lowering of the furnace and changing temperatures. Hence, experiments and calculations were done to investigate these effects which is given in Appendix A. The main findings from this investigation are given below.

An example of the weight loss from the sample as a function of time is shown in Figure 3-7. The reduction part of the experiment is indicated by the vertical dashed lines which are placed at the points where the furnace reaches its top position (surrounding the crucible) and the point where the furnace goes down after the completion of an experiment. Ideally, the weight loss occurring between those points, B and C, are associated with the weight loss from chemical reactions in the crucible.

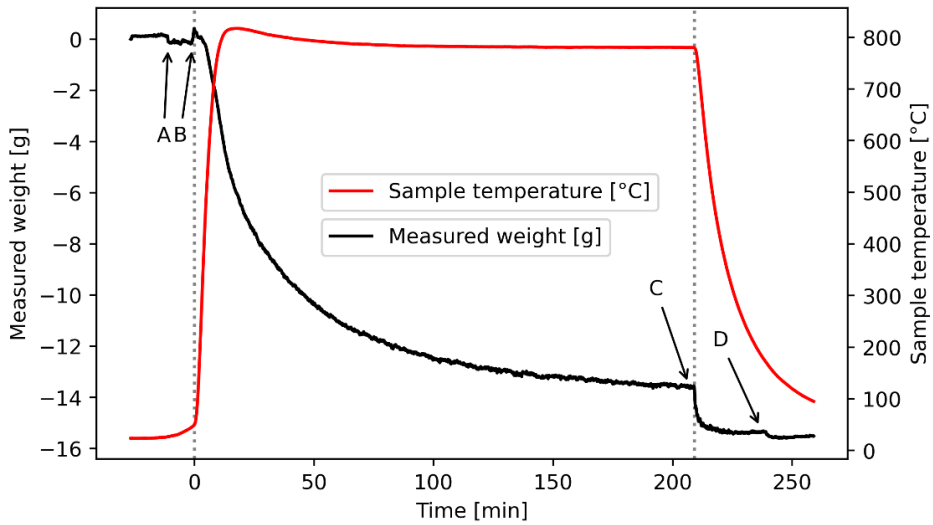

Figure 3-7: Example of recorded weight loss from an experiment. (Exp. A29B) Nchwaning ore reduced in a 70 % CO – 30 % CO_2 gas mixture at 800 °C. Vertical dashed lines indicates where the furnace is raised and lowered. The annotations indicate points of interest;
A: Changing from Ar to reducing gas.
B: Raising the preheated furnace to surround the crucible
C: Lowering the furnace and replacing the reducing gas with Ar (same flow rate of 4 l/min)
D: Changing the flowrate of Ar from 4 l/min to 2 l/min

The weight step indicated with point A in Figure 3-7 is associated with the change from Ar gas to the reducing gas mixture. Ar is purged prior to the experiment, however the change to reducing gas was put 10 min prior to rising the

furnace to separate this weight influence from the others. Reducing gas is run between points A-C. The jump in weight in point B is associated with the change in buoyancy of the crucible between room temperature and furnace temperature. At point C, the furnace is lowered, and the gas is changed from reducing gas to Ar. The observed weight loss in C is thus influenced by both the buoyancy and the changed density of the internal gas. In point D, the gas flow of Ar is changed from 4 l/min to 1l/min, which also influences the weight. The gas flow rate is never changed during the reduction period, so this effect was not studied further.

The weight changes associated with the furnace changes with factors such as temperature and gas mixture are not consistent, as observed in this and other works. Hence, the influence from the furnace itself cannot be easily removed to yield higher accuracy in the results. It is observed that the weight in the initial part of the experiments changes for reasons other than the behavior of the sample, which must be taken into account in the data analysis. Figure 3-8 shows the weight as measured by the furnace balance (point B to point C in Figure 3-7) plotted against the weight loss measured on the external balance where the furnace balance seems to give a slightly lower weight loss in general compared to the external weight.

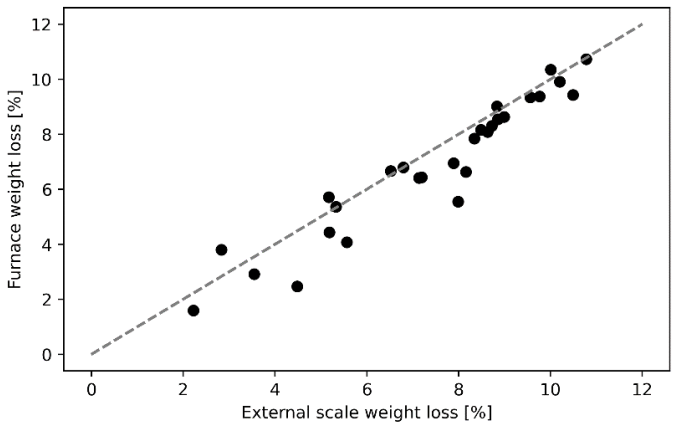

Figure 3-8: Shows the weight loss from the furnace balance vs the externally measured weight loss for the Nchwaning experiments. Points on the dashed line (y=x) have the same weight in both measurements.

Figure 3-9 shows the first 10 minutes of weight loss as a function of time for the CO/CO_2 parallels of the Nchwaning ore experiments where the weight loss calculated from the off-gas analysis and the furnace balance has been plotted together. From comparison with the off-gas curves it is clear that no reduction takes place until approximately 4 minutes into the experiments. The weight effects

mentioned above can be observed in the curves prior to reduction and it is also seen that they are inconsistent for parallel experiments.

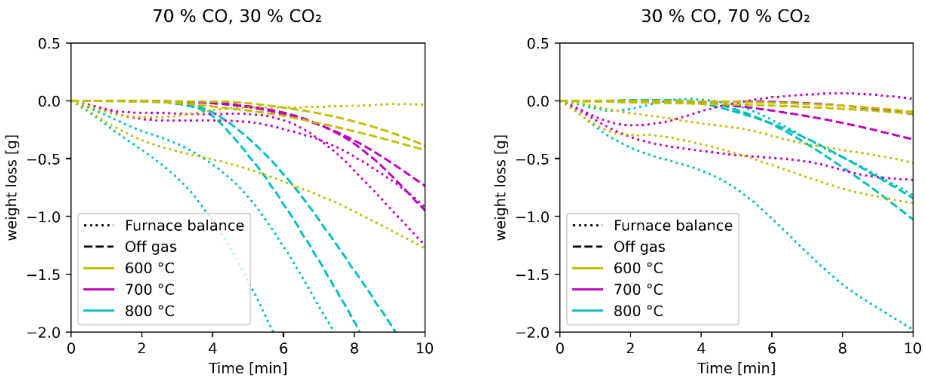

Figure 3-9: Shows the weight loss curves from the furnace balance and the off-gas analysis for the first ten minutes of reduction of Nchwaning ore in CO/CO₂ atmospheres

In the experiments conducted in gas mixtures containing hydrogen, one of the products of reduction is water vapor. The experimental setup is such that the gas is cooled prior to being analyzed by the gas analyzer, causing the water vapor to condense, and an accurate description of the reduction path based on the off-gas analysis to be erroneous. To account for the fluctuations in the furnace balance in the initial parts of the Nchwaning experiments, the furnace balance is set to zero for the first four minutes in the Nchwaning experiments, assuming that the same effect is taking place in the parallels containing hydrogen gas. Figure 3-10 shows the weight loss curves after this adjustment is made for the CO/CO$_2$ parallels. The original and corrected values for Comilog ore are shown in Figure 3-11. Due to the possible occurrence of water decomposition above 100 °C in Comilog ore, only the first two minutes where the temperature was below 100 °C, were set to zero.

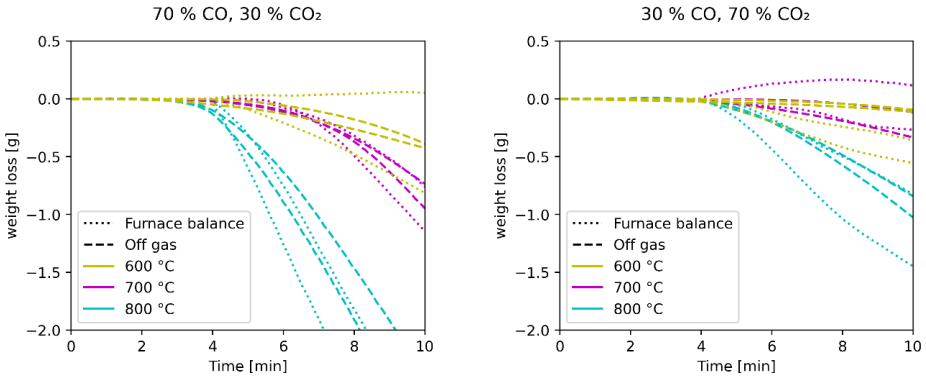

Figure 3-10: Shows the corrected weight loss as a function of time based on the furnace balance measurements and the off-gas measurements.

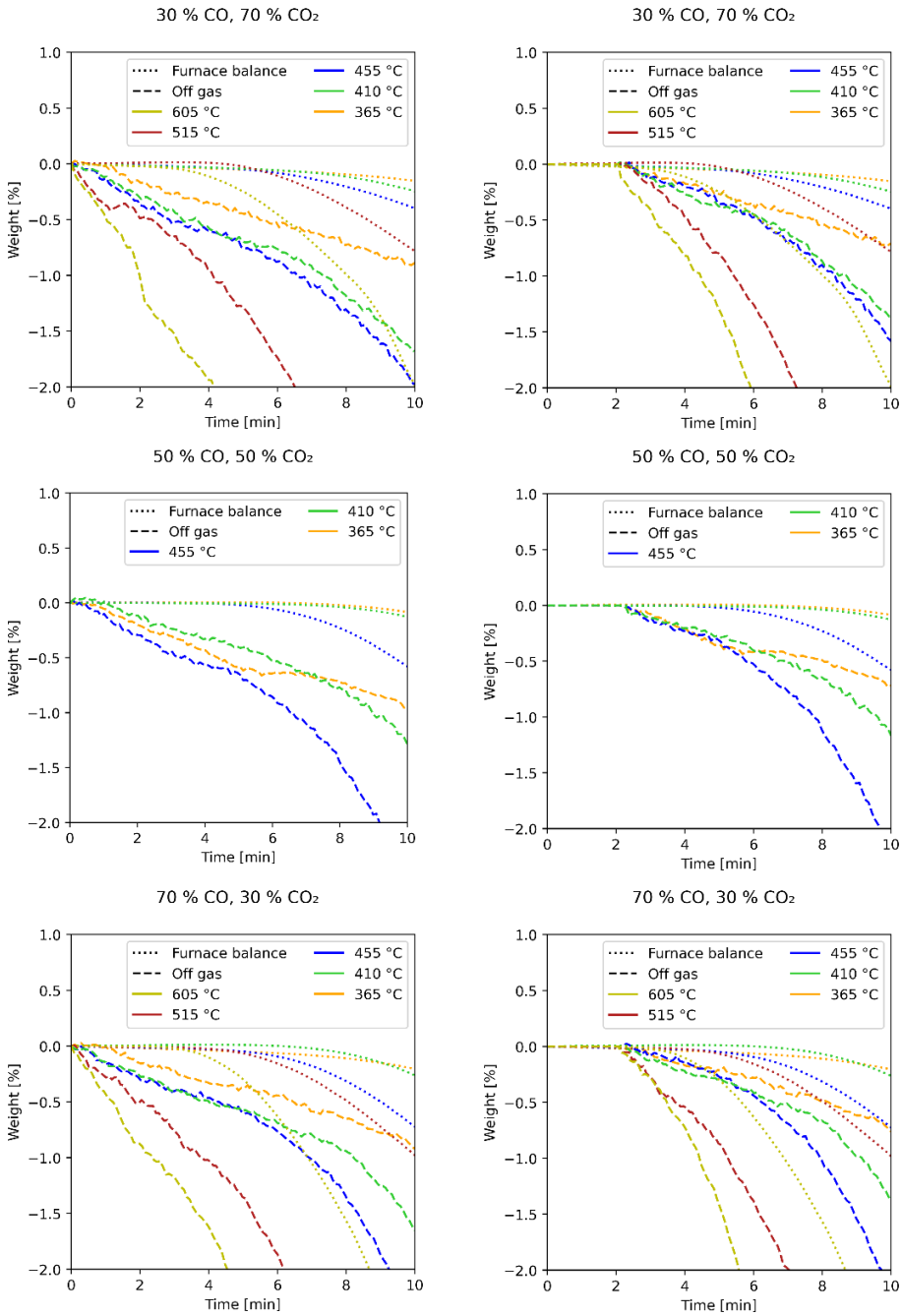

Figure 3-11: Original (left) and corrected (right) weight loss for the Comilog experiments.

3.5 Characterization

The chemical analysis was conducted by SINTEF Norlab by X-ray fluorescence (XRF) (Bruker AXS S4 Pioneer X-Ray fluorescence spectrometer) using the fused bead technique. The excess oxygen was measured by titration (ASTM 465-11:2017)[143], and the CO_2 content was measured by combustion IR (ELTRA).

X-ray diffraction (XRD) was done using a Bruker D8 A25 DaVinci X-ray Diffractometer with Cu-Kα radiation and a LynxEye SuperSpeed detector scanning the range 15–75° with a 0.013° step size. Phases were indexed using the DIFFRAC.EVA V5.1 software coupled with the PDF-4+ database. After reduction, one-quarter of the material was split from each sample and crushed in a ring mill (Retch RS 200) for 90 s at 900 rpm. From the crushed material, samples were taken for chemical analysis and XRD.

The µCT (computed tomography) data was acquired by SINTEF Industry, using a Nikon XT H 225 instrument (cone beam volume CT). A tungsten reflection target was used, with a 200 kV acceleration voltage and a 40 µA current. The X-rays were not filtered. Imaging was done with an integration time of 500 ms and an amplification of 24 dB with 4476 projections per 360 ° rotation. The detector panel has 2850x2850 pixels sized 150x150 µm. The distance from the source to the sample was 55.79 mm and the distance from the source to the detector was 947.19 mm, resulting in a voxel size of 8.84 µm. The images were processed using SINTEF-developed scripts in ImageJ[144]. A general description of the method has previously been published[145].

Scanning electron microscopy (SEM) was used to investigate selected samples. The raw ore was investigated with a Zeiss Sigma 300 field emission Scanning electron microscope (SEM) with Mineralogic software for Quantitative Mineralogical Analysis (AMS). The microscope was equipped with two 6|60 Bruker Energy-dispersive spectroscopy (EDS) detectors that was used for element mapping. An acceleration voltage of 15 kV was applied and a step size of 2.38 µm was used for the element mapping. Samples for AMS (150 g unreduced ore) were crushed in a ring mill (Retch RS 200) for 90 s at 900 rpm and embedded in epoxy. To avoid unwanted influence from segregation due to sedimentation in the epoxy, these samples were cut in half at the center and the cross-section was used for examination. A general description of the method has previously been published[146]. Partly reduced Nchwaning samples were investigated using a JEOL JXA-8500F Electron Probe Micro analyzer (EPMA) with a 15 kV acceleration voltage. The EPMA is equipped with wavelength dispersive x-ray spectrometers (WDS) that has a high accuracy for quantitative analysis, including the analysis of light elements. Images from SEM are acquired using backscatter contrast, which gives higher intensity (brightness) with higher mean atomic number of any particular phase.

3.6 Gas atmospheres and oxygen pressure

Experiments were run in different CO/CO_2 mixtures containing with a gas flow of 4 Nl/min for all experiments. The effect of hydrogen on the reduction rate was investigated using gas mixtures with pH_2 = pCO. The thermodynamic characteristics of hydrogen as a reducing agent differ from those of CO. Table 4 shows the Gibbs free energy for reduction of Mn_3O_4 at selected temperatures, and it can be seen that the thermodynamic driving force of reduction with H_2 and CO is equal at 815.5 °C. Reduction with H_2 has a higher driving force compared to CO at higher temperatures and vice versa.

Table 3-5: The Gibbs free energy for the reduction of Mn_3O_4 by H_2 and CO at selected temperatures. Data from HSC chemistry.

Reaction	$\Delta G_{700°C}$	$\Delta G_{815.5°C}$	$\Delta G_{900°C}$
$Mn_3O_4 + CO(g) = 3MnO + CO_2(g)$	−81.6	−83.5	−85.6
$Mn_3O_4 + H_2(g) = 3MnO + H_2O(g)$	−76.9	−83.5	−88.2

The pO_2 of the gas mixtures were calculated using HSC chemistry[18], allowing for O_2 and H_2O in addition to the input gases, which is equivalent to determining pO_2 from equations (13)- (15). Figure 3-12 shows the equilibrium gas composition of a 37 % CO – 26 % CO_2 – 37 % H_2 gas mixture. Since no water vapor is added, the composition remains constant at lower temperatures where the water gas shift reaction (reaction (13)) is shifted to the right. When increasing the temperature, H_2 reduces CO_2 and increases the CO and H_2O content of the gas mixture. The pO_2 increases with temperature for all gas mixtures.

$$CO(g) + H_2O(g) = H_2(g) + CO_2(g) \quad (13)$$

$$2CO(g) + O_2(g) = 2CO_2(g) \quad (14)$$

$$2H_2(g) + O_2(g) = 2H_2O(g) \quad (15)$$

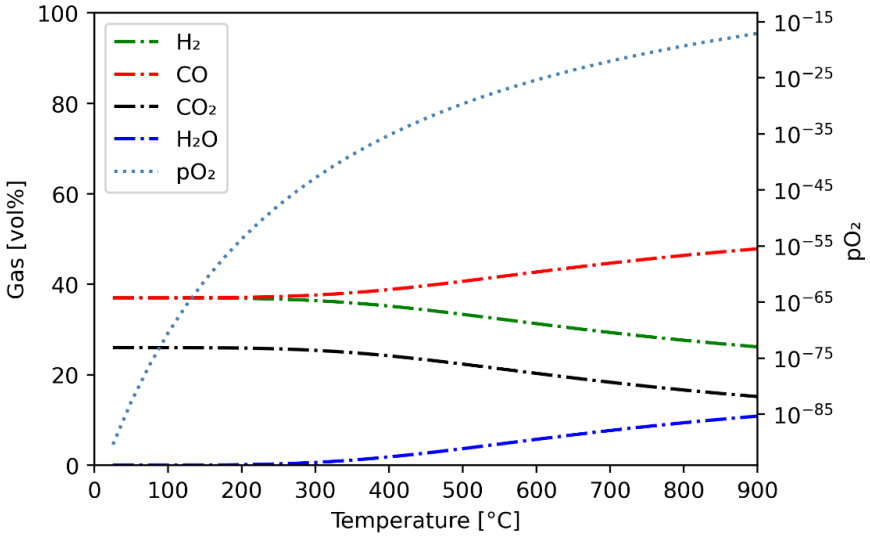

Figure 3-12: Shows the equilibrium composition and oxygen partial pressure of a 37 % CO – 26 % CO_2 – 37 % H_2 gas mixture as a function of temperature. Calculated using HSC chemistry 9[18]

The pO_2 as a function of temperature is shown for the different gas compositions in Figure 3-13, where it can be seen that the hydrogen containing, and the hydrogen free parallels are equal at about 600-650 °C.

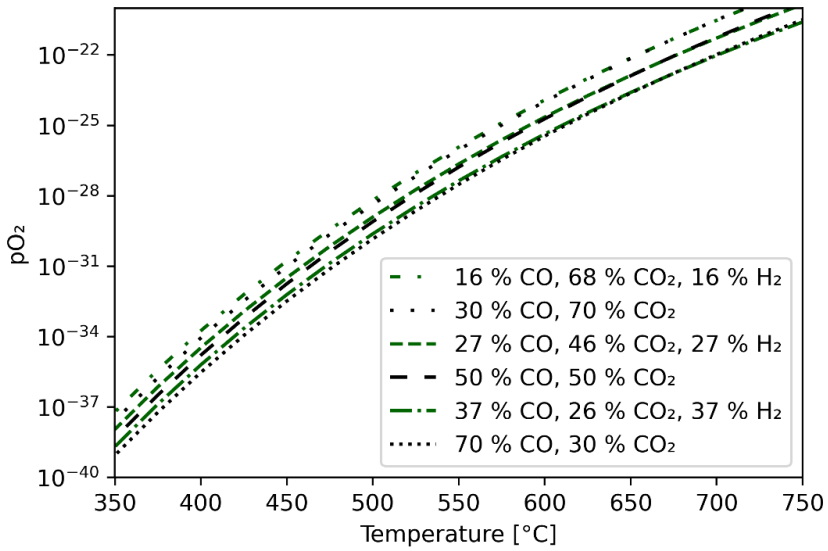

Figure 3-13: The equilibrium oxygen partial pressure of selected gas mixtures. The composition of the hydrogen containing gases (green diamond and green square) have been chosen to give a similar oxygen partial pressure as their 70/30 (black circle) and 30/70 (black triangle) CO/CO_2 counterparts. Legend read vol% CO-CO_2-H_2. Calculated using HSC chemistry 9[18]

3.7 Experiment overview

Table 3-6 contains an overview of the temperatures and gas mixtures investigated for the different ores.

Table 3-6: Experimental overview showing utilized temperatures and gas mixtures for the two ores. Parentheses show number of parallel experiments.

Ore	Temperature [°C] (#experiments)					Gas mixture		
						CO [%]	CO_2 [%]	H_2 [%]
Nchwaning	790(3)	700(1)	605(2)			5	95	0
	790(4)	700(4)	605(4)			70	30	0
	790(4)	700(4)	605(4)			30	70	0
	790(2)	700(2)	605(1)			37	26	37
	790(2)	700(2)	605(2)			16	68	16
Comilog	605(1)	515(1)	455(1)	410(1)	365(1)	70	30	0
			455(1)	410(1)	365(1)	50	50	0
	605(1)	515(1)	455(1)	410(1)	365(1)	30	70	0
		515(1)		410(1)	365(1)	37	26	37
			455(1)	410(1)	365(1)	27	46	27
	605(1)	515(1)	455(1)	410(1)	365(2)	16	68	16

Initial experiments showed that parallels of Nchwaning ore behaved differently hence it was decided to run additional duplicates for most experimental conditions in order to reduce the uncertainties. Comilog ore was seen to have a strong exothermal peak for the experiments set to 605 °C and 500 °C such that most kinetic data in both cases was obtained around 700 °C (measured temperature). For modeling purposes, it is desirable to investigate a range of temperatures. Hence, a lower temperature range for reduction of Comilog ore was selected.

3.8 Related work

Two parallel MSc-studies were undertaken under the course of this work, where prereduction of manganese ores were studied.

Reiersen[92] investigated the prereduction behavior of Comilog, Nchwaning and UMK ore using non-isothermal experiments up to 1000 °C. Heating rates of 3, 6 and 9 °C/min were employed, and the experiments were conducted in the same apparatus as used in this work. An article was written based on this work[87], and both the thesis and the article have been discussed in the literature review.

Davies[84] investigated the prereduction behavior of UMK ore by isothermal reduction. The ore was investigated at 700 °C, 800 °C and 900 °C in three different gas mixtures: 70 % CO – 30 % CO_2, 70 % H_2 – 30 % H_2O and 100 % H_2O, using the

same apparatus and experimental setup as in this work. An article was written based on this work[85].

4 Results

4.1 Reduction of Nchwaning ore

As described in the previous section, Nchwaning ore was reduced at 605 °C, 700 °C and 790 °C in CO/CO_2 and $CO/CO_2/H_2$ gas mixtures. The CO/CO_2 gas mixtures were chosen to investigate the reduction rates with high and low reducing gas potential while the hydrogen containing gas mixtures were selected such that they had a similar thermodynamic driving force as the CO/CO_2 mixtures, making it possible to study the influence of hydrogen on reduction directly. The pairs of gas mixtures yield a high and low oxygen partial pressure relative to each other, which is indicated together with the gas composition in Table 4-1. Experiments were also conducted in a gas mixture consisting of 5 % CO and 95 % CO_2. Carbon deposition was observed in one experiment in the low pO_2 hydrogen containing gas mixture.

Table 4-1: The gas mixtures used in reduction of Nchwaning ore where the pairs of mixtures yield a high and low oxygen partial pressure, respectively. The logarithm of the partial pressures at 650 °C was included for reference.

pO_2	$\log(pO_2)$ | 650 °C	CO	CO_2	H_2
Very high	-20.3	5	90	0
High	-22.1	30	70	0
		16	68	16
Low	-23.6	70	30	0
		37	26	37

4.1.1 Weight loss and reduction behavior

Figure 4-1 shows the measured weight loss from the furnace balance for the Nchwaning ore experiments sorted by gas mixture. The theoretical weigh loss to Mn_3O_4-Fe_3O_4, MnO-FeO and decomposition of carbonates is indicated by the horizontal lines in the figure. The dotted lines connect the end of the experimental curves as measured by the furnace balance with the value of the weight loss as determined by the external weight measurement. In the experiment conducted using low pO_2 in a H_2 containing atmosphere at 605 °C, the sample and the crucible interior was covered in soot after the experiment, hence the measured weight is uncertain, and this curve is removed from further analysis.

None of the experiments reduced without hydrogen using high or very high pO_2 were fully reduced to MnO-FeO. For the other three gas mixtures, all samples reduced at 790 °C was reduced beyond MnO-FeO, indicating that some carbonates decomposed. The samples reduced at 700 °C all ended up with a weight loss close to the expected weight loss for reduction to MnO-FeO. The weight curves in Figure 4-1 have not flattened completely, hence, some reactions are still occurring at the time of termination of the experiments. Since no metallic

iron was found in the subsequent analysis, these reactions may be explained by the decomposition of carbonates in the cases where the oxides are fully reduced (below MnO-FeO).

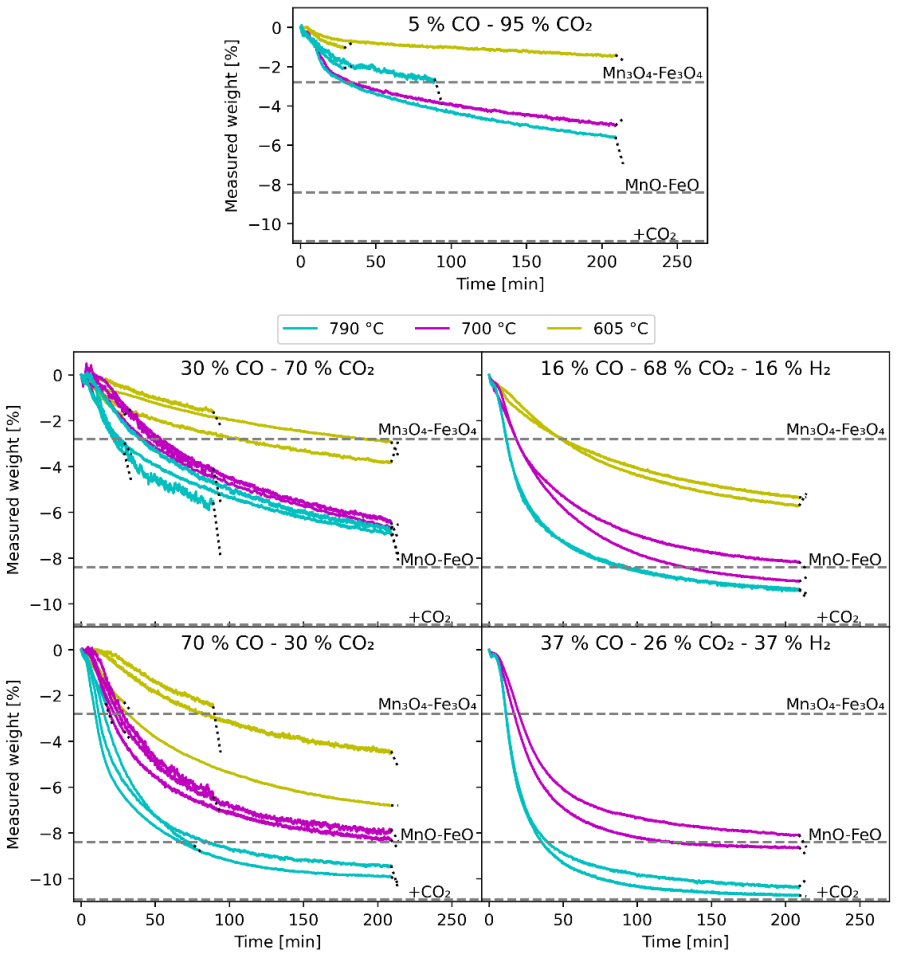

Figure 4-1: Shows the measured weight loss curves as a function of time from the furnace balance for reduction of Nchwaning ore in different gas mixtures. The dotted lines at the end of each experimental curve connects the final weight measured by the furnace and that measured by the external balance. Horizontal dashed lines indicate the expected weight loss when ore is reduced to Mn_3O_4-Fe_3O_4, MnO-FeO and MnO-FeO + decomposed carbonates (+CO_2), respectively, as indicated on each line.

Figure 4-2 shows the fractional conversion and the reduction rate of the Nchwaning ore samples reduced in high and low oxygen partial pressures with and without H_2 in the gas mixture. Each conversion curve has been marked at the point where the sample temperature reached the set temperature. It can be seen that part of the reduction occurred prior to this point, i.e., about 20 % of the reduction occurred below the set temperature in the low pO_2 hydrogen containing gas

mixture reduced at 790 °C. For all gas mixtures, it is seen that the rate and extent of reduction increase with increasing temperature. The rate and extent of reduction increases with the addition of H_2 at constant partial pressure and with decreasing pO_2 of the gas mixture for both the CO/CO_2 and hydrogen containing mixtures.

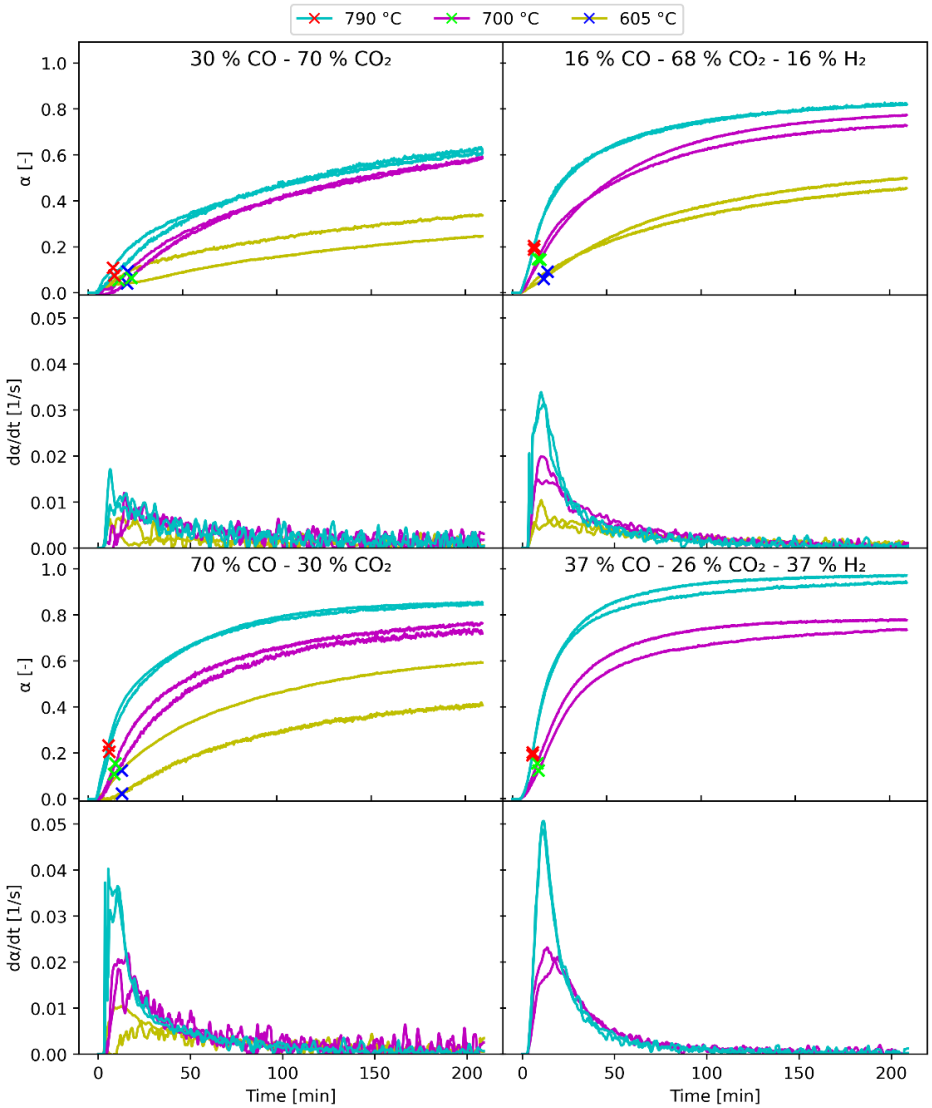

Figure 4-2: Shows the fractional conversion and the reduction rate for reduction of Nchwaning ore in the utilized gas mixtures. Markings (x) in contrasting colors indicate the point where the sample temperature reaches the set temperature (temperature in the legend). The two gas mixtures at the top represent the high oxygen partial pressure whereas the gas mixtures at the bottom represent the low oxygen partial pressure (Table 4-1).

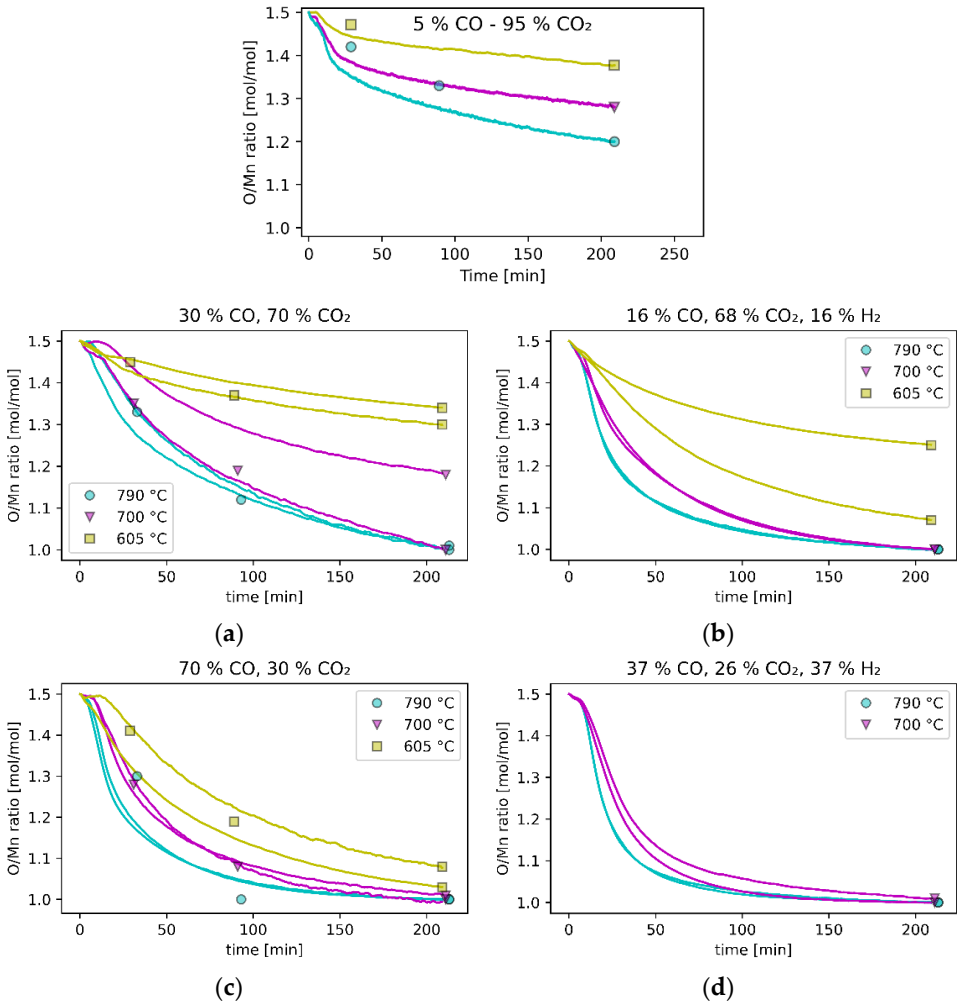

*Figure 4-3: Shows the O/Mn ratio as a function of time for the 210-minute experiments. Markers indicate the analyzed O/Mn ratio from conducted experiments at 30, 90, and 210 min and are shifted by ±2 minutes to avoid overlapping. (**a**): high pO_2 hydrogen-free experiments; (**b**): high pO_2 hydrogen-containing experiments; (**c**): low pO_2 hydrogen-free experiments; (**d**): low pO_2 hydrogen-containing experiments.*

To focus on the reduction of oxides in the ore, the weight curves were adjusted in such a way that they start at the initial O/Mn ratio of the unreduced ore and end at the O/Mn ratio determined by the chemical analysis of the reduced samples. This adjustment implicitly assumes that any carbonate decomposition is distributed evenly throughout the experiment and that Fe and Mn is at the same oxidation state throughout the experiment since the general shape of the curve is maintained. These results are shown in Figure 4-3, where the curves from the analyzed experiments run for 210 minutes is shown, and the final O/Mn ratio from

all experiments are indicated by symbols. The figure shows that the samples are fully reduced at 700 °C and 790 °C at 210 min, except for one of the 700 °C parallels in 30 % and all in the 5 % CO containing mixtures. Some deviation between the chemical analysis and the weight loss is seen in high pO_2 parallels (700 °C without H_2 and 605 °C with H_2). The samples reduced in in 30 % CO – 70 % CO_2 have achieved a higher degree of reduction when considering the chemical analysis (Figure 4-3a) compared to the weight loss (Figure 4-1), whereas for the other gas mixtures the results are consistent between the two.

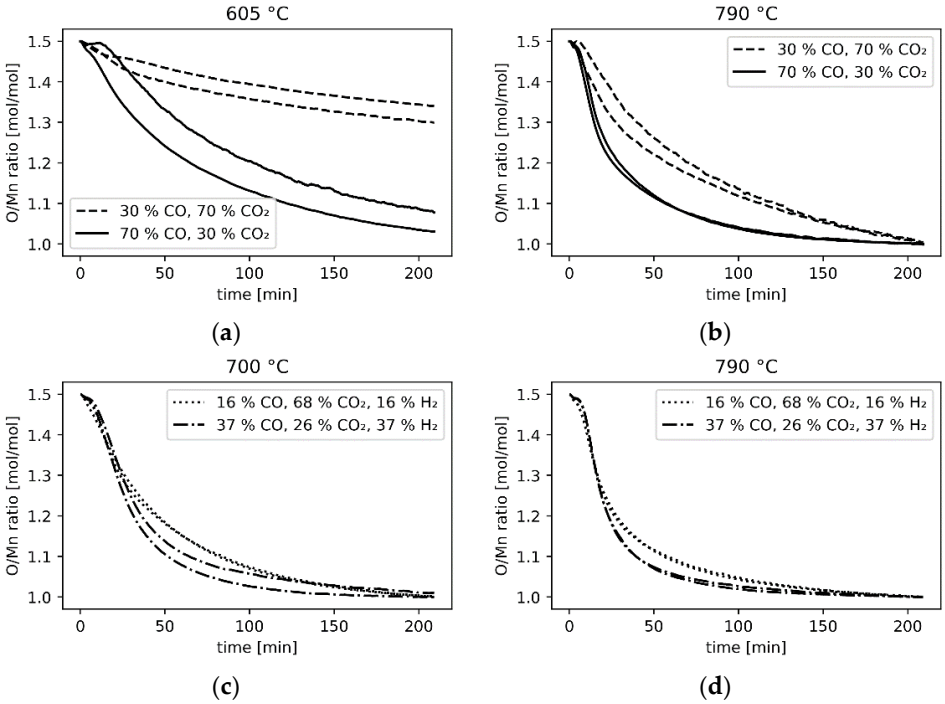

Figure 4-4: Selected curves from Figure 4-3 showing the effect of changing between high and low oxygen partial pressure of the hydrogen free gas mixtures at (a) 605 °C and (b) 790 °C, and the hydrogen containing gas mixtures at (c) 700 °C and (d) 790 °C.

In Figure 4-4 and Figure 4-5, selected curves from Figure 4-3 are compared. The reduction rate is seen to increase with decreasing oxygen partial pressure in Figure 4-4, for both the CO/CO_2 and the hydrogen containing gas mixtures. Figure 4-5 shows that the reduction rate is higher for the hydrogen containing gas mixtures compared to the hydrogen free gas mixtures when the oxygen partial pressure is kept constant.

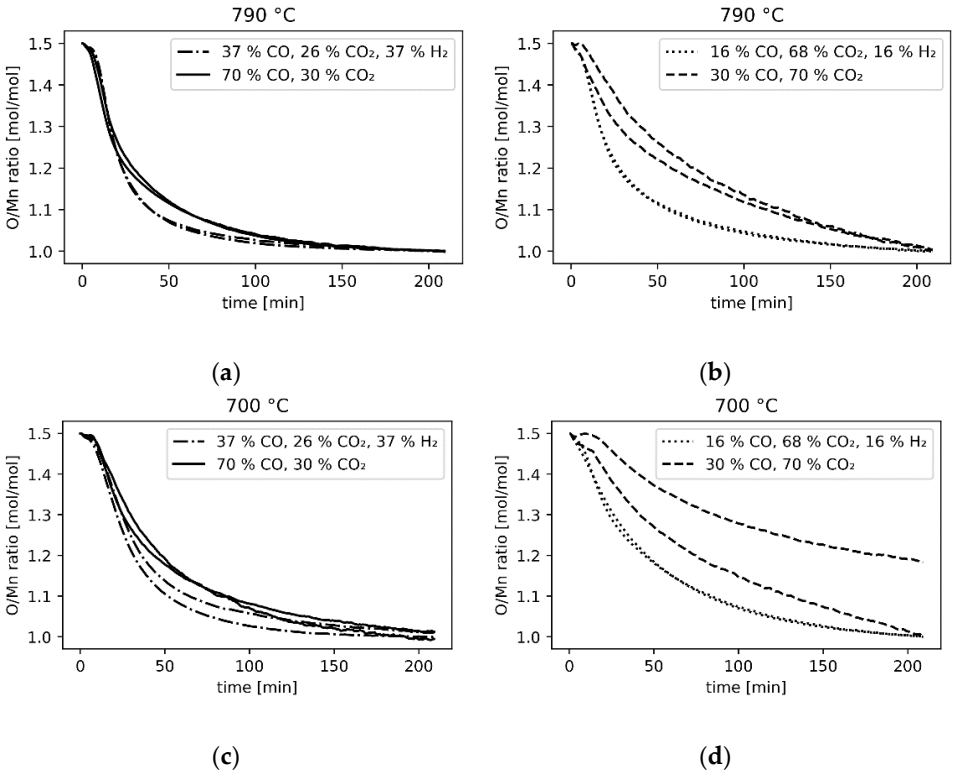

Figure 4-5: The effect of hydrogen at constant oxygen partial pressure at 790 °C for (a) low pO_2, and (b) high pO_2.

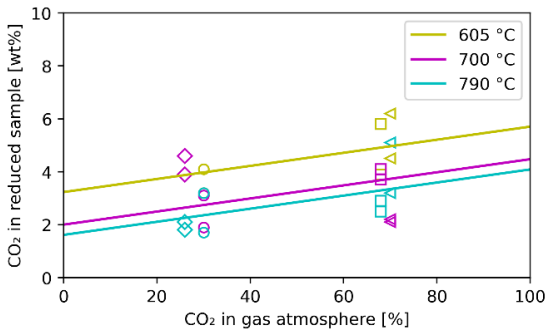

Figure 4-6: Shows the remaining CO_2 from chemical analysis of the reduced samples as a function of CO_2 in the reducing atmosphere. The slope of the trendlines was determined by linear regression of all measurements and the y intercept was determined by linear regression at each temperature. Only samples reduced for 210 minutes at high and low pO_2, are included.

Figure 4-6 shows the remaining carbonates, from chemical analysis, as a function of the CO_2 content of the reducing atmosphere after 210 min. The slopes of the lines were calculated from the linear regression of all points, while the *y*-intercepts were calculated from fitting at each temperature. It can be seen that for

decreasing temperature and for increasing CO_2 content of the reducing atmosphere, more carbonates remained in the sample after reduction for 210 min. According to the differences in the lines in Figure 14, on average, the samples lost 1.3 wt.% more mass from carbonates when increasing the temperature from 605 °C to 700 °C and 0.4 wt.% more mass when increasing the temperature from 700 °C to 790 °C.

From the chemical analysis of the unreduced ore, the CO_2-content of Nchwaning was seen to be 2.5 ± 0.5 % (Table 3-1). If the oxides are reduced without any decomposition of carbonates, the carbonate content would increase to 2.73 ± 0.55 % by concentration due to the removal of oxygen, which is lower than many of the measurements in Figure 4-6. The variance in the figure, as well as the deviation from the expected results, show that the carbonate content can vary a lot from batch to batch, more than what was indicated by the initial variance in the raw material.

4.1.2 Off-gas analysis

The off-gas analysis from the furnace was calibrated to the known composition of reducing gas at the start of each experiment. Details regarding these corrections are given in Appendix D. The reduction in CO content of the off-gas is caused by the CO consumed in the reduction while increased CO_2 in the off-gas stems from the reduction of oxides in addition to any carbonate decomposition. Figure 4-7 and Figure 4-8 shows the off-gas analysis for the CO/CO_2 gas mixtures with high and low pO_2 respectively. The y-axis in these figures have been given similar ranges for consistency. The CO_2 content of the off-gas from the very high pO_2 experiments exceeded the capacity of the CO_2 analyzer and are thus not included further.

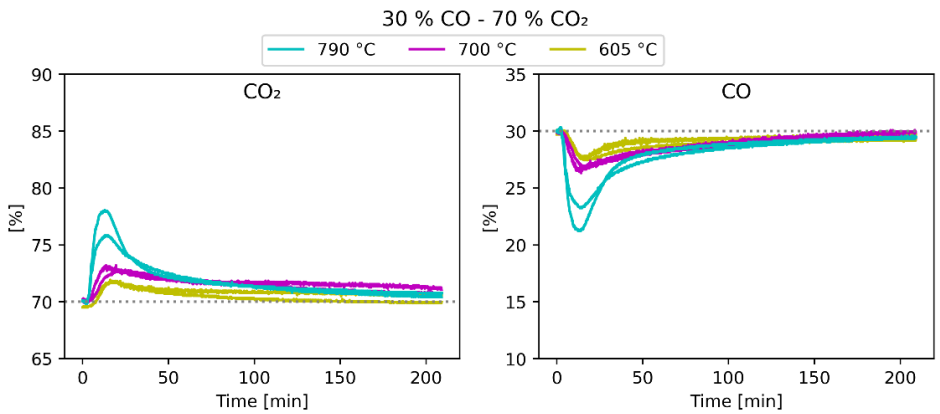

Figure 4-7: CO and CO_2 from the off-gas analysis from the high pO_2 hydrogen free parallels. The dashed lines indicate the input composition.

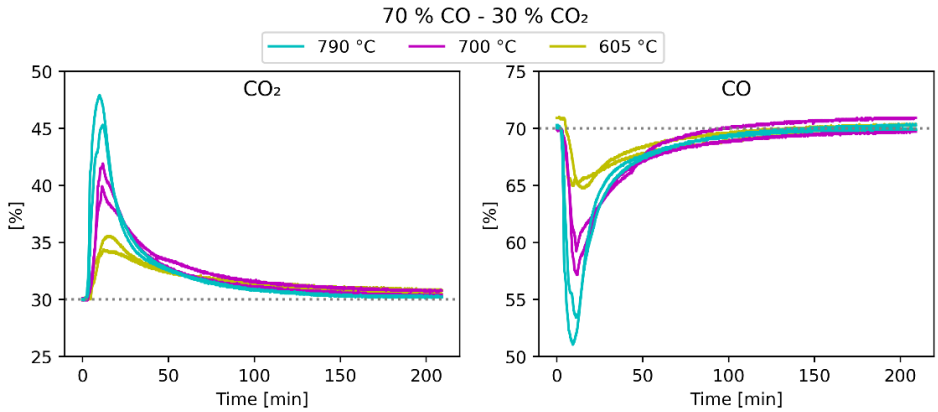

Figure 4-8: CO and CO_2 from the off-gas analysis from the low pO_2 hydrogen free parallels. The dashed lines indicate the input composition.

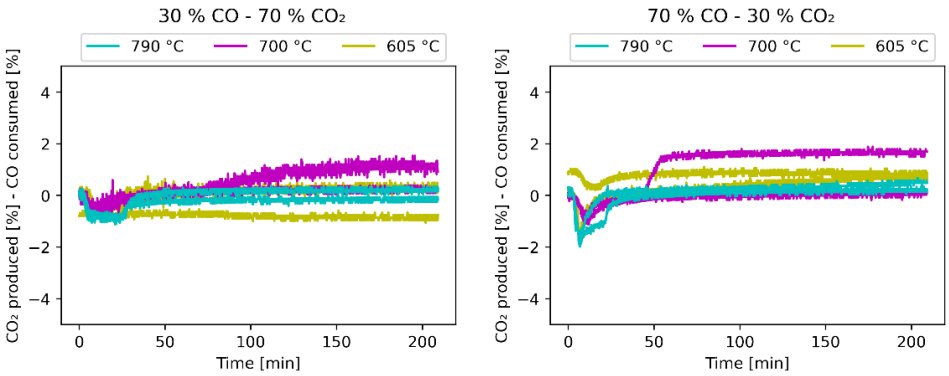

Figure 4-9: Show the difference between the produced CO_2 and the consumed CO from the off-gas analysis of the CO/CO_2 experiments.

From Figure 4-7 and Figure 4-8 it appears that the CO_2 and CO curves are opposites of each other. For closer comparison, the difference between the consumed CO and produced CO_2, taken as the difference between the input concentration and the measured concentration, was calculated, and is shown in Figure 4-9. This difference should be 0 if the off-gas analyzers are perfectly accurate and all CO_2 originates from reduction of oxides with CO. Carbonate decomposition will increase the CO_2 produced and not affect the CO consumed (other than by dilution). Any carbon deposition by the reverse Boudouard reaction ($2CO=C+CO_2$), will increase the CO consumed two times more than the CO_2 produced. If these two effects happen simultaneously, they might be obscured by each other. Carbonate decomposition was seen to increase the CO_2 content in the off gas to around 0.5-1 % in Ar atmosphere at the early stages of the experiment

(10-30 min, Figure A-1). Carbonates will decompose slower when CO_2 is present in the atmosphere. If all CO_2 in the sample (2.5 % carbonates) decomposed evenly over 210 minutes, it would produce less than 0.1 % of the input gas volume and might not be noticed.

The dip in the initial part of many of the curves in Figure 4-9 indicates that more CO is consumed than CO_2 is produced, which is consistent with carbon deposition by the Boudouard reaction ($2CO=C+CO_2$) and/or carbonate decomposition. However, the difference is lower than the observed variability in the analysis and may simply be a result of high reaction rates yielding a gas composition with a high deviation from the off-gas composition used during calibration. Carbon deposition was not observed in any of the experiments without H_2 in the gas mixture.

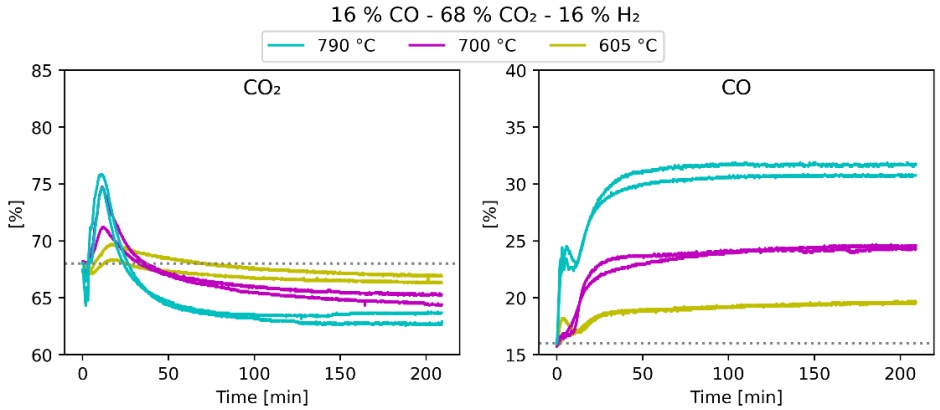

Figure 4-10: The measured off-gas from the high pO_2 hydrogen containing parallels. The dashed lines indicate the input composition.

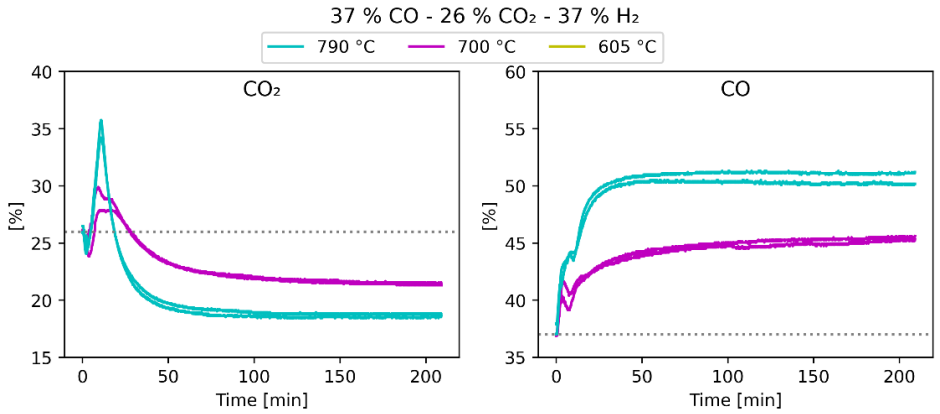

Figure 4-11: The measured off-gas from the low pO_2 hydrogen containing parallels. The dashed lines indicate the input composition.

Figure 4-10 and Figure 4-11 shows the measured CO and CO_2 in the off-gas of the hydrogen containing parallels with high and low pO_2, respectively. For both gas mixtures, the CO_2 content in the off-gas increases in the initial part of the experiment where the reduction rate is high, before it stabilizes at a value lower than the input composition towards the end of the experiments. The measured CO content increases compared to the added amount and remains at a higher concentration compared to the input composition. Both these observations are indications that the water gas shift reaction (WGSR: $CO+H_2O=CO_2+H_2$) is shifted to the left.

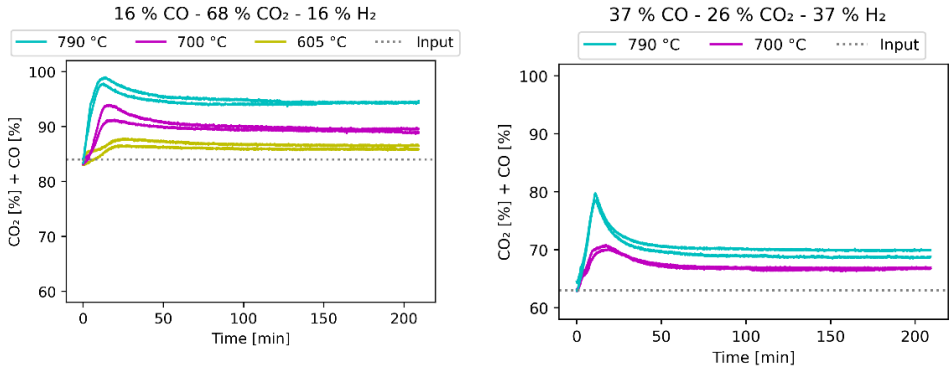

Figure 4-12: $CO+CO_2$ from the off-gas analyzer for the hydrogen containing gas mixtures. The input $CO+CO_2$ is indicated by the dotted gray lines.

Figure 4-12 shows the sum of CO and CO_2 analysis from the experiments using hydrogen containing gas mixtures. It can be seen that the sum of CO and CO_2 does not add up to 100 %. Since H_2O condenses in the wash bottles prior to the off-gas analyzer, it is assumed that the difference up to 100 % (in Figure 4-12) is the H_2 content. Due to the H_2O condensation, the measured CO, CO_2 and H_2 (by difference) is higher than that of the gas exiting the crucible. To assess the H_2O content of the off-gas, it is assumed that the sum of CO and CO_2 entering and exiting the crucible is the same. This requires the assumptions that carbonate decomposition gives an insignificant impact on the off-gas analysis, and that no carbon deposition by the reverse Boudouard reaction ($2CO=C+CO_2$) occurs. To calculate the amount of H_2O exiting the crucible, H_2O is added such that $CO^{in}+CO_2{}^{in}=CO^{out}+CO_2{}^{out}$ for the duration of the experiments.

The adjusted CO, CO_2 and H_2 content and the calculated H_2O content in the off-gas is shown in Figure 4-13 together with the equilibrium gas compositions for each temperature. Two experiments are plotted in each graph with the exception of the 605 °C experiment at low pO_2 where only one experiment was conducted. The equilibrium gas compositions are determined by the WGSR ($CO+H_2O=CO_2+H_2$) and is shown by dotted lines for each gas and temperature in Figure 4-13.

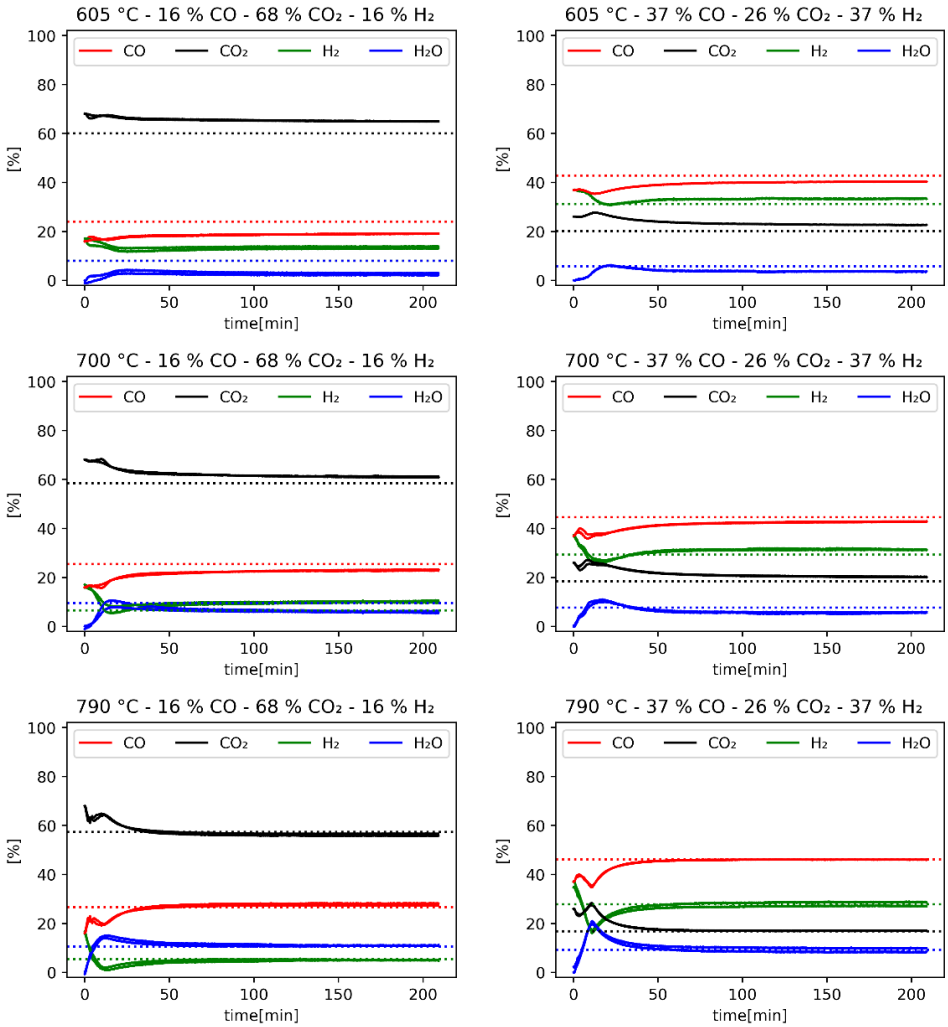

Figure 4-13: Shows the adjusted CO, CO_2 and H_2 composition with the calculated H_2O composition for the 210-minute experiments in hydrogen containing gas mixtures. The 605 °C experiment at low pO_2 was included despite the observed carbon deposition. In the other gas mixtures and temperatures, results from two (all) experiments are plotted. Dotted lines show the equilibrium composition (calculated by HSC chemistry 9[18]) of the gas mixtures at each temperature and gas mixture.

At 605 °C, water vapor is produced and H_2 is consumed in the early parts of the experiments. This is consistent with reduction of oxides with hydrogen. A small increase in CO coupled with a similar decrease in CO_2, indicates that the WGSR occurs, however it is seen that the gases has not reached the equilibrium composition. At 700 °C, the same tendencies are observed as at 605 °C, however it is seen that the gas composition at the end of the experiments where the reduction rate is low, is closer to the equilibrium composition predicted by the

WGSR compared to the experiments at 605 °C. At the end of the 790 °C experiments, the gas compositions are consistent with the equilibrium composition of the WGSR for both gas mixtures.

4.2 Characterisation of Nchwaning ore

Reduced samples were analyzed by X-ray diffraction (XRD) to investigate the evolution of phases during reduction. The unreduced Nchwaning was investigated using quantitative mineralogy analysis (AMS). The content of different minerals was quantified, and selected microstructures were investigated. Additional data from AMS can be found in Appendix F. Partly reduced samples were examined by Electron Probe Micro analysis (EPMA). The decrepitation of the reduced samples was also measured.

4.2.1 XRD - Phase evolution

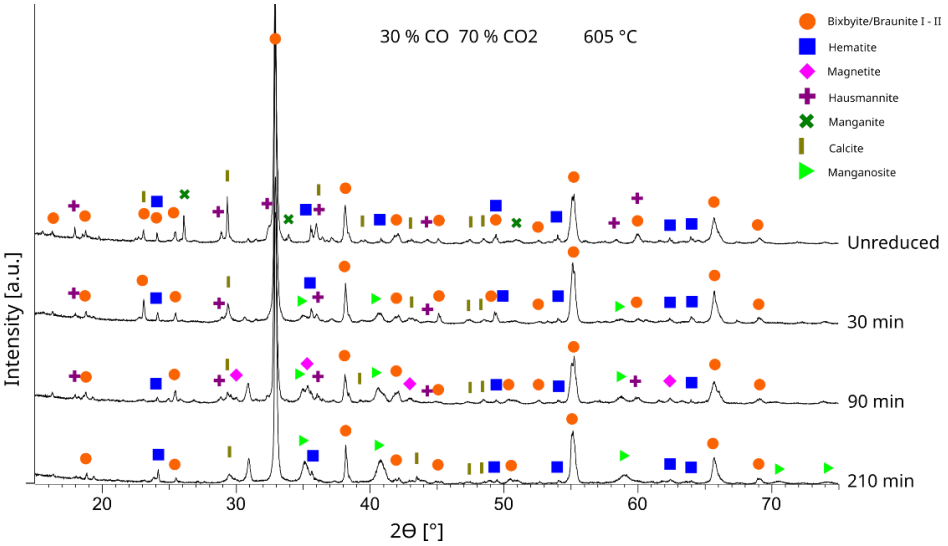

Figure 4-14: X-ray diffraction patterns and identified phases in unreduced ore and samples reduced in 30 % CO and 70 % CO_2 at 605 °C. The main Bixbyite/Braunite peak (33°) has been cropped for clarity in the figure.

4.2.1.1 High pO_2 without Hydrogen

The XRD results of the samples reduced at 605 °C in the hydrogen free, high pO_2 atmosphere are shown in Figure 4-14. After 30 min at 605 °C, the intensity of the bixbyite/braunite peaks increased despite chemical analysis showing a slight reduction in oxygen content (O/Mn: 1.50 → 1.45). This may be explained by the decomposition of manganite, which is known to decompose to Mn_2O_3 at this temperature. Hematite, hausmannite, and calcite are still present, and the formation of the monoxide phase (MnO–FeO solid solution) commenced. After 90 min, magnetite was identified in the diffraction pattern, and the increased manganosite content is consistent with the lower O/Mn ratio in the chemical analysis. After reduction for 210 min, magnetite and hausmannite can no longer be seen in the XRD spectrum, although the average composition from the chemical

analysis indicates a composition close to Mn_3O_4. This implies that the original content of hausmannite is reduced and that it is not a stable intermediary in the reduction of bixbyite/braunite to MnO.

After 30 min reduction in the same gas atmosphere at 700 °C, the XRD pattern and the O/Mn ratio was similar to the samples reduced for 210 min at 605 °C. There was less oxygen left in the samples reduced at 790 °C compared to 605 °C and 700 °C. The XRD shows that some Mn_2O_3 (bixbyite/braunite) was still present in the fully reduced (O/Mn = 1.00–1.01) samples. The XRD patterns can be found in Appendix B (Figure B-1 and Figure B-2). Magnetite was identified after 90 min reduction at 700 °C, but no iron-containing phases were identified after 210 min reduction. The higher oxides of iron may have been dissolved in the bixbyite phase or reduced to FeO and dissolved in the MnO phase. The experiments reduced for 210 min at 700 °C obtained O/Mn ratios of 1.18 and 1.00. A significant difference in the chemical analysis between the two parallels was their Mn/Fe ratio which were 2.4 and 8.9 compared to 5.6 for the unreduced ore. Magnetite was identified after 210 min at 790 °C, in the fully reduced sample with the highest iron content (13.5% Fe).

4.2.1.2 Low pO2 without hydrogen

Samples reduced in the hydrogen free, low pO_2 atmospheres had a lower O/Mn ratio compared to their high pO_2 counterparts, which is consistent with the reduction curves (Figure 4-1). The XRD patterns can be found in Appendix B (Figure B-3, Figure B-4 and Figure B-5). At 605 °C, the bixbyite/braunite and hematite content decreased as time progressed. Hematite was identified up until 90 min, whereas, at 210 min, magnetite was identified. The 90 min and 210 min samples had a relatively high iron content (11.5% and 12.8% Fe, respectively). At 700 °C, hausmannite disappeared after 90 min, whereas hematite was still present at 210 min, parallel with the highest iron content (14.5 wt.%). At 790 °C, there was no hausmannite in the samples reduced for 30 min. After 90 and 210 min, tephroite was observed, while hematite and magnetite were not present.

4.2.1.3 Hydrogen containing atmospheres

Figure 4-15 and Figure 4-16 shows the XRD spectra for the samples reduced in hydrogen containing atmospheres, at high and low pO_2, respectively. The amount of bixbyite/braunite decreased, and the monoxide increased with increasing temperature for both gas mixtures. Tephroite was found when the ore was reduced at 790 °C for both gas mixtures. At 700 °C and 790 °C, the samples were fully reduced according to the chemical analysis (O/Mn = 1.00–1.01), although there were traces of Mn_2O_3. No hematite or magnetite was identified in any of the samples reduced with H_2 present in the gas.

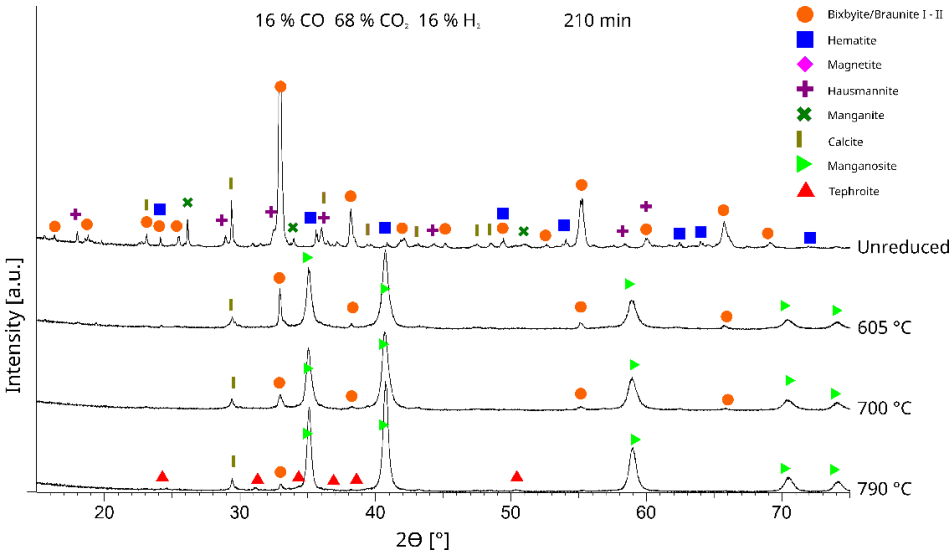

Figure 4-15: X-ray diffraction patterns from the experiments conducted with the 16 % CO/68 CO_2/16 % H_2 gas mixture. The main Bixbyite/Braunite peak (33°) has been cropped for clarity in the figure.

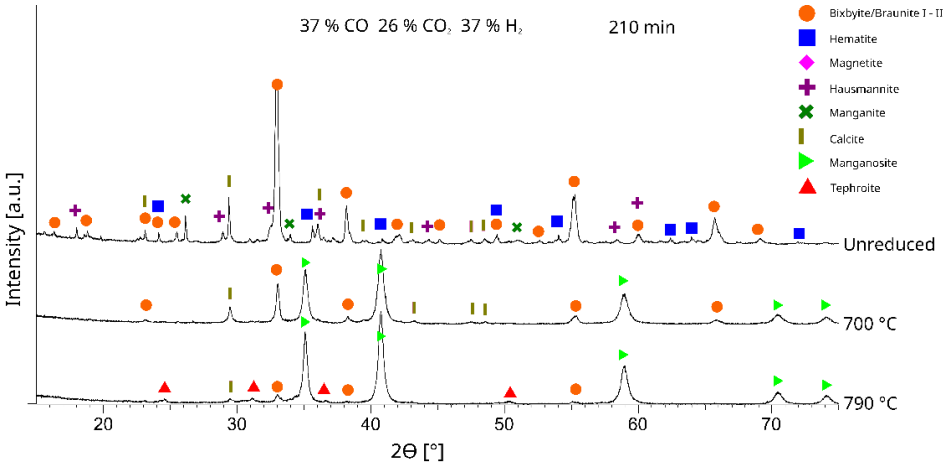

Figure 4-16: X-ray diffraction patterns from the experiments conducted with the 37 % CO/26 CO_2/37 % H_2 gas mixture. The main Bixbyite/Braunite peak (33°) has been cropped for clarity in the figure.

4.2.2 Quantitative Mineralogical Analysis - Unreduced ore

Different minerals were identified using the chemical composition acquired by Energy-dispersive spectroscopy (EDS) measurements. Two different areas of the sample were investigated covering 32.5 mm^2 and a few thousand different particles. Due to carbon coating of the specimen, carbon cannot be accurately quantified, but carbonates are identified based on the composition of the other constituents. Hydrogen is undetectable; hence, manganite (MnOOH) falls within the bixbyite classification. An example of the mineral identification of a particle is shown in Figure 4-17 where neltnerite, braunite I and braunite II and calcite are the most predominant phases.

Table 4-2 shows the content of different minerals in the sample. It is seen that the manganese is distributed between the oxide (bixbyite, hausmannite, manganite, and marokite) and silicates (braunite I, braunite II and neltnerite), with a higher proportion belonging to the latter category. From the perspective of reduction, most of the manganese is in the form of Mn^{3+} (Mn_2O_3). In regard to the iron content, some hematite is identified in the sample, however most of the iron is contained in the manganese oxides. About 50 % of the carbonates were characterized as pure calcite, while the remaining 50 % contained various degrees of other cations (Mg, Mn and Fe).

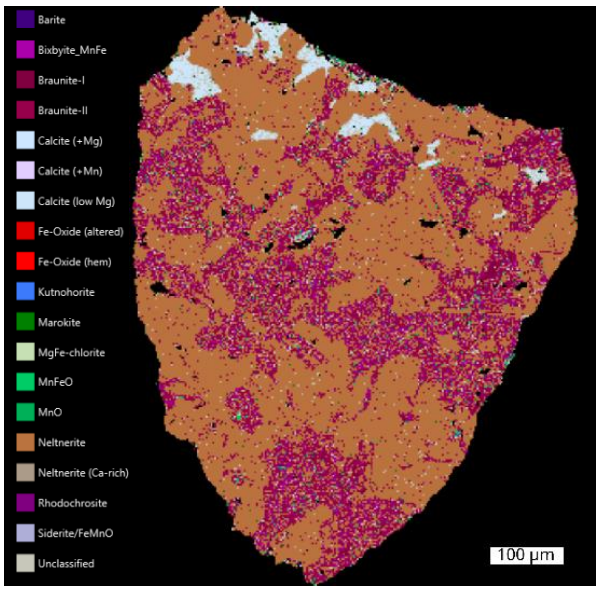

Figure 4-17: Shows the mineral identification of a particle. The orange mineral is identified as neltnerite, the purple areas contain mostly braunite I and braunite II, and the light areas consist of calcite.

Table 4-2: Shows the abundance of different minerals in Nchwaning ore. Includes the minerals with more than 5 wt% of the sample in addition to hematite and carbonates. The range in composition is given by the difference between the analysis of two different areas in the sample.

Mineral	**Formula**	**Area%**	**Wt%****
Bixbyite, Hausmannite, Manganite	$(Mn,Fe)_2O_3$, Mn_3O_4, MnOOH	27-29	33-35
Braunite-II	$7(Mn,Fe)_2O_3*CaSiO_3$	20-23	24-27
Neltnerite	$3(Mn,Fe)_2O_3*CaSiO_3$	10-14	12-15
Braunite-I	$3(Mn,Fe)_2O_3*MnSiO_3$	11	13
Marokite	$CaMn_2O_4$	6-7	7-8
Hematite	Fe_2O_3	0.7-1.2	0.9-1.5
Carbonates	CaCO3*	4.1-4.8	3.0-3.7

**Carbonates with Mn, Mg, and Fe cations are included in the total number*

***Calculated using the average composition of the identified phase*

Selected grains with different microstructures were investigated closer, Figure 4-18 and Figure 4-19 shows the backscatter (BS) image together with the Energy-dispersive spectroscopy (EDS) analysis of Mn, Fe, Ca and Mg from two different particles. The particle in Figure 4-18 is the same as the particle shown in Figure 4-17. The microstructures in Figure 4-18 and Figure 4-19 are highly similar to the two main types of microstructure observed in Nchwaning ore by Larssen et al.[70] where the brighter phases (BS) generally were Mn or Fe rich and the darker phases were identified as carbonates. All manganese rich phases commonly identified in Nchwaning ore may contain Fe[139,147].

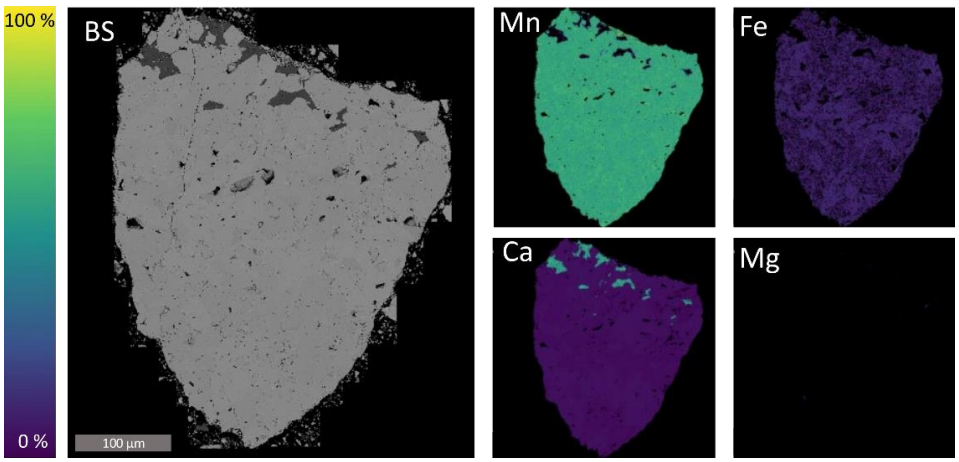

Figure 4-18: Shows the backscatter image for a particle (BS) and EDS analysis for Mn, Fe, Ca and Mg. The color scale at the left of the figures relates to the wt% of elements in the EDS analysis images.

The particle in Figure 4-18 mainly consists of a Mn rich Fe and Ca containing phase, which is consistent with braunite II or neltnerite. There are variations in the Mn/Fe ratio though the Ca content is stable. These variations can also be observed in the slight intensity differences of the BS image, where the brightest phase has the higher iron content. A few islands of a calcium rich phase (e.g., Calcite) is also observed. The BS image in Figure 4-19 show an equal distribution between the two different phases. The bright phase contains Mn, Fe and Ca which is consistent with braunite II or neltnerite, and the darker phase with carbonate. The carbonate phase is seen to contain Mn and Mg in addition to Ca.

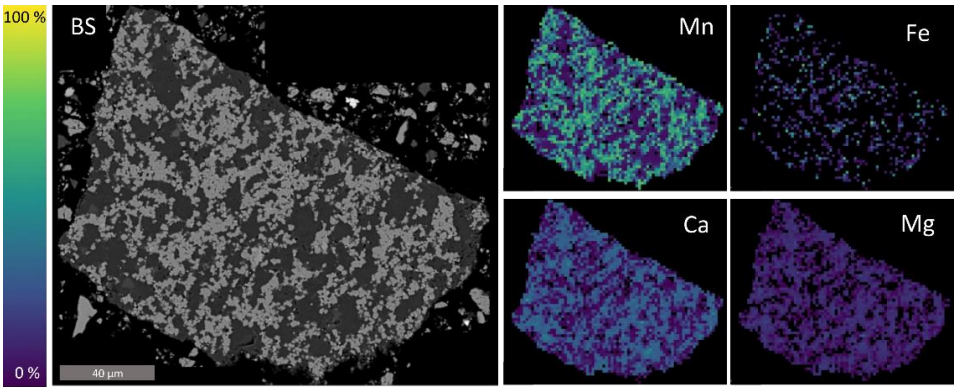

Figure 4-19: Shows the backscatter image for a particle (BS) and EDS analysis for Mn, Fe, Ca and Mg. The color scale at the left of the figure relates to the wt% of elements in the EDS analysis images.

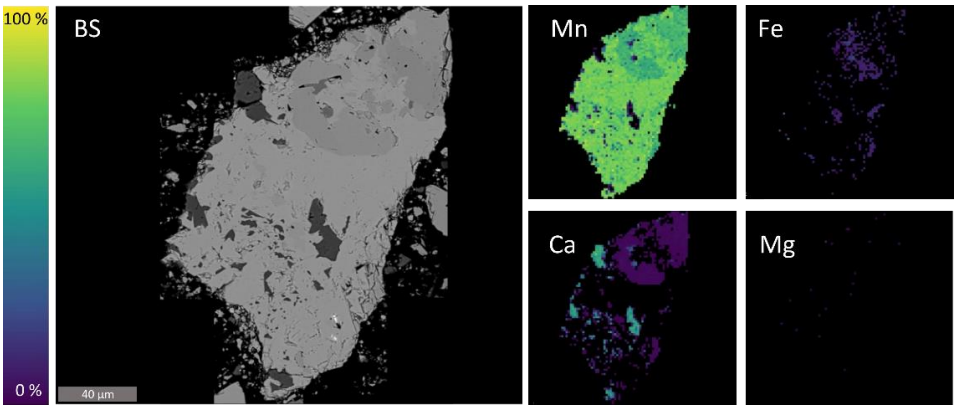

Figure 4-20: Shows the backscatter image (BS) and EDS analysis of the particle for Mn, Fe, Ca and Mg. The color scale at the left of the figure relates to the wt% of elements in the EDS analysis images.

Figure 4-20 shows one of the grains with the highest manganese content. Manganese rich areas containing Ca, Ca + Fe can be seen, which corresponds to the phase boundaries observed in the backscatter (BS) image. Ca in a manganese

rich phase suggests the occurrence of Braunite II (Table 2-2). The phase with the highest manganese content has a composition consistent with Mn_3O_4. Similar to the particle shown in Figure 4-18, some Ca-rich areas (e.g., Calcite) are observed that correspond to the low intensity areas in the BS image.

In areas with high Mn content in Figure 4-21, different grayscales in the BS image correlate with differences in Ca and Fe contents. The Ca content implies braunite II, while the lack of Ca corresponds to braunite I, bixbyite or hausmannite. Some pockets of carbonates are also observed. The BS contrast increases with increasing average atomic number hence it is expected to increase with increased iron content in the phase. However, in these phases the Fe is associated with Ca, which reduces the BS contrast. In sum, the brightest areas correspond to the highest manganese content.

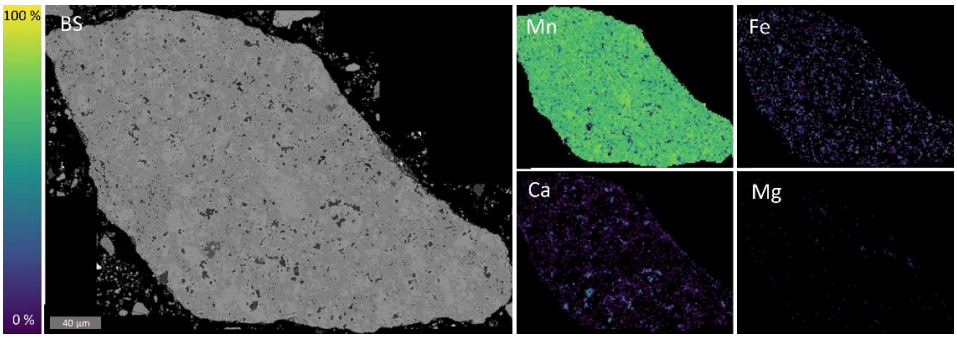

Figure 4-21: Shows the backscatter image for a particle (BS) and EDS analysis for Mn, Fe, Ca and Mg. The color scale at the left of the figure relates to the wt% of elements in the EDS analysis images.

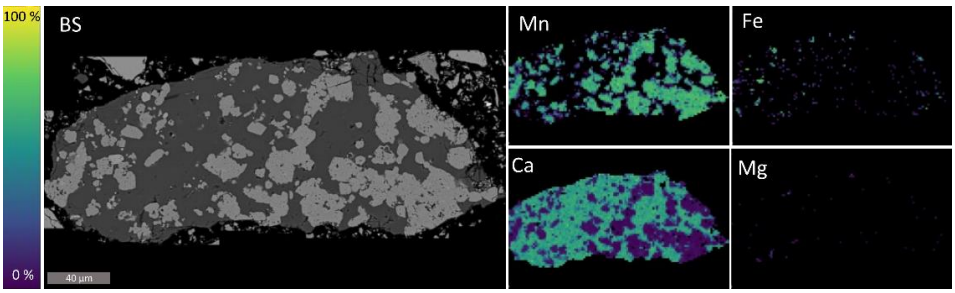

Figure 4-22: Shows the backscatter image (BS) and EDS analysis of the particle for Mn, Fe, Ca and Mg. The color scale at the left of the figure relates to the wt% of elements in the EDS analysis images.

The BS image in Figure 4-22 has a coarser but somewhat similar structure to the particle in Figure 4-19 in that there is a relatively even distribution between the bright and dark phase. The bright phase in Figure 4-22 is consistent with braunite II due to its calcium content, and the dark phase is consistent with calcite.

4.2.3 EPMA - Partly reduced ore

After reduction of Nchwaning ore, some broken ore pieces revealed a pattern that indicated topochemical reduction. A picture of such pieces, from the same particle, is shown in Figure 4-23, where the outer edge has changed color to green while the center of the particle remains grey as the initial ore. The green edge seems to have a consistent thickness, following the contours of the particle. Particle from the samples reduced for 30 minutes in CO/CO_2 gas mixtures at 700 °C and 790 °C were analyzed by EPMA to investigate this. The investigated particles were randomly selected from the particles that were intact after reduction.

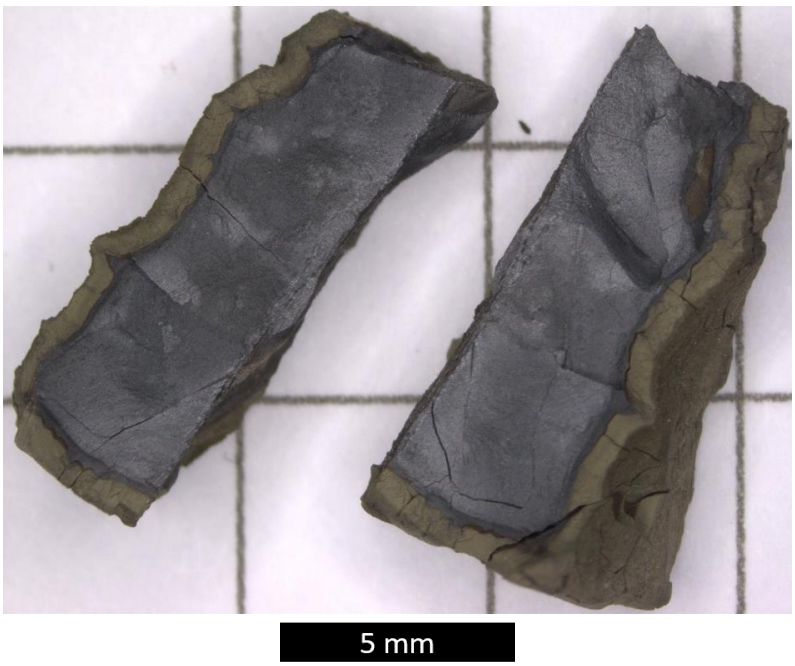

Figure 4-23: Picture of a partially reduced Nchwaning ore piece that has been broken after reduction. Reduced for 30 min at 790 °C in the high pO_2 hydrogen free atmosphere.

Figure 4-24 shows the EMPA results from a particle reduced at 790 °C in the low pO_2 hydrogen free gas. The outer edge of the particle is oriented towards the top. From the oxygen analysis (top right picture), it can be seen that the oxygen has been depleted from the edge of the particle while the oxygen content is higher towards the center. The Mn, Fe and Si contents are similar on both sides of the border between the oxygen rich and the oxygen depleted zone. This indicates that the same phase was present on both sides of the border prior to oxygen removal and that the observed difference is a result of reduction rather

than an artifact of the original mineral distribution. The increased carbon content towards the edge is caused by epoxy that fills the cracks and pores.

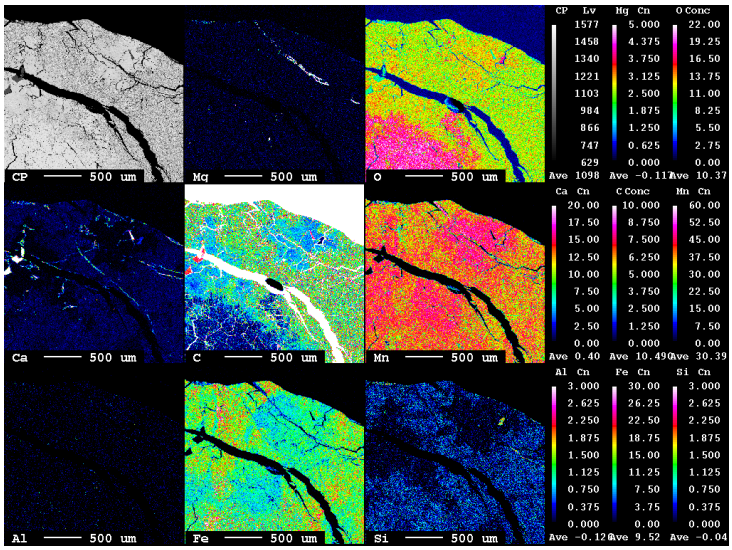

Figure 4-24: EPMA results from the sample is reduced for 30 minutes at 790 °C in the high pO_2 hydrogen free gas mixture. The edge of the particle is at the top of the images. The O/Mn ratio from the sample was 1.33 after reduction.

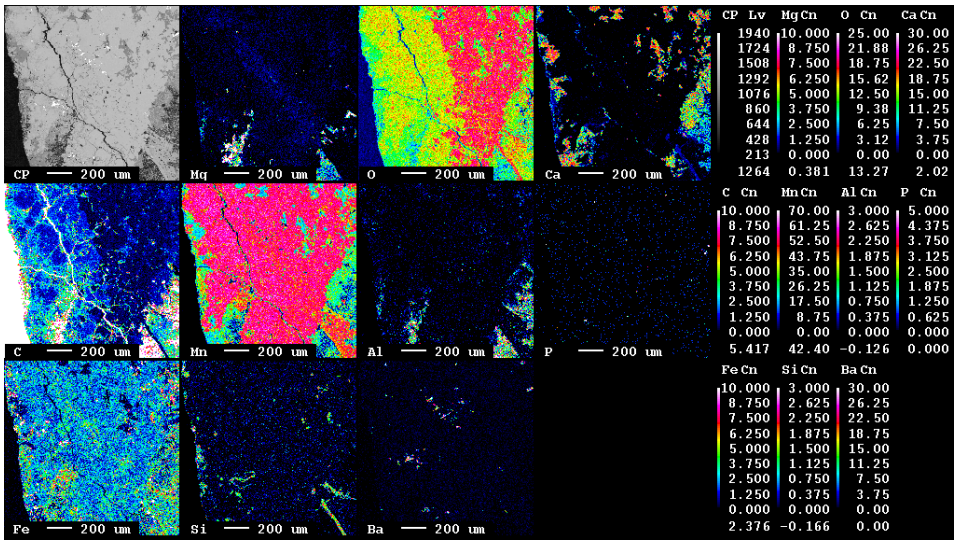

Figure 4-25: EPMA results for particle B from the sample reduced for 30 minutes at 700 °C in the high pO_2 hydrogen free gas mixture. The edge of the particle is at the left of the images. The O/Mn ratio from the sample was 1.35 after reduction. Particle A

EPMA results from two different particles from the same experiment, particle A and B, is shown in Figure 4-25 and Figure 4-26, respectively. The experiment was conducted at 700 °C in the high pO_2 hydrogen free gas mixture. Particle A is seen to display the same behavior as the particle in Figure 4-24, in that the oxygen is depleted from the edge of the particle (left hand side). The border of oxygen depletion does not correlate with significant changes in the other elements; hence, the oxygen depletion is a result of reduction. A region with lower oxygen content can be observed at the lower right-hand side of the image. This region has a high content of Ca, Al and Mg which explains the relatively lower oxygen content. Particle B shows no such oxygen depleted zone. The pixel wide line at the edge for the oxygen measurement stems from the measurement itself; the analysis from the pixel on the edge shows part sample and part epoxy and can also be observed in the carbon analysis. The particle is seen to have a rather consistent structure, with some pockets of carbonates. The absence of an oxygen depleted zone indicates that oxygen is released evenly throughout the particle, or that the particle is not reacting at all. Particle B is seen to have a higher Ca and Si content throughout the structure compared to particle A and the particle in Figure 4-24. Hence, whether or not a particle displays topochemical behavior during reduction depends on which particle is reduced and both behaviors can be expressed in different particles in the same experiment.

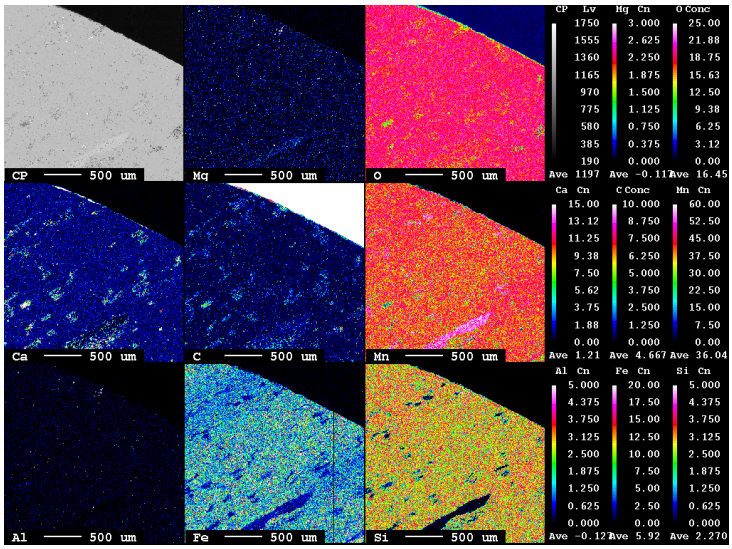

Figure 4-26: EPMA results for particle B from the sample reduced for 30 minutes at 700 °C in the high pO_2 hydrogen free gas mixture. The edge of the particle is at the top of the images. The O/Mn ratio from the sample was 1.35 after reduction.

4.2.4 Decrepitation

Multiple sieve sizes were used to determine the decrepitation behavior of Nchwaning ore, and the full dataset is given in Appendix E. Similar behavior was observed for most of the different particle size fractions. To assess the decrepitation behavior, the weight fraction of particles above 3.35 mm was used. Figure 4-27(a) shows the decrepitation as a function of temperature for the Nchwaning ore samples reduced for 210 minutes. No particular trend is identified between the different gas mixtures; however, it is seen that decrepitation increases with increasing temperature.

Figure 4-27(b) Shows the decrepitation as a function of O/Mn ratio after reduction for the Nchwaning experiments. Samples reduced for 30, 90 and 210 minutes are included. The decrepitation is seen to increases with increasing degree of reduction (reduced O/Mn ratio), which is expected since the temperature and degree of reduction also are correlated (section 4.1.1).

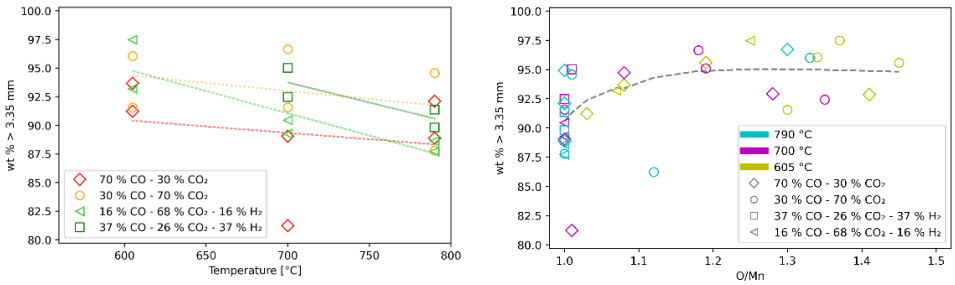

(a) (b)

Figure 4-27: Shows the decrepitation as wt% above 3.35 mm from samples reduced for 210 minutes in different gas mixtures as a function of (a): temperature, where trendlines were added for each gas mixture, and (b) of O/Mn ratio after reduction. The O/Mn ratios were determined by chemical analysis. The trendline was made using a Lowess filter with a smoothing parameter of 0.6.

4.3 Reduction of Comilog ore

Reduction of Comilog ore was investigated in the pairs of gas mixtures used for the Nchwaning experiments in addition to a gas mixture pair with an intermediate pO_2. The composition of the utilized gas mixtures can be seen in Table 4-3. As previously mentioned, Comilog ore was mixed with an equal amount of quartz (by weight) to suppress the exothermal effect on temperature. Samples were reduced in the temperature range 365 °C - 605 °C. The ore was observed to oxidize after being removed from the crucible, hence the samples were not sent for chemical analysis. A method was devised to measure oxidation and it was measured for more than half the Comilog experiments. Carbon deposition was observed in two experiments conducted with hydrogen containing gas mixtures at low and medium pO_2.

Table 4-3: The gas mixtures used in reduction of Comilog ore where the pairs of mixtures yield a high, medium, and low oxygen partial pressure, respectively. The logarithm of the partial pressures at 650 °C was included for reference.

pO_2	$\log(pO_2)$ | 650 °C	CO	CO_2	H_2
High	-22.1	30	70	0
		16	68	16
Medium	-22.9	50	50	0
		27	46	27
Low	-23.6	70	30	0
		37	26	37

4.3.1 Weight loss and reduction behavior

Figure 4-28 shows the measured weight loss from the furnace balance for the Comilog experiments. The horizontal dashed lines indicate different points of theoretical weight loss which is marked on the right-hand side of the figure. H_2O refers to evaporation of bound water, while the Mn_yO_x-Fe_yO_x indicate the theoretical average composition of the Mn and Fe oxides at the specific weight.

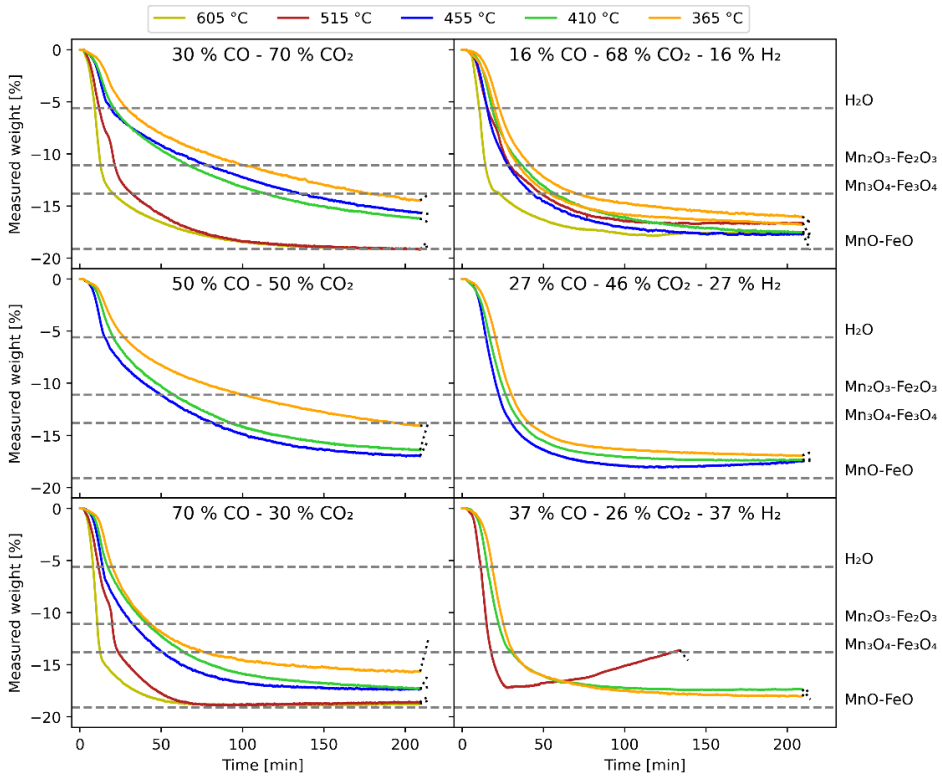

Figure 4-28: Shows the measured weight loss from the furnace balance as a function of time for the Comilog experiments in different gas mixtures. The dotted lines at the end of each experimental curve connects the final weight measured by the furnace balance and that measured on the external balance. Dashed lines indicate the contributions where the lines marked H_2O indicates the weight loss to the point where all bound water has evaporated. The other dashed lines indicate the weight loss corresponding to when the average composition of the ore has reached Mn_2O_3-Fe_2O_3, Mn_3O_4-Fe_3O_4 and MnO-FeO in addition to the evaporation of water.

It is seen that all samples have achieved a weight loss consistent with reduction to Mn_3O_4-Fe_3O_4 or below and that a higher weight loss was reached in most of the experiments conducted at 605 °C and 515 °C. The dotted line at the end of each experimental curve ends at the measured weight loss from the external balance and it can be seen that the samples reduced in the CO/CO_2 atmospheres has a larger deviation between the furnace weight and external weight compared to the samples reduced in the hydrogen containing gas mixtures. This is consistent with the observation of higher reoxidation in the CO/CO_2 experiments compared to the experiments in H_2 containing gases (section 4.3.6). The sample reduced in 37 %CO – 26 % CO_2 – 37 % H_2 lost weight for approximately 25 minutes before the weight started to increase. After termination of the

experiment, it was discovered visually, that the source of the increased weight was carbon deposition.

4.3.2 Reduction behavior of Comilog at 605 °C and 515 °C

In the initial experiments on Comilog ore at 605 °C and 515 °C, a high reduction rate and an exothermal peak was observed (section 2.4.2). This is shown in Figure 4-29, where the weight loss, CO in the off gas and measured temperature is plotted as a function of time for the experiments conducted at 605 °C and 515 °C in the 70 % CO – 30 % CO_2 atmosphere.

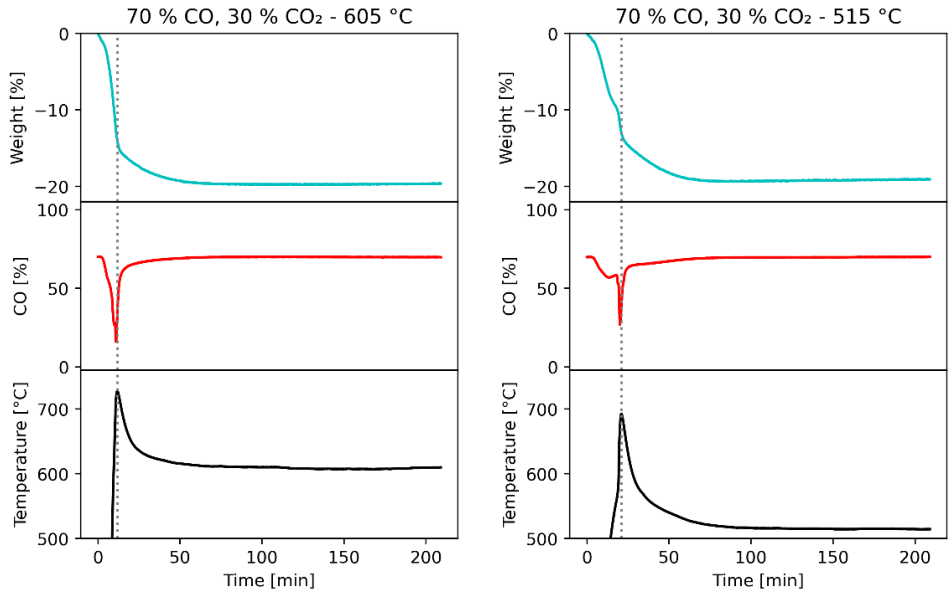

Figure 4-29: Shows the measured weight, CO in the off-gas and temperature from the experiments using low pO_2 without hydrogen at (a): at 605 °C and (b) at 515 °C. The vertical dotted line indicates the point where the highest temperature is reached.

It can be seen that a high reduction rate and high consumption of CO results in an exothermal peak. After the peak temperature was reached, there was an abrupt change in the reduction rate, coinciding with the normalization of the temperature and the CO content in the off-gas. In the 70 % CO – 30 % CO_2 gas mixture at 605 °C (Figure 4-29a), the peak temperature was 728 °C whereas the minimum CO content measured in the off-gas was 16 %. In the 30 % CO – 70 % CO_2 experiment at 605 °C, the peak temperature was 697 °C while the CO in the off-gas reached a minimum of 5.6 %. Much of the reduction had thus occurred at gas compositions and temperatures far from the intended parameters. Similar observations were made at 515 °C (Figure 4-29b).

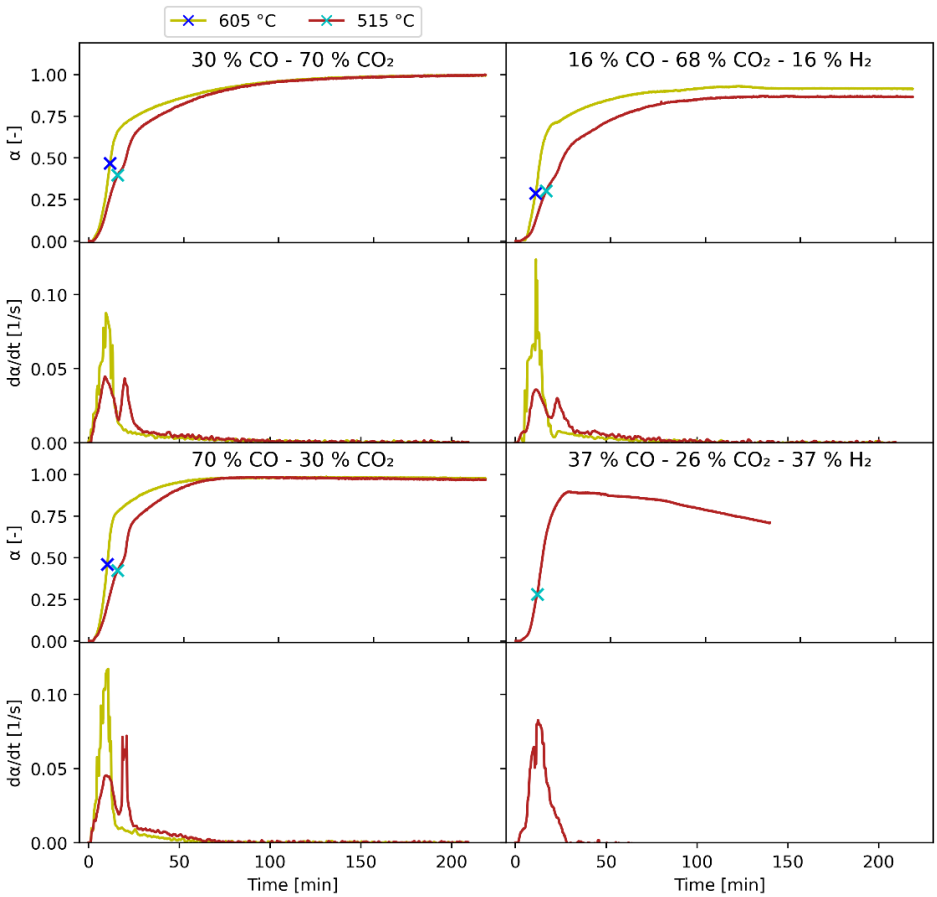

Figure 4-30: Shows the fractional conversion and the reduction rate for reduction of Comilog ore at 605 °C and 515 °C. Markings (x) in contrasting colors indicate where the sample temperature reaches the set temperature (set temperature in legend). The oxygen partial pressures correspond to the High and Low pO_2 (Table 4-3).

Figure 4-30 shows the fractional conversion and the reduction rate of the Comilog ore samples reduced at 605 °C and 515 °C as a function of time. Each conversion curve has been marked at the point where the sample temperature reached the set temperature. It can be seen that the degree of conversion in these experiments is around 0.25-0.50 at the point where the sample reaches the set temperature. However, as exemplified in Figure 4-29, a significant overshoot of the set temperature was observed. For reference, α=0.59 corresponds to the evaporation of all bound water in addition to reduction of all MnO_2 to Mn_2O_3 (Table 3-4). The highest reduction rates are observed in the samples reduced at 605 °C, whereas at 515 °C there is a double peak where the second peak is associated with the high temperature increase (Figure 4-29b).

4.3.3 Off-gas analysis for Comilog at 605 °C and 515 °C

The measured off-gas was calibrated in the same way as for Nchwaning ore (details in Appendix D). It is expected that bound water is released in the early stages of the experiment, however this cannot be observed directly in the off-gas analysis since water is condensed prior to the off-gas analyzer.

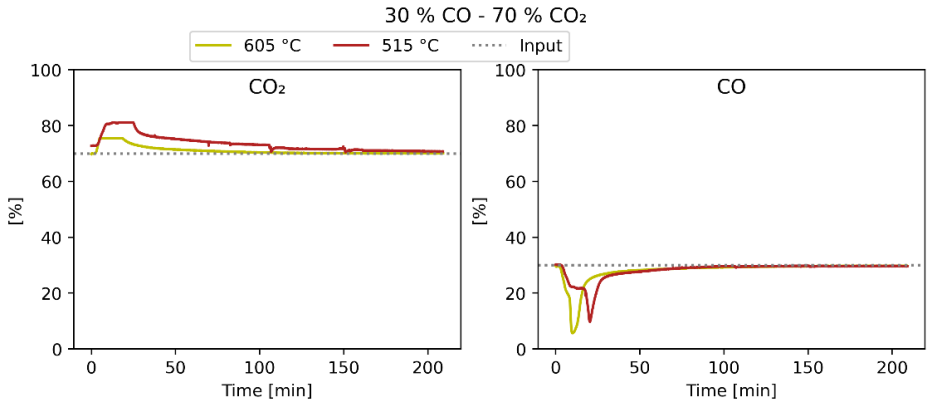

Figure 4-31: Shows the measured CO_2 and CO from the off-gas during reduction of Comilog ore in the high pO_2 hydrogen free gas mixture.

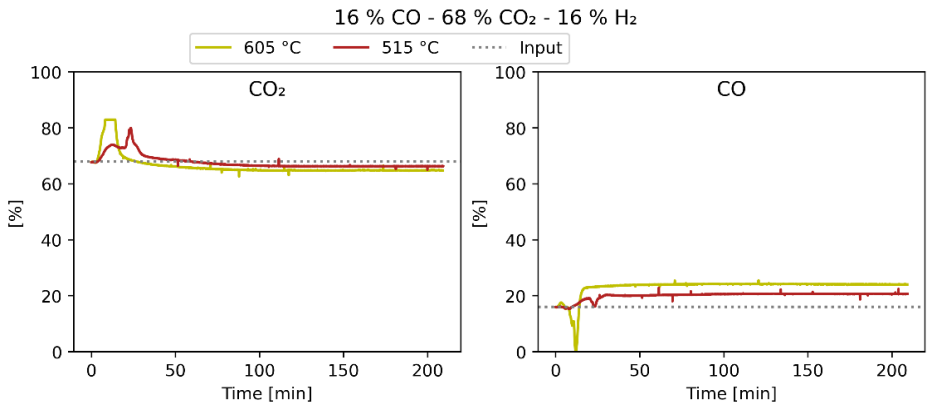

Figure 4-32: Shows the measured CO_2 and CO from the off-gas during reduction of Comilog ore in the high pO_2 hydrogen containing gas mixture.

The off-gas measurements from the high pO_2 hydrogen free and hydrogen containing gas mixture are shown in Figure 4-31 and Figure 4-32, respectively. There were problems with the CO_2 analysis in the 30 % CO – 70 % CO_2 experiment conducted at 515 °C (Figure 4-31), causing erroneous values for the most part of the experiment. During the rapid reduction stage in the high pO_2 gas mixtures, the CO_2 content exceeded the capacity of the analyzer on several occasions (Figure 4-31 and Figure 4-32). The difference plateau values of the maximum limit of CO_2 is

partly due to that the calibration of the off-gas analyzer drifts to different absolute values over time. In the 605 °C experiment in Figure 4-31, a software error caused the cutoff value from the off-gas analyzer to be further decreased.

In the hydrogen free high pO_2 gas mixture (Figure 4-31), the CO and CO_2 approaches the input concentration towards the end of the experiment. The reduction starts rapidly at the initial stages of the experiments and decelerates until the point where the exothermal reactions cause a temperature and reduction rate peak. A similar behavior can be observed from the CO_2 analysis of the high pO_2 hydrogen containing gas mixture (Figure 4-32) at 515 °C. However, it is seen that the CO concentration is higher than the input composition for a major part of the experiments, indicating that the water gas shift reaction (WGSR: $CO+H_2O=CO_2+H_2$) is shifted to the left.

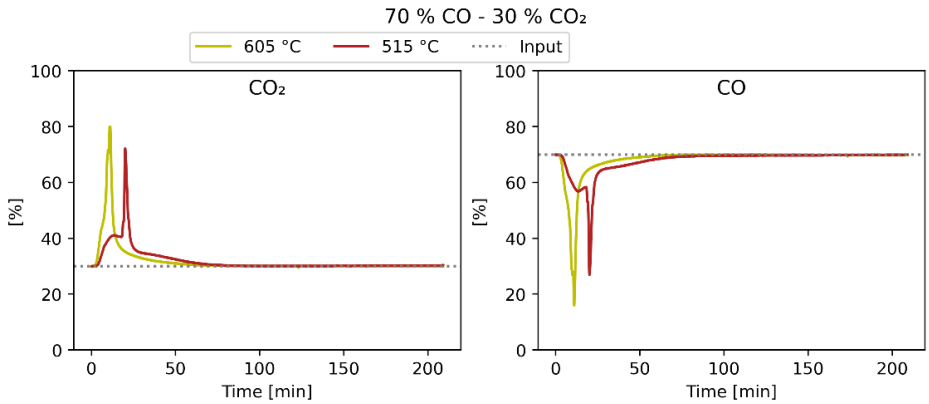

Figure 4-33: Shows the measured CO_2 and CO from the off-gas during reduction of Comilog ore in the low pO_2 hydrogen free gas mixture.

Figure 4-33 and Figure 4-34 shows the off-gas analysis for the low pO_2 gas mixtures. CO and CO_2 in the hydrogen free gas mixture (Figure 4-33) display similar but opposite behavior and stabilizes at the input composition after approximately 90 minutes, i.e. no more reduction occurs, which is consistent with the observations based on the weight loss (Figure 4-30). In the hydrogen containing gas mixture (Figure 4-34), CO is seen to stabilize at a higher level compared to the input composition whereas CO_2 stabilizes close to the input composition, i.e. the CO_2 content is higher than expected when considering the increased CO content, which is consistent with carbon deposition by the Boudouard reaction ($2CO=C+CO_2$). Carbon deposition was observed in this experiment.

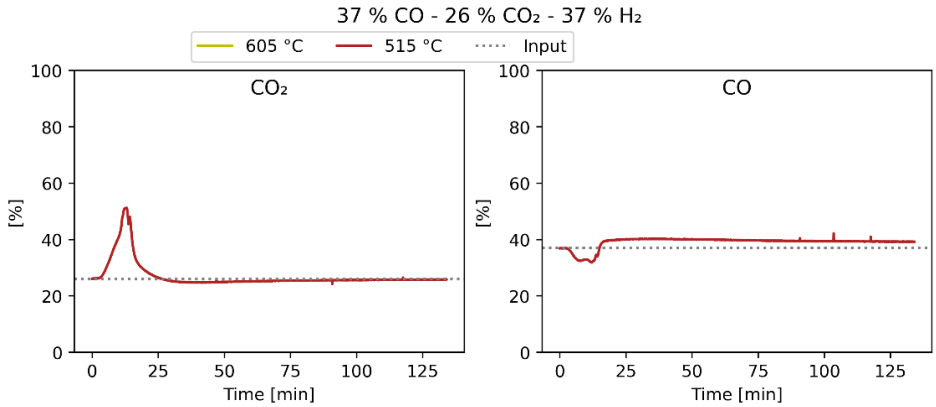

Figure 4-34: Shows the measured CO_2 and CO from the off-gas during reduction of Comilog ore in the low pO_2 hydrogen containing gas mixture.

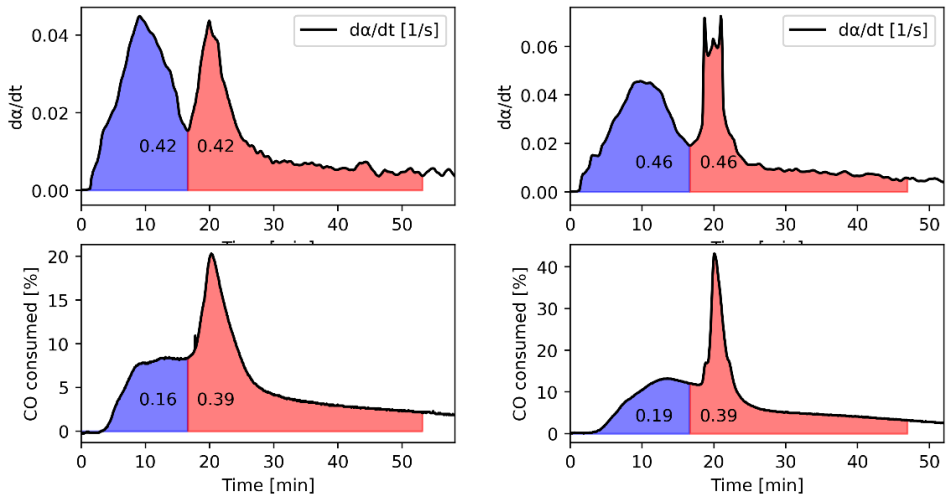

Figure 4-35: Shows reduction rate (top) based on weight measurements and the reduction rate based on the consumed CO (bottom) from the first ~ 50 minutes of reduction from Comilog ore reduced at 515 °C in (a) 30 % CO – 70 % CO_2 and (b) 70 % CO – 30 % CO_2 gas mixture. The blue and red fields are separated at the minimum reduction rate between the peaks in the reduction rate curve. The numbers are the contribution to the total degree of reduction by integrating the separate fields.

For the CO/CO_2 experiments, the consumption of CO is proportional to the reduction rate of oxides. At 515 °C, it can be seen that the consumed CO in Figure 4-31 and the reduction rate in Figure 4-30 behave differently in the initial part of the experiment. The reduction rate displays two peaks with similar intensity, whereas the consumed CO show one small and one large peak. In Figure 4-35, the reduction rate and the consumed CO has been plotted for the initial stages of the (a) high and (b) low pO_2 CO/CO_2 experiments at 515 °C. The second filled area in

the reduction rate curves is selected to have an equal area to the first peak. The corresponding degree of reduction for each part is calculated by integration and is shown by the numbers on figure. The total conversion from the consumed CO is assessed by comparing it to the consumed CO for the whole experiment and removing the contribution from water evaporation. The difference between the contribution to the degree of reduction between the rate and the consumed CO for the first peak in both gas mixtures is 0.26-0.27 which is close to the expected value from decomposition of bound water (=0.26, Table 3-4). Hence, most of the water is evaporated in the first reduction rate peak, and the exothermal second peak initiates when there is no bound water left in the sample.

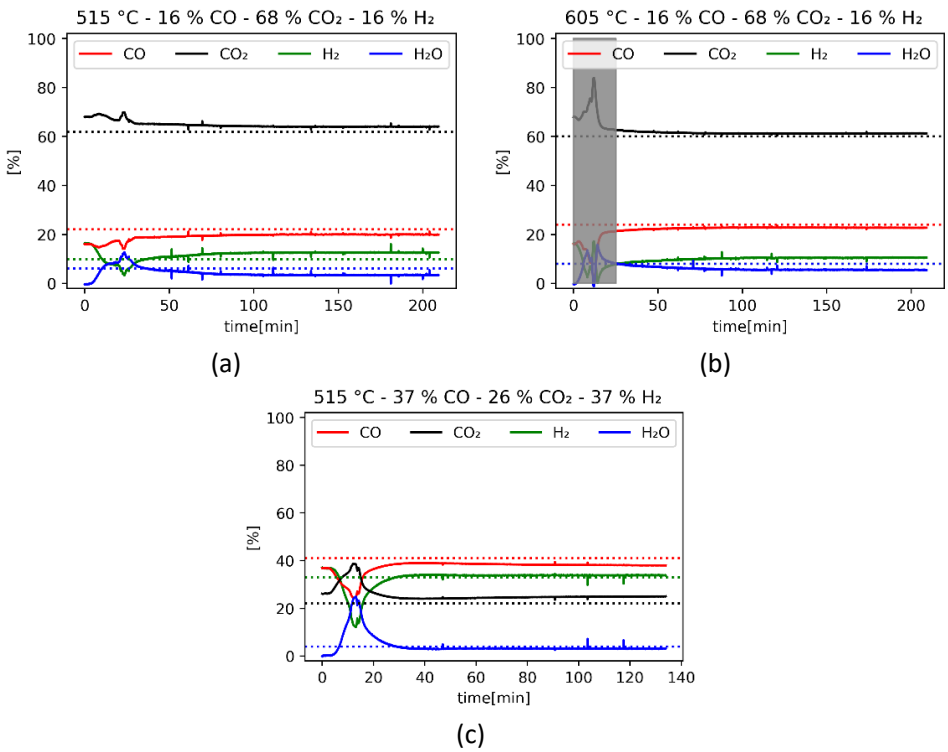

Figure 4-36: Shows the adjusted CO, CO_2 and H_2 composition with the calculated H_2O composition for the off-gas in the hydrogen containing gas mixtures at 515 °C and 605 °C. The shaded area in (b) is to indicate the area of where the CO_2 content exceeded the capacity of the off-gas analyzer. (c): Carbon deposition was observed in the experiment. Dotted lines show the equilibrium composition of each gas mixture at the given temperature. Equilibrium gas compositions are calculated using HSC chemistry 9[18]. The equilibrium partial pressure of H_2 and H_2O are nearly identical (=8.0) in the 16 % CO – 68 % CO_2 – 16 % H_2 gas mixture at 605 °C.

Figure 4-36 shows the calculated off gas composition from the experiments run in hydrogen containing gas mixtures at 515 °C and 605 °C. Similar to the calculations on the Nchwaning ore experiments, the hydrogen content of

the off gas is taken as the remainder up to 100 % from the off-gas analyzer and the H_2O content is calculated by assuming that the sum of CO and CO_2 entering and exiting the crucible is constant. In the high pO_2 experiment at 515 °C (Figure 4-36a) it can be seen that CO is consumed at the start of the experiment and at the peak corresponding to the exothermal peak (~ 20 min) where also significant amounts of H_2 is consumed. In the remainder of the experiment, the concentration of the components in the gas stabilizes between the input composition and the equilibrium composition of the WGSR. In the high pO_2 experiment at 605 °C (Figure 4-36b) it seems to be a discrepancy between the relative distance from equilibrium comparing the carbon containing gases and the hydrogen containing gases. However, this may simply be caused by the known error in the CO gas analysis in this experiment.

In the low pO_2 experiment at 515 °C (Figure 4-36c), both CO and H_2 are consumed in the initial part of the experiment to produce CO_2 and H_2O. Carbon deposition was observed in this experiment after most of the reduction had taken place (Figure 4-30). From the off-gas analysis it is seen that the H_2 and H_2O is close to the equilibrium composition determined by the WGSR while the CO and CO_2 composition is further away. This may be explained by the combination of the WGSR ($CO+H_2O=CO_2+H_2$) and the reverse Boudouard reaction ($2CO=C+CO_2$). When the reverse Boudouard reaction occurs, CO is consumed, and CO_2 is produced which causes the WGSR to be shifted further to the left. More H_2 is consumed, and more H_2O is produced, as seen in Figure 4-36c, while the CO content is lower, and the CO_2 content is higher than what would be expected from the occurrence of the WGSR alone.

Based on the gas composition at the end of experiments, it is seen that the WGSR is active but not at equilibrium. These experiments describe the behavior of the ore at 605 °C and 515 °C under these conditions, however it was decided to continue further investigations at lower temperatures to get higher resolution data and to avoid the exothermal peak.

4.3.4 Reduction behavior of Comilog at 455 °C, 410 °C and 365 °C

During reduction at 455 °C, 410 °C and 365 °C, the exothermal reactions increase the temperature compared to the set temperature, though the large accelerating CO consumption and temperature spike observed at higher temperatures (i.e., Figure 4-29), was avoided. Figure 4-37 shows the measured weight, CO and temperature from the hydrogen free experiments at 455 °C. It can be seen that the highest consumption of CO and the highest reduction rate occurs prior to the peak temperature for both gas mixtures, thus the changes are caused by the reduction behavior of the ore itself, rather than the increased temperature.

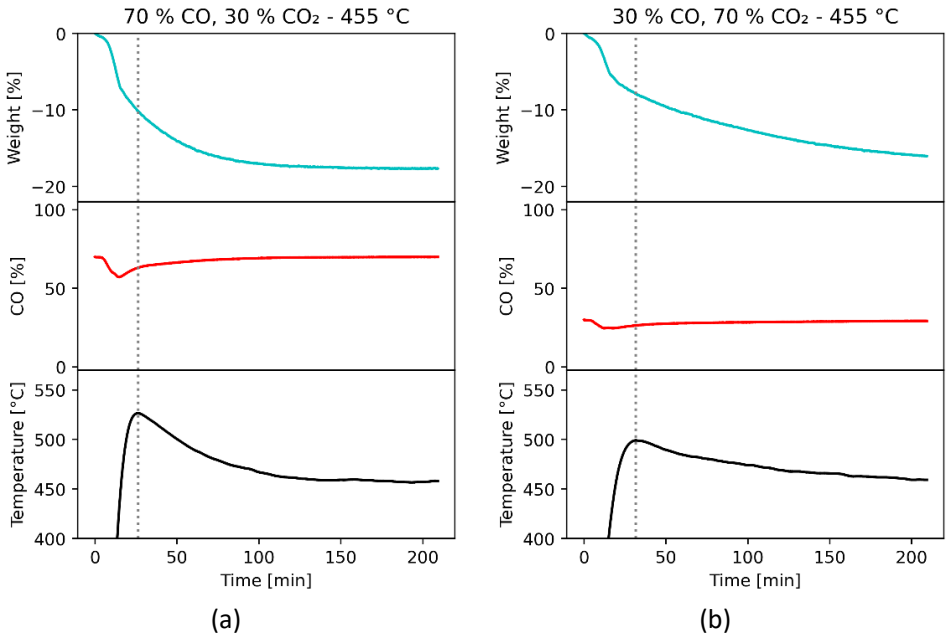

Figure 4-37: Shows the measured weight, CO in the off-gas and measured temperature from experiments conducted at 455 °C, at (a): low pO_2 and (b): high pO_2. The vertical dotted line indicates where the highest temperature has been reached.

The fractional conversion and reduction rate of the Comilog samples reduced in the different gas mixtures at 455 °C, 410 °C and 365 °C, is shown in Figure 4-38. The marks (x) on the curves indicate where the sample reaches the set temperature. The samples reduced at 410 °C and 455 °C show a similar extent of reduction, as do the samples reduced at 410 °C and 365 °C in the 37 %CO – 26 % CO_2 – 37 % H_2 gas mixture. The reduction rate is seen to increase with increasing temperature for all gas mixtures. Carbon deposition was observed in the 27 % CO – 46 % CO_2 – 27 % H_2 experiment at 455 °C, which correlates with the decrease in fractional conversion at the end of the experiment.

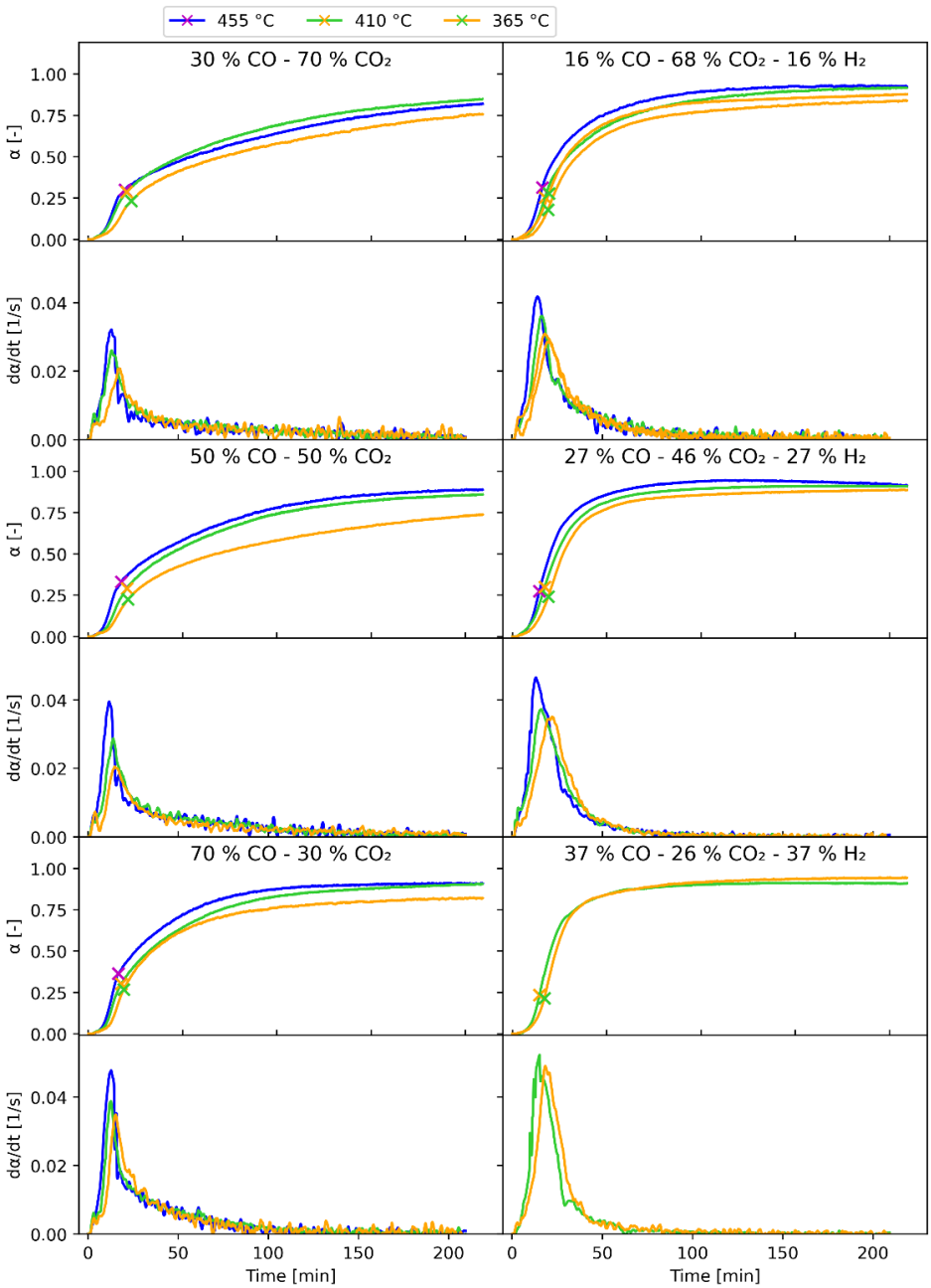

Figure 4-38: The fractional conversion and the reduction rate for Comilog ore reduced at 365 °C, 410 °C and 455 °C in different gas mixtures. Markings (x) in contrasting colors indicate the point where the sample temperature reaches the set temperature (temperature in the legend). pO_2 decreases when moving down in the figure (low, medium and high pO_2, Table 4-3)

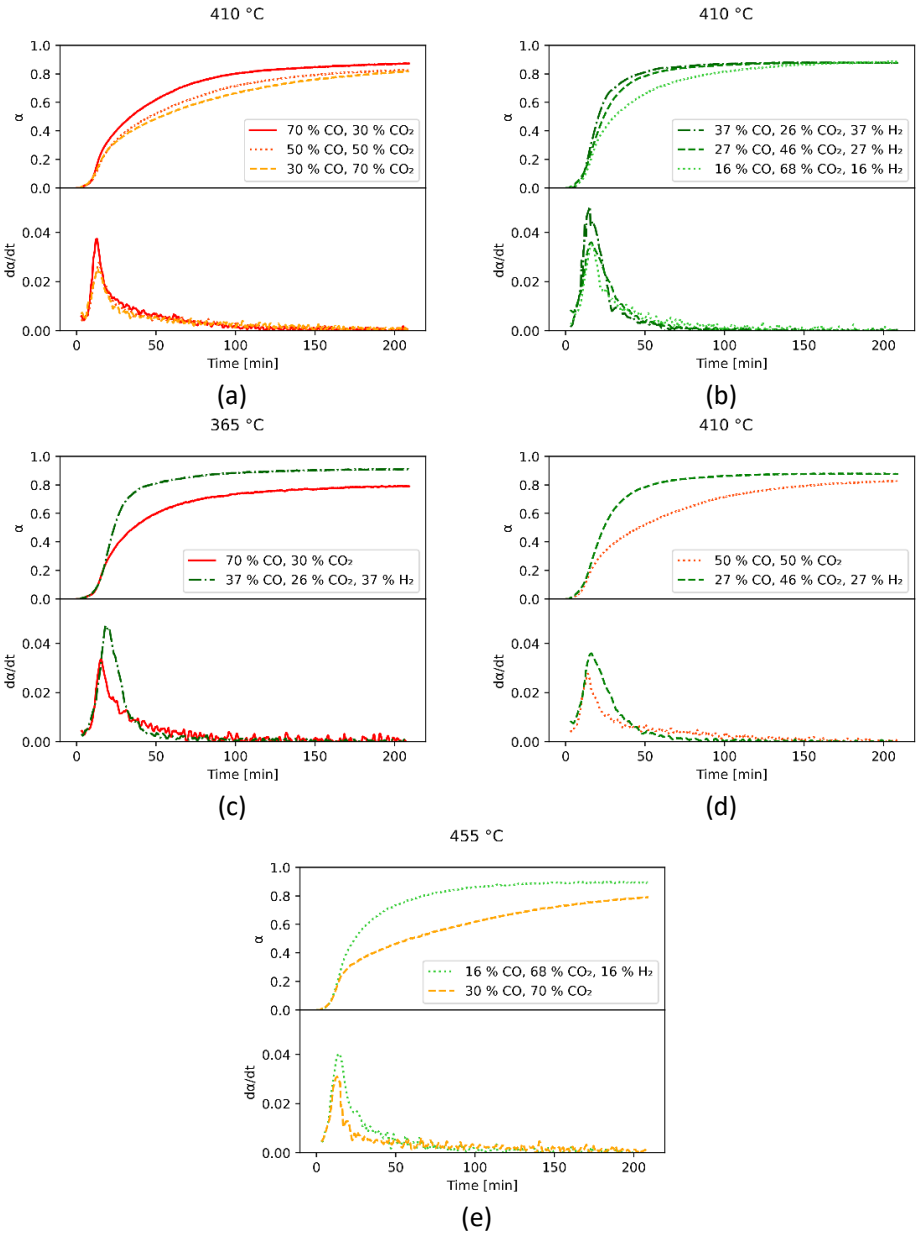

Figure 4-39: shows the fractional conversion curves for selected experiments; (a) - hydrogen free gas mixtures at 410 °C, (b) - hydrogen containing gas mixtures at 410 °C, (c) - low pO_2 at 365 °C, (d) – medium pO_2 at 410 °C, (e) - high pO_2 at 455 °C.

Figure 4-39 shows conversion curves and reduction rates for selected samples. The reduction rate increase with decreasing pO_2 in the hydrogen free (Figure 4-39a) and in the hydrogen containing (Figure 4-39b) gas mixtures. The reduction rate and the reduction extent increases with addition of hydrogen at

constant pO_2 for low (Figure 4-39c), medium (Figure 4-39d) and high (Figure 4-39e) pO_2, however it is seen that up to a conversion of approximately 0.2 the reduction rate (and the degree of conversion) are equal for the hydrogen containing and hydrogen free parallels at the same temperature.

4.3.5 Off-gas analysis for Comilog at 455 °C, 410 °C and 365 °C

The measured off-gas was corrected in the same way as for the 605-515 °C Comilog ore experiments and Nchwaning ore experiments (details in Appendix D).

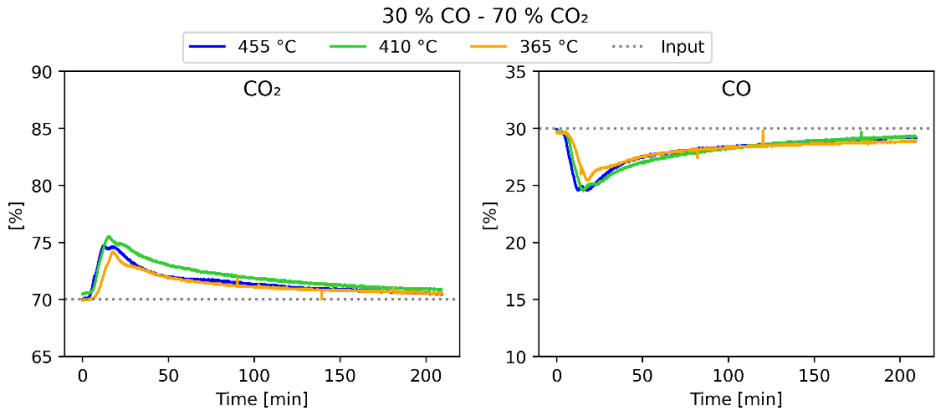

Figure 4-40: Corrected CO and CO_2 off-gas content from the experiments conducted in high pO_2 hydrogen free atmospheres.

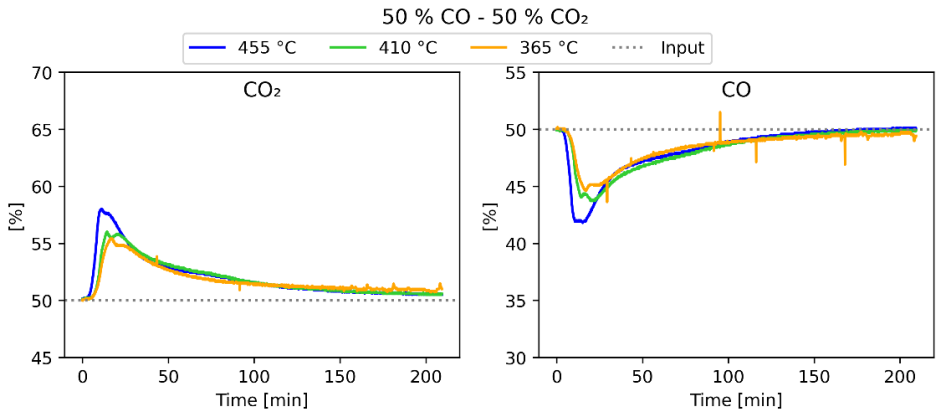

Figure 4-41: Corrected CO and CO_2 off-gas content from the experiments conducted in medium pO_2 hydrogen free atmospheres.

Figure 4-40, Figure 4-41 and Figure 4-42 shows the corrected CO and CO_2 off gas concentration from the hydrogen free experiments at high, medium, and low pO_2, respectively. The CO and CO_2 curves are seen to behave similarly but

opposite of each other, which is consistent with CO being consumed in the reduction of the oxides to produce CO_2. The high consumption of CO as a result of the rapid reduction stage at higher temperatures (i.e., Figure 4-33) is not observed in this temperature range. The measured off-gas composition is within ±10 percentage points of the input composition for all experiments, with one exception (70 % CO – 30 % CO_2, 455 °C). It is seen that the consumed CO (and produced CO_2) increases with decreasing oxygen partial pressure and with increasing temperature, which is consistent with the observations from the weight loss behavior.

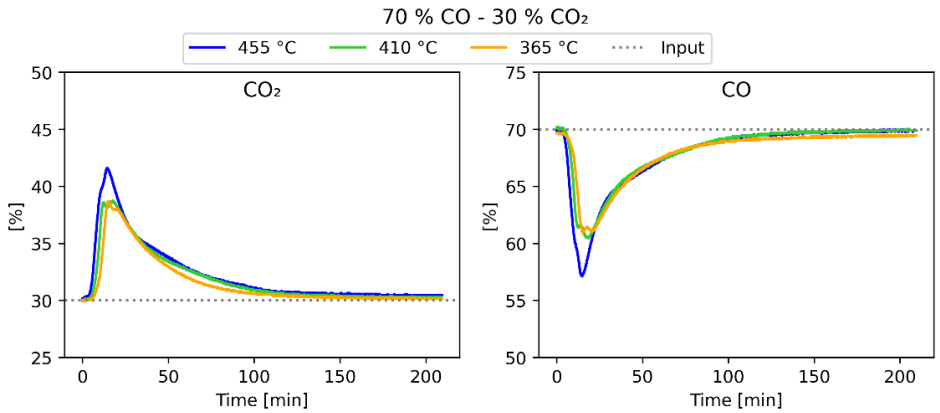

Figure 4-42: The corrected CO and CO_2 concentration in the off-gas from the hydrogen free experiments at different pO_2.

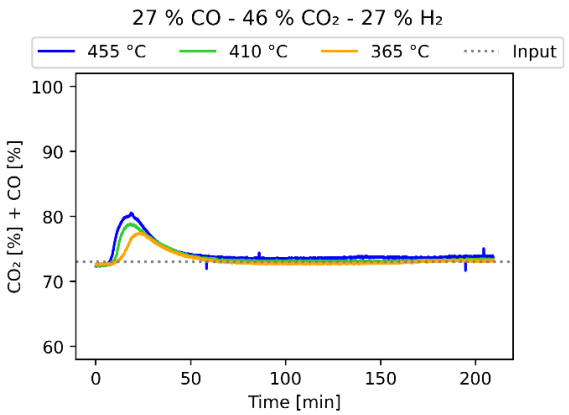

Figure 4-43: The sum of CO and CO_2 from the off-gas analysis of the medium pO_2 hydrogen containing experiments.

Figure 4-43 shows the sum of the analyzed CO and CO_2 from the medium pO_2 hydrogen containing experiments. Similar to the observation from Nchwaning

ore, the sum of CO and CO_2 exiting the crucible is higher than the input amounts for the early stages of the experiments. As explained previously, this is caused by condensation of the water content of the off-gas, effectively concentrating the remaining species.

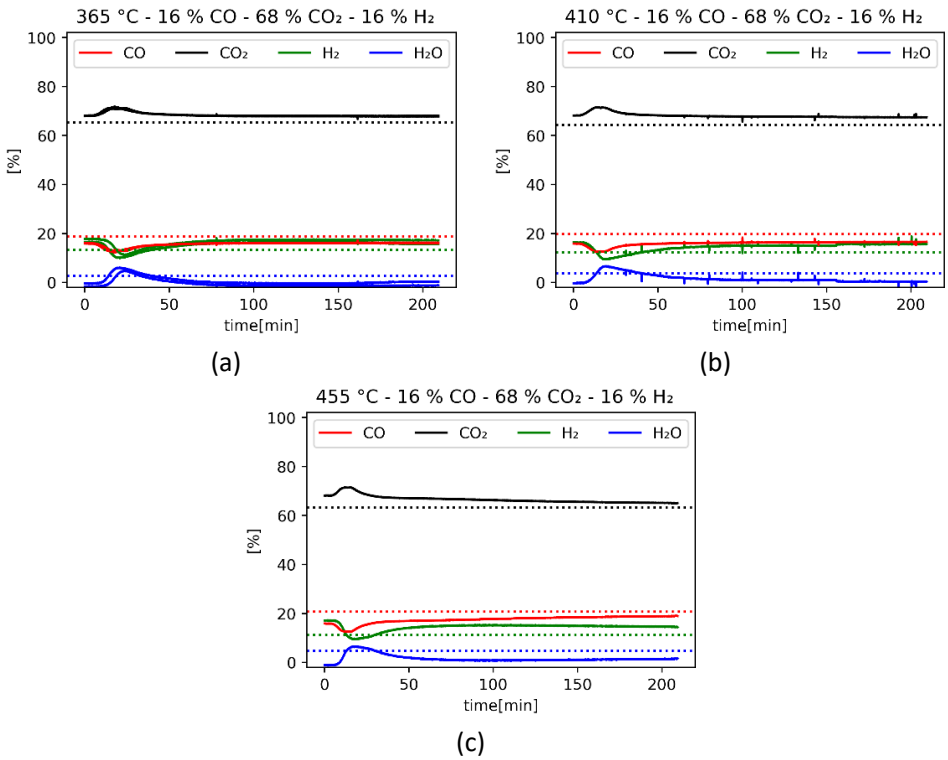

Figure 4-44: Shows the adjusted CO, CO_2 and H_2 composition with the calculated H_2O composition from the high pO_2 hydrogen containing experiments. Dotted lines show the equilibrium composition (calculated by HSC chemistry 9[18]) of the gas mixtures at each temperature and gas mixture.

In Figure 4-44 and Figure 4-45, the adjusted CO, CO_2 and H_2 content and the calculated H_2O content are shown as a function of time for the high and medium pO_2 experiments, respectively. In the initial part of the experiments where reduction occurs, it is seen that CO and H_2 is consumed, while CO_2 and H_2O is produced. At the end of the 365 °C experiments, the off-gas composition is seen to stabilize at a similar level to the input composition. Hence, the rate of the WGSR is low, or it is not occurring at all at this temperature. At the 410 °C and 455 °C, it can be seen that the off-gas composition at the end of the experiments is shifted toward the equilibrium composition established by the WGSR, hence, the WGSR is occurring but is not at equilibrium. Figure 4-46 shows the gas composition from the low pO_2 experiments, where it is seen that the input composition is close to the equilibrium composition of the WGSR for both temperatures.

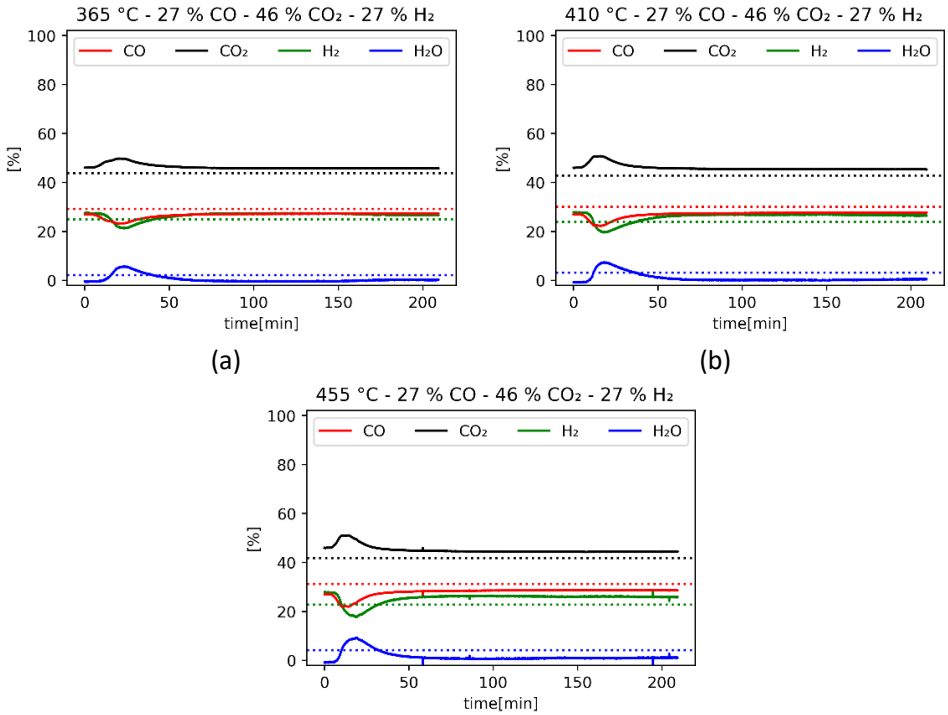

Figure 4-45: Shows the adjusted CO, CO_2 and H_2 composition with the calculated H_2O composition from the medium pO_2 hydrogen containing experiments. Dotted lines show the equilibrium composition (calculated by HSC chemistry 9[18]) of the gas mixtures at each temperature and gas mixture.

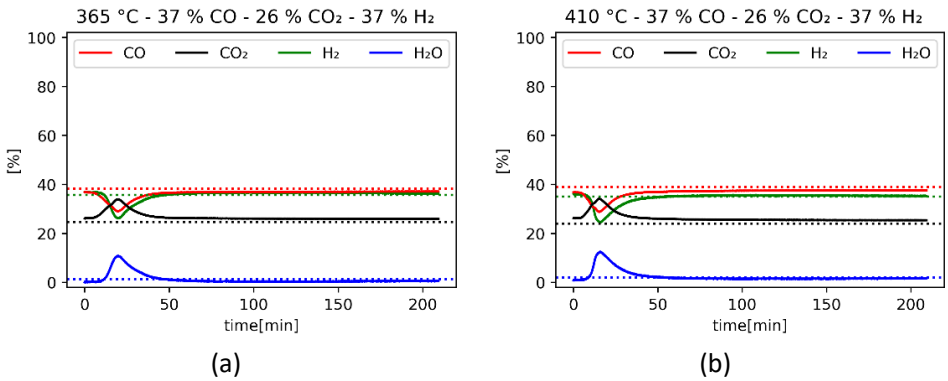

Figure 4-46: Shows the adjusted CO, CO_2 and H_2 composition with the calculated H_2O composition from the low pO_2 hydrogen containing experiments. Dotted lines show the equilibrium composition (calculated by HSC chemistry 9[18]) of the gas mixtures at each temperature and gas mixture.

4.3.6 Reoxidation after reduction

The oxidation after the experiments was measured after the reduced samples had cooled to below 25 °C in flowing Ar gas. Following the introduction of synthetic air, an increased temperature and weight was observed. Figure 4-47 shows an example of such measurement. There is a weight loss of 0.41 g (Figure A-4) associated with the introduction of synthetic air due to its lower density compared to Ar. Compensating for this weight loss, it is seen that the weight and the temperature starts to increase immediately after introducing the synthetic air. The measured oxidation, compensated for the gas density differences, are given in Table 4-4. A duplicate was measured on the high pO_2 hydrogen containing parallel, where the difference between the two duplicates were less than 0.35 %.

Table 4-4: Shows the measured oxidation in wt% of the initial sample weight for the samples reduces at high, medium and low partial pressures with and without H_2 in the reducing atmosphere.

pO_2	***High***		***Medium***		***Low***	
T [°C]	*CO/CO_2*	*w/H_2*	*CO/CO_2*	*w/H_2*	*CO/CO_2*	*w/H_2*
365	1.05	0.54*	1.46	0.65	3.83	1.01
410	-	-	2.99	0.49	-	-
455	1.40	-	2.89	0.41	2.78	-

*Two measurements within ±0.002 wt%

- = not analyzed

The reoxidation is seen to be higher for the samples reduced without H_2 in the gas mixture and it increase with decreasing pO_2 with one exception; The samples reduced in the CO/CO_2 gas mixture at 455 °C shows a slight decrease in oxidation from medium to low pO_2.

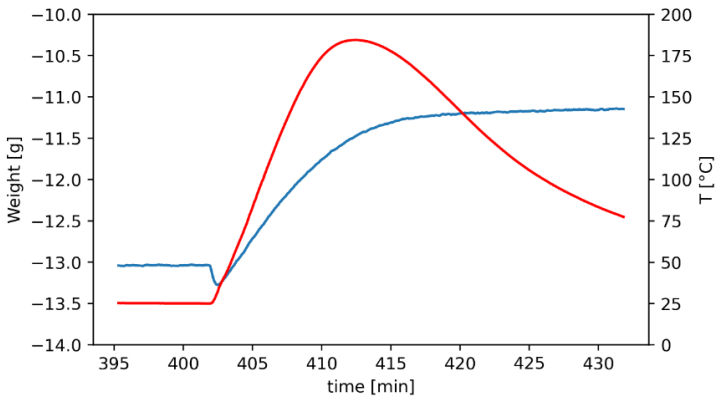

Figure 4-47: Example from the measured reoxidation of the sample reduced using with medium pO_2 at 410 °C in the hydrogen free gas mixture. Developed temperature in red and measured weight in blue.

4.4 Characterization of Comilog

The unreduced Comilog ore was investigated using quantitative mineralogy analysis (AMS). The content of different minerals was quantified, and selected microstructures were investigated. Additional data from AMS can be found in Appendix F. Selected lumps from the reduced Comilog ore were analyzed by µCT

4.4.1 AMS - Unreduced ore

Various minerals were identified using the chemical composition acquired by Energy-dispersive spectroscopy (EDS) measurements. Two different areas of the sample were investigated covering a total of 33.7 mm^2 and a few thousand different particles. Table 4-5 shows the content of different minerals in the sample. It is seen that MnO_2 – type oxides are most predominant. The most predominant gangue mineral in Comilog is quartz. Since hydrogen is undetectable, pyrolusite and nsutite are classified as the same mineral, as are hematite and goethite. Some of the phases in the microstructure of Comilog ore are finely intergrown, hence there are some uncertainties regarding the quantification of the phases since measurement on parts of the microstructure may include several minerals. In the case of bixbyite, the Mn/Fe ratio was close to 1 for about 50 % of the phase, which may indicate intergrown iron and manganese oxides. Bixbyite is not commonly found in Comilog ore[73,90].

Table 4-5: Shows the abundance of different minerals in Comilog ore. Includes the minerals with more than 5 wt% of the sample in addition to hematite and quartz. The range in composition is given by the difference between the analysis of two different areas in the sample.

Mineral	**Formula**	**Area%**	**Wt%*****
Nsutite, Pyrolusite	$Mn(O,OH)_2$, MnO_2	63-64	71-72
Lithiophorite	$(Al,Li)MnO_2(OH)_2$	10-11	10-10
*Bixbyite**	$(Mn,Fe)_2O_3$	5-7	6-8
Cryptomelane	KMn_8O_{16}	5-8	5-8
*Hematite***	Fe_2O_3	2.4-2.5	2.4-2.4
Quartz	SiO_2	1.2-3.6	0.7-2.2

**High (~50%) Fe content*

***Includes all phases with >50 %Fe*

****Calculated using the average composition of the identified phase*

An example of the mineral identification of a particle is shown in where nsutite/MnO_2 and lithiophorite is seen to be the most predominant phases. Different microstructures in Comilog ore were investigated and is presented using the backscatter (BS) image together with the Energy-dispersive spectroscopy (EDS) analysis of Mn, Fe, Al, K and Si. Manganese oxides in Comilog are mainly in the form of MnO_2, where different oxides may be distinguished based on their content

of additional elements, e.g. cryptomelane and lithiophorite contain K and Al, respectively[49].

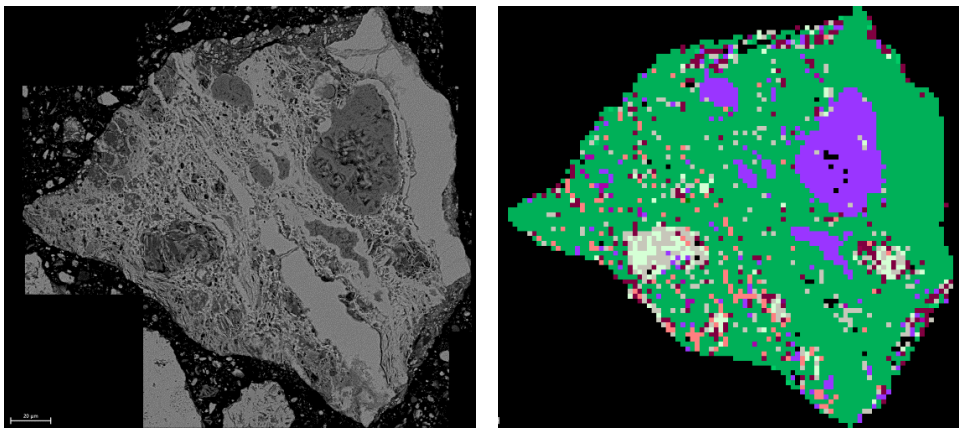

(a) (b)

Figure 4-48: Shows the backscatter image and the quantification of a particle from Comilog ore. Green =nsutite/MnO_2, purple – lithiophorite. Minor areas of clay minerals and cryptomelane are also identified.

Figure 4-49 shows two particles with plain microstructures and similar element content based on the backscatter image. The lack of additional elements in Figure 4-49a indicates that the particle may consist of nsutite or pyrolusite, which are prevalent phases in Comilog ore[49,133]. The potassium content of the particle in Figure 4-49b, indicates cryptomelane.

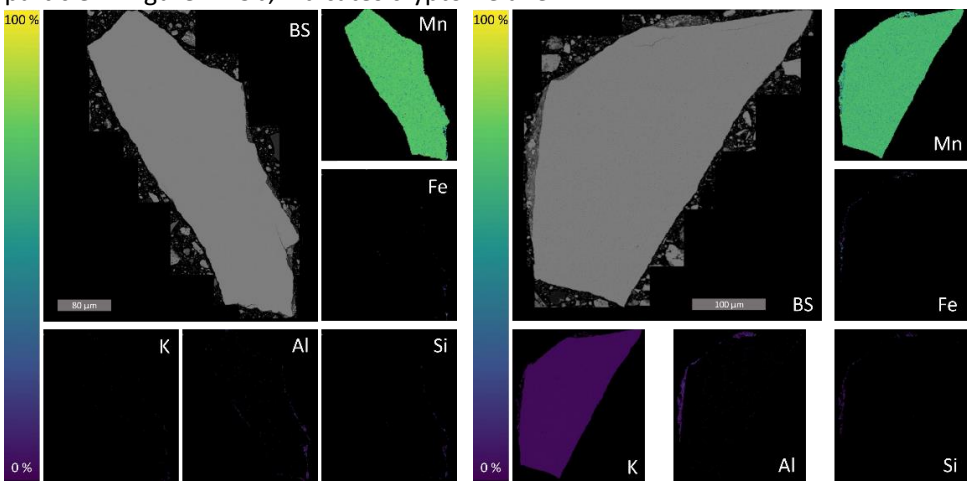

(a) (b)

Figure 4-49: Shows the backscatter image and EDS analysis for Mn, Fe, K, Al and Si for two grains (a) and (b). The color scale at the left of each figure relates to the wt % of each element in the EDS images.

Figure 4-50 shows a grain of manganese oxide that contains both Al and K. The Al content indicates the lithiophorite phase while the K indicates cryptomelane. Based on the distribution of Al and K, the grain consists of a mixture between the two minerals.

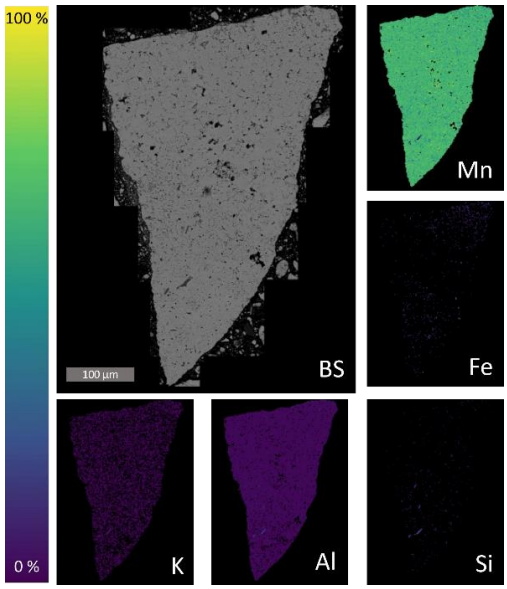

Figure 4-50: Shows the backscatter image and EDS analysis for Mn, Fe, K, Al and Si. The color scale at the left relates to the wt% of each element in the EDS images.

In Figure 4-51, a composite structure is seen, with nsutite or pyrolusite at the center, which is surrounded by a ring of cryptomelane inside a ring of lithiophorite.

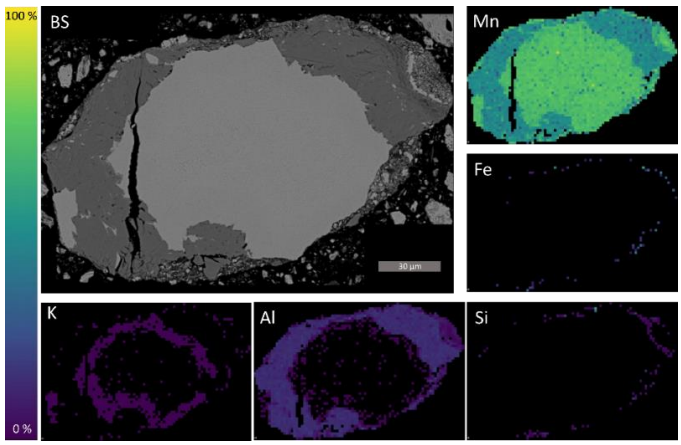

Figure 4-51: Shows the backscatter image and EDS analysis for Mn, Fe, K, Al and Si. The color scale at the left relates to the wt% of each element in the EDS images.

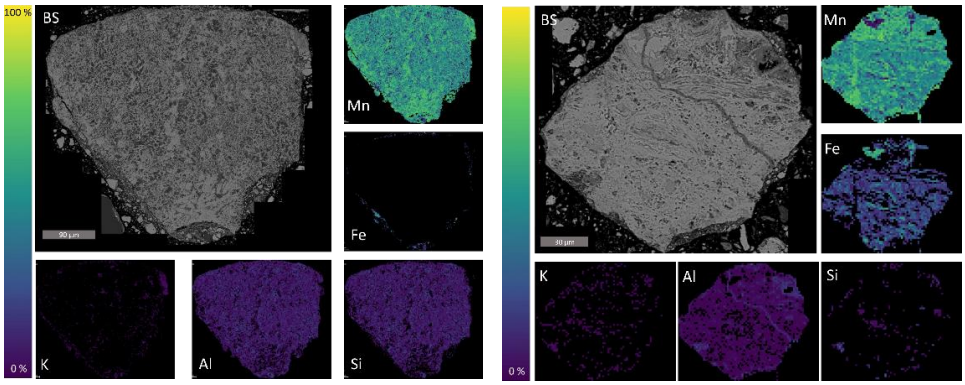

Figure 4-52: Shows the backscatter image and EDS analysis for Mn, Fe, K, Al and Si for two grains (a) and (b). The color scale at the left of each figure relates to the wt % of each element in the EDS images.

Figure 4-52 shows two examples of microstructures with intergrown phases/minerals where both are predominately manganese oxides. Figure 4-52a contains Al and Si whereas the particle in Figure 4-52b contains Al and Fe.

4.4.2 µCT measurements

One lump of unreduced ore and four lumps of reduced ore were analyzed by µCT. The microstructure of the different lumps was seen to be quite different from each other, though there were some similarities and a few observations based on these similarities could be made.

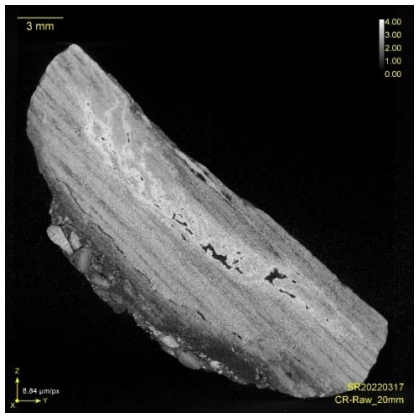

Figure 4-53: µCT image of unreduced Comilog ore.

The reduced samples were selected from the low pO_2 experiments at 410 °C and the high pO_2 experiments at 605 °C to investigate differences between samples reduced with and without hydrogen in the reducing atmosphere. The

reduced samples ended up with a fractional reduction (α) in the range 0.87-0.96. For reference, an average composition of $(Mn,Fe)_3O_4$ and (Mn,Fe)O corresponds to α=0.75 and α=1, respectively (Table 3-4). The results are shown as cross sections from the different particles obtained in the µCT analysis.

Figure 4-53 shows a cross section of an unreduced Comilog ore lump. The dark areas inside the particle are natural porosity and a layered structure of minerals with different average densities can be observed.

Figure 4-54 shows µCT images from samples reduced in low pO_2 atmosphere at 410 °C. The samples are seen to have similar appearance and density; hence it is assumed that their microstructure is the same. It can be seen that the areas surrounding the cracks for the sample in Figure 4-54a has a lower intensity, which is consistent with oxygen depletion, i.e., the diffusional resistance of the reducing gas is lower in the open cracks, increasing the degree of reduction in the surrounding areas. This is not seen in the sample reduced in the presence of hydrogen (Figure 4-54b). The gas transport may still be improved by the existence of cracks; however, it seems that hydrogen is able to penetrate deeper into the uncracked microstructure. In further work, these indications should be verified by SEM investigations.

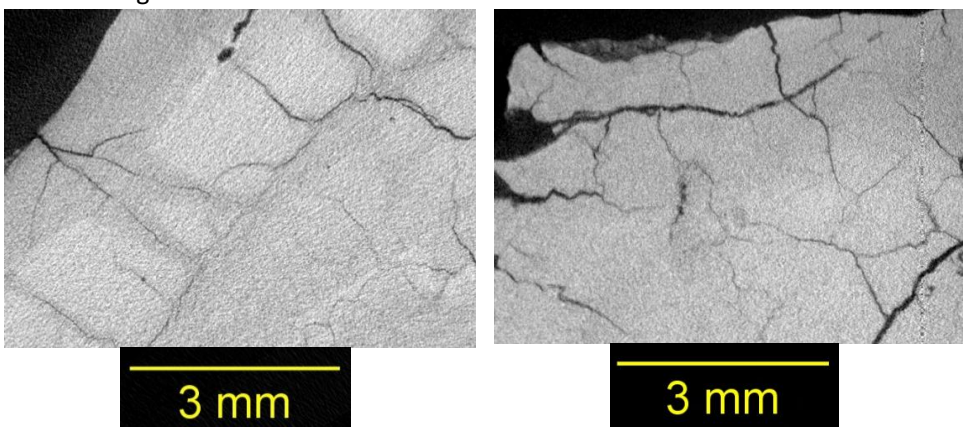

Figure 4-54: µCT images of Comilog ore reduced at 410 °C at low pO_2 in (a) hydrogen free and (b) hydrogen containing atmospheres. The degree of conversion based on the furnace weight loss are (a): 0.90 and (b): 0.91.

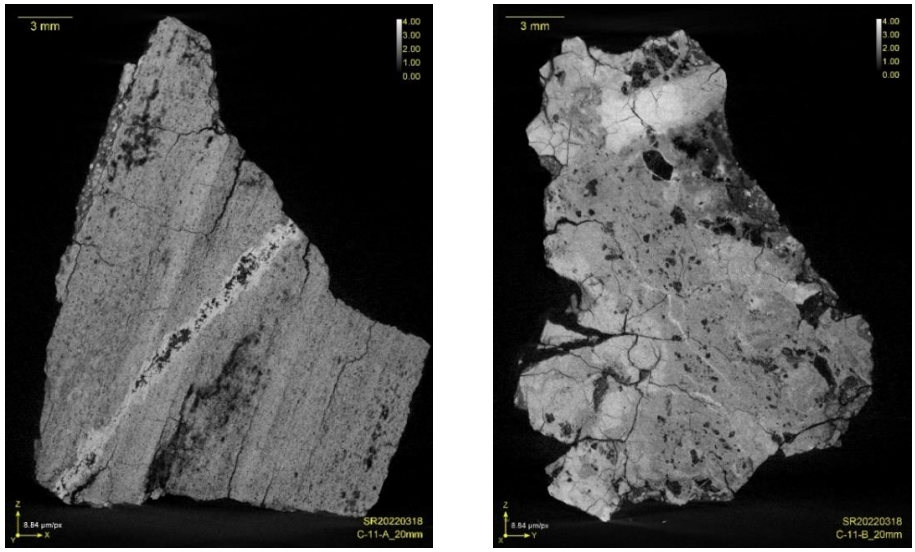

(a) (b)

Figure 4-55: µCT images of Comilog ore reduced at 605 °C at high pO_2 in (a) hydrogen free and (b) hydrogen containing atmospheres. The degree of conversion based on the furnace weight loss are (a): 1 and (b): 0.92.

In Figure 4-55, the µCT images from samples reduced in high pO_2 atmosphere at 605 °C, is shown. The microstructure of these samples is markedly different from the microstructure seen in Figure 4-54. The sample reduced without hydrogen (Figure 4-55a) is seen to have a region of natural porosity through the center and a layered structure similar to the structure observed in the unreduced lump (Figure 4-53). These are compared in Figure 4-56. However, the density (intensity) is generally lower for the reduced sample, which is consistent with reduction. In addition, the reduced sample is seen to be more porous and contain cracks.

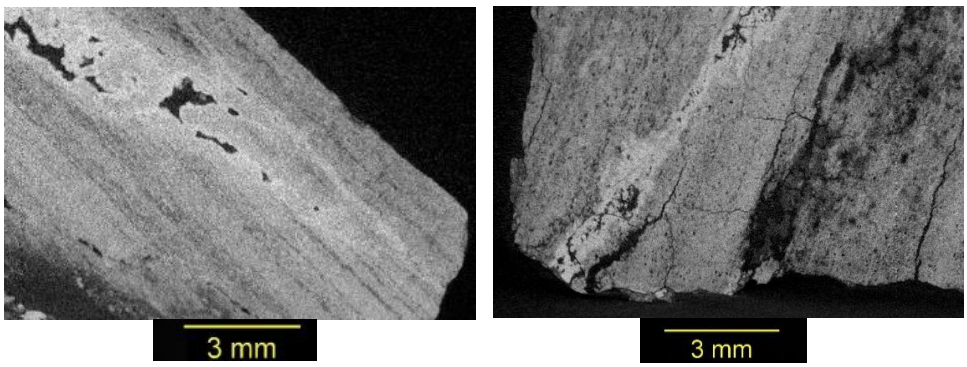

(a) (b)

Figure 4-56: Shows similar microstructures in (a): Unreduced Comilog lump (close up of Figure 4-53) and (b): reduced Comilog lump (close up of Figure 4-55a).

4.4.3 Decrepitation

Multiple sieve sizes were used to determine the decrepitation behavior. To assess the decrepitation of Comilog ore, the weight fraction of particles above 3.35 mm was used. The full dataset is given in Appendix E. Figure 4-57 shows the decrepitation behavior of Comilog ore as a function of temperature. The decrepitation is seen to increase with decreasing temperature.

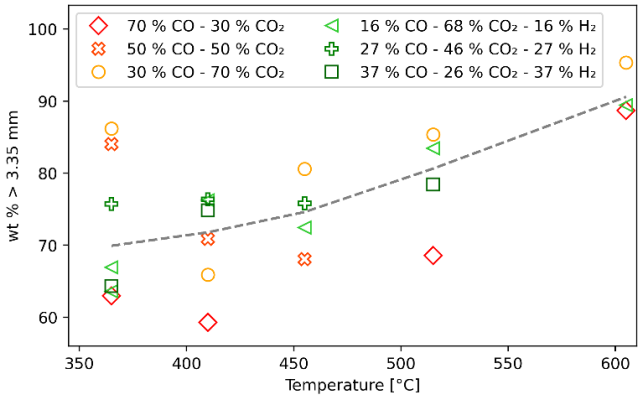

Figure 4-57: Shows the decrepitation as wt% above 3.35 mm from Comilog samples reduced in different gas mixtures as a function of temperature. The trendline was made using a Lowess filter with a smoothing parameter of 0.9.

Figure 4-58 shows the decrepitation as a function of O/Mn ratio after reduction for the Comilog experiments. The decrepitation is seen to increases with increasing degree of reduction (reduced O/Mn ratio) for O/Mn above 1.15. Between O/Mn = 1.15-1, the decrepitation decreases with increasing degree of reduction. The samples reduced at 605 °C and 515 °C have been reduced the most and decrepitated the least.

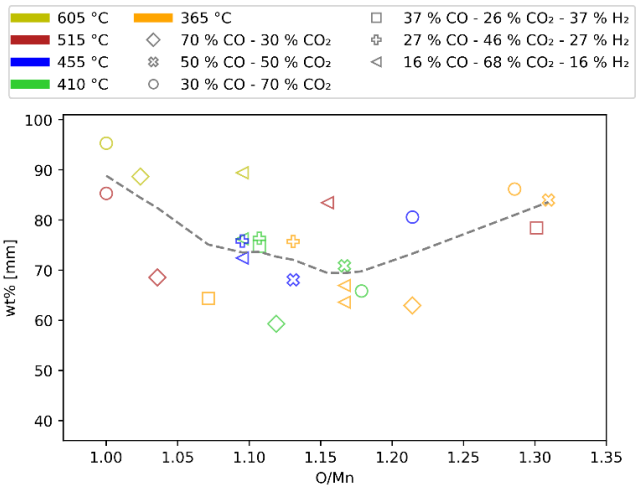

Figure 4-58: Shows the decrepitation as wt% above 3.35 mm from Comilog samples reduced in different gas mixtures as a function O/Mn ratio. The O/Mn ratio is calculated from the measured weightloss assuming all bound water has decomposed. The trendline was made using a Lowess filter with a smoothing parameter of 0.6.

4.5 Carbon deposition

Carbon deposition was observed in some of the experiments reduced in hydrogen containing gases. Figure 4-59 shows the two Comilog samples where carbon deposition was observed; reduced at 515 °C in low pO_2 (Figure 4-59a) and reduced at 455 °C in medium pO_2 (Figure 4-59b). The pictures were taken directly after removal from the crucible.

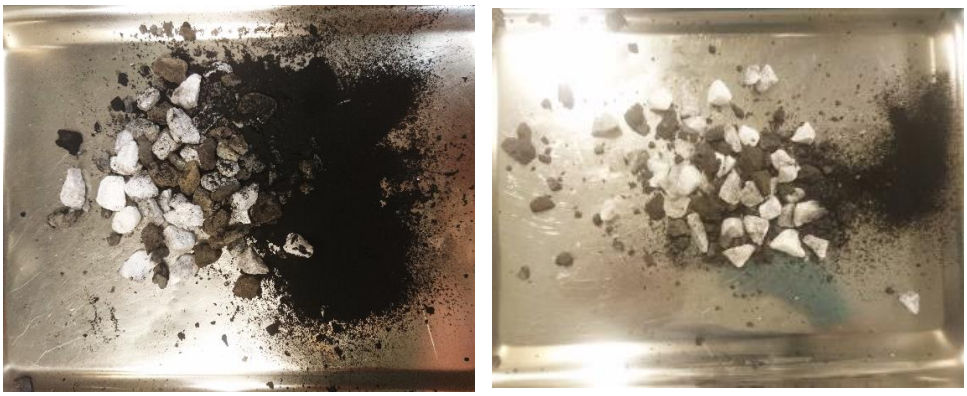

(a) (b)

Figure 4-59: Samples from experiments where carbon deposition was observed after extraction from the crucible. (a): Sample reduced at 515 °C in the low pO_2 H_2 containing atmosphere. (b): Sample reduced at 455 °C in the medium pO_2 H_2 containing atmosphere.

Figure 4-60: Shows the +9.5 mm particles from the Nchwaning ore sample reduced in the low pO_2 gas mixture at 605 °C.

Figure 4-60 shows the larges particles after reduction in the low pO2 gas mixture at 605 °C. Some of the carbon is sticking to the particles, two of the particles in the highlighted area are almost completely covered with carbon. Carbon was also observed in the other particle size fractions of the same sample, particularly in the <500 µm fraction.

5 Discussion

The behavior of Nchwaning and Comilog ore has been investigated at different temperatures when exposed to gas mixtures with and without hydrogen varying the oxygen partial pressures of the gas mixtures. In this chapter the results are analyzed and discussed.

In the first section, the reduction behavior of the ores is discussed with emphasis on the observations during the experiments and analysis. The second section focuses on the reduction rate, and in that context a model is developed and compared to a previously developed model based on other types of experiments. In the third section, the focus is put on other observations during reduction of manganese ore, some that were planned to be measured prior to the experimental work, i.e., decrepitation and the water gas shift reaction, and some that were discovered during the experimental work i.e., reoxidation and carbon deposition. In the last section, the experimental results from this work is put into context of industrial production.

5.1 Reduction behavior

Both Nchwaning and Comilog ore have high manganese content, but as seen in the literature review and results sections they are mostly different when it comes to chemical and mineralogical composition, gangue mineral content and reduction behavior. Consequently, the reduction behavior of each ore is discussed separately.

5.1.1 Reduction behavior of Nchwaning ore

From the mineralogical analysis and XRD it was seen that the manganese content in Nchwaning ore is in $(Mn,Fe)_2O_3$ type oxides (bixbyite, braunite (I and II) and neltnerite) with minor amounts of manganite (MnOOH) and hausmannite (Mn_3O_4). The mineralogical analysis indicated 0.9-1.5 wt% hematite (corresponding to 0.6-1 % Fe) while the chemical analysis revealed a content of 8.75 wt% Fe in the unreduced ore. Hence, most of the iron in the ore is in solid solution with the manganese oxides.

Hausmannite (Mn_3O_4) is identified in the raw ore, in all samples reduced for 30 minutes and in most of the samples reduced for 90 minutes. By the intensity of the diffraction pattern peaks, the content of hausmannite does not increase compared to the content in the unreduced ore. Hence, the hausmannite initially present in the ore is reduced, and the Mn_2O_3 oxides are reduced to manganosite without the formation of stable hausmannite as an intermediary phase. There were several samples where bixbyite/braunite and monoxide were present, without indications of hausmannite. This is in agreement with previous observations by Berg and Olsen[78], who observed mostly manganosite and bixbyite

after partial reduction at 700-800 °C, and Larssen[133], who found that any hausmannite formed as an intermediary product, rapidly converted to manganosite during reduction. From studies of synthetic manganese oxides, stepwise reduction was only observed in oxidizing and inert atmospheres, whereas, in reducing atmospheres, MnO_2 reduced to MnO without the formation of stable intermediaries[113,123,125].

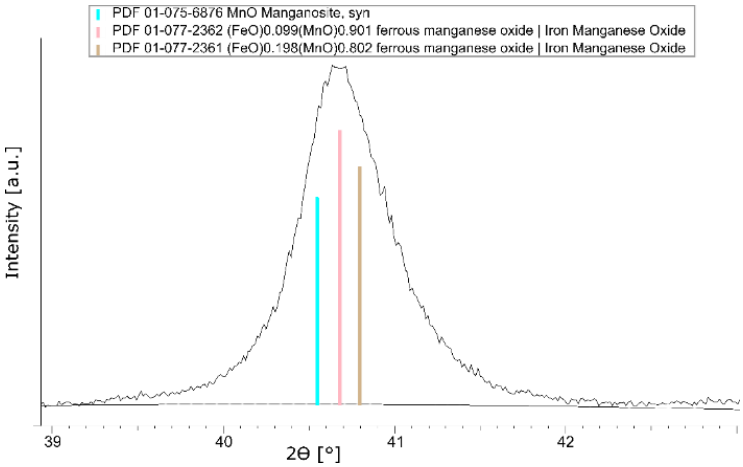

Figure 5-1: Main peak from the monoxide phase of one of the samples reduced for 210 min in 70% CO–30% CO_2 at 700 °C.

The XRD analysis also showed that samples with high iron content (chemical analysis) often retained hematite or magnetite when reduced in CO/CO_2, but not when hydrogen was used. This indicates that the presence of hydrogen improves the reduction of iron oxides, as previously observed in the reduction of iron ores[148–150]. No metallic iron was seen in any of the samples, but iron was observed to dissolve as FeO in manganosite (MnO), as shown in Figure 5-1 where the monoxide (MnO-FeO) peak from the XRD-pattern of a fully reduced sample is shifted towards higher iron contents. Figure 5-2 shows the Mn-Fe-O phase diagram at 600 °C where the ore composition and utilized oxygen partial pressures are indicated. From the figure it is seen that for pure iron oxide, metallic iron is the stable iron containing phase for low pO_2 gas mixtures and magnetite is stable for the high pO_2 gas mixtures. The presence of MnO however effectively enlarges the stability range of FeO due to its lowered activity in solid solution with MnO thus making FeO the stable iron oxide. This applies for the whole temperature range used in this work for Nchwaning ore. The existence of the MnO phase thus aids the reduction of magnetite to FeO, while it simultaneously inhibits the reduction of FeO to metallic iron. The stabilization of FeO by MnO has also been observed in other investigations[65,67–70].

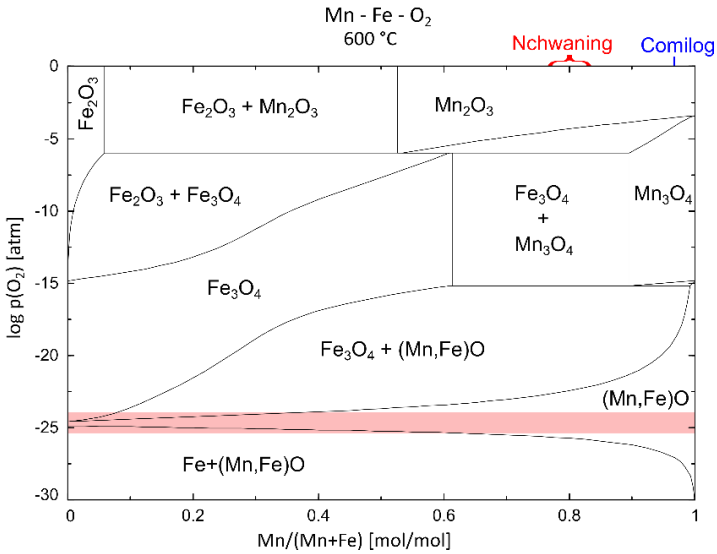

Figure 5-2: Phase diagram for the Mn-Fe-O system showing the stable phases as functions of oxygen partial pressure and composition. Calculated with Factsage using the FToxid, FTmisc and FactPS databases[27]. Composition of Nchwaning and Comilog ore is indicated. The shaded area indicates the range of oxygen partial pressured utilized in this work.

According to the stoichiometry of the minerals, the reduction of braunite (I and II) and neltnerite to (Mn,Fe)O should leave excess CaO and SiO_2 in the reduced sample. The chemical analysis of the unreduced ore showed that the total content of SiO_2 and CaO is 4.4 and 5.93 wt%, respectively. Neither SiO_2 or CaO were observed in the XRD patterns, thus the content of free SiO_2 and CaO were below the detection limit of XRD (i.e. ~ 1 %[49]) or accumulated in the remaining Mn_2O_3 oxides. The different braunite type minerals (braunite (I and II) and neltnerite) display a wide range of solid solubility, and braunite with twice the amount of SiO_2 and three times the amount of the CaO, compared to the stoichiometric composition, has been measured in samples from the same ore body as Nchwaning ore[49,95]. A significant fraction of CaO is bound as carbonate and free CaO may have entered the monoxide phase. Formation of tephroite (Mn_2SiO_4) was seen in most of the samples reduced at 790 °C for 210 minutes. Manganese in tephroite has the same oxidation state as manganese in manganosite; hence, the formation of tephroite has no further impact on prereduction compared to reduction to manganosite.

Mn_2O_3-phases were measured in many of the samples where chemical analysis stated that they were fully reduced (O/Mn) = 1. In all cases where parallel experiments were analyzed, the sample with the higher iron content had a lower or equal O/Mn ratio. This implies that the oxygen measurement in the chemical analysis underestimates the oxygen content of the sample. Recent work by Bao et

al. [Prema project – unpublished[151]], showed that the lower oxides of iron (Fe_3O_4 or FeO) indeed gives an underestimation of the oxygen content. The measured weight loss however (Figure 4-1), indicated that the samples in question were close to fully reduced, thus the O/Mn measurement from chemical analysis is close to the actual composition. The degree of conversion for the different gas mixtures and temperatures can be seen in Figure 5-3, where according to the average composition most of the samples reduced at 700 °C is close to fully reduced with no or limited carbonate decomposition, whereas for the samples reduced a 790 °C, some carbonates have decomposed in addition to the reduction.

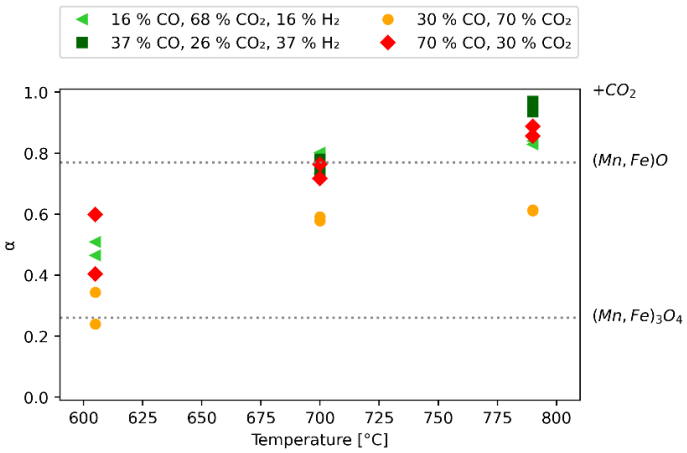

Figure 5-3: Shows the degree of conversion at the end of the Nchwaning experiments. The horizontal lines indicate the corresponding oxides (average composition). Reduction from (Mn,Fe)O to +CO_2 (α=1) indicates the decomposition of carbonates.

Carbonates were present in all XRD patterns with lower peak intensity compared to the unreduced material, which is consistent with the measured weight loss that indicated that a fraction of the carbonates has decomposed (Figure 5-3). From chemical analysis it was seen that carbonate decomposition increased with increasing temperatures, albeit the differences were small (Figure 4-6). The observed carbonate decomposition can be explained by the fraction of Mg, Mn and Fe in the carbonate phase(s), which was observed in the mineralogical analysis. Calcite ($CaCO_3$) is stable at the investigated temperatures. This is consistent with the observations from Ringdalen et al.[90], where carbonate decomposition in Nchwaning ore was seen to occur in two distinct stages, where the stage at the highest temperature was consistent with calcite decomposition. Similar observations has also been made for UMK ore[86,87,92]. The observed temperature dependence indicates that most of the Mg, Mn and Fe carbonates decomposes throughout the course of the experiments and that the remaining fraction of carbonates is predominantly calcite.

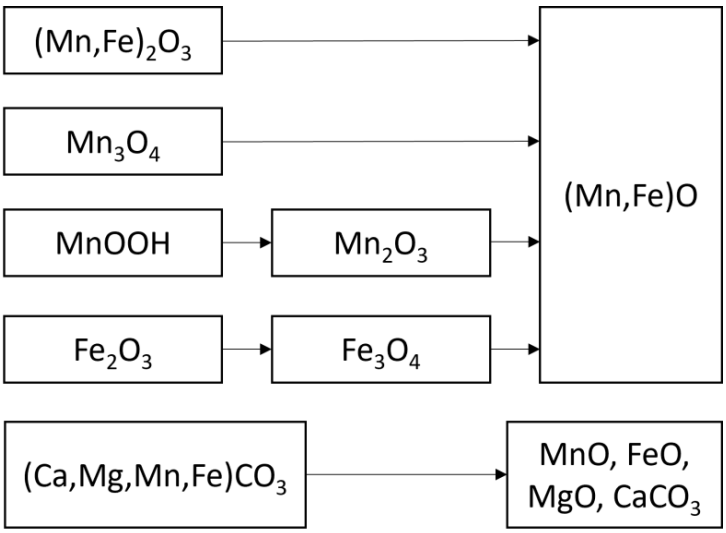

Figure 5-4: Shows an overview of the reaction paths of Nchwaning ore in the temperature range 605 – 790 °C.

Nchwaning ore is relatively heterogeneous, as seen by the content and distribution of different phases, evidenced by the different microstructures and XRD analysis. The reduction occurs in different manners in the different minerals, as seen from the EPMA results where particles from the same experiment are reduced differently, one displaying a topochemical reduction mechanism while the other does not. These details account for some differences at the microscopic level, nevertheless, the overall reduction of Nchwaning ore follow a consistent trend. Figure 5-4 summarizes the main observations of the reduction path of Nchwaning ore between 605 °C and 790 °C; $(Mn,Fe)_2O_3$-type oxides are reduced to (Mn,Fe)O without the formation of stable intermediary oxides. Hausmannite (Mn_3O_4) originally present in the ore is reduced to MnO while hematite (Fe_2O_3) is reduced to magnetite (Fe_3O_4) and further to FeO which enters the MnO-FeO solid solution phase. A fraction of carbonates associated with Fe, Mn and Mg cations decompose to their respective monoxides while calcite remains in the samples.

5.1.2 Reduction behavior of Comilog ore

As in Nchwaning ore, Comilog ore contains a range of minerals. Most of the minerals in Comilog are of the MnO_2 type oxides, i.e., nsutite, pyrolusite, lithiophorite and cryptomelane. A minor content of bixbyite was identified in the mineralogical analysis. Iron is found as hematite/goethite and in bixbyite, while quartz is the most predominant gangue mineral. The chemical analysis shows about 5 wt% Al_2O_3, which is mostly found in the lithiophorite and 0.8 % K_2O which originates from the cryptomelane. Chemically bound water is found in nsutite, lithiophorite and goethite. With the exception of bixbyite, the same phases were

identified by Rietveld analysis by Sorensen et al.[49] (Table 2-2) albeit the distribution of minerals were somewhat different. The bixbyite was identified based on the relative manganese and iron content, however as seen in the microstructure (e.g. Figure 4-48), Comilog ore contains finely distributed and intergrown phases that are close to the resolution limit of the mineralogical analysis, hence the identified bixbyite may simply be an artifact of analysis points falling on the boundaries between iron and manganese rich minerals.

Due to oxidation of the Comilog samples after reduction, it was not possible to verify the extent of reduction with chemical analyses after the experiments. The extent of reduction was hence determined by the weight loss and initial chemical analysis. The total bound water content was estimated using the reduction curves and off gas analysis from the samples reduced in the low pO_2 hydrogen free mixture at 515 °C and 605 °C (Figure 5-5). Reduction was complete after approximately 90 minutes. Assuming that the samples are fully reduced at this point and comparing with the theoretical weight loss, a bound water content of 4.9 % is found. This value is in the middle of the range reported in other investigations for Comilog ore[39,87,92,133]. Variation in the bound water content of the ore will impact the contribution to the fractional conversion (α). For the range reported in literature (3.2-6-5 %), the contribution to the fractional conversion based on the chemical analysis in this work is 0.18-0.31, while the value of 4.9 % found in this work gives a contribution of 0.26.

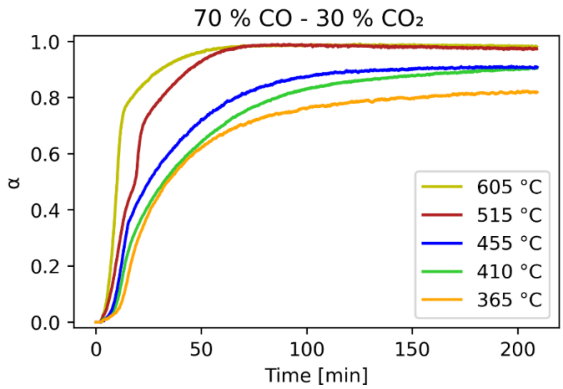

Figure 5-5: Fractional conversion for the low pO_2 hydrogen free gas mixture as a function of time.

It was previously seen (Figure 4-35) that at 515 °C, the decomposition of bound H_2O and reduction of oxides run in parallel in the initial part of the experiments until all H_2O had evaporated. This was also seen in Reiersen[92] and in Larssen[133]. The off-gas analysis from the CO/CO_2 experiments can be used to estimate the weight loss from the reduction of oxides based on the produced CO_2 throughout the experiments.

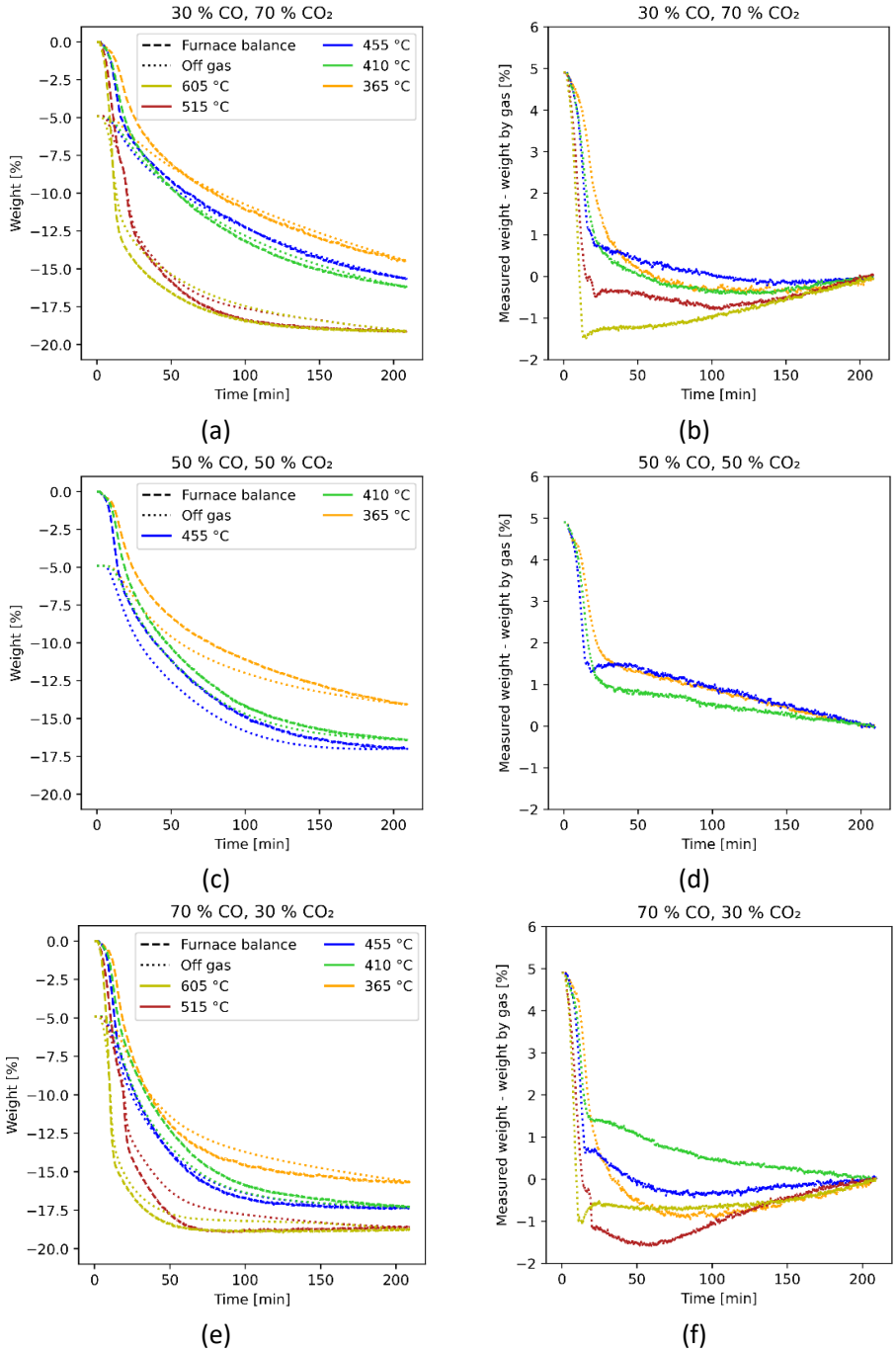

Figure 5-6: Shows (a),(c),(e): the reduction curves from the measured weight and from the off-gas analysis for reduction of Comilog ore in CO/CO2 gas mixtures and (b),(d),(f): The difference in between the measured weight and off-gas weight corresponding to the water content.

In Figure 5-6 a, c and e, the measured weight loss and the weight loss based on the off-gas analysis have been plotted together and it can be seen that the start of the off-gas curve has been set to -4.9%, which corresponds to the measured water content. Figure 5-6 b, d and f, shows the difference in weight loss between the two approaches. This difference is equivalent to the removal of bound water since the reduction of oxides by CO gas should give the same behavior in the weight measurements and the off-gas analysis. In the initial part of the experiments, the bound water is removed rapidly, and the rate of water removal increases with increasing temperature.

For the lower temperatures (365-455 °C), it does not seem like the water is fully removed i.e., the curves in Figure 5-6 b, d and f does not reach zero after the initial rapid decline. Conversely, the experiments at higher temperatures show a higher weight loss from water compared to the theoretical water content. If these discrepancies were caused by variation in the water content between samples, the removal of water would not be expected to depend on temperature, as appears to be the general trend (Figure 5-6 b, d and f). The temperature dependency may have the simple explanation that not all water is removed at the lower temperatures. However, as seen in the work of Doose and Donne[152] more than 90 % of the structural water had decomposed at 350 °C in synthetic nsutite. In addition, Larssen[133] reduced Comilog ore with a similar particle size distribution as the one used in this work, and found that all bound water had decomposed below 360 °C, where XRD analysis revealed that all nsutite and lithiophorite had dehydrated and converted to pyrolusite after isothermal reduction at 400 °C. Hence it is improbable that there is a significant content of bound water in the samples after the reduction is complete in the current experimental conditions. The heating rates are significantly higher in this work, however since the utilized gas mixtures (in Figure 5-6) has no retarding effect on water evaporation (no H_2O in the input gas) the water decomposition is only a function of temperature, thus altering the heating rate should only affect the rate of decomposition, not the extent. In the experimental section, the buoyancy of the crucible in the setup was seen to give a temperature dependent deviation on the measured weight loss. This deviation mostly canceled itself out as time progressed and a thermal steady state was reached i.e., about 40 minutes into the experiment, making it a possible influence to the discrepancy between the theoretical water loss and the observations from Figure 5-6. In addition, it was seen that the error in the CO off gas analysis is highest during the initial part of the experiments when the high consumption of CO causes the largest differences from the calibrated value. The deviation is not entirely systematic in relation to temperature and while some degree of random variation of the weight loss can be expected, such as observed in the experimental section, different samples may in fact contain different

amount of bound water due to differing distribution of minerals. Based on the time it takes for the curves to stabilize to a near linear trend (i.e., similar behavior of weight loss and consumed CO) it seems like a small fraction of the bound water is slowly decomposing up until 90-100 minutes for the lower temperatures, particularly at 365 °C.

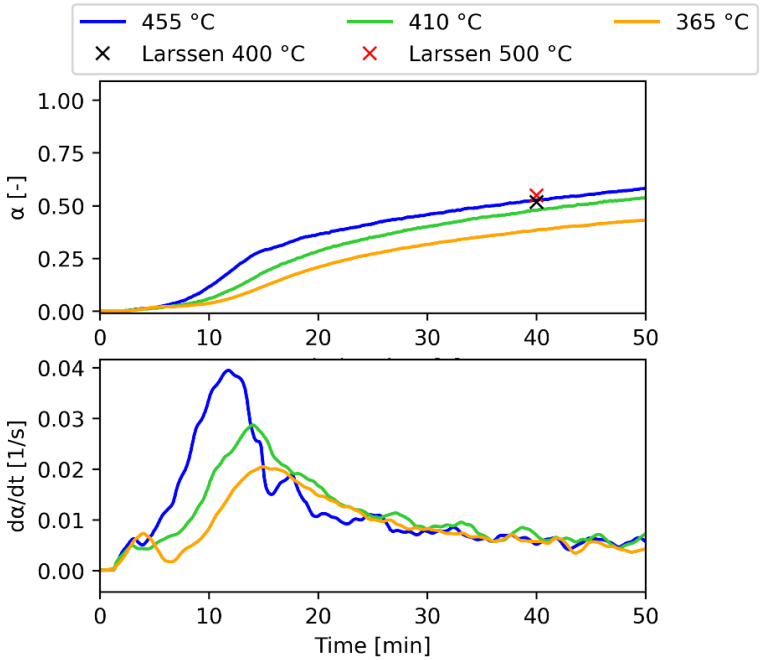

Figure 5-7: Shows the fractional conversion and reduction rate from the first 50 minutes of the 50% CO – 50 % CO_2 experiments (this work) compared to conversion based on chemical analysis from Larssen[133] using the same gas mixture.

Figure 5-7 shows the fractional conversion and the reduction rate from the initial part of the medium pO_2 CO/CO_2 experiments in addition to the conversion based on chemical analysis from Larssen[133] for the same gas mixture where it can be seen that the reduction obtained in Larssen is similar to the reduction obtained in this work. Larssen[133] found that the product from MnO_2 reduction was predominantly Mn_3O_4 and MnO below and above 370 °C, respectively. The very same behavior was observed during reduction of synthetic MnO_2 by de Bruijn et al.[113] i.e. MnO_2 reduced stepwise via Mn_3O_4 to MnO at lower temperatures (275 °C – 325 °C) while MnO_2 was reduced directly to MnO at 400 °C. In Figure 5-8, two peaks in the CO consumption can be seen at about 15-20 minutes reduction. After the sample reach 370 °C, the CO consumption increases due to the increased reduction rate of Mn_3O_4 above this temperature.

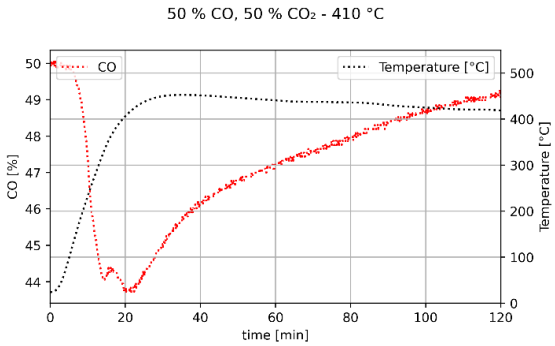

Figure 5-8: Shows the measured temperature and CO in the off gas for the first 120 minutes of the medium pO_2 hydrogen free experiment conducted at 410 °C.

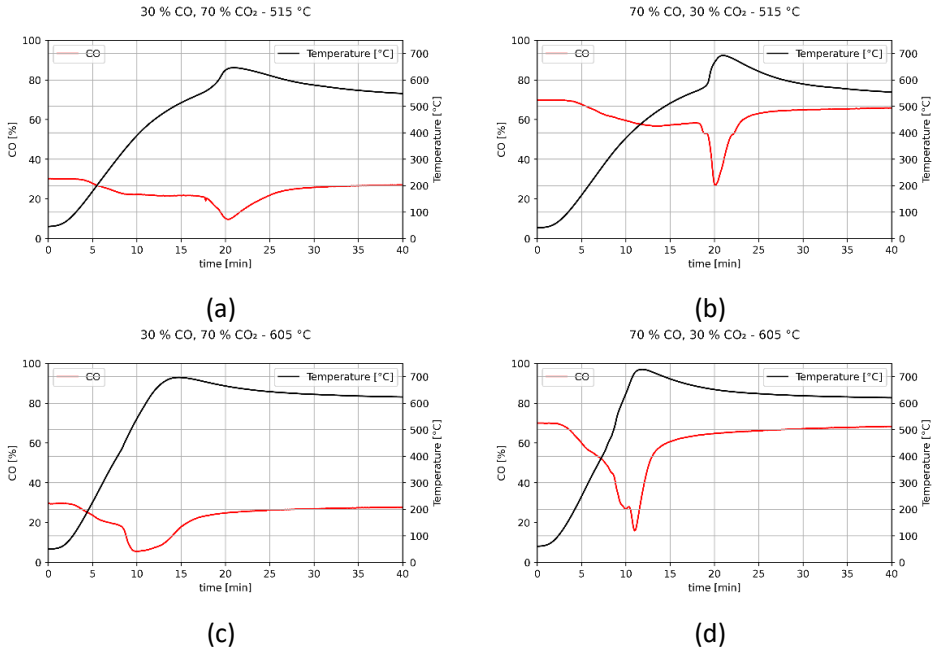

Figure 5-9: The measured temperature and CO content in the off-gas for the Comilog experiments run at 515 °C and 605 °C in CO/CO_2 gas mixtures.

Another feature that was apparent from the Comilog experiments was the rapid reduction and high exothermal peak at the higher temperature experiments (515 °C and 605 °C). This behavior has been observed in several studies during non-isothermal reduction of different MnO_2 type ores[37,42,54,87,92,94,98,126,127,133]. Figure 5-9 shows the measured CO and temperature in the initial 40 minutes of the 515 °C and 605 °C experiments using CO/CO_2 gas mixtures. For the 515 °C experiments,

this exothermal peak is seen to initiate close to 20 min reduction time when the sample reached a temperature of about 550-580 °C (Figure 5-9 a and b), which is similar to the threshold temperature for the exothermal peak identified by Larssen[133] for Comilog ore (580 °C), where it was seen that the remaining MnO_2 converted to Mn_2O_3 in a combination of reduction and thermal decomposition. Exothermal reactions are also occurring prior to this point, as evidenced by the measured temperature surpassing the set temperature of the experiment. The occurrence of Mn_2O_3 after the rapid reduction step may be due to that the rapid reduction causes more oxidizing conditions. Ringdalen et al.[90] found that oxygen was present in the off-gas during the rapid reduction stage of Comilog ore using a 70 % CO – 30 % CO_2 gas mixture. This confirms the observation from Larssen[133] that during the rapid reduction stage, a combination of reduction and thermal decomposition occurs. It also shows the presence of more highly oxidized conditions, making it possible for Mn_2O_3 to be stable during this event. In the samples reduced at 605 °C (Figure 5-9 c and d), the exothermal temperature peak is obscured by the increased temperature due to high heating input from the furnace. However, a high consumption of CO is seen to initiate around 9.5 minutes for both gas mixtures, which corresponds to a temperature of about 400 - 500 °C. This is lower than the threshold temperature identified previously, however it could indicate the change between MnO_2 reducing via Mn_3O_4 to MnO and the direct reduction of MnO_2 to MnO which was seen to occur above 370 °C. An additional peak initiate at about 580 °C for the 70 % CO gas mixture (Figure 5-9d) which correlates in temperature to the rapid reduction observed in the 515 °C experiments and from other works. This is not seen in the 30 % CO experiment (Figure 5-9c), which may be due to the fact that the CO in this experiment is nearly exhausted at this point.

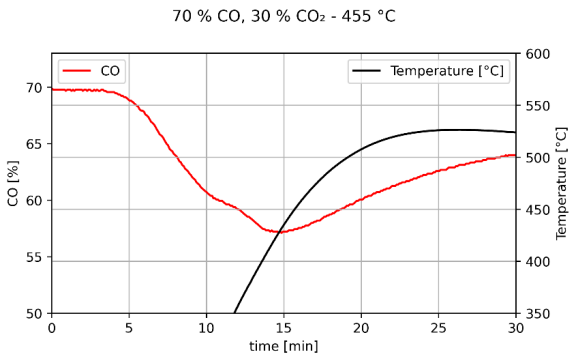

Figure 5-10: Shows the measured temperature and CO in the off-gas from the initial part of the low pO_2 CO/CO_2 experiment at 455 °C.

The rapid reduction and high exothermal peak ($MnO_2 \rightarrow Mn_2O_3$ reduction/decomposition) was not observed at the lower temperature experiments (365 - 455 °C). Figure 5-10 shows the CO and temperature measurements from the first 30 minutes of the low pO_2 CO/CO_2 experiment conducted at 455 °C. The maximum CO consumption, i.e., the highest reduction rate of oxides, is seen to occur prior to the sample reaching the set temperature, and the temperature overshoots the set temperature due to the continued occurrence of the exothermal reduction reactions as seen by the consumed CO. From the peak reduction rate, the sample temperature increases about 100 °C in the 10 minutes following the peak reduction rate and the reduction rate decreases continuously throughout this period. This may be explained by increased diffusion resistance within the particles as reaction progresses, where the reduction rate is decreased due to the diffusion resistance to such an extent that it overcomes the increased driving force due to the increased temperature. This is also consistent with the observed content of intermediate oxides in Larssen[133] since a concentration gradient through the product layer of the particles will expose the phases to less reducing conditions compared to the bulk gas composition[89]. This is consistent with previous observations where during reduction of GE ore (a high MnO_2 ore), Berg[77] found that the ore was reduced in a shrinking core fashion, where reduction was controlled by diffusion. Also Larssen[133] observed that Comilog samples reduced isothermally followed a shrinking core pattern. Reduction was seen to occur from the edge towards the center of the particle and along cracks in the particles, which is in agreement with this work.

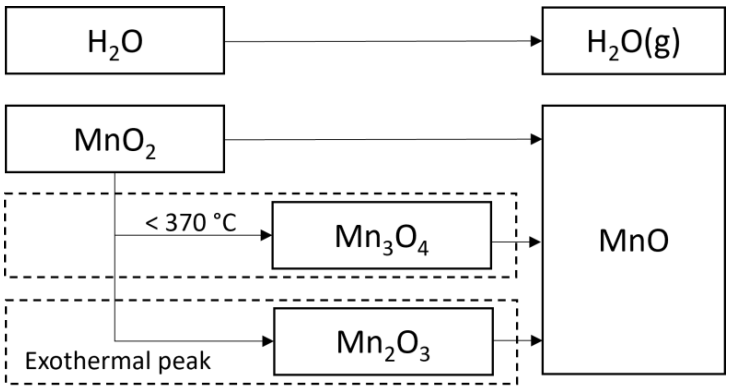

Figure 5-11: Shows an overview of the reduction path for Comilog ore.

Figure 5-11 shows the main reduction paths for Comilog ore. The main product from reduction of MnO_2 phases are Mn_3O_4 and MnO, where the latter is predominant above 370 °C. Below this temperature, the reduction rate of Mn_3O_4 to MnO is slower than the reduction rate of MnO_2 to Mn_3O_4 causing an

accumulation of Mn_3O_4 in the sample. The decomposition of bound H_2O seen to occur at the initial part of the experiments with the rate of decomposition increasing with increasing temperature. The O/Mn ratio from chemical analysis of 1.91 corresponds to 83.4 % MnO_2 and 16.6 % Mn_2O_3. Mn_2O_3 phases are generally not found in unreduced Comilog ore[49,133]. When hydrated manganese minerals such as lithiophorite and nsutite decompose, the fraction of manganese previously bound to water may convert into Mn_2O_3 which explains its occurrence during reduction at lower temperatures. If the sample reaches the point of rapid reduction and high exothermal temperature peak, any remaining MnO_2 reduces and decomposes to Mn_2O_3. The continued presence of intermediate oxides at higher temperatures[133] may be explained by a concentration gradient through the particles caused by diffusion limitation giving less reducing conditions in the interior of the particles[77,89]. Comilog ore contains a relative low amount of iron as hematite and goethite that will eventually enter in solid solution with the manganese oxides.

5.2 Reduction rate

The degree of conversion and the reduction rates was shown in the results section for Nchwaning (Figure 4-2) and Comilog ore (Figure 4-30 and Figure 4-38) where it was seen that the reduction rate increased with increasing temperature, decreasing pO_2 and with the addition of H_2 at constant pO_2. Due to the reduction during the heating period of the ore, a significant fraction of the samples was converted prior to the samples reaching the set temperature of the experiments i.e., during the heating period. After reaching the set temperature, the sample temperature increased further due to the ongoing exothermal reactions, hence a significant proportion of the reduction occurred at temperatures other than the set temperature of the experiment. Figure 5-12 shows the reduction rate as a function of degree of reduction for (a): the Nchwaning experiments conducted at 790 °C and (b): the Comilog experiments conducted at 410 °C. The symbols on the graph indicate the points where the set temperature (X) and the peak temperature (triangle) of each experiment is reached. The vertical dotted lines indicate the average composition and are added for reference even though the specific phases are not necessarily present (see section 5.1.1 and 5.1.2).

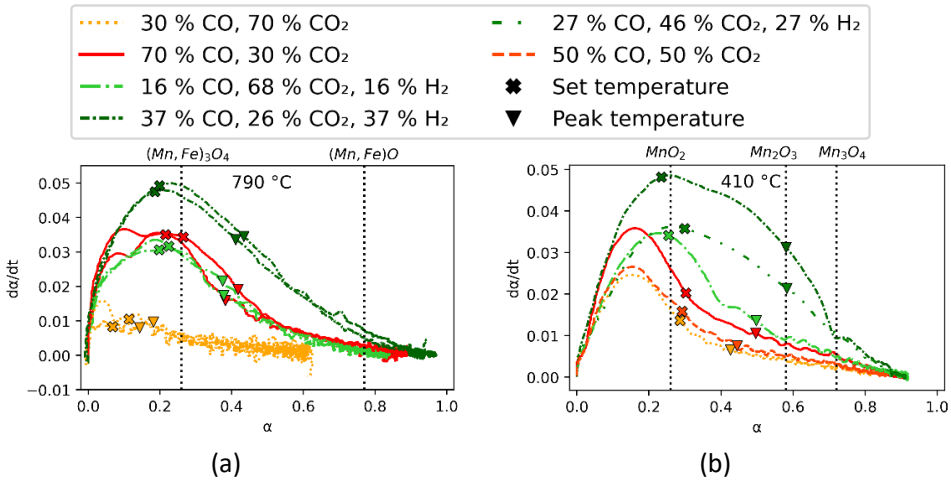

Figure 5-12: Shows the reduction rate as a function of degree of reduction for the Nchwaning experiments conducted at 790 °C and the Comilog experiments conducted at 410 °C, (a) and (b) respectively. The set temperature is indicated in each figure and the point where the sample reaches the set temperature is marked (X) for each experiment. Triangles mark the point at which the highest temperature is reached in each experiment. Vertical dashed lines indicate the average composition of stable oxides. Reduction past (Mn,Fe)O is decomposition of carbonates.

For Nchwaning ore, the set temperature is reached close to the point of maximum reduction rate and the peak temperature is reached at a later stage due to the continued occurrence of exothermal reactions. However, despite that the

temperature increase following the set temperature, the reduction rate decreases. This was also pointed out previously when looking at the consumption of CO (Figure 5-10) and is consistent with diffusion controlled reduction[153,154]. Comilog ore is seen to behave similarly as the Nchwaning ore in that the set temperature is reached at or after the peak reduction rate. The reduction of Comilog ore is more complex compared to Nchwaning ore in that twice as much oxygen has to be removed to achieve full reduction and that hydrated minerals decompose at the same time as the reduction of oxides and is concentrated in the initial part of the experiments.

5.2.1 The effect of hydrogen on reduction

The presence of hydrogen has a significant positive effect on reduction rate and extent of reduction for both Nchwaning and Comilog ore at the temperatures investigated in this work. Figure 5-13 shows the fractional conversion as a function of time for the Nchwaning samples reduced at 790 °C and the Comilog samples reduced at 410 °C where all gas mixtures are included. The improved reduction rate when using hydrogen seen in this work is consistent with the observations during non-isothermal reduction by Larssen and Tangstad[127] and by Ngoy et al.[126]. In these studies, as well as in the current work, each pair of gas mixtures were chosen such that a hydrogen free and hydrogen containing gas mixture would yield an equal thermodynamic driving force (pO_2).

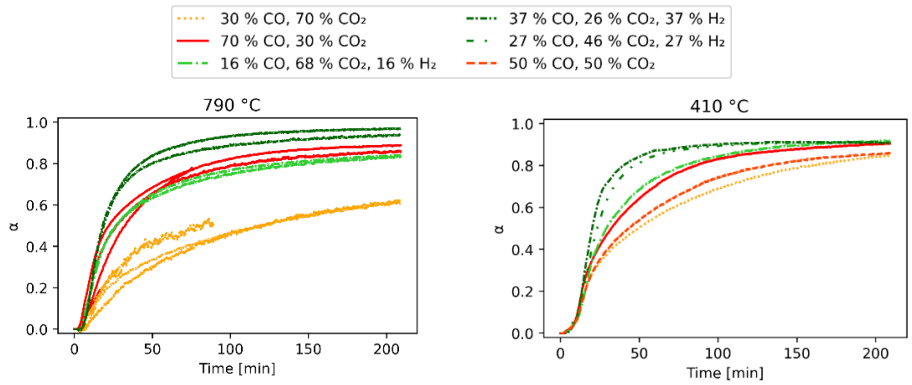

(a) (b)

Figure 5-13: The fractional conversion as a function of time for the (a) Nchwaning experiments at 790 °C and (b) Comilog experiments at 410 °C.

The established oxygen partial pressures in the gas mixture pairs in this work, is equal at about 650 °C and varies slightly over the temperature range studied. Above 650 °C, the driving force is slightly higher in the hydrogen containing gas compared to the hydrogen free ones and vice versa. The hydrogen containing atmospheres were seen to yield significant improvements in the

reduction rates for both ores, regardless of temperature. Hence, these slight differences in applied thermodynamic driving force is insignificant compared to the effect hydrogen in the gas mixture. Similar observations of the improved effect of hydrogen in the gas mixture has also been done in the reduction of iron ores, where addition of H_2 while keeping the driving force similar greatly improves reduction due to the improved diffusion of H_2 compared to CO[155,156]. To compare the diffusion of different gases, the binary diffusion coefficients for H_2-CO_2, CO-CO_2 and H_2-H_2O are shown in Figure 5-14. The diffusion coefficient of H_2 in CO_2 is about 4 times higher than CO in CO_2 while the diffusion coefficient of H_2 in H_2O is 5.5 times that of CO in CO_2. Hence, it is not only the presence of H_2, but also the reaction product H_2O that improves the diffusion properties of hydrogen containing gas mixtures. In this work, the presence of hydrogen improved the reduction at constant thermodynamic driving force of the reducing gas mixture; hence it can be concluded that the improved reduction rate was a result of improved mass transfer properties of the reducing gas and the product gas.

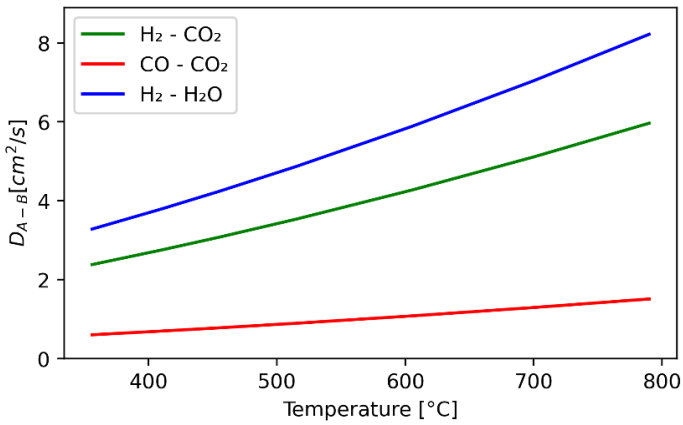

Figure 5-14: The binary diffusion coefficients for H_2-H_2O, H_2-CO_2 and CO-CO_2. Calculated by the method of Fuller et al.[157], details in Appendix G.

The effect of improved mass transfer is not unique for the change of mass transfer characteristics of the reducing gas. Improved reduction has also been seen using the same gas mixtures but changing the mass transfer characteristics of the solid material, i.e., the porosity. The positive correlation between reactivity of manganese raw materials and increased porosity was shown in Figure 2-9. It could be argued that some of these differences is caused by unequal chemical composition and/or heat treatment (e.g., pellets and sinter). However, after changes in the materials while retaining similar properties by cold pressing of pellets[53] or by engineering the porosity of a material while using the same thermal

treatment[68], it has been seen that increased porosity improves the reduction of manganese materials.

5.2.2 Modeling

It has been seen that the different prereduction reactions occur in series and/or in parallel. To further analyze the prereduction rates of the ores under different conditions, modeling is done. This type of experiment is designed to look at the overall kinetics of the pre-reduction process, so the purpose of modeling is to obtain a quantitative description of the prereduction process in different gas mixtures that includes the total contributions from all the prereduction reactions. To obtain this, the reaction order model was utilized, and is shown in equation (*16*), where dα/dt is the reduction rate, k_0 is the apparent pre-exponential constant, E_a is the apparent activation energy, R is the universal gas constant, T is temperature, α is the degree of conversion and x is the reaction order. The modeling equation was fitted to the experimental data using a nonlinear least squares method.

$$\frac{d\alpha}{dt} = k(T)f(\alpha) = k_0 \exp\left(-\frac{E_a}{RT(t)}\right)(1-\alpha)^x. \qquad (16)$$

All experiments at a given temperature was conducted using the same experimental program, except for the input gas composition. Despite this, the exothermal reactions create different temperature regimes for the parallel gas mixtures. An example of this is shown in Figure 5-15, where the measured sample temperature in the medium pO_2 Comilog experiments can be seen. The measured temperature for each experiment was used in the modeling to account for the variations in temperature, as indicated by the T(t) in equation (*16*).

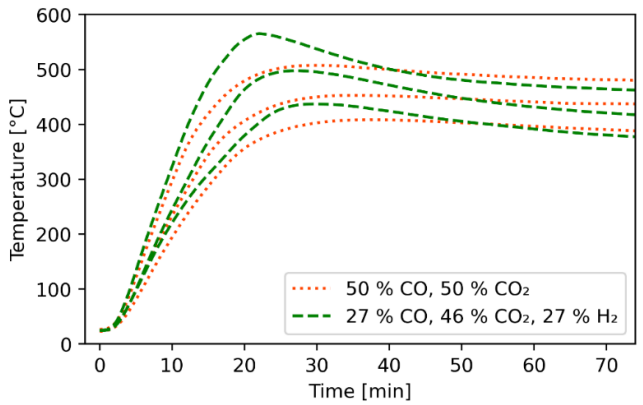

Figure 5-15: Shows the measured temperature during reduction of Comilog samples using the medium pO_2 gases.

To isolate the effect of the CO content in the CO-CO_2 gas mixtures, k_0 in equation (*16*) is separated into the apparent pre-exponential constant for the reactions, k, and the CO-content contribution according to equation (17)[101]:

$$k_0 = k\left(p_{CO}^m - \left(\frac{p_{CO_2}}{K}\right)^m\right) \cong k p_{CO}^m \qquad (17)$$

Where pCO and pCO_2 are the partial pressures of CO and CO_2 respectively, K is the equilibrium constant, and m is the order of which the partial pressure of CO in the CO-CO_2 gas mixtures affect the reaction rate. The simplification in the latter part of the equation is valid under the assumption that the forward reaction is much larger than the back reaction. For the reduction of Mn_3O_4 to MnO, the error by this assumption is less than 0.03 % in the experimental range. The H_2 containing parallels have an equal oxygen partial pressure, thus the thermodynamic driving force is the same as in the CO-CO_2 parallels. To compare the two, the driving force is represented as (1-pCO_2). The values of m and k are obtained by taking the slope and intercept of the linear regression of the plot ln(k_0) vs ln(1-pCO_2) and the following model expression is obtained (equation (*18*)):

$$\frac{d\alpha}{dt} = k \exp\left(-\frac{E_a}{RT(t)}\right)(1-\alpha)^x p_{(1-CO_2)}^m \qquad (18)$$

Each ore was fitted to a single activation energy and reaction order. This approach allows for the direct comparison of the pre-exponential constant to assess the relative effects of changing partial pressure or adding hydrogen. For Nchwaning ore, an apparent activation energy from the high and low pO_2 parallels of 68 kJ/mol and a reaction order of 2 was found from the model fitting. The reduction rate curves in Figure 5-16 is seen to fit reasonably well with the superimposed model (dashed lines). The apparent pre-exponential constants from the model fitting are shown in Table 5-1.

Table 5-1: Shows the pre-exponential constants, k_0, according to equation (17) from modeling of the Nchwaning results. E_a = 68 kJ/mol and x = 2. The predicted reduction curves from the model parameters are superimposed on the measured reduction rate in Figure 5-16.

pO_2	Gas Mixture	k_0 [1/min]
High	30% CO - 70% CO_2	24
	16% CO - 68% CO_2 - 16% H_2	82
Low	70% CO - 30% CO_2	85
	37% CO - 26% CO_2 - 37% H_2	156

The low pO_2 hydrogen containing gas mixture gives the highest reduction rates while the high pO_2 hydrogen free gas gives the lowest. Reducing the oxygen partial pressure in the hydrogen free gas (increasing the CO content from 30 % to 70 %) increases the reduction rate by a factor 3.5 at constant temperature. The model derived from non-isothermal experiments in Larssen et al.[100] predicts a 3.6-fold increase in the reduction rate by increasing the CO content from 30% to 70%, which is very similar to this model.

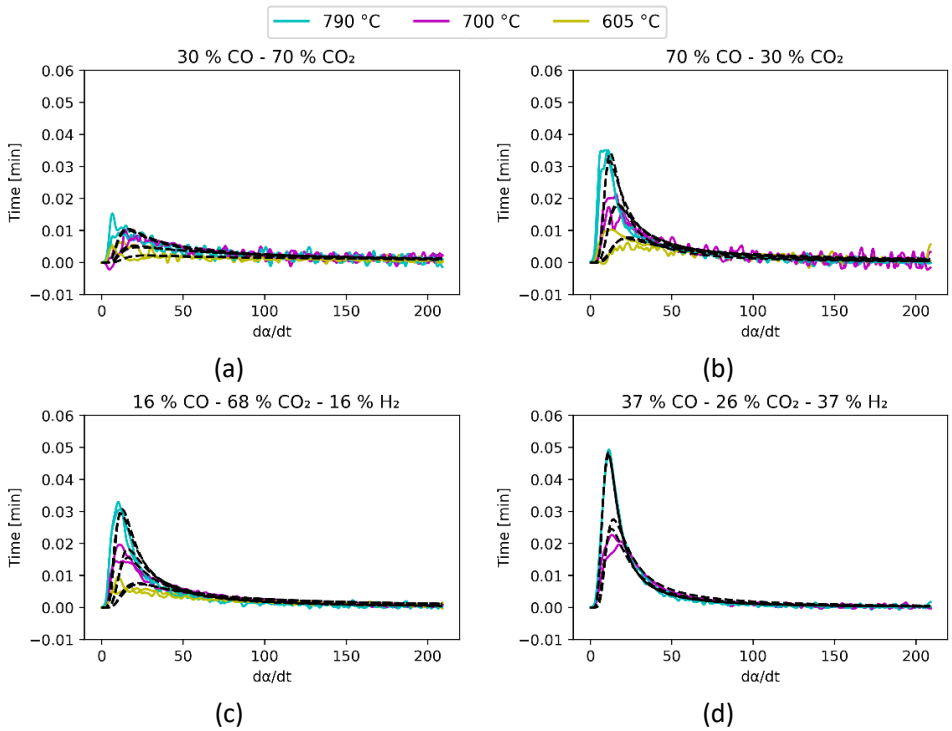

Figure 5-16: Shows the reduction rate with superimposed model predictions for each temperature. Nchwaning ore experiments at high and low oxygen partial pressure.

For Comilog ore, an apparent activation energy of 23.2 kJ/mol and a reaction order of 2 was found to best represent the reduction rate. The apparent pre-exponential constants from the model fitting are shown in Table 5-2. The predicted reduction rates based on the model parameters are superimposed (dashed lines) on the reduction rate curves in Figure 5-17. It can be seen from the figure that a reasonable fit is achieved in most of the gas mixtures. The largest deviations are seen in the medium pO_2 hydrogen free gas mixture. This value of the preexponential constant gives the lowest sum of squares. The misfit between the measured and predicted curves is caused by the high reduction rate difference

between the rapid decomposition of water, which is only temperature dependent, and the relatively slower reduction of oxides that follows (Figure 5-12).

Table 5-2: Shows the pre-exponential constants, k_0, according to equation (17) from modeling of the Comilog results. E_a = 23 kJ/mol and x = 2. The predicted reduction curves from the model parameters are superimposed on the measured reduction rate in Figure 5-17.

pO_2	Gas Mixture	k_0 [1/min]
High	30% CO - 70% CO_2	1.88
	16% CO - 68% CO_2 - 16% H_2	2.91
Medium	50% CO - 50% CO_2	1.55
	27% CO - 46% CO_2 - 27% H_2	4.27
Low	70% CO - 30% CO_2	3.77
	37% CO - 26% CO_2 - 37% H_2	4.99

To assess the dependency of reaction rate on reducing gas composition, equation (17) is utilized. In Figure 5-18, the logarithm of k_0 is plotted as a function of ln(1-CO_2) and the parameters m and k are determined based on the slope and y-intercept of the linear regression between the points.

Table 5-3 contains the kinetic parameters based on the results obtained in this work. The determined kinetic parameters apply for reduction of Nchwaning and Comilog ore in CO/CO_2 gas mixtures and in in CO/CO_2 gas mixtures containing hydrogen containing where the H_2/CO ratio is 1. Comparing the rate constants, and including the influence from the reducing gas content, it is seen that the introduction of hydrogen at constant partial pressure improves the reduction rate by factors of 1.8-3.4 and 1.7-1.9 for Nchwaning and Comilog ore, respectively, for the conditions studies in this work. In Figure 5-18b, the medium pO_2 rate constant for the hydrogen free gas mixtures is seen to be off the perceived line between the low and high pO_2 points. The values of k and m excluding this point was also calculated and is given in parenthesis in the table.

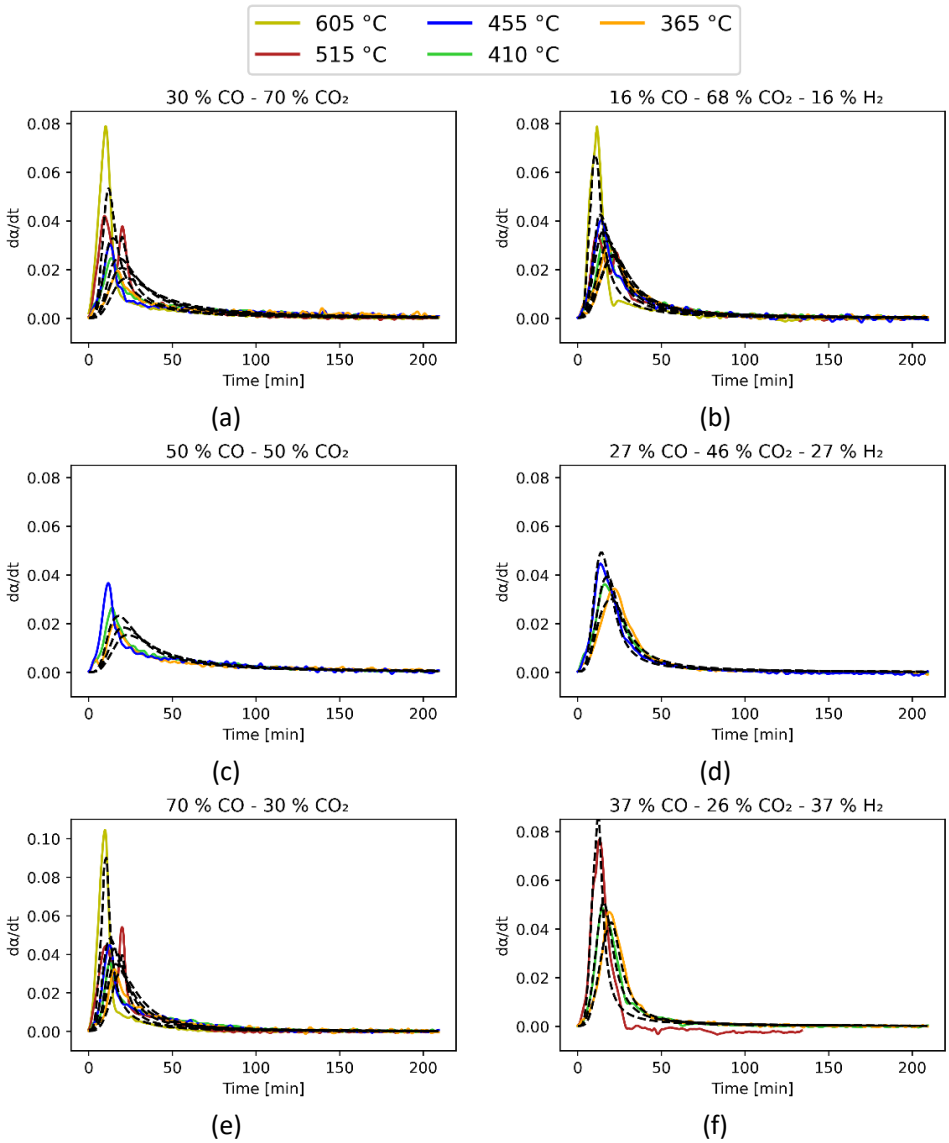

Figure 5-17: Shows the reduction rate with superimposed model predictions for each temperature and gas mixture for Comilog ore.

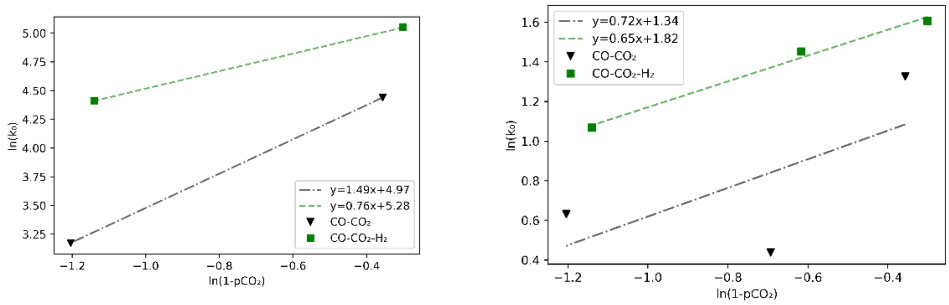

(a) (b)

Figure 5-18: The dependency of reaction rate on gas composition for (a): Nchwaning ore and (b): Comilog ore.

Table 5-3: Values obtained from modelling of Nchwaning and Comilog ore using equation (18). Numbers in parenthesis are excluding the medium pO_2

Parameter		Nchwaning		Comilog	
		CO/CO_2	*$CO/CO_2/H_2$*	*CO/CO_2*	*$CO/CO_2/H_2$*
k	Rate constant	144	196	3.82 (5.05)	6.18
Ea	Activation energy	68.1	68.1	23.2	23.2
x	Reaction order	2	2	2	2
m	Order of 1-CO_2	1.49	0.76	0.72 (0.82)	0.65

Gao et al[101] investigated fines of an undisclosed manganese ore in CO/CO_2 gas mixtures between 400-700 °C and found that the reduction rate was dependent on the p_{CO} (=1-p_{CO2} for CO/CO_2 gas mixtures) to the power of 1, which is approximately midway between the dependencies of Comilog and Nchwaning found in this work. Larssen[133] found the same dependency to be 0.7 and 1.5 for Comilog and Nchwaning ore, respectively, when reducing the ores non-isothermally up to 1000 °C, which is very similar to the observed dependency in this work.

5.2.3 Model simulations

The kinetic model developed in this work is based on isothermal experiments whereas the model developed in Larssen[133] was based on non-isothermal

experiments. As seen in the previous section, the models are similar in some respects, i.e., the dependency on CO content, however there are also differences.

The rate constant in this work and in the work of Larssen[133] are not directly comparable due to slight differences in the activation energies and since Larssen[133] also included the contribution from the particle size distribution. The model expression from Larssen is given in equation (19) where r_p^n is the particle size dependency, β is the heating rate and dα/dT is the reduction rate on a temperature basis while the other variables are the same as described in equation (17) and (18).

$$\frac{d\alpha}{dT} = \frac{k_0}{\beta}\exp\left(-\frac{E_a}{RT(t)}\right)(1-\alpha)p_{CO}^m r_p^n \qquad (19)$$

Using the particle size distribution from this work in Larssens[133] model and converting the temperature-based rate to the time-based rate $\left(\frac{d\alpha}{dt} = \frac{d\alpha}{dT}\frac{dT}{dt}, \frac{dT}{dt} = \beta\right)$, the two models can be compared directly.

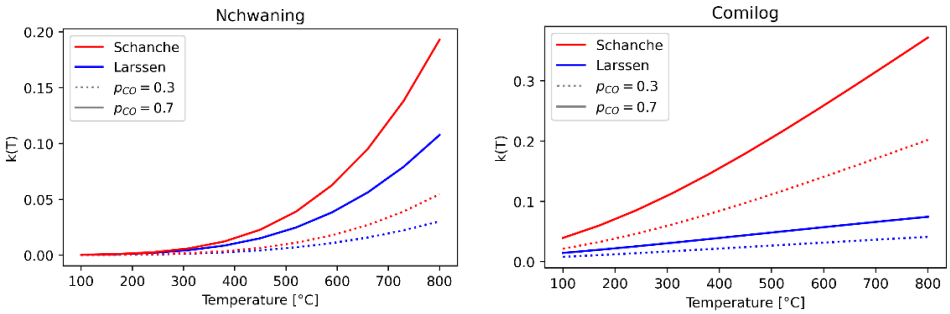

(a) (b)

Figure 5-19: The rate constant k(T) with p_{CO} 0.3 and 0.7, as a function of temperature for (a): Nchwaning ore and (b) Comilog ore using the models from this work (Schanche) and from Larssen[133].

The general expression for the reduction rate is $\frac{d\alpha}{dt} = k(T)f(\alpha)$. In Figure 5-19, the rate constant, k(T), from the two models are calculated as a function of temperature for Nchwaning and Comilog ore using p_{CO} of 0.3 and 0.7. It is seen that the rate constant in this work is higher under all conditions compared to the rate constant in Larssen[133]. The rate constants for Comilog are higher compared to Nchwaning ore, which reflects the higher reactivity of Comilog ore that was observed experimentally. The same reaction model (f(α)) is used for both ores within each investigation i.e. (1-α) in Larssen[133] and $(1-\alpha)^2$ in the current work. The reaction models give different contributions to the reduction rate and must be included to fully describe the reduction of the ores. Figure 5-20 shows simulated reduction rates for the first 30 minutes of isothermal reduction of Nchwaning and Comilog ore using the models developed in this work and by Larssen[133] for

reduction at low pO_2. The simulations show that the model developed in this work has a higher initial reduction rate and a low final reduction rate compared to the model from Larssen[133]. The hydrogen containing gas mixture obtains a higher initial reduction rate compared to the hydrogen free gas mixtures, which is as expected based on the experimental results.

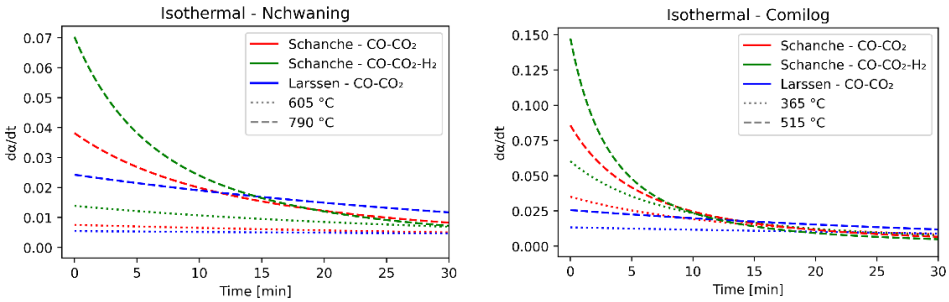

(a) (b)

Figure 5-20: Simulated reduction rates for the initial part of isothermal reduction of (a) Nchwaning and (b) Comilog ore. Reduction at low pO_2 based on the model expressions in this work (Schanche) and in Larssen[133]. pCO = 0.7 for hydrogen free gas mixtures and (1-pCO_2) = 0.74 for the hydrogen containing gas mixture.

The effect of the different reduction rates for the different models on the degree of reduction is shown in Figure 5-21. The figure shows simulated reduction curves for isothermal and nonisothermal reduction of Nchwaning and Comilog ore, plotted using the model developed in this work and the model developed by Larssen[133], for reduction at low pO_2. The temperatures and heating rates for the simulations were selected based on temperatures and heating rates in the respective investigations.

The reduction rates from the model in this work is higher in the initial part of the reduction, as was seen in Figure 5-20, however it is seen that the degree of reduction based on Larssen's model eventually exceeds the degree of reduction based on the model in this work. This is a consequence of the different mathematics used for the rate expressions; however, the mathematics is selected to best represent the experimental observations. From the Nchwaning ore results in this work, it was seen that limited decomposition of carbonates occurred. This was as expected in this temperature range; however, the slow decomposition rate of carbonates causes the model to rightfully predict a slow reduction rate towards the end of the experiments (Figure 5-21a and c). This effect is not prevalent in the work of Larssen[133] where the bulk of the experiments were ended at 1000 °C and carbonate decomposition occurred between 800-1000 °C. In Mukono et al.[87] it was found that the peak reduction rate of carbonates in Nchwaning ore occurred at

about 900 °C, hence, during the experiments up to 1000 °C in Larssens work, the reduction rate was not impeded due to slow carbonate decomposition.

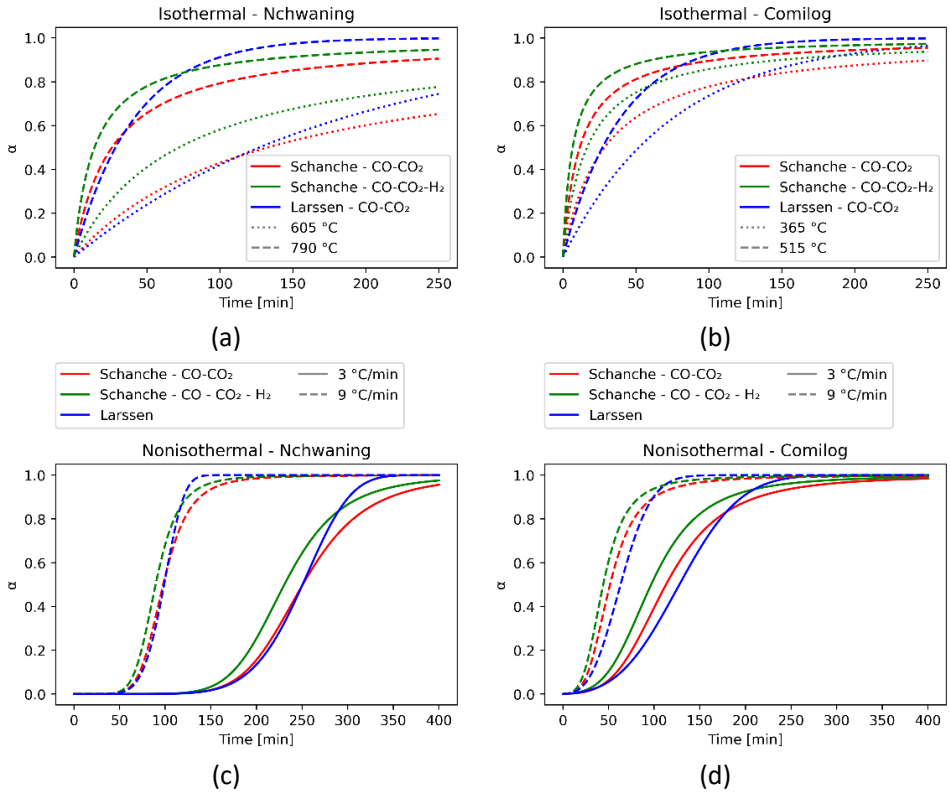

Figure 5-21: Shows simulated reduction curves for reduction at low pO_2 based on the model expressions in this work (Schanche) and in Larssen[133]. pCO = 0.7 for hydrogen free gas mixtures and (1-pCO_2) = 0.74 for the hydrogen containing gas mixture.

For Comilog ore, the deviation between the simulated curves from the two different models are more prevalent in the initial part of the reduction curve (Figure 5-21b and d). Due to the rapid heating rate in the isothermal experiments, water was expelled at a high rate from early stages of the experiments in this work. Coupled with the reduction of oxides, this gave a large reaction rate peak in the initial part of the experiments. In most of Larssen's experiments, the rapid reduction/decomposition peak occurred around 580 °C thus giving a larger contribution to the reduction rate at higher temperatures, which is consistent with the deviation between the different models.

5.3 Miscellaneous side effects

Reactions besides reduction and decomposition of original constituents of the ore was also seen to occur during the experiments. This section covers the occurrence of the water gas shift reaction, soot formation and reoxidation of the ore after reduction as well as decrepitation.

5.3.1 Water gas shift reaction

The occurrence of the water gas shift reaction (WGSR, equation (13)), which is repeated below for convenience, was observed during reduction with hydrogen containing gas mixtures, and it was seen that the extent of the reaction increased with increasing temperature. Figure 5-22 shows the reaction quotients (Q) calculated from the gas composition at the end of the experiments and equilibrium constants (K_{eq}) of the WGSR. The equilibrium constants are strictly different for the different gas mixtures, however the maximum deviation between the calculated Keq's for the different gas mixtures is less than 0.05, making it practically indistinguishable in the graph.

$$CO(g) + H_2O(g) = H_2(g) + CO_2(g) \qquad (13)$$

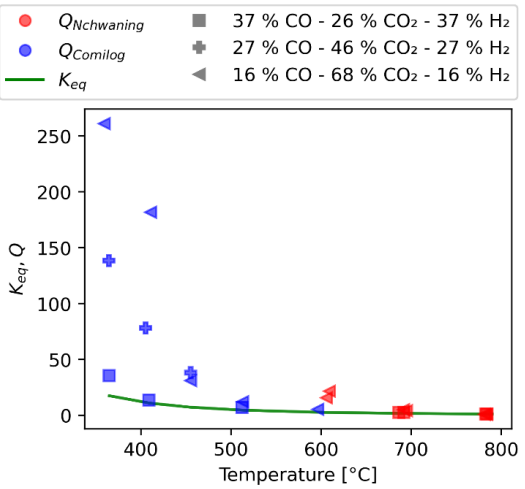

Figure 5-22: Shows the reaction quotients (Q) from the final gas composition of the hydrogen containing experiments and the equilibrium constant, Keq, from the water gas shift reaction, as a function of temperature. The equilibrium constants were calculated using HSC Chemistry[18]

At 365 °C, the gas composition was similar to the input composition, and there is a large deviation between the reaction quotient and the equilibrium constants (Figure 5-22), indicating that the WGSR is inactive at this temperature.

As the temperature increases, the deviation between the reaction quotients and the equilibrium constants decreases, and it is seen that the WGSR is close to equilibrium at 790 °C. These findings are in agreement with previous observations; Davies[84] observed that a significant fraction of CO_2 from decomposition of carbonates was converted to CO during reduction of UMK ore in H_2 and H_2/H_2O gas mixtures at 700-900 °C. During reduction of Comilog ore in $CO/CO_2/H_2O$ and CO/CO_2 gas mixtures with similar pO_2, Larssen and Tangstad[127] observed that the reduction rate of Comilog ore was improved due to the occurrence of the WGSR above 430 °C. Lobo[67] reduced Nchwaning ore isothermally at 950 °C and found that the WGSR was close to equilibrium for all tested CO - CO_2 - H_2 - H_2O gas mixtures.

5.3.2 Carbon deposition

Carbon deposition has been observed for several conditions in this and in other investigations during reduction of manganese ores[70,87,92,126,127,133]. The conditions at which carbon deposition was observed has been summarized in Table 5-4, and deposition generally occurs in gas mixtures with high CO content or when H_2 is present.

Table 5-4: Show the material, gas composition and temperatures where carbon deposition was identified in various investigations. Single temperatures indicate isothermal experiments and ranges indicate the temperature range where carbon deposition occurred in non-isothermal experiments.

Atmosphere *[%CO/%CO_2/%H_2]*	**Temperature** *[°C]*	**Material**	**Source**
27/46/27	455	Comilog	This work
37/26/37	515	Comilog	This work
37/26/37	605	Nchwaning	This work
41/41/18	630-800	Comilog	Ngoy et al.[126]
41/18/41	630-800	Comilog	Ngoy et al.[126]
80/20/0	400-780	Comilog	Larssen[133]
80/20/0	400-780	Quartz	Larssen[133]
70/17.5/12.5	390-500	Comilog	Larssen and Tangstad[127]
70/17.5/12.5	550-700	Nchwaning	Larssen and Tangstad[127]
43.8/43.8/12.5	400-700	Nchwaning	Larssen and Tangstad[127]

Carbon deposition was not seen in any of the experiments conducted in CO/CO_2 gas atmospheres in this work, however it has been seen in other works when using high CO contents. Larssen[133] compared the carbon deposition during reduction, with carbon deposition on a quartz sample using the same temperature conditions in a 80 % CO – 20 % CO_2 atmosphere. Carbon deposition occurred to a

lesser extent when the temperature range of carbon deposition overlapped with temperatures where ore was reduced due to depletion of the CO. A similar observation was done in this work and can be seen in Figure 5-23 which shows the weight loss as a function of time for reduction of Comilog ore in the low pO_2 atmosphere. An increase in the weight after about 30 minutes reduction can be seen for the experiment conducted at 515 °C. This weight increase was caused by carbon deposition, however prior to the weight increase, the weight behaves as expected, i.e., higher reduction rate compared to the lower temperature experiments. No evidence of carbon deposition was seen prior to this point, presumably due to depletion of CO and H_2 by reduction of the ore.

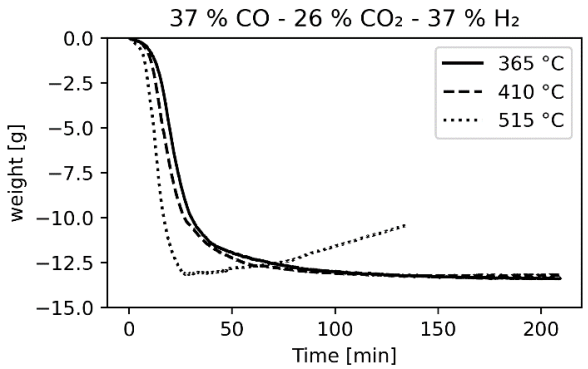

Figure 5-23: Shows the weight loss as a function of time for Comilog ore reduced at low pO_2.

The stability of CO increases with temperature (e.g., Figure 1-3); hence carbon deposition is expected at low temperatures and high CO contents. If the carbon deposition is governed by the Boudouard reaction (reaction (9), repeated below for convenience), the activity of carbon can be calculated for different CO/CO_2 ratios using the equilibrium constant (i.e. $a_c = \frac{1}{K_{eq}} \frac{p_{CO}^2}{p_{CO_2}}$). In hydrogen containing atmospheres, carbon deposition may also be caused by the reaction between H_2 and CO (reaction (20))[158].

$$C + CO_2 = 2CO \quad (9)$$

$$CO(g) + H_2(g) = C + H_2O(g) \quad (20)$$

The calculated activity of carbon as a function of temperature for the input composition of the gas mixtures utilized in this work is shown in Figure 5-24. When the activity of carbon reaches unity, solid carbon is stable and carbon deposition is possible, and below 580 °C carbon is stable for all gas compositions. The driving force for carbon deposition increases with increasing carbon activity, hence the carbon deposition is expected to increase with increasing CO/CO_2 ratio and

decreasing temperature. The input gas composition of the hydrogen containing gas mixtures in this work has a lower CO/CO_2 ratio compared to the corresponding CO/CO_2 gas mixtures which results in a lower a_C by the Boudouard reaction (Figure 5-24). On the other hand, the driving force for carbon deposition by reaction (20) is high since there is no H_2O in the input gas.

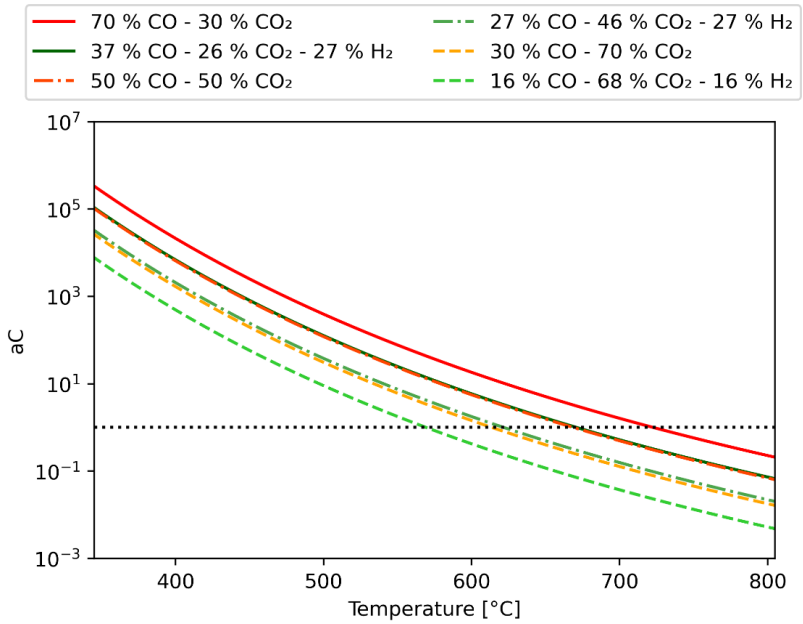

Figure 5-24: The activity of carbon based on the Boudouard reaction as a function of temperature for the gas mixtures used in this work. Solid lines – Low pO_2, dash-dot lines – medium pO_2, dashed lines – high pO_2.

As seen from the previous section, the WGSR is active under most conditions. Assuming that the WGSR is at equilibrium, increases the CO content and decreases the CO_2 content for the hydrogen containing gas mixtures used in this work. The increased CO content due to the WGSR was also seen in Larssen and Tangstad[127] where it was correlated with carbon deposition. Figure 5-25 shows the measured CO/CO_2 ratio and the equilibrium CO/CO_2 ratio, assuming the WGSR is at equilibrium, from the experiments conducted in hydrogen containing gas mixtures. The CO/CO_2 ratio from the hydrogen free experiment is also indicated in the figure. Below about 650 °C, the measured and the equilibrium CO/CO_2 ratios is seen to be lower compared to the corresponding CO/CO_2 gas mixtures, i.e., the WGSR establish conditions where carbon deposition according to the reverse Boudouard reaction has a lower driving force in hydrogen containing gases compared to the CO/CO_2 gas mixtures at the same pO_2. Regardless, carbon deposition was only observed in the H2 containing gas mixtures, indicating that the carbon deposition

is more kinetically favorable in hydrogen containing gas mixtures compared to CO/CO_2 gas mixtures.

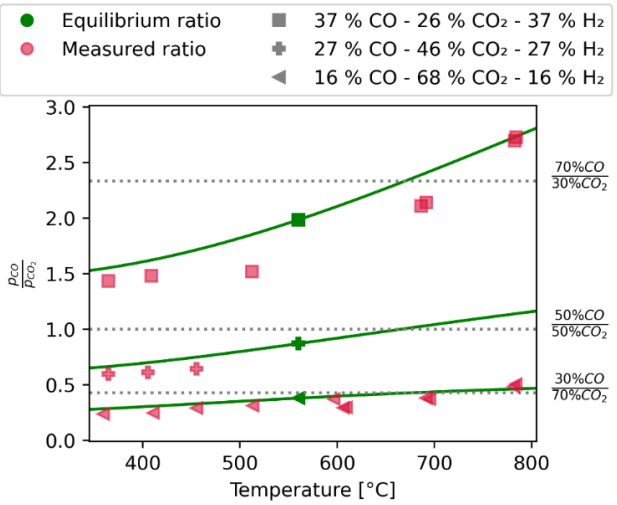

Figure 5-25: Shows the CO/CO_2 ratio for the measured off-gas composition at the end of the experiments with hydrogen containing gas mixtures and the CO/CO_2 ratio from the WGSR at equilibrium as functions of temperature. Dotted lines indicate the CO/CO_2 ratios for the CO/CO_2 gas mixtures used in this work.

5.3.3 Reoxidation

The occurrence of reoxidation of Comilog ore was discovered about halfway into the experimental series, and the reoxidation at room temperature was measured for the remaining experiments. Oxidation of manganese oxides has been investigated previously. Teguri et al.[41] reduced manganese ore with solid carbon in a rotating kiln in the temperature range 1000-1150 °C. Reoxidation of prereduced ore in air was investigated where the ore was found to oxidize rapidly above 600 °C. Chemical analysis indicated that the product of oxidation was Mn_3O_4 at 600 °C and 700 °C while limited oxidation was observed in the temperature range 300-500 °C. Barner and Mantell[112] observed that MnO from reduction of synthetic pyrolusite oxidized in air when reduction was conducted at temperatures ≤ 500 °C. No oxidation occurred in the partially reduced samples that did not contain MnO. Nanjundaswamy and Sankarshanamurthy[159] devised a method to stabilize MnO against oxidation in air. Heat treatment at 750-800 °C was seen to remove the active sites for oxidation of MnO and the produced MnO was stable upon heating in air up to 440 °C. Above this temperature, the MnO oxidized to Mn_3O_4. Heating in inert or reducing atmospheres at 1000 °C or doping with other oxides would achieve the same stabilizing effect on MnO[159]. Thus, it is seen that MnO may oxidize to Mn_3O_4 in air if it is produced at low temperatures.

In this work, all measurements were done on samples reduced at low temperatures (≤ 455 °C) since the reoxidation was discovered after the higher temperature experiments (515 °C and 605 °C) were conducted. The degree of reduction before and after reoxidation is shown in Figure 5-26 where the hollow and filled symbols represent the degree of conversion before and after reoxidation, respectively. The reduction degree of the samples reduced in CO/CO_2 atmospheres were close to or exceeded the average composition of Mn_3O_4 after reoxidation, indicating that all or most of the MnO oxidized. The samples that exceeded an average composition of Mn_3O_4 probably had remaining MnO_2 and/or Mn_2O_3 since oxidation of MnO does not exceed Mn_3O_4 during heating in air up to 440 °C[159]. This is also consistent with the observed reduction paths (Figure 5-11).

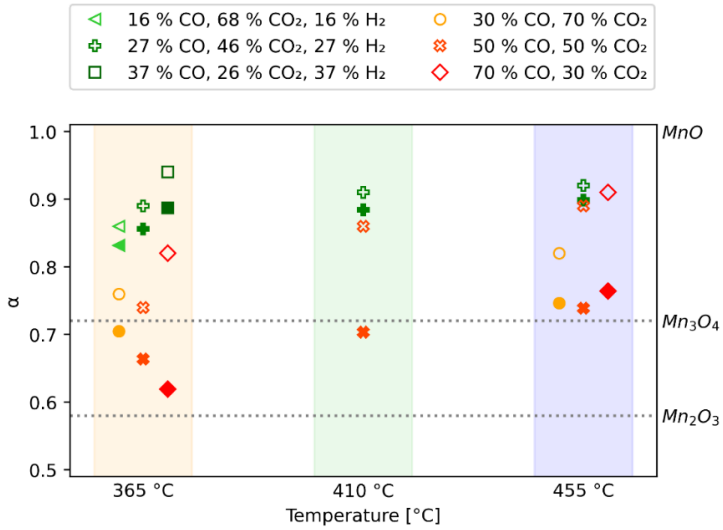

Figure 5-26: The degree of reduction before reoxidation (hollow symbols) and after reoxidation (filled symbols) for different temperatures. Horizontal lines indicate the manganese oxide corresponding to the degree of reduction.

In the samples reduced in the hydrogen containing gas mixtures, only a small proportion of the MnO was oxidized (Figure 5-26). This may indicate that the presence of hydrogen somehow reduces the amount of active sites for reoxidation of MnO, however in the work of Barner and Mantell[112], reduction was done in pure hydrogen and reoxidation was still observed.

The fraction of produced MnO in the hydrogen containing experiments may not be accessible to O_2 due to different diffusion properties. In Figure 5-27, it can be seen that CO and O_2 has similar diffusion coefficients in CO_2 while the diffusion coefficient of H_2 is significantly higher. This is also consistent with the observations from CT analysis (Figure 4-54), where after reduction with H_2, the

remaining higher oxides were seen to be more evenly distributed. Differences in mineral distribution may also affect reoxidation since it is the MnO that oxidizes. As an example, a composition of 100 % Mn_3O_4 and a composition of 38% MnO_2 – 62 % MnO both correspond to a degree of conversion of 0.72 (e.g., Figure 5-26). No definitive conclusion can be made based on the results in this work, further investigation is needed since reoxidation is an important factor that needs to be accounted for in the design and operation of a pre-treatment unit.

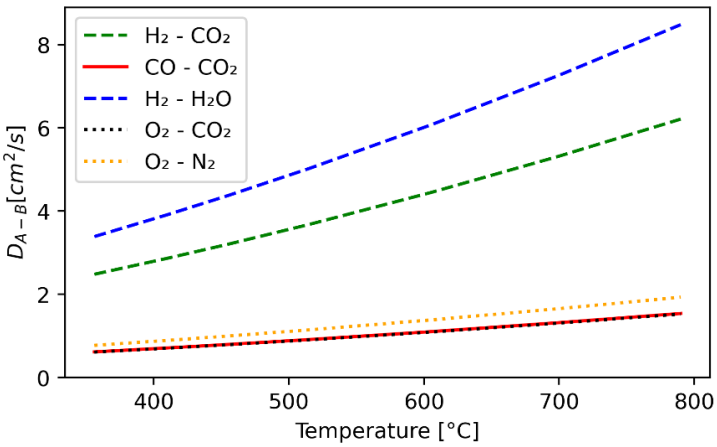

Figure 5-27: The binary diffusion coefficients of selected pairs of gases. Calculated by the method of Fuller et al.[157], details in Appendix G. The binary diffusion coefficient of O_2 – N_2 is included for reference

Oxidation of Nchwaning ore was not observed. The characteristic olive green color of MnO[112,159] was retained in fully reduced Nchwaning samples, indicating that Nchwaning ore did not oxidize. The MnO produced by reduction of Nchwaning ore was previously shown to contain significant quantities of FeO which may have stabilized the MnO against oxydation[159].

5.3.4 Decrepitation

It was seen in the results section that the decrepitation of Nchwaning ore was correlated with temperature, reducing gas mixture and degree of reduction. The reduction temperature directly influences the degree of reduction since the reduction rate is higher at higher temperatures, as does the different gas mixtures due to their influence on the reduction. Comparing different gas mixtures and temperatures at similar degree of reduction did not reveal any trends, hence it seems that the decrepitation of Nchwaning ore is dependent on the degree of reduction and that the degree of reduction in turn is dependent on temperature and reducing gas mixture. Similar observations were made in Larssen[133] and in Biørnstad[94,98]. Figure 5-28 shows the decrepitation as wt % larger than 3.35 mm for

reduction of Nchwaning ore as a function of O/Mn ratio from this and other investigations. The decrepitation of Nchwaning ore is similar for different heating regimes, thus supporting the observation that decrepitation is a function of degree of reduction for Nchwaning ore.

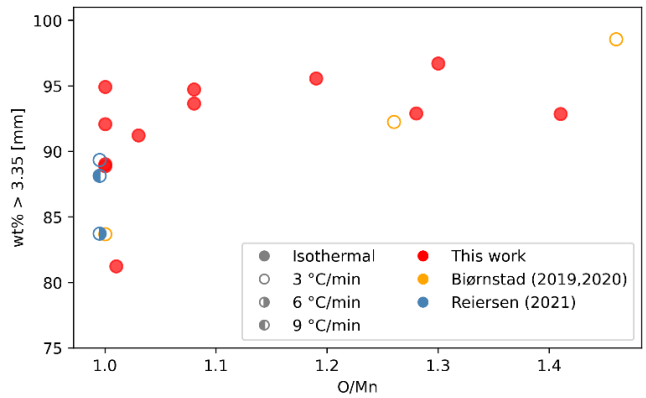

Figure 5-28: The wt% larger than 3.35 mm after reduction of Nchwaning ore, as a function of O/Mn ratio. The initial particle size in Biørnstad[94,98], Reiersen[92] and this work were 10-13.2 mm, 10-12.5 mm, and 9.5-15 mm, respectively.

For Comilog ore it was seen that the decrepitation decreased with increasing temperature, particularly the samples reduced at 605 °C and 515 °C displayed low degree of decrepitation despite them being close to fully reduced. Figure 5-29 shows the decrepitation of Comilog ore from this and other works as a function of O/Mn ratio. Both Larssen[133] and Reiersen[92] observed that decrepitation increased with decreasing heating rate for Comilog ore (Figure 5-29). Biswas et al.[129] investigated an Indian ore and found that the main mechanism for decrepitation was rapid expulsion of water and phase changes causing stress and rupture in the particles. However in Faria et al.[22], it was observed that the decomposition of hydrated minerals had a lower effect on decrepitation in the ores with highest porosity. Larssen[133] observed that samples that obtained a higher degree of reduction prior to the rapid exothermal peak decrepitated more, i.e. low temperature reduction increases decrepitation for Comilog ore. This is consistent with the observations in this work where the samples that reached the rapid reduction and decomposition stage i.e., samples reduced at 605 °C and 515 °C, decrepitated less compared to samples reduced at lower temperatures despite the lower degree of reduction for the latter. Hence, it seems that Comilog ore has a low sensitivity to decrepitation caused by H_2O decomposition which may be due to its high porosity. In addition, the phase changes occurring below the rapid reduction/decomposition peak cause more decrepitation compared to the rapid phase changes associated with the peak itself.

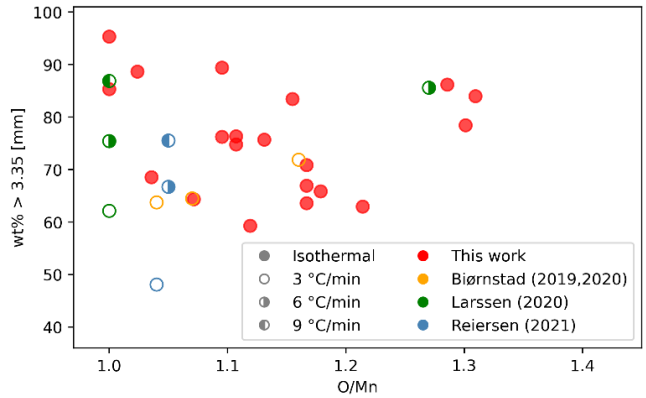

Figure 5-29: The wt% larger than 3.35 mm after reduction of Comilog ore, as a function of O/Mn ratio. The initial particle size in Biørnstad[94,98], Reiersen[92], Larssen[133] and this work were; 10-13.2 mm, 10-12.5 mm, 11.2-15 mm and 9.5-15 mm, respectively.

5.4 Industrial implications

It has been shown that by adding pretreated materials to the submerged arc furnace (SAF), carbon and energy consumption can be reduced. The energy and carbon consumption in any particular case is a function of factors such as type of raw materials and operational strategy (Table 2-1), however, industrial measurements[17,34] and calculations[19,33] give remarkably similar values for the excess consumption of carbon and energy. About 69 kg C and 300 kWh of energy per ton alloy produced can be saved if the Boudouard reaction is avoided. Similar figures were found in calculations done in this work (Figure 1-5). To produce a ferromanganese alloy with 78 % Mn, 7 % C and 15 % Fe, 171 kg C is consumed in the reduction of MnO, 70 kg C enters the alloy and 30 kg is consumed in the reduction of FeO to Fe making a total of 271 kg C per ton produced alloy as a theoretical minimum value. For every kg C consumed by the Boudouard reaction, 3.7 kg of CO_2 is produced, and 4 kWh of energy is consumed. The results in this work showed that reduction to MnO-FeO was possible during pretreatment below 800 °C, and if carbonates are disregarded, this prereduction will results in savings of about 40 kg C and 160 kWh per ton alloy produced.

Carbonates are present in many ores and may be required to adjust the chemistry of the slag, however there are some opportunities to reduce the amount of CO_2 from carbonates reacting in the Boudouard reaction. Replacing calcite with dolomite or magnesite may reduce available CO_2 in the furnace due to the lower decomposition temperature of magnesium carbonate compared to calcite. Replacing the calcite with burnt lime (CaO) is also an option, provided that it does not react with the CO_2 in the off-gas. It is also possible to achieve full pretreatment to MnO and metallic Fe. Obtaining metallic Fe requires higher temperatures or higher reduction potentials than what is used in this work due to the stabilization of FeO in the MnO phase. In Davies et al.[85], the iron oxides were reduced to metallic iron after reduction of UMK ore in 100 % H_2 at 700-900 °C, however the MnO-FeO solid solution is stable up to 1000 °C in 80 % CO[70] (Nchwaning and Comilog ore). The use of H_2 or H_2/H_2O atmospheres in prereduction facilitates carbonate decomposition[85], though it hinders the utilization of the furnace off-gas. Reduction of the flux additions to reduce the energy and carbon consumption is also an option that has been implemented successfully in industrial operation[4]. Larssen et al.[70] observed that the carbonates in Nchwaning ore decomposed in the temperature range 800-1000 °C in $CO\text{-}CO_2$ atmospheres. However, If the pretreatment temperature is increased to above 800 °C, the reductant cannot be passed through the pretreatment unit due to the possible occurrence of the Boudouard reaction.

Assuming 69 kg excess carbon consumption in standard production, 322 kg CO (257.5 Nm^3) is produced per ton alloy. The 171 kg C is consumed for reduction

of MnO alone yields 398 kg (318.2 Nm^3) CO for every ton alloy produced. Hence 44% of the gas volume exiting the furnace is supplied by the Boudouard reaction in this case. From previously reported materials balances, a gas volume of 615 Nm^3/ton alloy (DPR = 22 %)[16] and 586 Nm^3/ton alloy (DPR = 100 %)[12] has been calculated. Other contributions to the amount and composition of the off-gas are type and amount of carbonates, moisture, bound water and amount of excess oxygen in the raw materials. Nevertheless, it is seen that the occurrence of the Boudouard reaction gives a significant contribution to the composition and amount of off-gas. Hence, if prereduction is improved, it has the direct consequence that less CO is produced in the furnace, and there might be a need for additional reducing gas to fully prereduce the raw materials. Based on the results in this work, hydrogen is seen to be an excellent option for this purpose. Hydrogen may be obtained from CO_2 neutral sources, thus reducing the carbon footprint of the production. In addition, hydrogen is seen to improve the kinetics of prereduction.

From industrial production, Pais et al.[34] reported a gas volume of 500 Nm^3/ton alloy measured from a furnace running on a 100 % sinter charge. The inner diameter of the furnace was 12.8 m, and the production was 442 ton alloy/day. This yields a plug flow velocity in the furnace crucible of 0.020 m/s (at 0 °C). The plug flow velocity in the experiments in this work is 0.11 m/s (at 0 °C). If a pretreatment unit with a cross-sectional area of is 1/5 of the furnace is installed, the gas flow is directly comparable to the flow used in the experiments in this work.

6 Conclusions and future work

The reduction of Nchwaning and Comilog manganese ore was investigated at different oxygen partial pressures using CO/CO_2 gas mixtures with and without H_2. The reduction rate was seen to increase with increasing temperature and with decreasing oxygen partial pressure. Addition of hydrogen at constant oxygen partial pressure significantly increased the reduction rate for both ores.

The reduction of Nchwaning ore was investigated between 605-790 °C at two different oxygen partial pressures using CO/CO_2 gas mixtures with and without H_2. The Mn_2O_3 oxides initially found in the ore reduce to MnO in a single step, i.e., the reduction rate of Mn_3O_4 to MnO is greater or equal to the reduction rate of Mn_2O_3 to Mn_3O_4 between 605 °C and 790 °C. Hematite is reduced via magnetite to FeO which dissolves in the MnO-FeO solid solution. The reduction of iron oxides is improved by the presence of hydrogen. A small fraction of carbonates, associated with manganese, magnesium and iron decomposed under the current conditions while calcium carbonate was stable.

Comilog ore was investigated between 365-605 °C at three different oxygen partial pressures using CO/CO_2 gas mixtures with and without H_2. The reduction of Comilog ore is characterized by a rapid initial reduction rate due to simultaneous decomposition and reduction of H_2O and MnO_2. Reduction at lower temperatures is characterized by Mn_3O_4 and MnO being the main reduction products below and above 370 °C, respectively. A rapid reduction stage occurred in the experiments where the temperature of the ore reached 550-580 °C. This rapid reduction stage is caused by simultaneous reduction and decomposition of MnO_2.

The reduction rate of Comilog ore was higher compared to Nchwaning ore, partially due to the MnO_2 phases in Comilog being more reactive compared to the Mn_2O_3 phases in Nchwaning ore, but also it was seen that Comilog ore was fully reduced to MnO-FeO after reduction for 210 minutes at 605 °C while about 50 % of the oxides (on average) were reduced in Nchwaning ore at the same temperature and time. The highest reduction rate occurred prior to the occurrence of the highest temperatures during reduction of both ores, showing an increased resistance towards reduction as a function of reduction degree. This is consistent with increased diffusion resistance within the particle. The decelerating reduction rate as a function of conversion is another indication of diffusion controlled reduction.

The addition of hydrogen was seen to improve the reduction rate under all the studied conditions for both ores. The improved reduction rate with addition of hydrogen under constant thermodynamic driving force shows that the reduction rate is improved due to the improved diffusion rates in gas mixtures containing H_2 and H_2O. A kinetic model was developed to describe the overall reduction for each

ore. The model was seen to represent the reduction behavior of both ores under the applied conditions in this work. Under the current conditions, the addition of hydrogen was seen to improve the reduction rate by factors of 1.8-3.4 and 1.7-1.9 for Nchwaning and Comilog ore, respectively. Hydrogen addition also contributed to reactions from the gas phase; The water gas shift reaction occurred above 410 °C and approaches equilibrium at 790 °C. Hydrogen in the gas was also seen to facilitate carbon deposition in the temperature range 455-605 °C. Carbon deposition was suppressed by the depletion of CO and H_2 during reduction of the oxides.

The decrepitation of Nchwaning ore is a function of reduction extent while the decrepitation of Comilog ore is affected by at which temperature the reduction has occurred. Low temperature reduction increases the decrepitation of Comilog ore.

Future work

Some questions were answered, and new ones created during this work which may require an answer prior to industrial implementation of pretreatment.

The use of hydrogen in this work was studied in mixtures where $CO/H_2=1$. Some other ratios have been studied previously; however it would be interesting to investigate the limits of how much hydrogen needs to be added to improve prereduction and also if different compositions will influence the severity of carbon deposition.

Reoxidation of Comilog ore was seen to occur for the samples reduced at low temperatures and it was seen to have some dependence on which gas atmosphere was used for reduction. If prereduction is to be implemented industrially the temperature range and reducing gas where reoxidation should be fully mapped.

Carbon deposition in hydrogen containing atmospheres can be a disadvantage due to depletion of the reducing gas content causing incomplete prereduction if hydrogen is supplied in the pretreatment unit. On the other hand, if the deposited carbon can be reutilized in the SAF it may displace a fraction of the required reductant thus lowering the effective carbon consumption and ultimately lowering the CO_2 emissions for production. Further study to reveal the range of temperatures and gas compositions at which carbon deposition occurs, and at which conditions carbon can be reutilized, could be useful knowledge for industrial implementation of pretreatment units.

It was seen that the within the same ore, different phases and microstructures exists, both within the same particle and between different particles. If CT-analysis is done on an entire sample before and after an experiment, the differences in reduction behavior of separate particles and phases

may be studied closer. This could be coupled with mineralogical analysis with selected samples of reduced and partly reduced material, that are selected based on CT-results, which will give quantitative results regarding the phase development of manganese ores.

7 References

1. *The Norwegian Process Industries' Roadmap*. Norsk industri; 2016. Accessed June 20, 2019. https://www.norskindustri.no/siteassets/dokumenter/rapporter-og-brosjyrer/the-norwegian-process-industries-roadmap-summary.pdf

2. Surup GR, Trubetskaya A, Tangstad M. Charcoal as an Alternative Reductant in Ferroalloy Production: A Review. *Processes*. 2020;8(11):1432. doi:10.3390/pr8111432

3. Kaffash H, Surup GR, Tangstad M. Densification of Biocarbon and Its Effect on CO2 Reactivity. *Processes*. 2021;9(2):193. doi:10.3390/pr9020193

4. Davidsen J. *Reducing the CO2 Footprint from Simn Production by Optimization of Fluxes*. Social Science Research Network; 2021. doi:10.2139/ssrn.3926019

5. Bizhanov A, Kurunov I, Podgorodetskyi G, Dashevskyi V, Pavlov A. Extruded Briquettes – New Charge Component for the Manganese Ferroalloys Production. *ISIJ Int*. 2014;54(10):2206-2214. doi:10.2355/isijinternational.54.2206

6. Diaz L, Julia N, Amalric A, Nussbaum G, Bjelland KB. *Recycling of Mn-Rich Ore Fines, Dust and Sludge Briquettes in Mn Alloys Production*. Social Science Research Network; 2021. doi:10.2139/ssrn.3926126

7. Davey KP. The Development of an Agglomerate Through the Use of FeMn Waste. *Infacon X Int Ferro-Alloys Congr*.:9.

8. Fleuriault C, Bjelland KB. Carbon Footprint Reduction Opportunities in the Manganese Alloys Industry. In: Lazou A, Daehn K, Fleuriault C, Gökelma M, Olivetti E, Meskers C, eds. *REWAS 2022: Developing Tomorrow's Technical Cycles (Volume I)*. The Minerals, Metals & Materials Series. Springer International Publishing; 2022:573-576. doi:10.1007/978-3-030-92563-5_60

9. Wang H, Liu Y, Laaksonen A, et al. Carbon recycling – An immense resource and key to a smart climate engineering: A survey of technologies, cost and impurity impact. *Renew Sustain Energy Rev*. 2020;131:110010. doi:10.1016/j.rser.2020.110010

10. Haque N, Norgate T. Estimation of greenhouse gas emissions from ferroalloy production using life cycle assessment with particular reference to Australia. *J Clean Prod*. 2013;39:220-230. doi:10.1016/j.jclepro.2012.08.010

11. Dalaker H, Ringdalen E, Kolbeinsen L, Mårdalen J. *Road-Map for Gas in the Norwegian Metallurgical Industry: Greater Value Creation and Reduced Emissions*.; 2017. Accessed June 20, 2019. https://ntnuopen.ntnu.no/ntnu-xmlui/handle/11250/2488736

12. Tangstad M, Ichihara K, Ringdalen E. PRETREATMENT UNIT IN FERROMANGANESE PRODUCTION. *14th Int Ferroalloys Congr*. Published online 2015:8.

13. Transforming our world: the 2030 Agenda for Sustainable Development | Department of Economic and Social Affairs. Published 2015. Accessed May 24, 2022. https://sdgs.un.org/2030agenda

14. Kero IT, Dalaker H, Sende Osen K, Ringdalen E. *Some Carbon-Free Technologies for Manganese Ferroalloy Production*. Social Science Research Network; 2021. doi:10.2139/ssrn.3926069

15. Safarian J. A Sustainable Process to Produce Manganese and Its Alloys through Hydrogen and Aluminothermic Reduction. *Processes*. 2022;10(1):27. doi:10.3390/pr10010027

16. Olsen SE, Tangstad M, Lindstad T. *Production of Manganese Ferroalloys*. tapir academic press; 2007.

17. Ahmed A, Haifa H, El-Fawakhry MK, El-Faramawy H, Eissa M. Parameters Affecting Energy Consumption for Producing High Carbon Ferromanganese in a Closed Submerged Arc Furnace. *J Iron Steel Res Int*. 2014;21(7):666-672. doi:10.1016/S1006-706X(14)60103-5

18. Roine A. HSC Chemistry®. Published online 2018.

19. Cowx PM, Nussbaum G. A CRITICAL COMPARISON OF FeCr AND FeMn. *Infacon XV Int Ferro-Alloys Congr*. Published online 2018:12.

20. Larssen TA, Tangstad M, Kero IT. Energy distribution in HC FeMn and SiMn energy vs exergy analyses. *J South Afr Inst Min Metall*. 2019;119(12):1071-1076. doi:10.17159/2411-9717/788/2020

21. O'Shaughnessy P, Kon KJ, Wha LB. The Smelting of Manganese Carbonate Ore. *10th Int Ferroalloys Congr*. Published online 2004:8.

22. Faria GL, Jannotti N, Araújo FG da S. Decrepitation behavior of manganese lump ores. *Int J Miner Process*. 2012;102-103:150-155. doi:10.1016/j.minpro.2011.10.004

23. Visser M, Smith H, Ringdalen E, Tangstad M. PROPERTIES OF NCHWANINGAND GLORIA ORE IN THE PRODUCTION OF Mn FERRO-ALLOYS. *13th Int Ferroalloys Congr*. Published online 2013:14.

24. Pereira MJ, Lima MMF, Lima RMF. Calcination and characterisation studies of a Brazilian manganese ore tailing. *Int J Miner Process*. 2014;131:26-30. doi:10.1016/j.minpro.2014.08.003

25. Coetsee T. The role of manganese ore reduction morphology development in setting reduction mechanisms. *Miner Eng*. 2019;137:217-231. doi:10.1016/j.mineng.2019.04.006

26. Frondel C, Bauer LH. Kutnahorite: A manganese dolomite, CaMn(Co3)2*. *Am Mineral*. 1955;40(7-8):748-760.

27. Bale CW, Bélisle E, Chartrand P, et al. FactSage thermochemical software and databases, 2010–2016. *Calphad*. 2016;54:35-53. doi:10.1016/j.calphad.2016.05.002

28. Criado JM, Gonzalez F, Gonzalez M. Influence of the Co2 pressure on the kinetics of thermal decomposition of manganese carbonate. *J Therm Anal*. 1982;24(1):59-65. doi:10.1007/BF01914800

29. Wang Y, Lin S, Suzuki Y. Study of Limestone Calcination with CO2 Capture: Decomposition Behavior in a CO2 Atmosphere. *Energy Fuels*. 2007;21(6):3317-3321. doi:10.1021/ef700318c

30. Engler P, Santana MW, Mittleman ML, Balazs D. Non-isothermal, in situ XRD analysis of dolomite decomposition. *Thermochim Acta*. 1989;140:67-76. doi:10.1016/0040-6031(89)87285-5

31. Iwafuchi K, Watanabe C, Otsuka R. Thermal decomposition of magnesian kutnahorite. *Thermochim Acta*. 1983;60(3):361-381. doi:10.1016/0040-6031(83)80257-3

32. Ishak R, Tangstad M. DEGREE OF PREREDUCTION WITHOUT COKE CONSUMPTION IN INDUSTRIAL FURNACES. *11th Int Ferroalloys Congr*. Published online 2007:14.

33. Kazdal T, Haas-Wittmuess R, Richter S, Lang S, Binder C, Reuter M. *Process Design for the Pre-Treatment of Manganese Ores*. Social Science Research Network; 2021. doi:10.2139/ssrn.3926619

34. Pais J, Brown W, Saab MW. Production of HCFeMn Using High Proportions of Sinter in the Charge. In: ; 1998:6.

35. Schanche TL, Tangstad M. *Isothermal Reduction of Nchwaning Manganese Ore in CO/CO2/H2 Atmospheres*. Social Science Research Network; 2021. Accessed October 11, 2021. https://papers.ssrn.com/abstract=3926158

36. Swamy KN, Robertson DGC, Calvert P, Kozak D. Factors affecting Carbon Consumption in the Production of High Carbon Ferromanganese. *9th Int Ferroalloys Congr*. Published online 2001:9.

37. Turkova K, Slizovskiy D, Tangstad M. CO Reactivity and Porosity of Manganese Materials. *ISIJ Int*. 2014;54(6):1204-1208. doi:10.2355/isijinternational.54.1204

38. Eissa M, El-Faramawy H, Ahmed A, Nabil S, Halfa H. Parameters Affecting the Production of High Carbon Ferromanganese in Closed Submerged Arc Furnace. *J Miner Mater Charact Eng*. 2012;11(01):1-20. doi:10.4236/jmmce.2012.111001

39. Tangstad M, Calvert P, Brun H, Lindseth AG. USE OF COMILOG ORE IN FERROMANGANESE PRODUCTION. In: ; 2004:10.

40. TOMIOKA T, MlSAWA M, Ano TH. An Integrated Production System for Manganese Ferro-alloys. In: ; 1974:4.

41. Teguri D, Saito K, Miyauchi Y. Manganese ore pre-reduction using a rotary kiln to manufacture super-low-phosphorus ferromanganese. *Infacon XV Int Ferro-Alloys Congr*. Published online February 2018:14.

42. Pochart G, Joncourt L, Touchard N, Perdon C. METALLURGICAL BENEFIT OF REACTIVE HIGH GRADE ORE IN MANGANESE ALLOYS MANUFACTURING. *11th Int Ferroalloys Congr*. Published online 2007:14.

43. Soller A, Amalric A, Pochart G, Nussbaum G. MANGANESE ORE AND ALLOYS PILOTING TOOLS AT ERAMET RESEARCH. *12th Int Ferroalloys Congr*. Published online 2010:10.

44. Julia N, Hecquet A, Nussbaum G, Blancher S, Amalric A. *Pre-Heating Manganese Ore in a Pilot-Scale Rotary Kiln*. Social Science Research Network; 2021. doi:10.2139/ssrn.3926242

45. Yoshida F, Honma T, Sasaki T. Automation and Reduction of Labor in the Operation of Electric Arc Furnace for HCFeMn Production. *8th Int Ferroalloys Congr Proc*. Published online June 1998:6.

46. Ishitobi T, Ichihara K, Homma T. OPERATIONAL IMPROVEMENTS OF A SUBMERGED ARC FURNACE IN KASHIMA WORKS (KF-1) RELINED IN 2006. *Twelfth Int Ferroalloy Congr*. Published online 2010:8.

47. Gutzmer J, Beukes NJ. Mineral paragenesis of the Kalahari managanese field, South Africa. *Ore Geol Rev*. 1996;11(6):405-428. doi:10.1016/S0169-1368(96)00011-X

48. Singh V, Chakraborty T, Tripathy SK. A Review of Low Grade Manganese Ore Upgradation Processes. *Miner Process Extr Metall Rev*. 2020;41(6):417-438. doi:10.1080/08827508.2019.1634567

49. Sorensen B, Gaal S, Ringdalen E, Tangstad M, Kononov R, Ostrovski O. Phase compositions of manganese ores and their change in the process of calcination. *Int J Miner Process*. 2010;94(3):101-110. doi:10.1016/j.minpro.2010.01.001

50. Naruse W. The Production of Manganese Alloys by the Sintering Process. In: ; 1974:6.

51. Rao ChS, Bhargava NRMR. Manganese ferroalloys (FeMn & SiMn) and it's better smelting efficiency with more usage of quality agglomerate (Sinter). In: *2016 International Conference on Electrical, Electronics, and Optimization Techniques (ICEEOT)*. IEEE; 2016:3853-3858. doi:10.1109/ICEEOT.2016.7755434

52. Pienaar PC, Smith WFP. A Case Study of the Production of High-grade Manganese Sinter from Low-grade Mamatwan Manganese Ore. In: ; 1992:8.

53. Jesus LGMD, Tangstad M. CO Reactivity of Manganese Lumps Versus Briquettes. *ISIJ Int*. 2020;60(10):2129-2133. doi:10.2355/isijinternational.ISIJINT-2019-493

54. Tangstad M, Leroy D, Ringdalen E. BEHAVIOR OF AGGLOMERATES IN FERROMANGANESE PRODUCTION. *12th Int Ferroalloys Congr*. Published online 2010:11.

55. de Jesus LGM, Tangstad M. *Prereduction of Manganese Briquettes Produced with Tailing Dam Materials from Urucum/Brazil*. Social Science Research Network; 2021. doi:10.2139/ssrn.3926271

56. Dubos JL, Orberger B, Milazzo JM, et al. Agglomeration potential evaluation of industrial Mn dusts and sludges based on physico-chemical characterization. *Powder Technol*. 2020;360:1079-1091. doi:10.1016/j.powtec.2019.10.101

57. YOSHIKOSHI H, TAKEUCHI O, MIYASHITA T, KUWANA T, KISHIKAWA K. Development of Composite Cold Pellet for Silico-manganese Production. *Trans Iron Steel Inst Jpn*. 1984;24(6):492-497. doi:10.2355/isijinternational1966.24.492

58. Buyuran DMS, Yildirim G, BUtUn B. NODULIZING FINE MANGANESE ORES IN A PILOT PLANT ROTAR! KILN. In: Vol 2. ; 1982:947-953.

59. Reyes IA, Flores M, Palacios EG, et al. Kinetics of the Thermal Decomposition of Rhodochrosite. *Minerals*. 2021;11(1):34. doi:10.3390/min11010034

60. Tangstad M, Ringdalen E, Manilla E, Davila D. Production of FeMn Alloys with Heat Treated Mn-Nodules. In: Hwang JY, Jiang T, Pistorius PC, et al., eds. *7th International Symposium on High-Temperature Metallurgical Processing*. Springer International Publishing; 2016:181-188. doi:10.1007/978-3-319-48093-0_23

61. Tangstad M, Ringdalen E, Manilla E, Davila D. Pilot Scale Production of Manganese Ferroalloys Using Heat-Treated Mn-Nodules. *JOM*. 2017;69(2):358-364. doi:10.1007/s11837-016-2216-3

62. Ostrovski O, Anacleto N, Ganguly S. Reduction of Manganese Ores by Methane-containing Gas. *Infacon X Int Ferro-Alloys Congr*. Published online 2004.

63. Akdogan G, Eric RH. Carbothermic reduction behaviour of wessel manganese ores. *Miner Eng*. 1994;7(5):633-645. doi:10.1016/0892-6875(94)90095-7

64. Akdogan G, Eric RH. Kinetics of the solid-state carbothermic reduction of wessel manganese ores. *Metall Mater Trans B*. 1995;26(1):13-24. doi:10.1007/BF02648973

65. Fahim MS, El Faramawy H, Ahmed AM, Ghali SN, Kandil AEHT. Characterization of Egyptian Manganese Ores for Production of High Carbon Ferromanganese. *J Miner Mater Charact Eng*. 2013;01(02):68-74. doi:10.4236/jmmce.2013.12013

66. Wu P, Eriksson G, Pelton AD. Critical Evaluation and Optimization of the Thermodynamic Properties and Phase Diagrams of the CaO–FeO, CaO–MgO,

CaO–MnO, FeO–MgO, FeO–MnO, and MgO–MnO Systems. *J Am Ceram Soc*. 1993;76(8):2065-2075. doi:10.1111/j.1151-2916.1993.tb08334.x

67. Lobo S. *Reduction of Manganese Ores Using CO, H2, CO2 and H2 Blends*. Norwegian University of Science and Technology; 2015.

68. Liu B, Zhang Y, Su Z, Li G, Jiang T. Phase Transformation of MnO2 and Fe2O3 Briquettes Roasted Under CO–CO2 Atmospheres. In: Ikhmayies S, Li B, Carpenter JS, et al., eds. *Characterization of Minerals, Metals, and Materials 2017*. The Minerals, Metals & Materials Series. Springer International Publishing; 2017:311-319.

69. Liu B, Zhang Y, Wang J, et al. New understanding on separation of Mn and Fe from ferruginous manganese ores by the magnetic reduction roasting process. *Appl Surf Sci*. 2018;444:133-144. doi:10.1016/j.apsusc.2018.02.234

70. Larssen TA, Senk D, Tangstad M. Reduction of Manganese Ores in CO-CO2 Atmospheres. *Metall Mater Trans B*. Published online November 20, 2020. doi:10.1007/s11663-020-02018-0

71. Cheraghi A, Becker H, Eftekhari H, Yoozbashizadeh H, Safarian J. Characterization and calcination behavior of a low-grade manganese ore. *Mater Today Commun*. 2020;25:101382. doi:10.1016/j.mtcomm.2020.101382

72. Gao L, Liu Z, Pan Y, Feng C, Chu M, Tang J. Systematic study on separation of Mn and Fe from ferruginous manganese ores by carbothermic reduction roasting process: Phase transformation and morphologies. *J Mater Res Technol*. 2019;8. doi:10.1016/j.jmrt.2019.09.028

73. Sorensen B, Gaal S, Tangstad M, Ringdalen E, Kononov R, Ostrovski O. PROPERTIES OF MANGANESE ORES AND THEIR CHANGE IN THE PROCESS OF CALCINATION. *Infacon XII Int Ferro-Alloys Congr*. Published online 2010:10.

74. Kalenga M, Tangstad M, Pan X. Phase Relations in Ferromanganese Production During Prereduction: South African Ores. *Metallurgist*. 2019;62(11):1100-1114. doi:10.1007/s11015-019-00762-6

75. Grimsley WD, See JB, King RP. The mechanism and rate of reduction of Mamatwan manganese ore fines by carbon. *J South Afr Inst Min Metall*. Published online 1977:12.

76. Coetsee T, Reinke C, Nell J, Pistorius PC. Reduction Mechanisms in Manganese Ore Reduction. *Metall Mater Trans B*. 2015;46(6):2534-2552. doi:10.1007/s11663-015-0414-y

77. Berg KL. *Gaseous Reduction of Manganese Ores*. Norwegian University of Science and Technology; 1998.

78. Berg KL, Olsen SE. Kinetics of manganese ore reduction by carbon monoxide. *Metall Mater Trans B*. 2000;31(3):477-490. doi:10.1007/s11663-000-0154-4

79. Tangstad M, Wasb S, Sibony M, Tronstad R. Kinetics of the Prereduction of Manganese Ores. *Infacon IX Int Ferro-Alloys Congr*. Published online 2001:6.

80. Schanche TL, Tangstad M. Prereduction of Nchwaning Ore in CO/CO2/H2 Gas Mixtures. *Minerals*. 2021;11(10):1097. doi:10.3390/min11101097

81. Cheraghi A, Yoozbashizadeh H, Safarian J. Gaseous Reduction of Manganese Ores: A Review and Theoretical Insight. *Miner Process Extr Metall Rev*. Published online August 8, 2019:1-18. doi:10.1080/08827508.2019.1604523

82. El-Gawad HHA, Ahmed MM, El-Hussiny NA, Shalabi MEH. Reduction of Low Grade Egyptian Manganese Ore via Hydrogen at 800℃ - 950℃. *Open Access Libr J*. 2014;1(4):1-11. doi:10.4236/oalib.1100427

83. El-Hussiny N, H.Abd El-Gawad H, F.M. M, Shalabi M. Pelletization and Reduction of Egyptian Low Grade Manganese Ore Pellets via Hydrogen at 750-950°C. *Int J Sci Eng Res*. Published online Mai 2015.

84. Davies J. *The Use of Hydrogen as a Reductant in the Smelting Industry*. Master Thesis. North-West University; 2022.

85. Davies J, Tangstad M, Schanche TL, du Preez SP. Pre-reduction of United Manganese of Kalahari ore in CO/CO 2 , H2 /H2O, and H2 atmospheres. *Mater Sci Eng B*. To be published.

86. Sukhomlinov D, Tangstad M. Non-isothermal pre-reduction of carbonated manganese ore by carbon monoxide. *Be Publ*.

87. Mukono T, Reiersen HS, Schanche TL, Wallin M, Tangstad M. Prereduction Behavior of Manganese Ores With Solid Carbon and in CO/CO2 Gas Atmosphere. *Metall Mater Trans B*. Published online August 16, 2022. doi:10.1007/s11663-022-02611-5

88. Ling X, Elliott R, Barati M. Effect of Sintering and Porosity Development on Direct Reduction of Manganese Ore Pellets. *JOM*. 2021;73(1):334-344. doi:10.1007/s11837-020-04479-9

89. Szekely J, Evans JW, Sohn HY. *Gas-Solid Reactions*. Academic press; 1976.

90. Ringdalen E, Gjøvik JE, Larssen TA, Tangstad M. *Pretreatment of Manganese Ores in Different Gas-Atmospheres- a Method to Reduce Energy Consumption and Co2 Emissions in Mn-Alloy Production*. Social Science Research Network; 2021. Accessed October 5, 2021. https://papers.ssrn.com/abstract=3930059

91. Hamuyuni J, Saarenmaa J, Mäkelä P, et al. *Pretreatment of Manganese Ore for Improved Energy Efficiency and Smelting Furnace Stability*. Social Science Research Network; 2021. doi:10.2139/ssrn.3926120

92. Reiersen HS. *Behavior of Manganese Ores during Pre-Reduction in Small Scale Furnaces*. Master Thesis. Norwegian University of Science and Technology; 2021.

93. Mukono T, Gjøvik JE, Gærtner H, Wallin M, Ringdalen E, Tangstad M. *Extent of Ore Prereduction in Pilot-Scale Production of High Carbon Ferromanganese*. Social Science Research Network; 2021. doi:10.2139/ssrn.3926275

94. Biørnstad O. *Decrepitation of Comilog, Assmang and UMK Manganese Ores*. Master Thesis. Norwegian University of Science and Technology; 2020.

95. Kleyenstuber ASE. The mineralogy of the manganese-bearing Hotazel formation, of the Proterozoic Transvaal Sequence in Griqualand West, South Africa. *South Afr J Geol*. 1984;87(3):257-272.

96. Beukes NJ, Swindell EPW, Wabo H. Manganese Deposits of Africa. *Episodes*. 2016;39(2):285-317. doi:10.18814/epiiugs/2016/v39i2/95779

97. Ishak RJ. *Reaction Kinetics for Reduction of Manganese Ore with Carbon Monoxide in the Presence of Carbon*. PhD. Norwegian University of Science and Technology; 2002.

98. Biørnstad O. *Decrepitation of Comilog and UMK Manganese Ores during Pre-Reduction*. NTNU; 2019.

99. Larssen TA, Tangstad M, Kero IT. Gaseous Reduction of Mn Ores in CO-CO2 Atmosphere. In: Davis BR, Moats MS, Wang S, et al., eds. *Extraction 2018*.

The Minerals, Metals & Materials Series. Springer International Publishing; 2018:1093-1101.

100. Larssen TA, Senk D, Tangstad M. Reaction Rate Analysis of Manganese Ore Prereduction in CO-CO2 Atmosphere. *Metall Mater Trans B*. Published online April 29, 2021. doi:10.1007/s11663-021-02162-1

101. Gao YB, Kim HG, Sohn HY. Kinetics of pre-reduction of manganese ore by CO. *Miner Process Extr Metall Trans Inst Min Metall Sect C*. 2012;121(2):109-116. doi:10.1179/1743285512Y.0000000003

102. Eric RH, Burucu E. The mechanism and kinetics of the carbothermic reduction of mamatwan manganese ore fines. *Miner Eng*. 1992;5(7):795-815. doi:10.1016/0892-6875(92)90247-7

103. Kononov R, Ostrovski O, Ganguly S. Carbothermal Solid State Reduction of Manganese Ores: 2. Non-isothermal and Isothermal Reduction in Different Gas Atmospheres. *ISIJ Int*. 2009;49(8):1107-1114. doi:10.2355/isijinternational.49.1107

104. Kor GJW. The thermal decomposition of Mn2O3 and the reduction of Mn3O4 by C and CO. *Metall Trans B*. 1978;9(2):307-311. doi:10.1007/BF02653697

105. Anacleto N, Ostrovski O, Ganguly S. Reduction of Manganese Oxides by Methane-containing Gas. *ISIJ Int*. 2004;44(9):1480-1487. doi:10.2355/isijinternational.44.1480

106. Elliott R, Barati M. Reduction of Manganese Ore Pellets in a Methane-Containing Atmosphere. In: Davis BR, Moats MS, Wang S, et al., eds. *Extraction 2018*. Springer International Publishing; 2018:1129-1140. doi:10.1007/978-3-319-95022-8_92

107. Anacleto N, Ostrovski O, Ganguly S. Reduction of Manganese Ores by Methane-containing Gas. *ISIJ Int*. 2004;44(10):1615-1622. doi:10.2355/isijinternational.44.1615

108. Eric RH, Bhalla A, Halli P, Taskinen P. Solid State Reduction of Iron, Manganese and Chromium Oxide Ores with Methane. In: Wang S, Free ML, Alam S, Zhang M, Taylor PR, eds. *Applications of Process Engineering Principles in Materials Processing, Energy and Environmental Technologies*. The Minerals, Metals & Materials Series. Springer International Publishing; 2017:307-318.

109. Cheraghi A, Yoozbashizadeh H, Ringdalen E, Safarian J. Kinetics and Mechanism of Low-Grade Manganese Ore Reduction by Natural Gas. *Metall Mater Trans B*. 2019;50(4):1566-1580. doi:10.1007/s11663-019-01574-4

110. Cheraghi A, Yoozbashizadeh H, Safarian J. Carburization of Manganese Oxide Sources by Natural Gas. *Metall Mater Trans B*. Published online January 21, 2022. doi:10.1007/s11663-021-02398-x

111. Kononov R, Ostrovski O, Ganguly S. Carbothermal Solid State Reduction of Manganese Ores: 1. Manganese Ore Characterisation. *ISIJ Int*. 2009;49(8):1099-1106. doi:10.2355/isijinternational.49.1099

112. Barner HE, Mantell CL. Kinetics of Hydrogen Reduction of Manganese Dioxide. *Ind Eng Chem Process Des Dev*. 1968;7(2):285-294. doi:10.1021/i260026a023

113. De Bruijn TJW, Soerawidjaja TH, De Jongt WA, Van Den Berg PJ. Modelling of the reduction of manganese oxides with hydrogen. *Chem Eng Sci*. 1980;35(7):1591-1599. doi:10.1016/0009-2509(80)80052-2

114. Reuter MA, Van Deventer JSJ. Kinetic model for the carbothermic reduction of manganese dioxide. *Thermochim Acta*. 1988;125:99-106. doi:10.1016/0040-6031(88)87214-9

115. Rankin WJ, Van Deventer JSJ. The kinetics of the reduction of manganous oxide by graphite. *J South Afr Inst Min Metall*. 1980;80(7):239-247. doi:10.10520/AJA0038223X_1063

116. Abdel Halim KS, Bahgat M, Morsi MB, El-Barawy K. Pre-reduction of manganese ores for ferromanganese industry. *Ironmak Steelmak*. 2011;38(4):279-284. doi:10.1179/030192310X12827375731465

117. Eom CH, Min DJ. Kinetics of the formation reaction of manganese carbide under various gases. *Met Mater Int*. 2016;22(1):129-135. doi:10.1007/s12540-015-5419-1

118. Kononov R, Ostrovski O, Ganguly S. Carbothermal Reduction of Manganese Oxide in Different Gas Atmospheres. *Metall Mater Trans B*. 2008;39(5):662-668. doi:10.1007/s11663-008-9191-1

119. Elliott R, Coley K, Mostaghel S, Barati M. Review of Manganese Processing for Production of TRIP/TWIP Steels, Part 2: Reduction Studies. *JOM*. 2018;70(5):691-699. doi:10.1007/s11837-018-2773-8

120. Jayasekara AS, Monaghan BJ, Longbottom RJ. The kinetics of reaction of a coke analogue in CO2 gas. *Fuel*. 2015;154:45-51. doi:10.1016/j.fuel.2015.03.053

121. Yi L, Huang Z, Jiang T, Zhao P, Zhong R, Liang Z. Carbothermic Reduction of Ferruginous Manganese Ore for Mn/Fe Beneficiation: Morphology Evolution and Separation Characteristic. *Minerals*. 2017;7(9):167. doi:10.3390/min7090167

122. Morgan DJ, Milodowski AE, St J Warne S, Warrington S. Atmosphere dependence of the thermal decomposition of manganite, γ-MnO.OH. *Thermochim Acta*. 1988;135:273-277. doi:10.1016/0040-6031(88)87397-0

123. Zaki MI, Hasan MA, Pasupulety L, Kumari K. Thermochemistry of manganese oxides in reactive gas atmospheres: Probing redox compositions in the decomposition course MnO2 → MnO. *Thermochim Acta*. 1997;303(2):171-181. doi:10.1016/S0040-6031(97)00258-X

124. González C, Gutiérrez JI, González-Velasco JR, Cid A, Arranz A, Arranz JF. Transformations of manganese oxides under different thermal conditions. *J Therm Anal*. 1996;47(1):93-102. doi:10.1007/BF01982689

125. Zaki MI, Hasan MA, Pasupulety L, Kumari K. Thermochemistry of manganese oxides in reactive gas atmospheres: Probing catalytic MnOx compositions in the atmosphere of CO+O2. *Thermochim Acta*. 1998;311(1):97-103. doi:10.1016/S0040-6031(97)00417-6

126. Ngoy D, Sukhomlinov D, Tangstad M. Pre-reduction Behaviour of Manganese Ores in H2 and CO Containing Gases. *ISIJ Int*. 2020;60(11):7.

127. Larssen TA, Tangstad M. Effect of Moisture, Hydrogen, and Water–Gas Shift Reaction on the Prereduction Behavior of Comilog and Nchwaning Manganese Ores. *Metall Mater Trans B*. Published online April 16, 2022. doi:10.1007/s11663-022-02511-8

128. Hashizume T, Terayama K, Shimazaki T, Itoh H, Okuno Y. Reduction of MnFe2O4 without and with carbon. *J Therm Anal Calorim*. 2002;69(3):1045-1050. doi:10.1023/A:1020605416982

129. Biswas A, Das PKr, Singh V. Investigation of the decrepitation phenomenon of polymorphic materials: A theoretical and experimental study. *Powder Technol*. 2016;294:119-133. doi:10.1016/j.powtec.2016.02.020

130. International Organization for Standardization. *Iron Ores for Blast Furnace Feedstocks - Determination of the Decripitation Index*. International Organization for Standardization; 2015. Accessed January 9, 2019. http://www.iso.org/cms/render/live/en/sites/isoorg/contents/data/standard/06/21/62138.html

131. Faria GL, Vianna NCS, Jannotti N, Vieira CB. DECREPITATION OF BRAZILIAN MANGANESE LUMP. In: ; 2010:8.

132. Moholwa MS, Steenkamp JD, Rutto HL. Method to Quantify the Effect of Temperature and Rotational Speed on the Decrepitation of South African Manganese Ores in a Rotary Kiln. In: Peng Z, Hwang JY, Downey JP, et al., eds. *11th International Symposium on High-Temperature Metallurgical Processing*. The Minerals, Metals & Materials Series. Springer International Publishing; 2020:811-821. doi:10.1007/978-3-030-36540-0_72

133. Larssen TA. *Prereduction of Comilog- and Nchwaning-Ore*. PhD Thesis. Norwegian university of science and technology; 2020.

134. Moholwa MS. *Decrepitation of Manganese Ores during the Pre-Heating Process in a Rotary Kiln*. Master Thesis. Vaal University of Technology; 2020.

135. Faria GL, Tenório JAS, Jannotti N, da S. Araújo FG. Disintegration on heating of a Brazilian manganese lump ore. *Int J Miner Process*. 2013;124:132-137. doi:10.1016/j.minpro.2013.06.008

136. Faria GL, Tenório JAS, Jannotti N, Araújo FG da S. A geometallurgical comparison between lump ore and pellets of manganese ore. *Int J Miner Process*. 2015;137:59-63. doi:10.1016/j.minpro.2015.03.003

137. Faria GL, Jannotti N, Araújo FG da S. Particle disintegration of an important Brazilian manganese lump ore. *Rem Rev Esc Minas*. 2014;67(1):55-60. doi:10.1590/S0370-44672014000100008

138. Kalenga MK, Pan X. Pre-reduction of a South African manganese ore: more insight on the formation of phases. *Infacon XV Int Ferro-Alloys Congr*. Published online 2010:12.

139. Villiers JPRD. The crystal structure of braunite II and its relation to bixbyite and braunite. *Am Mineral*. 1980;65(7-8):756-765.

140. Naono H, Nakai K, Sueyoshi T, Yagi H. Porous texture in hematite derived from goethite: Mechanism of thermal decomposition of geothite. *J Colloid Interface Sci*. 1987;120(2):439-450. doi:10.1016/0021-9797(87)90370-5

141. Dose WM, Donne SW. Thermal Treatment Effects on Manganese Dioxide Structure, Morphology and Electrochemical Performance. *J Electrochem Soc*. 2011;158(8):A905. doi:10.1149/1.3597640

142. Ammasi A. Effect of Heating Rate on Decomposition Temperature of Goethite Ore. *Trans Indian Inst Met*. 2020;73(1):93-98. doi:10.1007/s12666-019-01806-w

143. ASTM E465:11. *Standard Test Methods for Determination of Manganese (IV) in Manganese Ores by Redox Titrimetry*. ASTM International; 2017.

144. Schneider CA, Rasband WS, Eliceiri KW. NIH Image to ImageJ: 25 years of image analysis. *Nat Methods*. 2012;9(7):671-675. doi:10.1038/nmeth.2089

145. Rørvik S, Lossius LP. Characterization of Prebake Anodes by Micro X-ray Computed Tomography. In: Ratvik AP, ed. *Light Metals 2017*. The Minerals, Metals & Materials Series. Springer International Publishing; 2017:1237-1245. doi:10.1007/978-3-319-51541-0_148

146. Røisi I, Aasly K. The effect of graphite filler in sample preparation for automated mineralogy – a preliminary study. Published online 2018:23.

147. Baron V, Gutzmer J, Rundlöf H, Tellgren R. The influence of iron substitution on the magnetic properties of hausmannite, Mn2+(Fe,Mn)3+2O4. Published online 1998. doi:10.2138/am-1998-7-810

148. Piotrowski K, Mondal K, Lorethova H, Stonawski L, Szymański T, Wiltowski T. Effect of gas composition on the kinetics of iron oxide reduction in a hydrogen production process. *Int J Hydrog Energy*. 2005;30(15):1543-1554. doi:10.1016/j.ijhydene.2004.10.013

149. Pineau A, Kanari N, Gaballah I. Kinetics of reduction of iron oxides by H2: Part I: Low temperature reduction of hematite. *Thermochim Acta*. 2006;447(1):89-100. doi:10.1016/j.tca.2005.10.004

150. Pineau A, Kanari N, Gaballah I. Kinetics of reduction of iron oxides by H2: Part II. Low temperature reduction of magnetite. *Thermochim Acta*. 2007;456(2):75-88. doi:10.1016/j.tca.2007.01.014

151. Bao S, Ringdalen E, Hanssen PØ, Julia N, Dabakk E. Evaluation of the analytical technique for determination of x in MnOx by titration method for Mn ore. *Int J Mater Res*. 2022;To be published.

152. Dose WM, Donne SW. Manganese dioxide structural effects on its thermal decomposition. *Mater Sci Eng B*. 2011;176(15):1169-1177. doi:10.1016/j.mseb.2011.06.007

153. Khawam A, Flanagan DR. Solid-State Kinetic Models: Basics and Mathematical Fundamentals. *J Phys Chem B*. 2006;110(35):17315-17328. doi:10.1021/jp062746a

154. Vyazovkin S, Burnham AK, Criado JM, Pérez-Maqueda LA, Popescu C, Sbirrazzuoli N. ICTAC Kinetics Committee recommendations for performing kinetic computations on thermal analysis data. *Thermochim Acta*. 2011;520(1):1-19. doi:10.1016/j.tca.2011.03.034

155. Bonalde A, Henriquez A, Manrique M. Kinetic Analysis of the Iron Oxide Reduction Using Hydrogen-Carbon Monoxide Mixtures as Reducing Agent. *ISIJ Int*. 2005;45(9):1255-1260. doi:10.2355/isijinternational.45.1255

156. Zuo H bin, Wang C, Dong J ji, Jiao K xin, Xu R sheng. Reduction kinetics of iron oxide pellets with H2 and CO mixtures. *Int J Miner Metall Mater*. 2015;22(7):688-696. doi:10.1007/s12613-015-1123-x

157. Fuller EN, Schettler PD, Giddings JCalvin. NEW METHOD FOR PREDICTION OF BINARY GAS-PHASE DIFFUSION COEFFICIENTS. *Ind Eng Chem*. 1966;58(5):18-27. doi:10.1021/ie50677a007

158. Ribeiro TR, Ferreira Neto JB, Takano C, Poço JGR, Kolbeinsen L, Ringdalen E. C–O–H2 ternary diagram for evaluation of carbon activity in CH4-containing gas mixtures. *J Mater Res Technol*. 2021;13:1576-1585. doi:10.1016/j.jmrt.2021.05.033

159. Nanjundaswamy KS, Sankarshanamurthy MN. Low-temperature stabilization of pure MnO. *Bull Mater Sci*. 1985;7(5):459-463. doi:10.1007/BF02744055

160. Todd B, Young JB. Thermodynamic and transport properties of gases for use in solid oxide fuel cell modelling. *J Power Sources*. 2002;110(1):186-200. doi:10.1016/S0378-7753(02)00277-X

161. Poling BE, Prausnitz JM, O'Connell JP. *The Properties of Gases and Liquids*. 5th ed. McGraw-Hill; 2001.

Appendix A Weight deviations

In weighing the crucible before and after cleaning, small weight differences were occasionally observed. Some dust from the sample material or from carbon deposition could be stuck to the walls or trapped between the double wall of the crucible, however scaling of the crucible material was also observed on some occasions. Hence, it is not clear that these weight changes were associated with the sample mass itself and it was not included in any calculations.

Several investigations has previously been conducted in the same experimental setup and both Larssen[133] and Reiersen[92] reported inconsistent drifting of the weight in non-isothermal experiments. Reiersen[92] conducted two experiments using quartz where the weight increased by about 1.5 g and 2.3 g for the parallel experiments. A linear function based on the early parts of these experiments was subtracted from all experimental curves to compensate for the drifting. Larssen[133] used the off-gas analysis to determine the weight loss behavior and scaled it to the measured sample weight before and after experiments. In this work, the off-gas analysis can be used for the CO/CO_2 gas mixtures, but not when hydrogen is used since hydrogen is not measured in the off gas and the quantity of condensed water at the gas outlet is unknown. Hence, the measured weight signal must be used, and some investigation was conducted to map different influences on the weight signal that is not related to the weight loss of the sample and to assess the consistency of weight deviations when utilizing an isothermal heating program.

Figure A-1 show the weight behavior from three experiments with Nchwaning ore in Ar. There is a peak in the weight at about 2 min that corresponds to when the furnace is raised to surround the crucible. The difference between the highest and the lowest weight loss was 1.3 g. Manganite is expected to decompose fully at this temperature. Chemical- and off-gas analysis indicated that some carbonates had decomposed. CO2 release initiated around 480-540 °C and is shown on the secondary axis in Figure A-1. Higher oxides may decompose in an Ar atmosphere; however, this was not apparent from the chemical analysis. To avoid the influence of carbonate decomposition and further investigate the behavior of the furnace itself, experiments were conducted in pure CO_2. The results from these experiments are shown in Figure A-2. In two of the experiments, the observed weight-loss was in a similar range to the Ar experiments, while the two others ended up at a similar weight to the initial weight peak. It was also observed that the furnace balance drifted (randomly) from the time when the crucible was mounted in the setup to the point where the experiments were started, and that this drifting was reduced with time. Thus, to reduce the impact of inconsistent drifting of the weight signal, subsequent experiments were prepared and mounted

in the setup the day before it was conducted. In both experiment types, the variation in measured weight is probably a combination of weight drifting and ore heterogeneity.

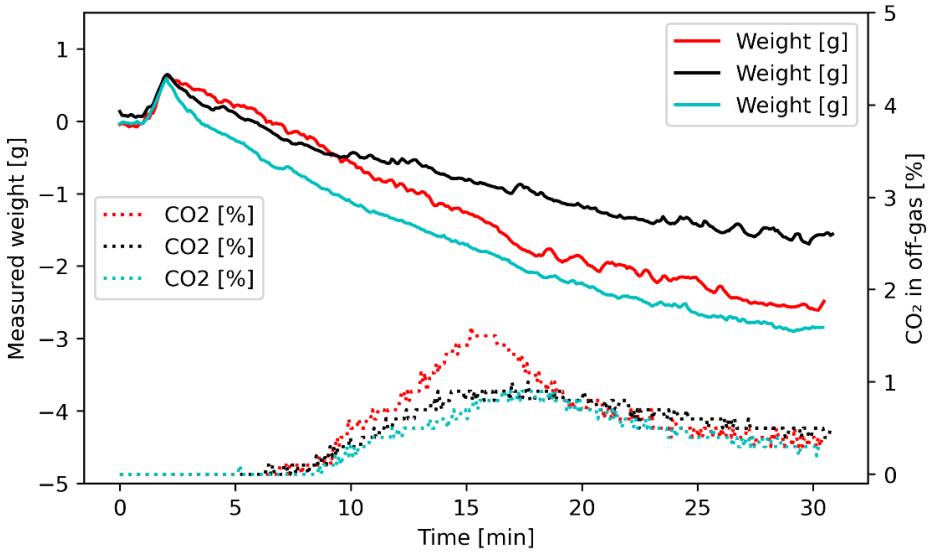

Figure A-1: Parallel experiments with Nchwaning ore in Ar gas at 790 °C. Shows the weight loss and CO_2 in the off gas as functions of time.

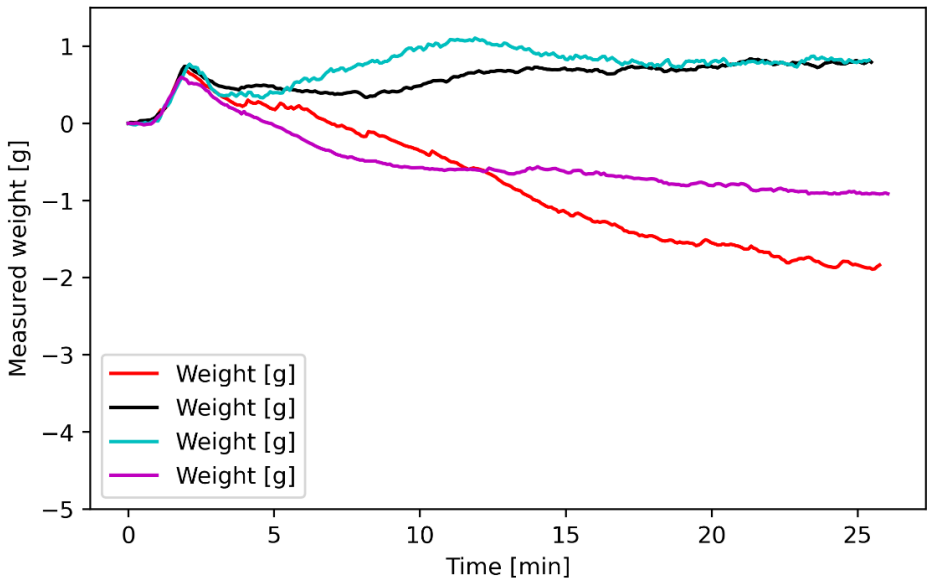

Figure A-2: The weight loss as a function of time for reduction of Nchwaning ore in CO_2 at 790 °C

To avoid weight changes caused by reactions in the ore, experiments using quartz as an inert material was conducted. The quartz was dried to remove potential moisture and experiments were conducted in Ar using 150 g quartz to keep the weight the same as in the reduction experiments. Different temperatures were investigated, and the results are shown in Figure A-3. The x-axis is set to 0 when the furnace is raised, and the peak observed in Figure A-1 and Figure A-2 is also observed here where the peak height is seen to increase with increasing temperature. Following this peak, the weight is seen to drop and increase again before it drops sharply at the end of the experiment as the furnace is lowered (~90 min).

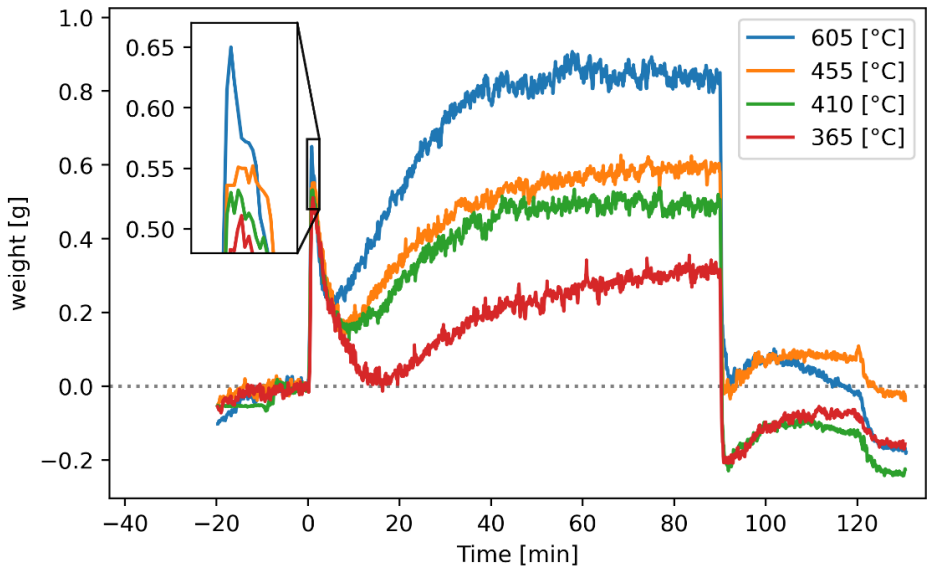

Figure A-3: Shows the weight behavior as a function of time when using 150 g inert material (quartz) in Ar.

The weight changes in Figure A-3 are associated with the behavior of the furnace, and some of the changes may be explained by buoyancy and density variations inside and outside the crucible. The densities of selected gases at 0 °C and 1 atm (=101.325 kPa) is given in Table A-1.

$$PV = nRT \tag{21}$$

The change of gas density as a function of temperature can be described using the ideal gas law, equation (21), where P is pressure [Pa], V is volume [m^3], n is number of moles [mol], R is the universal gas constant [J/mol·K] and T is temperature [K]. Substituting n with m/M, where M is the molar mass [g/mol] and m is mass [g], and rearranging yields:

$$\frac{m}{V}T = \rho T = \frac{PM}{R} \quad (22)$$

The expression on the right-hand side of equation (22) is constant for a specific gas composition in the current setup, hence:

$$\frac{m(T)}{V} = \rho(T) = \rho_0 \frac{T_0}{T} \rightarrow m(T) = \rho_0 V T_0 \frac{1}{T} \quad (23)$$

Where T_0 and ρ_0 are the reference temperature and density, respectively (Table A-1).

Table A-1: Densities of selected gases at 273.15 K. From HSC Chemistry 9 [18]

Gas	Density [kg/m^3]
Ar	1,782
CO	1,250
CO_2	1,964
H_2	0,090
H_2O	0,804
N_2	1,250
O_2	1,428
Syn. air*	1,287

*weighted average 21% O_2 – 79 % N_2

The internal and external volume of the crucible are not equal due to internal features of the crucible. In addition, there are uncertainties regarding the weight influence of the gas content inside the flexible tubes connected to the crucible. After reduction of Comilog ore, oxidation was observed and the magnitude of weight change when changing from Ar to synthetic air was needed to measure the weight gain during oxidation. Figure A-4 shows the measured weight loss from an experiment run to measure the influence of gas density at room temperature. The experiment was done with 150 g quartz in the crucible, which is the same sample weight used in all experiments in this work. The gas input was alternated between synthetic air and argon and the difference in weight was 0.41 g (horizontal lines, Figure A-4). A slight drifting in the weight signal can also be observed between the different gas changes. Fully exchanging the gas atmosphere at room temperature was seen to take about 1.5 minutes (88 s) (vertical lines, Figure A-4) at 21.9 °C.

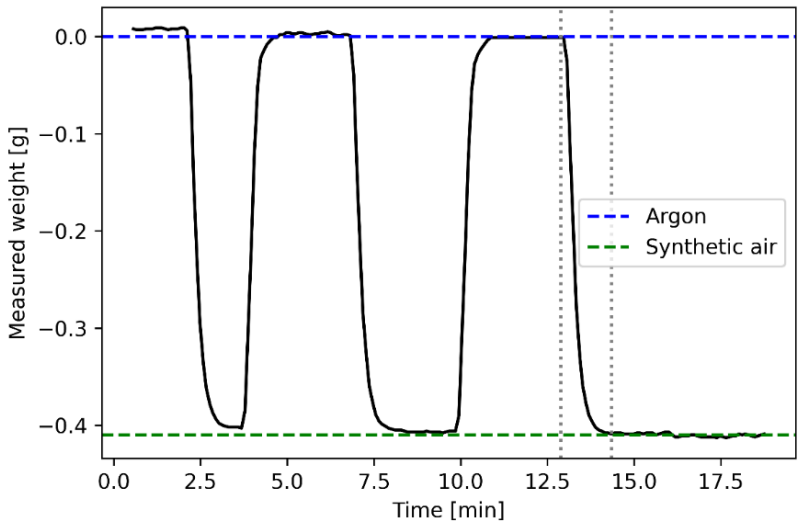

Figure A-4: Measured weight change following the change of input gas between pure argon and synthetic air (79 % N_2 – 21 % O_2). A slight drifting in the weight signal can be observed.

$$\rho_{Ar} - \rho_{Air} = \frac{m_{Ar}}{V_c} - \frac{m_{air}}{V_c} \rightarrow V_c = \frac{m_{Ar} - m_{Air}}{\rho_{Ar} - \rho_{Air}} \quad (24)$$

Using the densities (Table A-1) and measured temperature, the volume of gas in the crucible was found to be 0.894 dm^3 (89.4E-5 m^3) according to equation (24).

When the furnace is raised to surround the crucible, the decreased buoyancy of the crucible in the preheated furnace will cause an increase in the measured weight. This increase may be calculated using equation (23) and is shown in Figure A-5 (External buoyancy). According to equation (23), the weight should be lower with increasing temperature, which is in line with the observations from Figure A-3. The difference between the predicted and measured weight increase may be explained by that the crucible is not fully submerged in the furnace (Figure 3-4b) such that the effective volume of displaced hot air is lower than the full crucible volume.

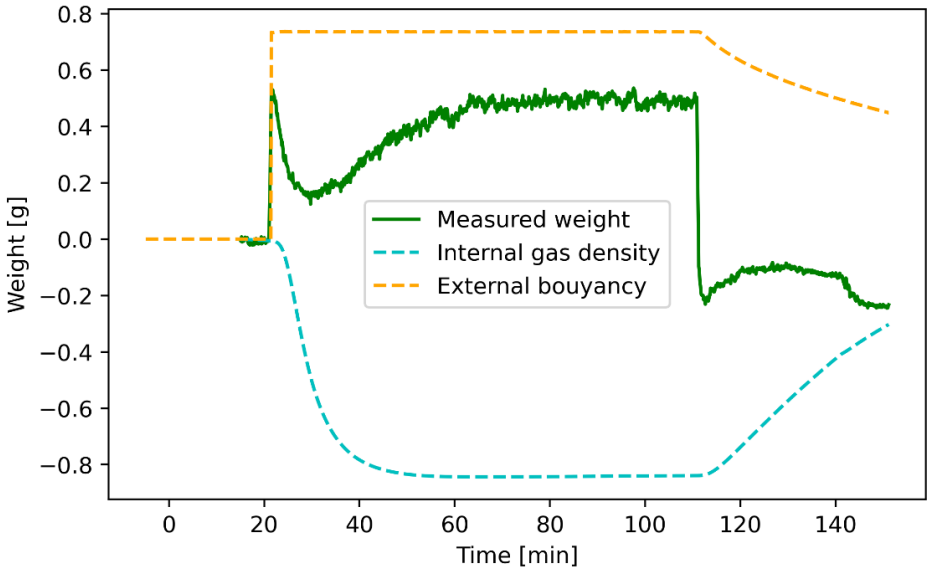

Figure A-5: Shows the measured weight from the 410 °C Ar -quartz experiment (Figure A-3) with the calculated weight changes from internal density change of the Ar gas and buoyancy based on the external dimensions of the crucible. The external buoyancy is calculated using the density of synthetic air.

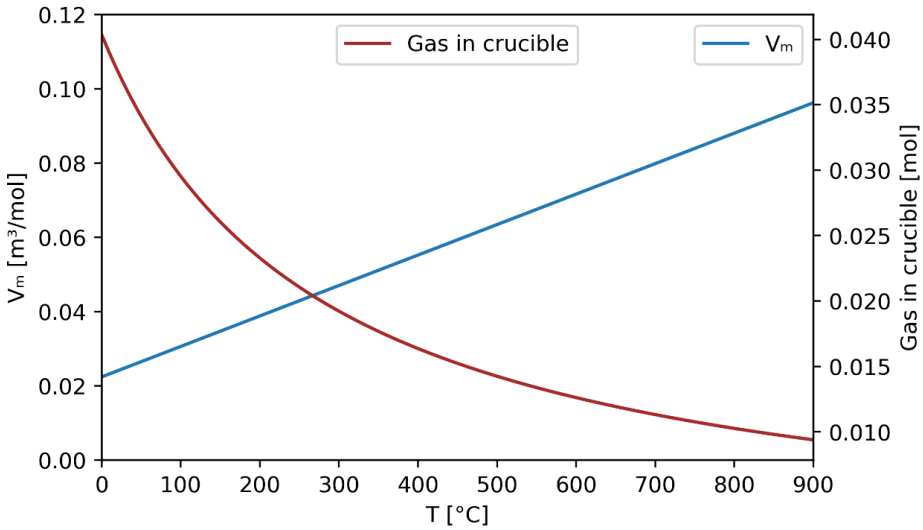

Figure A-6: The molar volume of gas and the number of moles of gas in the experimental setup as functions of temperature.

Figure A-6 shows the molar volume of gas and the number of moles of gas in the crucible, as functions of temperature based on equation (21). It is seen that the number of moles of gas in the crucible at 900 °C is about one quarter of that at

0 °C. Hence, a weight loss associated with the internal heating of the crucible is expected. Using the measured internal volume of the crucible and the density of Ar (Table A-1) together with the sample temperature measurements, the weight change associated with the changing gas density inside the crucible was calculated with equation (23), and is also shown in Figure A-5 (Internal gas density). The calculated weight loss due to reduced density of Ar is seen to be slightly larger compared to the buoyancy effect despite that the internal volume of the crucible is smaller than the external volume. This is due to the higher density of Ar compared to air. It is seen that the initial weight loss following the buoyancy peak corresponds to the weight loss predicted by the density change of Ar, however the weight is seen to increase again, an effect that is not explained by the buoyancy or density changes. This weight increase is suspected to be associated with the softening of the flexible rubber tubing due to increased temperature though it could not be verified experimentally at this point.

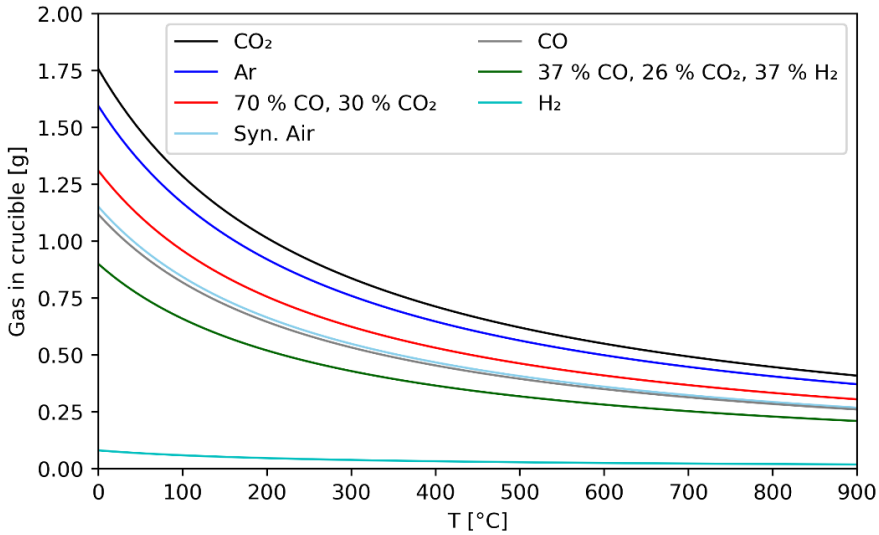

Figure A-7: The mass of gas contained in the crucible for the different gases and gas mixtures. The density of the gas mixtures was calculated using weighted averages

Figure A-7 shows the calculated weight of gas in the crucible for selected gas mixtures. Due to the different densities, the absolute weight change will be different for each gas mixture.

Appendix B XRD patterns for Nchwaning ore

This appendix contains the XRD data from the analysis of Nchwaning ore that is not included in the results section.

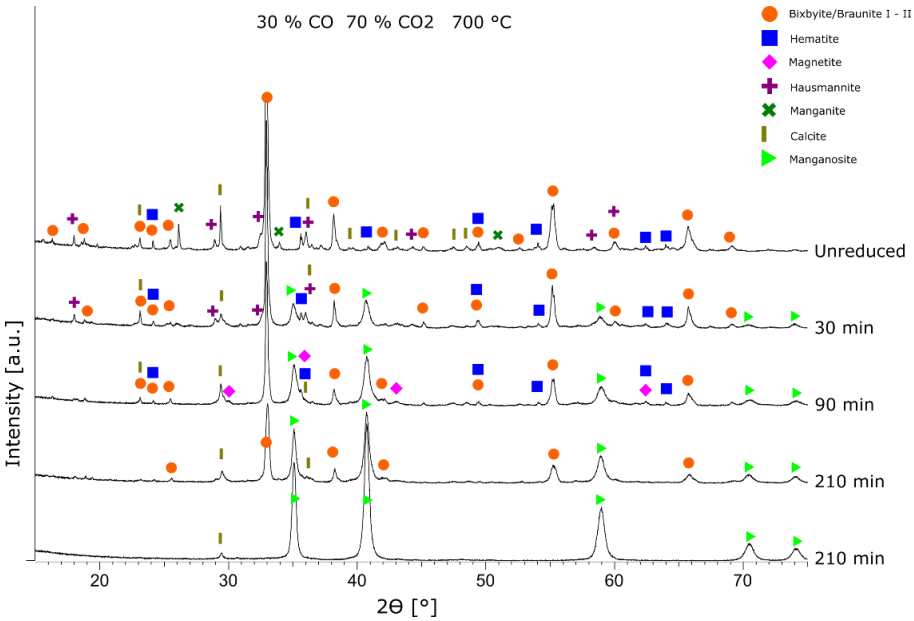

Figure B-1: X-ray diffraction patterns and identified phases in unreduced ore and samples reduced in 30% CO and 70% CO_2 at 700 °C. The main bixbyite/braunite peak (33°) is cropped for clarity in the figure.

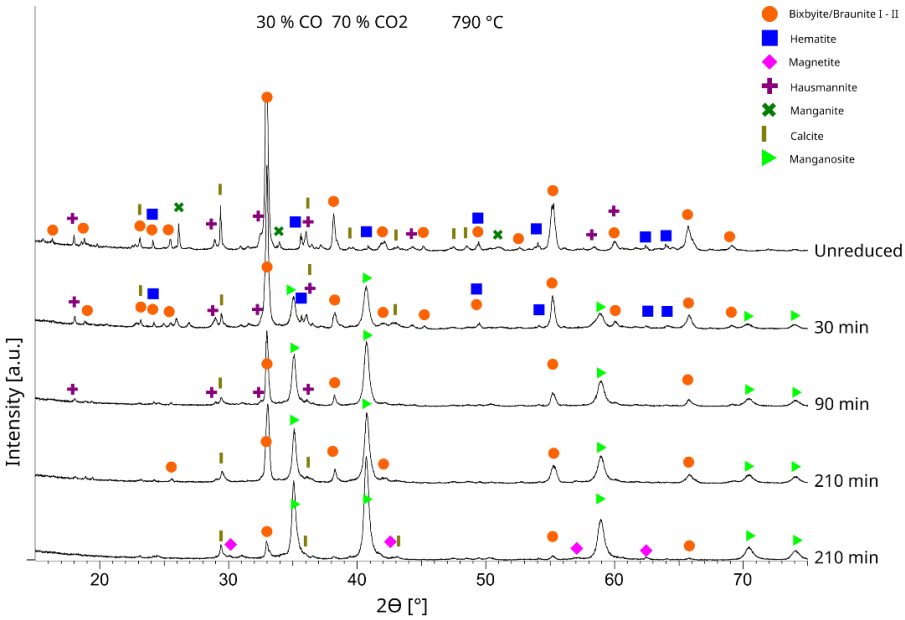

Figure B-2: X-ray diffraction patterns and identified phases in unreduced ore and samples reduced in 30% CO and 70% CO_2 at 790 °C. The main bixbyite/braunite peak (33°) is cropped for clarity in the figure.

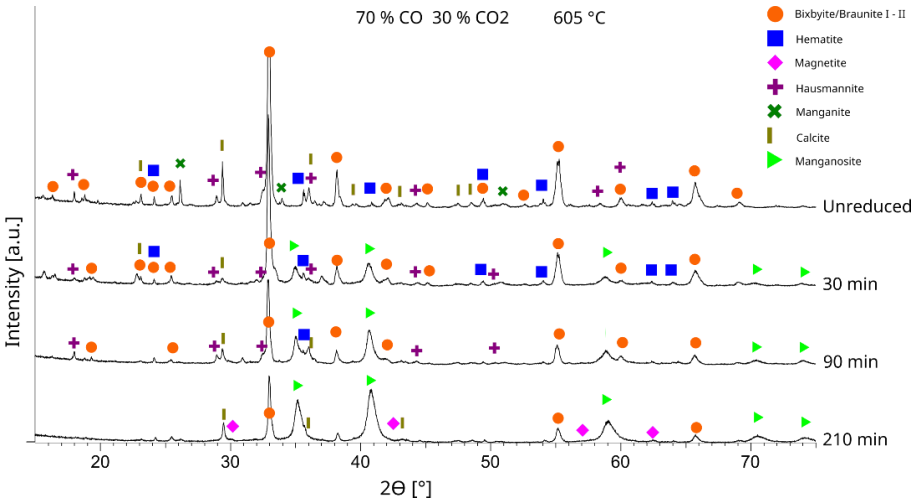

Figure B-3: X-ray diffraction patterns and identified phases in unreduced ore and samples reduced in 70% CO and 30% CO_2 at 605 °C. The main bixbyite/braunite peak (33°) is cropped for clarity in the figure.

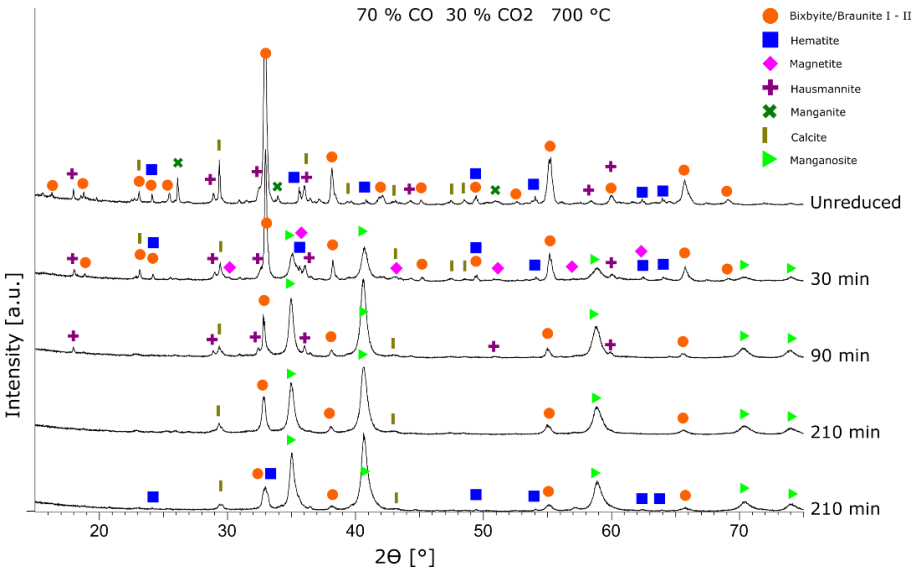

Figure B-4: X-ray diffraction patterns and identified phases in unreduced ore and samples reduced in 70% CO and 30% CO_2 at 700 °C. The main bixbyite/braunite peak (33°) is cropped for clarity in the figure.

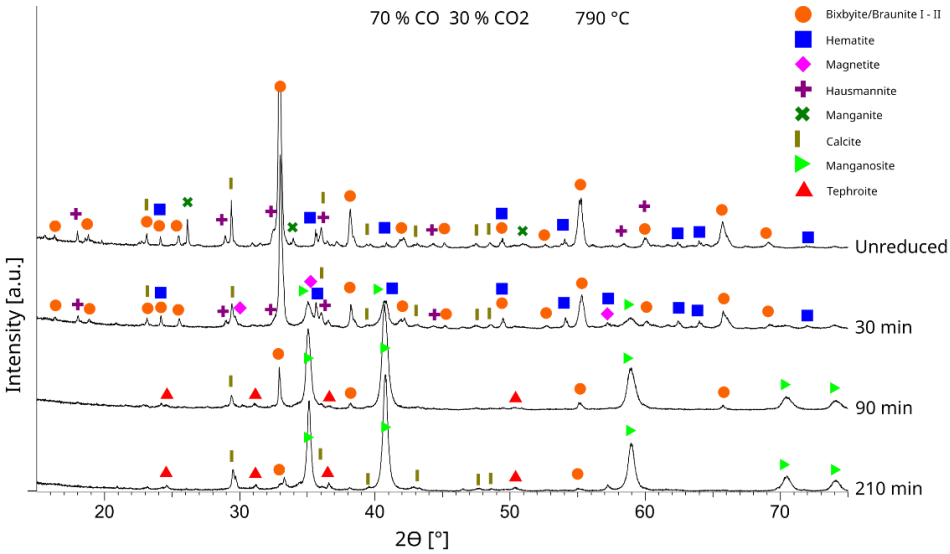

Figure B-5: X-ray diffraction patterns and identified phases in unreduced ore and samples reduced in 70% CO and 30% CO_2 at 790 °C. The main bixbyite/braunite peak (33°) is cropped for clarity in the figure.

Appendix C Thermocouple error correction

One experiment was conducted while the thermocouple was failing. The erroneous temperature values were removed, and the temperature measurements were recreated based on the remaining data (see Figure C-1)

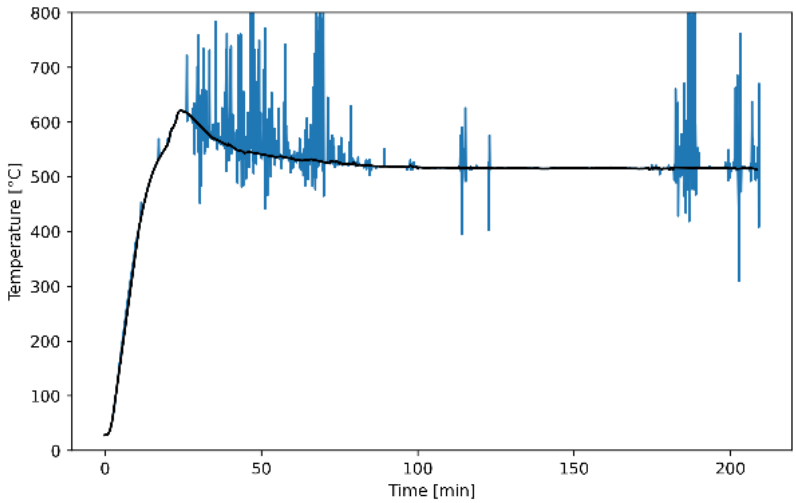

Figure C-1: Correction of temperature measurement in the 515 °C, 16 % CO – 68 % CO_2 – 16 % H_2 experiment (C11H). The blue curve is the original measurement, and the black curve is the recreated measurement.

Appendix D Off-gas analysis correction

The measured values from the off-gas analyzer connected to the furnace was observed to drift between experiments. To obtain consistent off-gas data, the curves were calibrated so that the gas concentration started on the input value of the utilized gas composition by using data from the initial part of the experiment, where the crucible was at room temperature and the gas composition is fixed (no reactions). Figure D-1 shows an example of the result from such calibration. Figure D-2 and Figure D-3 shows the method for calibration; two points from the data at room temperature with the specific gas composition were selected for each experiment, and the measured data was multiplied by a correction factor determined by these points. To assess this calibration, the sum of CO and CO_2 was plotted for the experiments in CO/CO_2 gas mixtures (Nchwaning), which should sum up to 100 %. Figure D-4 and Figure D-5 shows this sum before and after calibrations, respectively, where it can be seen that the calibration improved the consistency of the measurements.

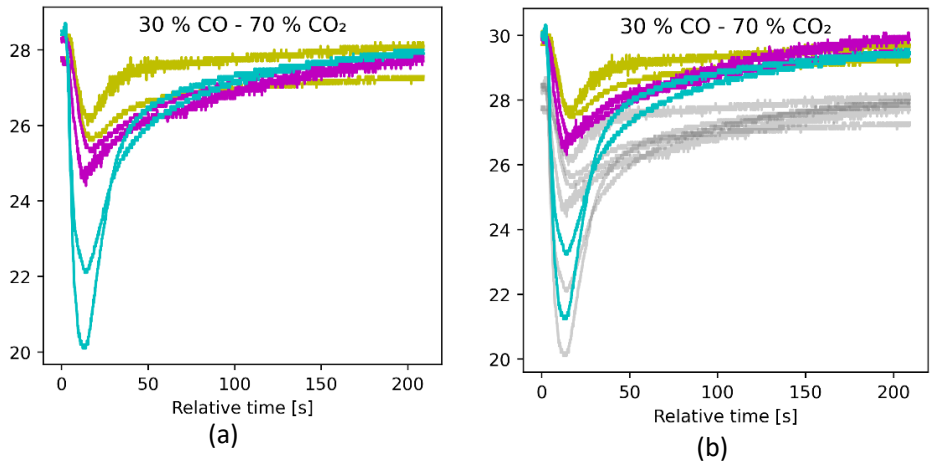

Figure D-1: Shows (a): the measured CO in the off-gas and (b) the corrected values (with original values in gray) for the 30% CO containing gas mixtures. Notice that the corrected values start at 30 % CO.

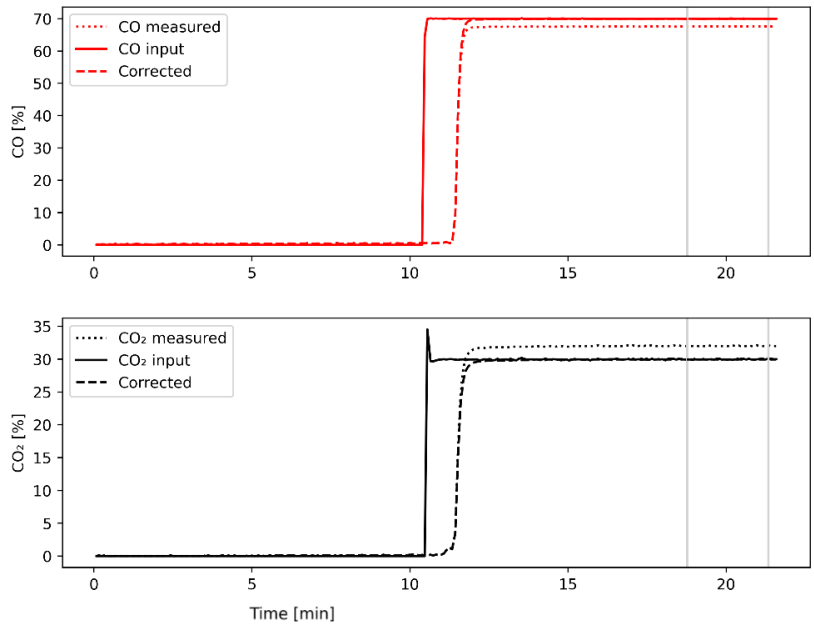

Figure D-2: Shows the measured, input and corrected CO and CO_2 for a 70% CO – 30 % CO_2 gas mixture

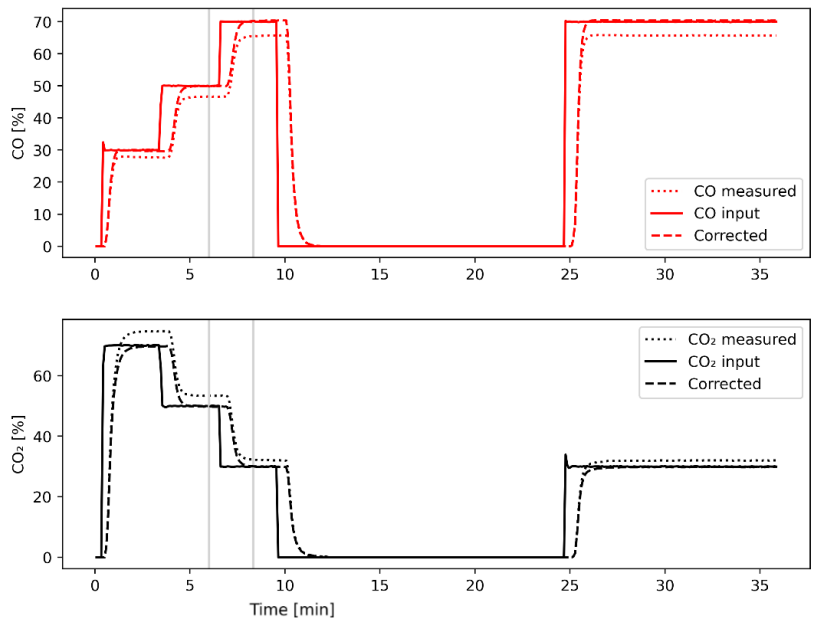

Figure D-3: Shows the measured, input and corrected CO and CO_2 for a 70% CO – 30 % CO_2 gas mixture

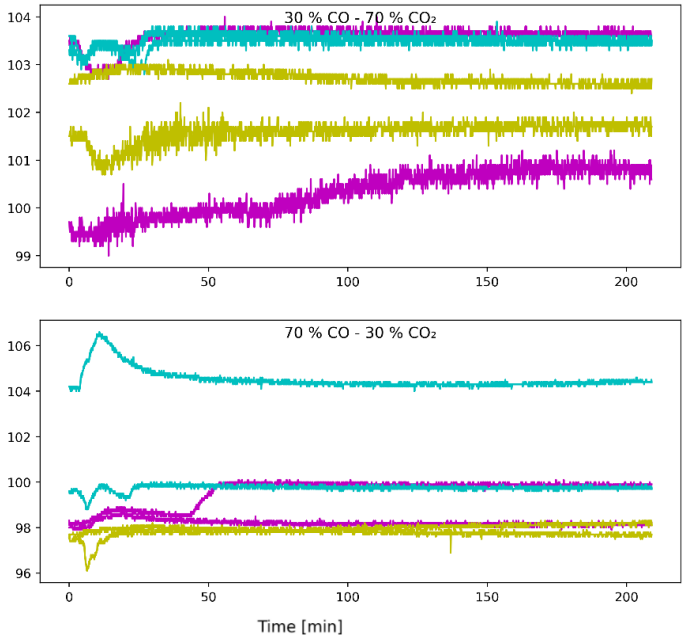

Figure D-4: %CO + %CO2 before correction, Nchwaning ore.

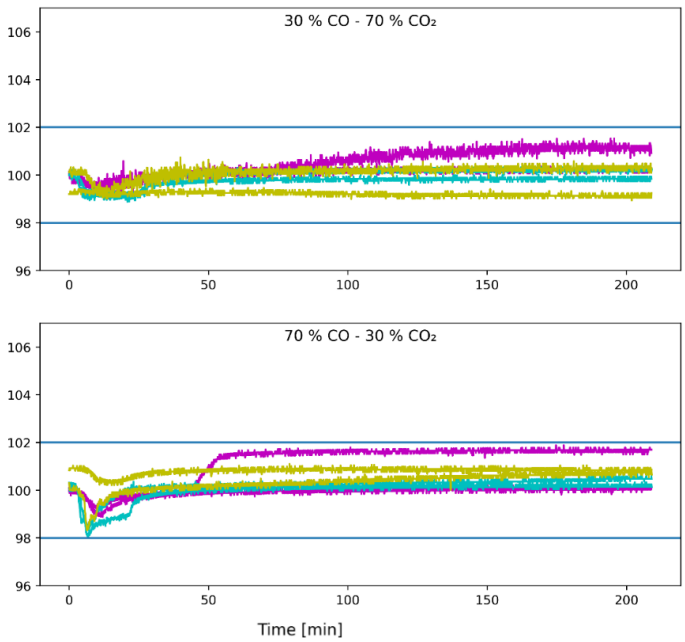

Figure D-5: %CO + %CO2 after correction, Nchwaning ore. Horisontal lines at 100 ± 2 %

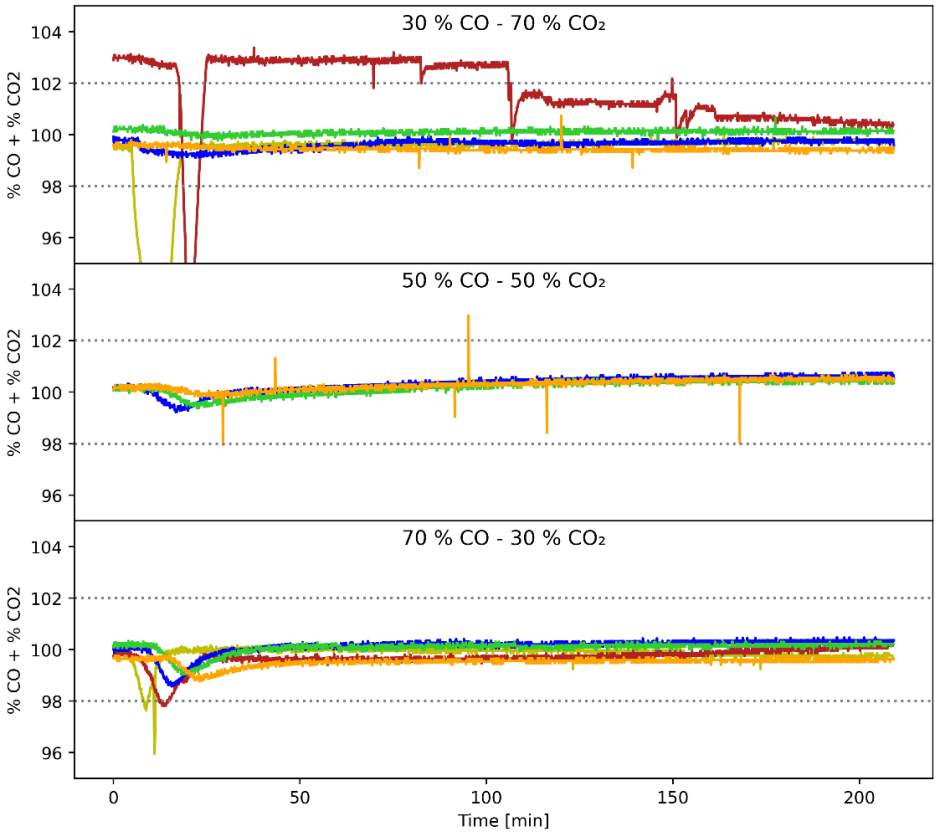

Figure D-6: %CO + %CO2 after correction Comilog ore. Horizontal lines at 100 ± 2 %

Appendix E Cumulative size distributions

The cumulative particle size distributions for Nchwaning and Comilog ore are given in Figure E-1 and Figure E-2, respectively.

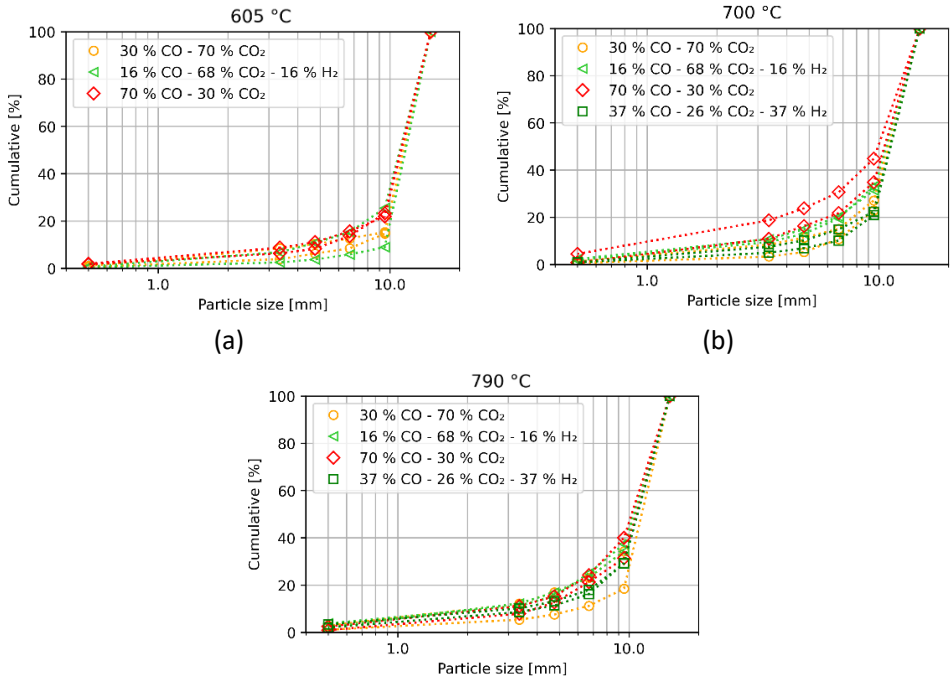

Figure E-1: Cumulative particule size distributions for Nchwaning ore.

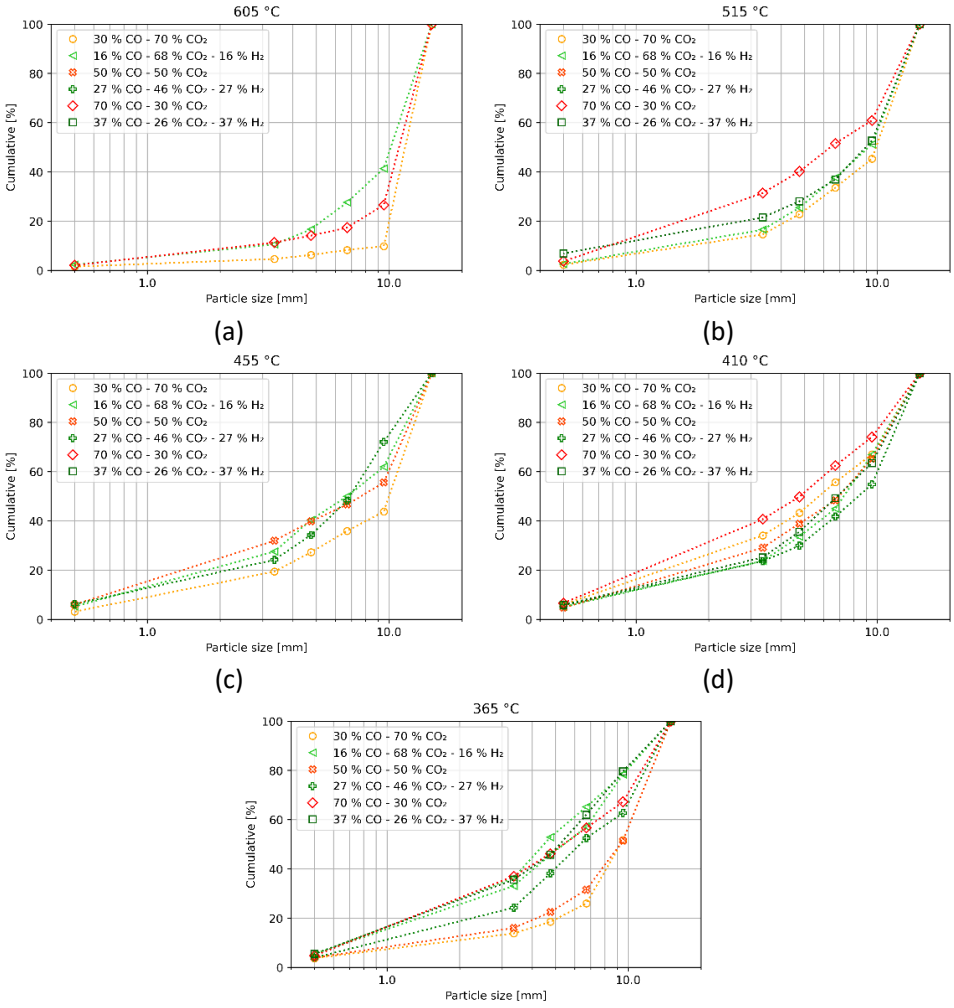

Figure E-2: Cumulative particule size distributions for Comilog ore

Appendix F Mineralogy measurements

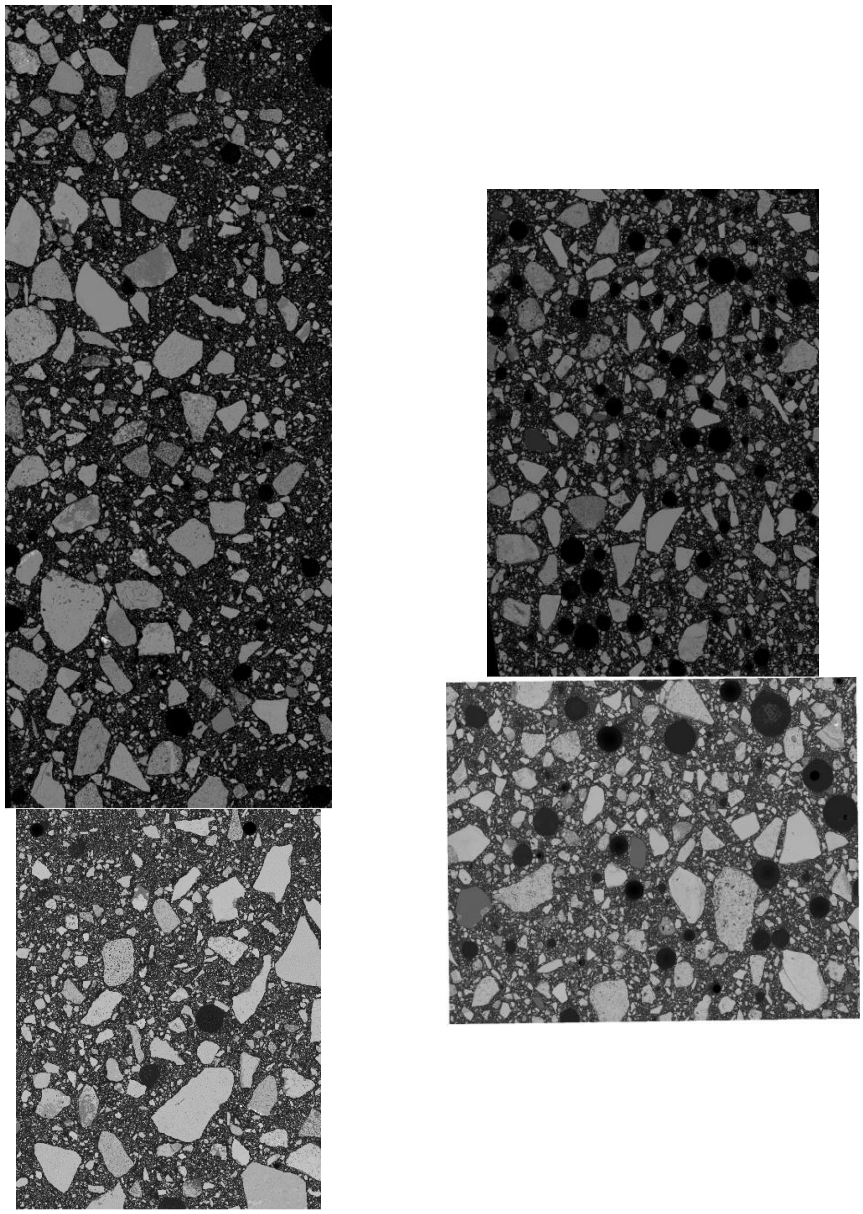

Figure F-1: Backscatter image of the areas used to characterize Nchwaning ore (AMS). (a): Nchwaning: 3 mm · 7.5 mm and 2.8 mm · 3.7 mm. (b) Comilog: 3.1 mm · 3.7 mm and 3.9 mm · 5.7 mm

Figure F-1 shows the backscatter images of the characterized areas. An example of the quantified grains is given in Figure F-2. The grains are from the top image in Figure F-1a.

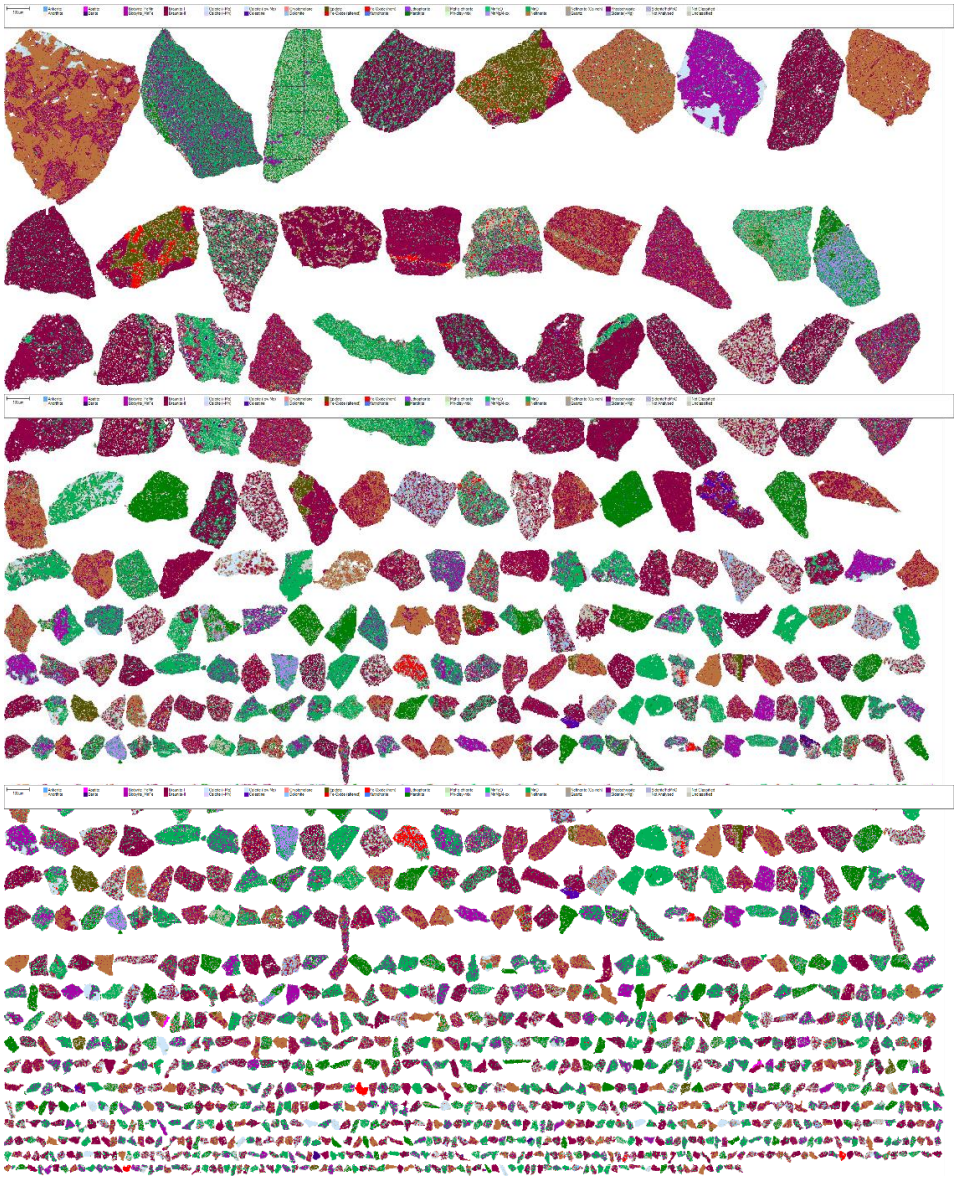

Figure F-2: An example of the quantified grains. Particles from Figure F-1a.

Appendix G Binary diffusion coefficients

Fuller et al[157] developed a method for predicting binary diffusion coefficients that was later was evaluated and recommended by Todd and Young[160] after comparison with other approaches. The binary diffusion coefficient [cm^2/s] can be calculated by equation (G1):

$$D_{AB} = \frac{0.00143T^{1.75}}{pM_{AB}^{\frac{1}{2}}\left[V_A^{\frac{1}{3}} + V_B^{\frac{1}{3}}\right]^2} \quad \text{(G1)}$$

where

$$M_{AB} = 2\left[\frac{1}{M_A} + \frac{1}{M_B}\right]^{-1} \quad \text{(G2)}$$

T is the temperature [K] p is the pressure M_i is the molar mass [g/mol] and V_i is the diffusion volume (Table G-1).

Table G-1: Diffusion volume for selected gases[160,161]

Gas	Diffusion volume
H_2	6.12
CO	18.0
H_2O	13.1
CO_2	26.7
O_2	16.3
N_2	18.5

ISBN 978-82-326-6893-9 (printed ver.)
ISBN 978-82-326-5267-9 (electronic ver.)
ISSN 1503-8181 (printed ver.)
ISSN 2703-8084 (online ver.)

NTNU

Norwegian University of
Science and Technology